

Application of a SPICE Model for Multiconductor Transmission Lines in Electromagnetic Topology

Haiyan Xie¹, Jianguo Wang^{1,2}, Ruyi Fan^{1,2}, and Yinong Liu¹

¹Department of Engineering Physics, Tsinghua University, China

²Northwest Institute of Nuclear Technology, China

Abstract— This paper presents a method in electromagnetic topology, which uses a SPICE model for multiconductor transmission lines excited by an incident electromagnetic field, while the conventional method uses the frequency domain Baum-Liu-Tesche (BLT) equation and inverse fast Fourier transform. The proposed method is used to compute three cases directly in time domain, and the transient load voltages of each case are obtained. The results agree very well with those through the conventional method. The proposed method can be used to compute the transient voltage responses of nonlinear or time-varying loads, while the conventional method can only be used for linear and time invariant loads. The time needed by the proposed method is much less than that cost by the conventional method. Further more, the proposed method is more convenient to use than the time domain BLT equation which calls for the costly temporal convolution.

1. INTRODUCTION

The frequency domain Baum-Liu-Tesche (BLT) equation [1, 2], derived from the transmission-line equations, has been used in the electromagnetic topology (EMT) to describe the behavior of voltages and currents at all the junctions of cables in the network. This method can only be used to compute linear and time invariant systems, however, most electronic systems nowadays are nonlinear and time-varying. The time domain BLT equation was developed by Baum [3], and illustrated by Tesche [4]. However, it needs time-consuming temporal convolution.

This paper proposes application of a SPICE model for lossless transmission lines excited by an incident electromagnetic field in electromagnetic topology. The SPICE model, developed by Paul [5, 6], is usually used in circuit analysis. We believe that it may be used in the EMT, because it is derived from the transmission-line equations as well. The SPICE model can be used to compute transient responses of the terminations of transmission lines. It can be implemented as SPICE subcircuit model and is independent of the terminations for which nonlinear or time variant loads can be easily incorporated. Transmission-line networks, playing an important role in electromagnetic topology, can be computed just by connecting the SPICE subcircuit model of each transmission line composing the network.

Three cases, two transmission lines and a transmission-line network, all excited by a plane-wave electromagnetic field, are studied in this paper. The results obtained by the proposed method are compared with those via the frequency-domain BLT equation and inverse fast Fourier transform (IFFT), and they agree well.

2. BRIEF REVIEW OF THE SPICE MODEL

The SPICE model for multiconductor lossless transmission lines can be derived from transmission-line equations. With a similarity transformation, the transmission-line equations can be transformed into the form of mode quantities, and the relation between the terminal mode voltages and currents can be obtained. For single line, the SPICE model has a simple form. Only a brief review of the SPICE model for a single lossless line will be given in what follows, due to the length of the paper.

For a single lossless line over an infinite and perfectly conducting ground excited by an incident electromagnetic field, the relation between the terminal voltages and currents the line can be written as (More details can be found in [6].)

$$V(0, t) - Z_C I(0, t) = [V(\mathcal{L}, t - T) - Z_C I(\mathcal{L}, t - T)] + E_0(t) \quad (1a)$$

$$V(\mathcal{L}, t) + Z_C I(\mathcal{L}, t) = [V(0, t - T) + Z_C I(0, t - T)] + E_{\mathcal{L}}(t), \quad (1b)$$

where $V(0, t)$, $V(\mathcal{L}, t)$ and $I(0, t)$, $I(\mathcal{L}, t)$ are the terminal voltages (with respect to the ground) and currents of the line, respectively. Z_C is the characteristic impedance of the line. \mathcal{L} is the length of

the line. T is the transit time of the waves on the line, defined as $T = \mathcal{L}/v$, where v is the velocity of the waves propagation. $E_0(t)$ and $E_{\mathcal{L}}(t)$ are controlled sources due to the incident electromagnetic field.

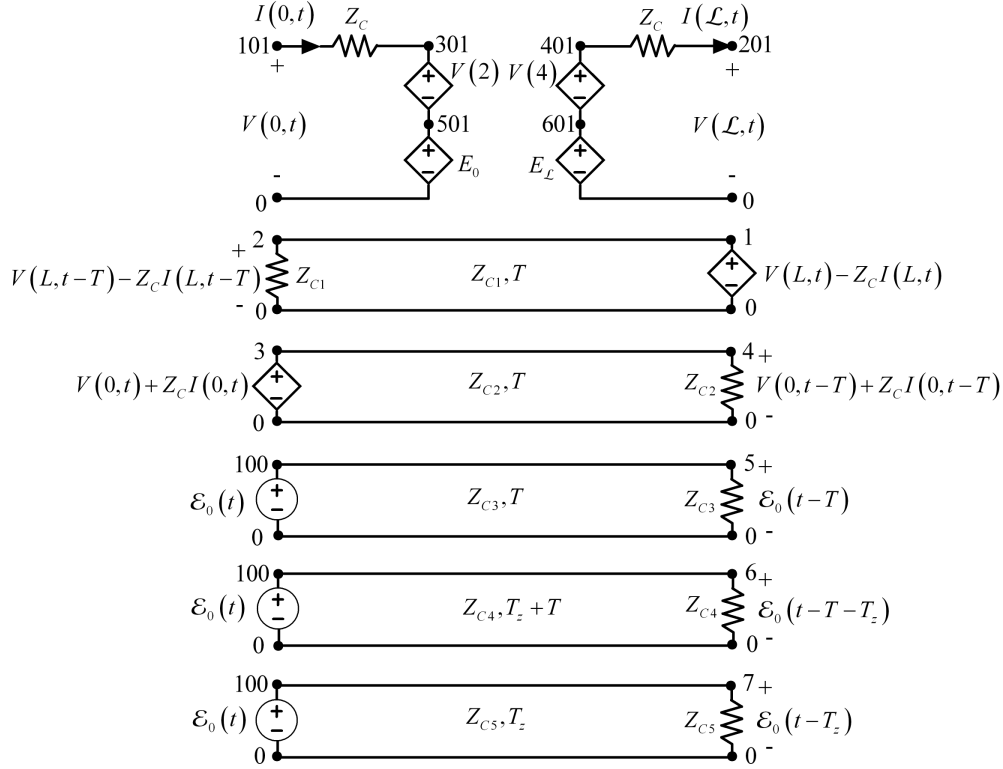


Figure 1: The SPICE model.

When the incident electromagnetic field is a plane wave, and the cross-sectional dimension of the line is electrically small compared with the wavelength of the incident field, $E_0(t)$ and $E_{\mathcal{L}}(t)$ can be simplified approximately as

$$E_0(t) \cong -2h \left[e_x - e_z \left(\frac{\mathcal{L}}{v_x(T_z + T)} \right) \right] [\varepsilon_0(t) - \varepsilon_0(t - T - T_z)] \quad (2a)$$

$$E_{\mathcal{L}}(t) \cong 2h \left[e_x - e_z \left(\frac{\mathcal{L}}{v_x(T_z - T)} \right) \right] [\varepsilon_0(t - T) - \varepsilon_0(t - T_z)], \quad (2b)$$

where e_x , e_y , and e_z are the components of the incident electric field vector along the x , y , and z axes. v_x is the velocity of the wave propagation along the x axis. T_z is the transient time along the line of the z component of the wave propagation vector, defined as $T_z = \mathcal{L}/v_z$, where v_z is the velocity of the wave propagation along the z axis. $\varepsilon_0(t)$ is the time waveform of the incident electric field.

The SPICE model for a single lossless line over an infinite and perfectly conducting plane excited by a plane-wave electromagnetic field is shown as Figure 1.

3. BRIEF INTRODUCTION TO THE BLT EQUATION

Using $[\hat{\mathbf{W}}(0)]$ and $[\hat{\mathbf{W}}_s]$ to represent outgoing and source wave supermatrices respectively, the frequency-domain BLT equation can be expressed as

$$\{[\mathbf{I}] - [\hat{\mathbf{S}}] \cdot [\hat{\mathbf{\Gamma}}]\} \cdot [\hat{\mathbf{W}}(0)] = [\hat{\mathbf{S}}] \cdot [\hat{\mathbf{W}}_s], \quad (3)$$

where $[\mathbf{I}]$ is the identity supermatrix. $[\hat{\mathbf{S}}]$ and $[\hat{\mathbf{\Gamma}}]$ are the network scattering and propagation supermatrices, respectively. The symbol \wedge denotes complex quantities.

In the case of transmission lines, the frequency-domain BLT equation can be written in a simple form. The simple form will not be given here due to the length of the paper, and can be found in [7].

4. COMPUTED RESULTS AND ANALYSIS

The transient voltages of three cases have been computed using the proposed method, and compared with those obtained with the frequency-domain BLT equation and IFFT. The latter method was used for both cases, with loss considered and with loss ignored.

The three cases are a single wire, multiconductor transmission lines, and a transmission-line network excited by an incident plane-wave electromagnetic field, where the first and third cases are over an infinite perfectly-conducting ground. The time waveform of the incident electric field is a biexponential pulse, described by the expression $\varepsilon_0(t) = e^{-t/t_1} - e^{-t/t_2}$ where $t_1 = 0.5$ ns and $t_2 = 0.2$ ns. The direction of the incident field is defined as Figure 2.

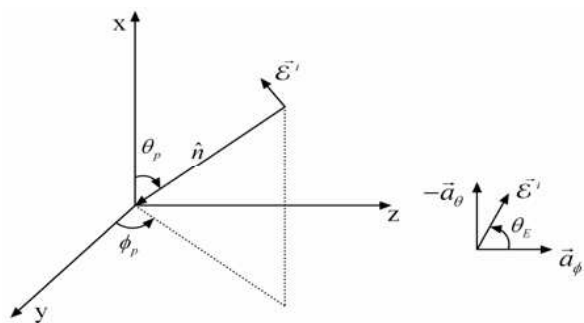


Figure 2: The direction of the incident field.

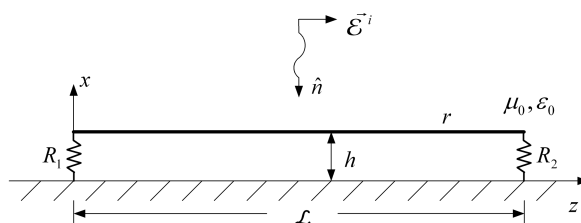


Figure 3: Single lossless wire over an infinite and perfectly conducting ground.

The first case is shown in Figure 3, where the length of the line is $\mathcal{L} = 1$ m, and the height and radius of the line are $h = 1$ cm and $r = 1$ mm, respectively. The loads of the line are $R_1 = 50 \Omega$ and $R_2 = 100 \Omega$. The angles describing the direction of the incident electric field are $\theta_p = 0$, $\phi_p = -90^\circ$, and $\theta_E = 90^\circ$. The transient voltages of the two loads are shown in Figure 4, where “BLT-lossy” refers to using the BLT equation with the loss of the line considered, while “BLT-lossless” with the loss ignored.

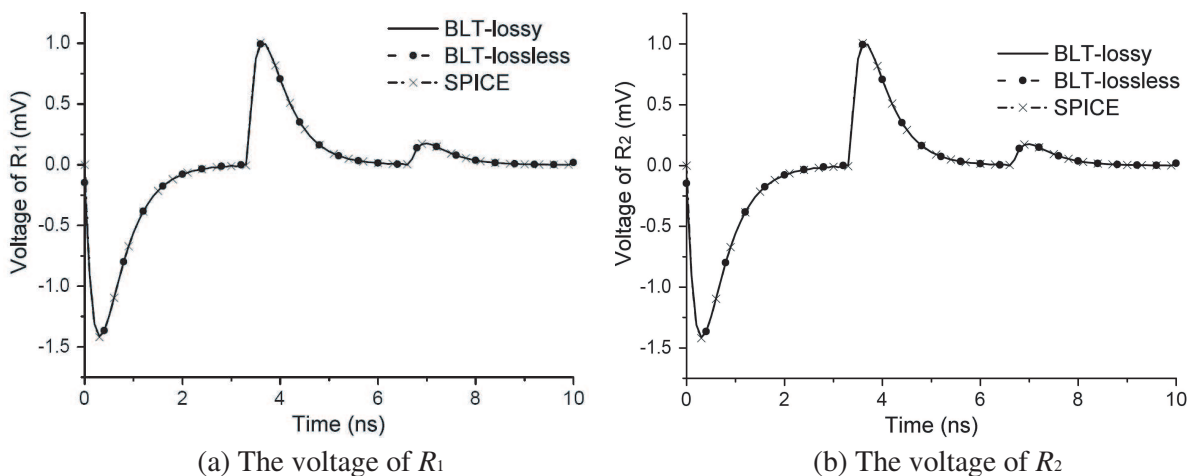


Figure 4: The transient voltages of the loads of the first case.

Figure 5 shows a multiconductor line excited by the incident field as the same as the one above. The length of the line is $\mathcal{L} = 2$ m, the radius is $r = 1$ mm, and the interval between wire 0 and wire 1 (or wire 2) is $h = 1$ cm. The loads are $R_1 = 100 \Omega$, $R_2 = 150 \Omega$, $R_3 = 50 \Omega$, and $R_4 = 200 \Omega$. And the angles are $\theta_p = 45^\circ$, $\phi_p = -30^\circ$, and $\theta_E = 90^\circ$. The transient voltage of R_1 is shown in Figure 6.

A transmission-line network over a ground excited by the incident field is shown in Figure 7. The lengths of transmission lines T_1 , T_2 , and T_3 are $\mathcal{L}_1 = 1$ m, $\mathcal{L}_2 = 1$ m, and $\mathcal{L}_3 = 2$ m, respectively. The heights and radiuses of all the lines are $h = 1$ cm and $r = 1$ mm, respectively. The loads are $R_1 = 50 \Omega$, $R_2 = 100 \Omega$, and $R_3 = 150 \Omega$. The angle between T_2 and the z axis is $\theta_1 = 30^\circ$, and

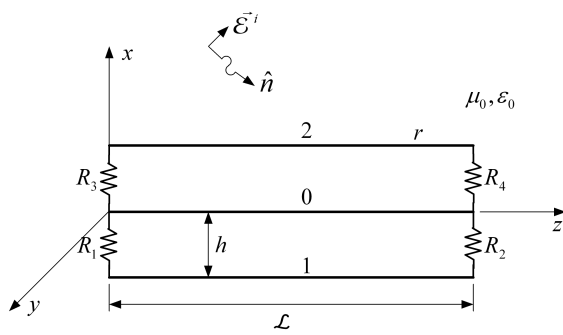


Figure 5: A multiconductor transmission line excited by an incident field.

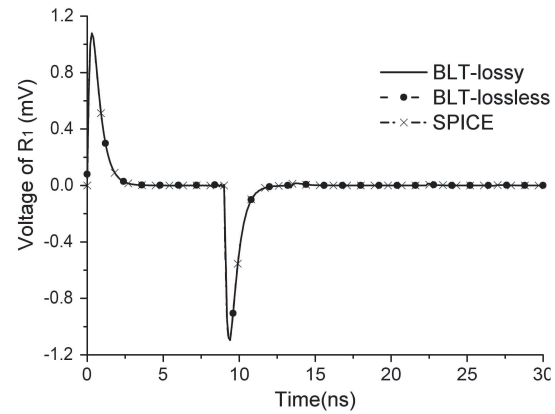


Figure 6: The transient voltage of R_1 .

that between T_3 and the z axis is $\theta_2 = 45^\circ$. The direction of the incident wave is as the same as that of the second case. And transient voltage of the load R_1 is shown as Figure 8.

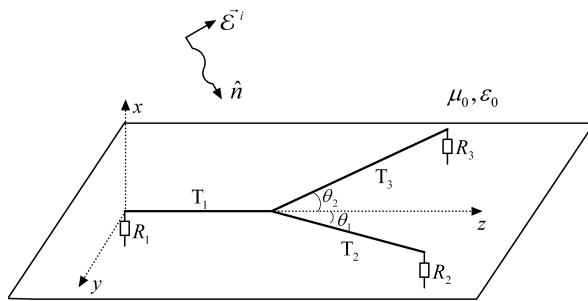


Figure 7: A transmission-line network excited by an incident field.

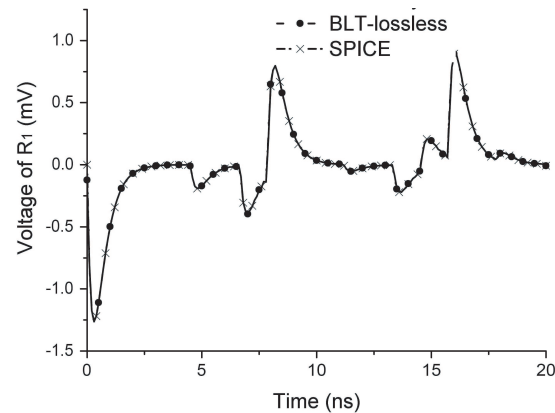


Figure 8: The transient voltage of R_1 .

Figure 4, Figure 6, and Figure 8 show that the results obtained by the proposed method agree very well with those through the BLT equation and IFFT. And the loss can be ignored in these three cases. The time cost by the two methods for the three cases is shown in Table 1. The time cost by the proposed method is much less than that of the conventional method.

Table 1: The time needed by the two methods.

	The proposed method	BLT-IFFT (lossless)	BLT-IFFT (lossy)
Case 1	2.13 s	9.37 s	11.50 s
Case 2	4.78 s	58.17 s	70.16 s
Case 3	7.50 s	35.72 s	44.40 s

5. CONCLUSIONS

Two transmission lines and a transmission-line network excited by an incident electromagnetic field have been studied. The excellent agreement between the SPICE model and the frequency-domain BLT equation with IFFT shows that the SPICE model may be used in electromagnetic topology. Because the proposed method is used directly in time domain, the time cost by it is much less than

that of the conventional method. Nonlinear or time-varying loads can be incorporated easily using the existing elements in the SPICE code, because the SPICE model is independent of the loads.

There are issues needed to be studied in relation to the application of the SPICE model in the EMT. The SPICE model above is for lossless transmission lines excited by an incident plane wave, so the effect of the loss will be studied, and the SPICE model for a nonuniform incident field will be developed.

REFERENCES

1. Baum, C. E., T. K. Liu, and F. M. Tesche, "On the analysis of general multiconductor transmission-line networks," *Interaction Note 350*, 1978.
2. Baum, C. E., "Generalization of the BLT equation," *Interaction Note 511*, 1995.
3. Baum, C. E., "Extension of the BLT equation into time domain," *Interaction Note 553*, 1999.
4. Tesche, F. M., "Development and use of the BLT equation in the time domain as applied to a coaxial cable," *IEEE Trans. Electromagn. Compat.*, Vol. 49, No. 1, 3–11, 2007.
5. Paul, C. R., "A SPICE model for multiconductor transmission lines excited by an incident electromagnetic field," *IEEE Trans. Electromagn. Compat.*, Vol. 36, 342–354, 1994.
6. Paul, C. R., *Analysis of Multiconductor Transmission Lines*, Wiley-Interscience, New York, 1994.
7. Tesche, F. M., M. V. Ianoz, and T. Karlsson, *EMC Analysis Methods and Computational Models*, Wiley-Interscience, New York, 1997.

Automation of a Clamp Mechanism for EMC Testing

Andrew Nafalski and Özdemir Gö1

University of South Australia, Mawson Lakes 5095, Australia

Abstract— This paper reports on the development of an automated absorbing clamp mechanism with video monitoring and position control to conduct the measurement process entirely from outside the screened room where the clamp is used for EMC tests. The system is implemented with a minimal change to the EMC measurement environment within the screened room.

1. INTRODUCTION

The issue of electromagnetic compatibility (EMC) has been of growing concern throughout the last century. Measurement and quantification of electromagnetic radiation has thus been the object of intense attention. Comité International Spécial des Perturbations Radioélectriques (CISPR) standards stipulate the use of an absorbing clamp for the measurement of radio disturbance power in the radiation frequency range of 30 MHz–1 GHz [1, 2]. An absorbing clamp consists of a calibrated ferrite-core current transformer and two sets of ferrite rings [3]. One set of ferrite rings surrounds the supply cable from the equipment under test (EUT) and acts as an absorber of energy and an impedance stabiliser to isolate the EUT from the external power source, illustrated in Fig. 1. The second set of ferrite rings is contained within the clamp body. This set surrounds the lead from the transformer to the electromagnetic interference (EMI) meter to minimise standing waves. The absorbing clamp moves along the track with the mains cable of the equipment under test (EUT) running through it as shown in Fig. 2.



Figure 1: Open absorbing clamp showing ferrite rings.

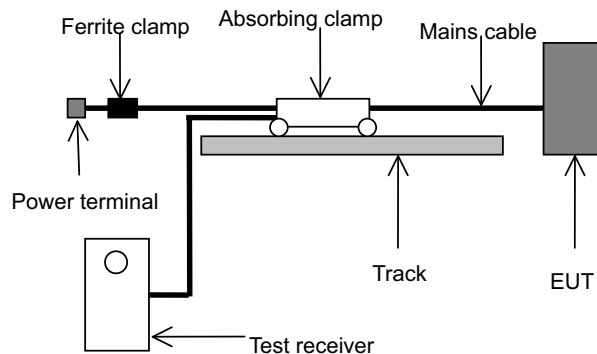


Figure 2: Measurement setup with an absorbing clamp.

Manual operation of the setup is cumbersome and time consuming; it requires setting up and recording the clamp position, leaving the room, closing the door, taking measurements and repeating the process for the next clamp position. Consequently, an automated system to control the clamp movement and its positioning has been designed to be controlled from outside the screened room. The system includes a monitoring camera inside the room. The main challenge was to design and implement a system which operates without affecting the operation of other devices, at the same time being immune to the external electromagnetic environment [4, 5].

2. EMI MITIGATION

The proposed mechanised clamp mechanism is based on the use of an air motor to avoid electromagnetic interference. The movement of the absorbing clamp along the track is monitored by means of an off-the-shelf closed circuit television (CCTV) camera (Fig. 3), mounted in the corner of the screened room.



Figure 3: Bullet size Sharp 1/4 CCD CCTV security color camera.

It was necessary to confirm whether the camera requires screening. The first radiated emission tests of the unshielded camera powered by 12 V power supply connected to the mains (Fig. 4) made it very clear that some remedial EMC action is definitely needed as EMI was higher than 40 dB μ V/m at certain frequencies as measured by a vertical bi-conical antenna [6].

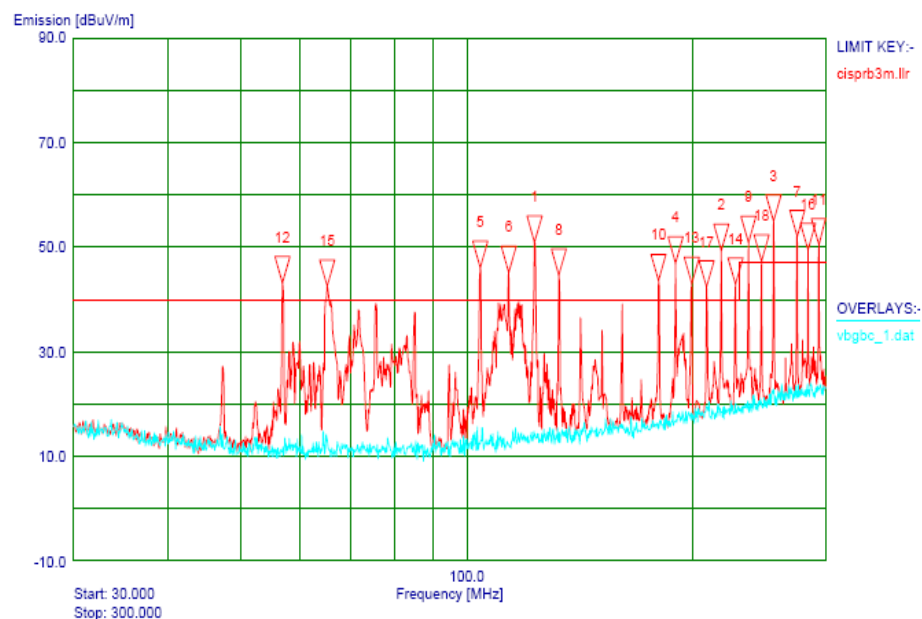


Figure 4: Radiated emissions from camera measured in screened room without shielding at frequencies from 30 MHz to 300 MHz.

The emissions exceeded those stipulated by CISPR standard [1] and a process of their reduction has been implemented starting with placing the camera together with a rechargeable battery in a die cast aluminium box (Fig. 5). Several further EMI mitigating steps were implemented and emission tests were conducted at each step. Final emission test was conducted with the camera sealed in the aluminium box, connected to the wall terminal of the screened room using a quad shielded RG6 coaxial cable, with the lens aperture provided with a metal mesh. To emulate the worst case scenario the box was placed in the middle of the screened room and connected to the wall terminal using a 5 m cable. Attenuating ferrite rings were placed around the cable. The radiation emission test of the camera under the conditions defined above confirms that its emissions are at the level of the ambient noise level and that the camera system complies with the CISPR norm (Fig. 6). Measurements repeated for frequencies between 300 MHz and 1 GHz also confirmed camera's compliance with the relevant standard [1].

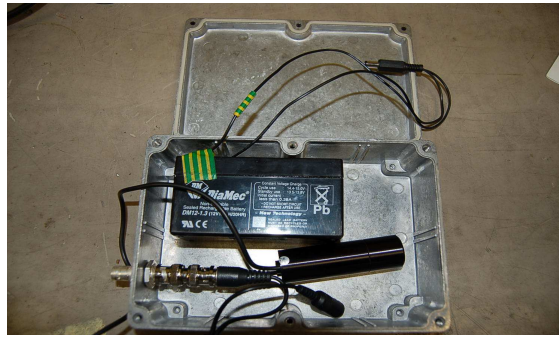


Figure 5: Camera, battery and bulkhead connector inside aluminum box, prior to sealing.

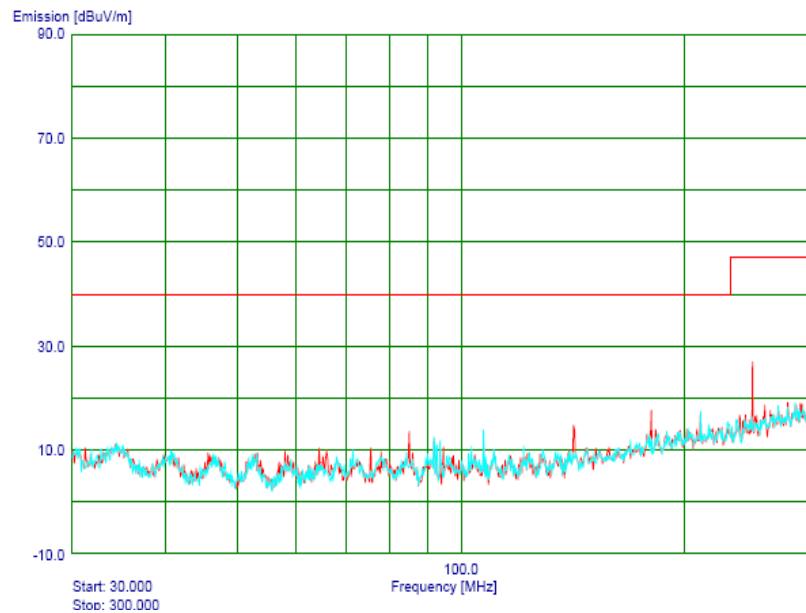


Figure 6: Radiated emissions from camera in aluminum enclosure with a shielded aperture, connected using a 5 m RG6 quad shielded coaxial cable with ferrite rings, measured at frequencies from 30 MHz to 300 MHz.

3. CLAMP MOVEMENT

The next stage of the project was to develop the motorized clamp mechanism illustrated in Fig. 7. The clamp moves along the 6 m track using a pulley system driven by an air motor. A standard off-the-shelf hand-held air drill was used to drive the clamp. The cable connecting the absorbing clamp was suspended from a rail on the ceiling, to ensure that it does not become entangled in the mechanism. Air for the actuator was supplied via non-metallic pipes connected to an air compressor outside the screened room.

The mechanical setup of the drive system is shown in Fig. 8 [7]. The air drill drives the main shaft that in turn through a pulley system moves the clamp. One of the geared down DC motors-linear actuators controls the On/off function of the droll, the other the direction of the clamp movement.

As the two DC motors are supplied and controlled electrically, a number of measures needed to be implemented to reduce EMI to the level compliant with the CISPR standard. These included: decoupling of the motors using a 1 μ F monolithic capacitors across each of the motor terminals, use of twisted pair cables throughout and application of ferrite beads on cables near the motor terminals.

4. POSITION MEASUREMENT

For position measurement of the clamp mechanism the rotary optical decoder Bourns ENA1J-B28-L00064 was used, principle of operation of which is shown in Fig. 9. Its output was connected to a

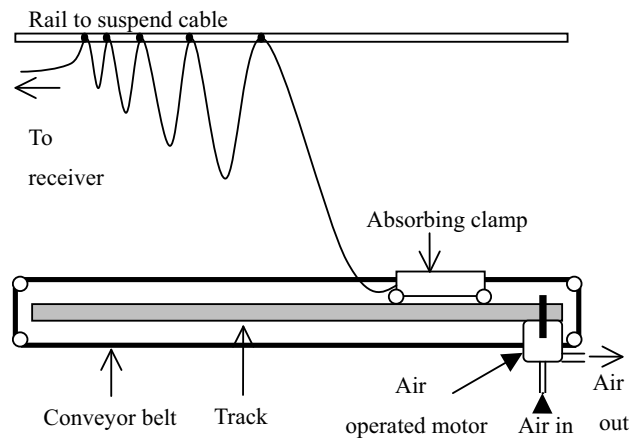


Figure 7: The conceptual setup of the motorised absorbing clamp mechanism.

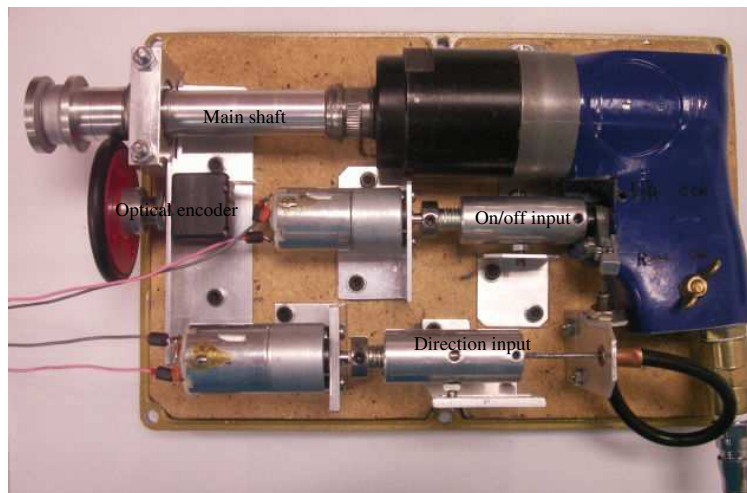


Figure 8: The mechanical setup for the motor and encoder assembly.

custom designed and constructed decoder (Fig. 10) that in turn communicated via RS-232 interface with a control program written in National Instruments LabVIEW 8.2. The same program also controlled the motor control unit (custom built PCB). The rotary incremental optical encoder was tested for emission EMI [1] and easily passed the tests in the frequency range 30 MHz–1 GHz [8].

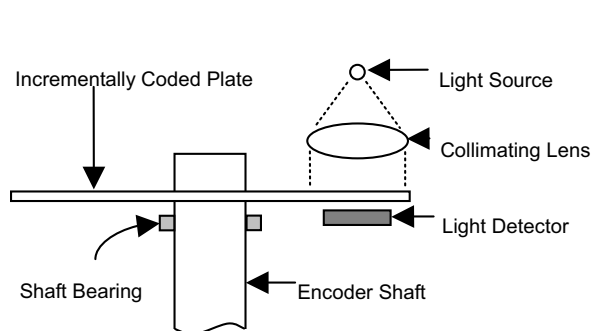


Figure 9: Operation of the optical encoder.

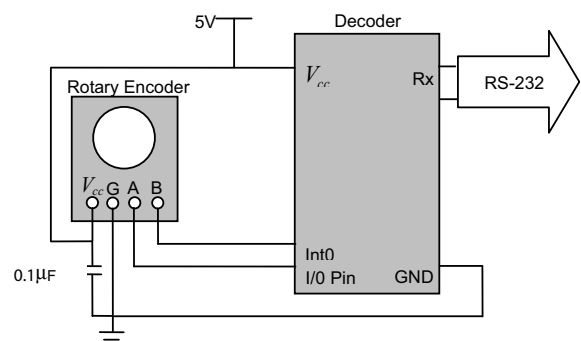


Figure 10: Rotary encoder interface.

5. CONCLUSIONS

The paper describes successful projects leading to a low-cost automation and monitoring of EMC testing in a screened room. Design objectives were achieved by a careful consideration of EMC principles at the design, prototyping, re-designing and testing stages.

ACKNOWLEDGMENT

The authors gratefully acknowledge the contribution of Mr. Chris Preece, General Manager of Wooddale EMC Consultants Pty. Ltd., Adelaide, Australia, to the technical aspect of the projects presented in the paper.

REFERENCES

1. AS/NZS 1052:1992 IEC/CISPR 16:1987, "CISPR specification for radio interference measuring apparatus and measurement methods," *Australian Standard/New Zealand Standard*, 1992.
2. IEC/CISPR 16-1-3-Ed.2.0, "Specification for radio disturbance and immunity measuring apparatus and methods - Part 1–3: Radio disturbance and immunity measuring apparatus - Ancillary equipment - Disturbance power," 2004.
3. Rhode & Schwarz Absorbing Clamp MDS-21/22, "Ferrite clamp EZ-24," *Rohde & Schwarz*, 2005.
4. Townsend, D. A., T. J. F. Pavlasek, and B. N. Segal, "Breaking all the rules: Challenging the engineering and regulatory precepts of electromagnetic compatibility," *IEEE Transactions on Magnetism*, 194, 1995.
5. Pratt, G. E., "A methodology for low cost electromagnetic compatibility testing at the prototype stage of development," *IEEE International Symposium on Electromagnetic Compatibility*, 285, 1995.
6. Preece, C., S. Shingadia, S. K. Tiong, L. Y. Yun, A. Nafalski, and Ö. Göl, "Motorised absorbing clamp mechanism," *Digests of Asia-Pacific Symposium on Applied Electromagnetics and Mechanics (APSAEM2006)*, 123, Sydney, Australia, 2006.
7. Ng, C. H. and T. N. Nguyen, "Remote sensing and automated positioning of an absorber clamp," *Final Year BEng Project 2007n*, School of Electrical and Information Engineering, University of South Australia, 2007.
8. Ng, C. H., A. Nafalski, and Ö. Göl, "Contactless position measurement for EMC apparatus," *Proceedings of the 17th Technical Seminar on Operation of Electrical Machines and Drives*, Research and Development Centre of Electrical Machines KOMEL, Rytro, Poland, May 28–30, 2008 (submitted for publication).

An Analytical Characterization of Metal Foams for Shielding Applications

O. Losito

ITEL Telecommunications Research Laboratory on EM
Via Labriola, 39-70037 Ruvo di Puglia, Italy

Abstract— The preliminary electromagnetic shielding behavior of metal foams, a novel class of materials, is developed and discussed. The use of metal foams in electromagnetic applications is a new field of scientific investigation. More specifically, the realization of electromagnetic shields has been considered and experimental Shielding Effectiveness (SE) measurements have been performed, demonstrating very good performance. In order to allow the design of metal foam EM shields, a double 3D wire-mesh screens, obtained as a development of previously 2D laminated shield, has been present, compared the relative results with experimental measure. The good agreement between the preliminary results, encourages the development of an efficiency analytical model of the complex electromagnetic behavior of metal foams.

1. INTRODUCTION

The development of the metal foams in the last decade, had produced many practical applications, thanks to the characteristic properties like low apparent (or actual) density guarantees, lightweight and high stiffness/specific-load ratios. Moreover, their porous structure and intrinsic non-homogeneity give good acoustic and thermal isolation properties and also strong impact-absorption and vibration damping capabilities [1].

However, new employment prospects could be determined by intensive electromagnetic analysis of metal foams. Fig. 1, shows an example of an open cell aluminium foam, produced by ERG Aerospace and called Duocel® foam. We can note that its low apparent density, (8%) and its capability to allow both light and air crossing, can be useful in several applications.

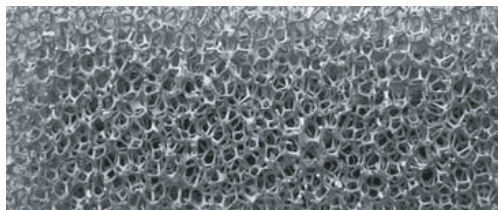


Figure 1: An example of Duocel® open cell aluminium foam $9 \times 3 \times 0.5 \text{ cm}^3$ slab (porosity: 10 PPI, app. density: 8%).

The analysis of the shielding properties of different kinds of Duocel® aluminium foams slabs obtained by varying porosity and apparent density, has been investigated, performed through experimental measurements, and their shielding properties has been shown and discussed [2].

Metal foams are complex and random structures which requiring sophisticated analytical models. Moreover, because of its versatility and its capability to deal with heterogeneous media, the Variable-Mesh Finite Difference Time Domain (VM-FDTD) method, is naturally the most appropriate approach [2], though unfortunately, it is computationally onerous. The 2D laminated wire-mesh screen model, developed by Casey [3] and compared with commercial aluminium shield perforated periodically with apertures [4], was a first step to solve the EM problem of the rigorous evaluation of the metal foam's shielding effectiveness [5]. Encouraged by the results, we have improved the previously 2D model, developing a preliminary analytical 3D models.

Therefore the electromagnetic shielding behavior of a slab of metal foam, has been investigated considering a model with a double wire-screens mesh, separated by an air space. The single screen, whose meshes are assumed to be square, is described by an equivalent sheet impedance operator as mentioned in [3]. The agreement of both experimental and theoretical data is a challenging to optimize this model in 3D.

We begin in the following section with a short review of metal foams manufacturing methodologies and on their properties. Then in Section 3 is described the analytical 3D models developed

to know the electromagnetic shielding behaviour of metal foams. In Section 4 results are given for experimental measurement of metal foam slab and theoretical double wire-mesh screens model. Finally conclusions are drawn in Section 5.

2. METAL FOAMS

One of the most adopted processes for the foams realization is the so called “gas-injection”, easiest to implement with aluminium alloy [1], in which a variety of gases can be used to create bubbles within liquid aluminium. Low relative density, closed-cell foams can be produced by carefully controlling the gas-injection process and the cooling rate of the foam. Another interesting set of manufacturing methodologies, is based on metal deposition on cellular preforms and on the liquid state processing, where a bed of leach able particles (such as salt) infiltrated with a liquid metal (such as aluminium or more one of its alloys) and dissolved in a suitable solvent (such as water) leaving a uniform strictures of open-cell foam.

The kind of foam which could be more interesting for EM application is the one produced by ERG Aerospace [6] and named Duocel®. These materials consist of small ligaments that are continuously connected in an open-celled foam structure (see Fig. 1). The manufacturing technology is based on the realization of a preliminary open-cell polymer foam mould template with the desired cell size and relative density. This can be coated with a mould casting (ceramic powder) slurry which is then dried and embedded in casting sand. The mould is then baked both to harden the casting material and to decompose (and evaporate) the polymer template, leaving behind a negative image of foam. This mould is subsequently filled with a metal alloy and allowed to cool. The use of a moderate pressure during melt infiltration can overcome the resistance to flow of some liquid alloy. After directional solidification and cooling the mould materials leaving behind the metal equivalent of original polymer foam [1].

The most important parameters of such a kind of metal foam are the base material, the relative density and the pore size. Relative (or apparent) density represents the volume of foam material relative to the volume of material in a solid block of the base material, and it influences foam stiffness, strength, and both electrical and thermal conductivity. It is important to observe, in fact, that by increasing relative density the ligaments become larger in diameter and stronger, increasing the strength of the foam structure. Pore size represents instead the pore dimension and is strongly connected to the number of pores for linear inch (PPI). The cells of Duocel® foams are generally 12 to 14 sided polyhedral whose pentagonal or hexagonal faces are formed by five or six ligaments. The open window in each of these faces defines the pore diameter which usually varies from 5 to 100 PPI. Pore size is the major determinant of foam characteristics such as optical capacity, specific surface area and fluid flow resistance. By realizing appropriate foams which specific values of PPI (and consequently of pore size) and relative density, it is possible to obtain a combination of properties which can be attractive from an EM point of view.

3. DOUBLE WIRE-MESCH SCREE MODEL

The first approaches to evaluation the metal foams shielding effectiveness, can be performed through the use of numerical techniques like FDTD algorithms. However, in order to accurately describe the complex foams structure, space step of the order of fractions of millimeters must be used, thus requiring huge computational efforts. For this reason we have begun the study of an analytical model to describe in simple way the electromagnetic behavior of metal foam. The results obtained in the 2D wire-mesh screen with bounded junction mentioned in [5], was the first step to developed a 3D model of metal foams, characterized with the same dimensions of the ligaments and pore of a thin metal foams slabs. This laminated shield can be described electromagnetically by an equivalent sheet impedance operator Z_s , when the mesh dimensions are small compared to wavelength [3]. The operator Z_s , relates the tangential electric field E_s to the surface current density on the screen J_s as:

$$E_s = Z_s^* J_s \quad (1)$$

The screen geometry, is shown in Fig. 2. The equivalent sheet impedance for a screen with square meshes of dimension $a_s^* a_s$ and r_w as dimension of mesh wires radius, is:

$$Z_s = (Z_w^* a_s + j\omega L_s)(I - n^* n) + \frac{j\omega L_s}{2K_0^2 \epsilon_r} \nabla_s^* \nabla_s \quad (2)$$

where Z_w is the internal impedance per unit length of mesh wires, K_0 is the free-space wave number and ∇_s denotes the surface del operator. I is the idem factor or identity dyadic and n is

a unit vector normal to the surface occupied by the mesh. If we use the plane wave with a normal incidence, in order to evaluate the effectiveness of a planar mesh screen, we need only evaluate the transmission coefficient that in the case where the mesh wires are perfectly conducting, we have [3]:

$$SE = -20 \log_{10} \frac{(2\omega L_s/Z_0)}{\sqrt{1 + (2\omega L_s/Z_0)^2}} \quad (3)$$

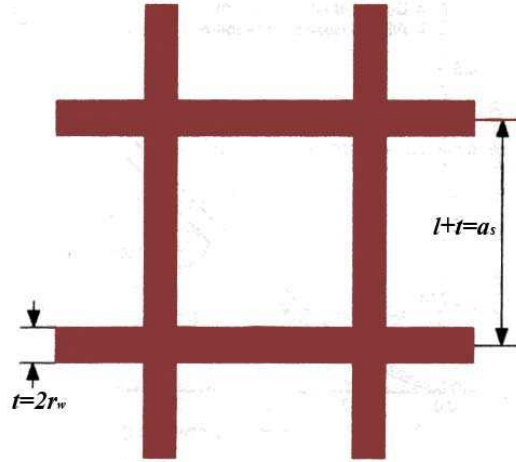


Figure 2: Geometry of individual square wire-mesh. The wire junctions are assumed to be bonded.

The agreement of the theoretical and experimental results of SE, using a square wire-mesh with the same geometry of holes and wire ligaments for a laminated perforated with periodically apertures was good [4].

Nevertheless the 2D model greatly undervalues the SE of metal foam. Consequently we have proposed a simple 3D model of metal foams slab that consider a double wire-mesh shielding consisting of two shielding sheets separated by an air space. In fact the shielding effectiveness of a “good conductor,” is given by [7]:

$$SE_{\text{single}} \cong 4 \frac{\eta_0}{\eta} e^{\frac{t}{\delta}}. \quad (4)$$

Considering a double shields of thickness $t/2$ each one, separated by an air space, if we disregard multiple reflections in this air space, the total SE is given by:

$$SE_{\text{double}} \cong \left[4 \frac{\eta_0}{\eta} e^{\frac{t}{2\delta}} \right]^2 = \left[4 \frac{\eta_0}{\eta} \right]^2 e^{\frac{t}{\delta}}. \quad (5)$$

Thus the “interface mismatched” contribute for double slab is the square of single slab. Translating this result to metal foam slab, we have the SE for 3D model proposed:

$$SE = -40 \log_{10} \frac{(2\omega L_s/Z_0)}{\sqrt{1 + (2\omega L_s/Z_0)^2}} \quad (6)$$

Therefore effective RF shields, for electric fields can be constructed from thin shields, because for far-field (uniform plane-wave) and near field sources, reflection loss, is the predominant shielding mechanism at the lower frequencies, while absorption loss is the predominant shielding mechanism at the higher frequencies [7].

Moreover from the shielding effectiveness analysis versus frequency of the double wire-mesh, shown in Fig. 3, we can note that the shielding effectiveness of double screen is more than the shielding effectiveness of single screens with double thickness. In fact for high frequency, if we

compare the double shielding effectiveness with a single shielding effectiveness of the same total metal thickness we have an increase of shielding effectiveness as [8]:

$$\Delta = S_{E_{double}} - S_{E_{single}} = 20 \log_{10} \frac{\pi \frac{l_{airgap}}{\lambda_0}}{\left| \frac{\eta}{Z_w} \right|} \quad (7)$$

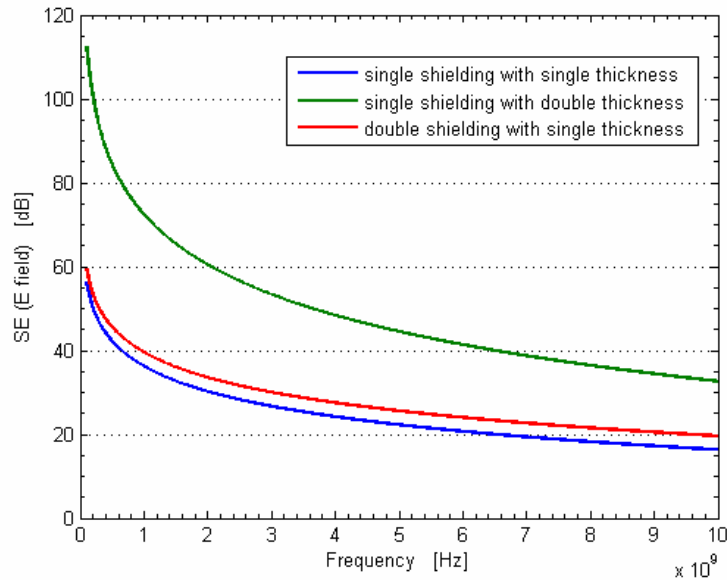


Figure 3: Shielding effectiveness (E field) for single and double wire-mesh screen with single and double thickness.

For example for a double shield of copper with 2.54 cm in spacing is 49 dB superior at 1 MHz to a single shield of the same total metal thickness [8].

4. RESULTS

In the following section we are going to show the results of the measurements, and the preliminary theoretical data of the SE of double wire mesh screens for different kinds of open cells of Duocel® aluminium foam slabs.

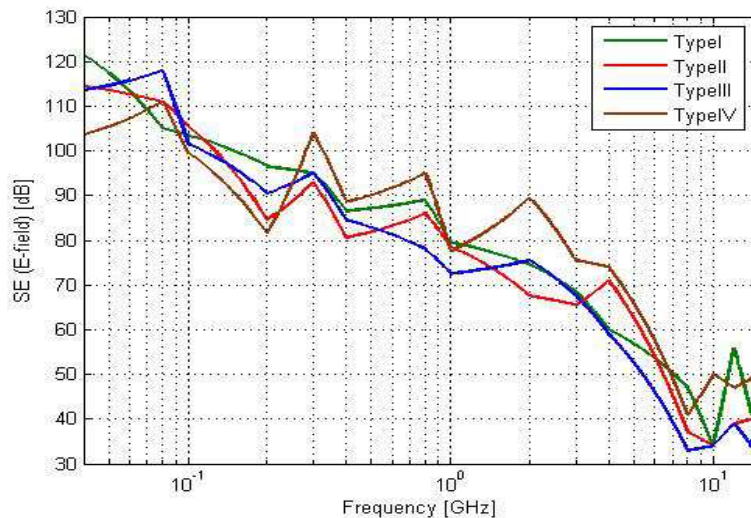


Figure 4: Shielding effectiveness (E field) for aluminum foam slabs described in Table 1. The thickness is 14 mm for all cases.

The electric field SE of Fig. 4 shows the trend of four open cell slabs of 1.4 cm thickness, obtained varying some structural properties according to data summarized in Table 1.

Table 1: Examined foam types.

Duocel® Aluminium foam			
<i>Type I</i>	<i>Type II</i>	<i>Type III</i>	<i>Type IV</i>
10 PPI, 6–8% nominal density, 6.1% actual density. Alloy 6101-F	20 PPI, 6–8% nominal density, 8.5% actual density. Alloy 6101-F	40 PPI, 6–8% nominal density, 7.9% actual density. Alloy 6101-F	40 PPI, 6–8% nominal density, 8.7% actual density. Alloy 6101-F

More specifically, type I–IV data have been experimentally obtained and measurements performed in the range 10 KHz–20 GHz. As commonly accepted, three different frequency ranges have been individuated (namely “low-frequency”, “resonance” and “high frequency”) and in each one appropriate sources have been used. The aluminium foam slabs have been carefully adapted to an aperture of a shielding room and measurements performed according to how described in the IEEE Std 299-1997 and using the following classical formula:

$$SE_e = 20 \log \left(\frac{E_1}{E_2} \right) \quad (8)$$

where E_1 and E_2 are the received E fields respectively, without and with the shield. It is apparent from Fig. 5 the good shielding capability of all the studied slabs in the whole frequency range and especially for frequencies up to 2 GHz. As expected, a SE reduction has been found for higher frequencies, because of the effects of the open cell nature of the considered aluminium foams. More in detail, by comparing the SE values of aluminium foam slabs of Type II with those of Type IV, it is apparent that for metal foams with the same apparent density, shielding capabilities decrease if PPI increases. Moreover, when comparing slabs with the same PPI but different relative density (Type III and Type IV), lower shielding performances are measured for higher density slabs. This is in agreement with what has been shown for mechanical property; i.e., increasing porosity most properties, including strength, stiffness and conductivity, decreasing exponentially.

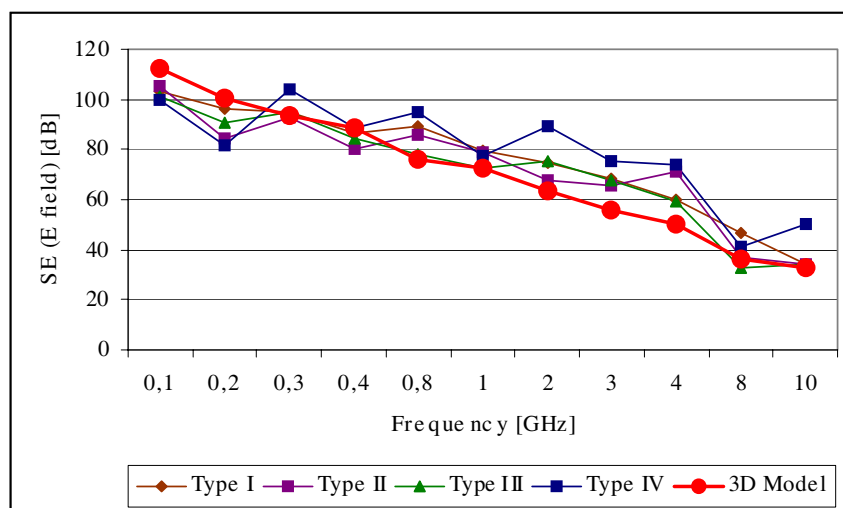


Figure 5: Shielding effectiveness (E field) for aluminum foam slabs described in Table 1, compared with theoretical values of 3D model.

The good result of experimental and theoretical results of 3D model (with the same total thickness of metal foams slab), shown in Fig. 5, encourages the optimized of this 3D bonded-junction wire-mesh screen model, paving the way for the interesting shielding capabilities of the investigated class of materials for our design purposes. In fact especially for the manufacturing costs, being not negligible, the possibility to preliminarily estimate the SE of metal foams with a certain combination of porosity and relative density, would become relevant.

5. CONCLUSIONS

In the previous sections we have considered an electromagnetic characterization of metal foams for their use in RF EM shields. The experimental results about the Shielding Effectiveness (SE) of some specific typologies of open cell aluminium foam slabs, were discussed showing quite good shielding properties for a wide frequency range. An analytical 3D double wire-mesh screens model, obtained as development of the model proposed by Casey [3], was developed to simulate the shielding properties of different kinds of metal foams.

The strong agreement between theoretical data and experimental results, encourages the optimized of this 3D model, to characterize the electromagnetic shielding behaviour of metal foams.

ACKNOWLEDGMENT

This work was supported by Regione-Puglia POR 2002-2006 (Axis 3, meas. 3.12 act. A, int. sp. A.1).

REFERENCES

1. Ashby, M. F., A. G. Evans, N. A. Fleck, L. J. Gibson, J. W. Hutchinson, and H. N. G. Wadley, *Metal Foams: A Design Guide*, Butterworth-Heinemann publications, 2000.
2. Catarinucci, L., O. Losito, L. Tarricone, and F. Pagliara, "High added-value EM shielding by using metal-foams: Experimental and numerical characterization," *Electromagnetic Compatibility, EMC 2006*, Vol. 2, 285–289, Aug. 2006. .
3. Casey, K. F., "Electromagnetic shielding behavior of wire-mesh screens," *IEEE Transactions on Electromagnetic Compatibility*, Vol. 30, 298–306, Aug. 1988.
4. Fanelli, A. E. and M. Bozzetti, "Indagini analitiche sull'efficienza di schermatura di strutture leggere," DEE-Politecnico di Bari, A.A. 1999–2000.
5. Catarinucci, L., O. Losito, and L. Tarricone, "On the use of metal foams in EM shielding applications," *Proceedings of the Mediterranean Microwave Symposium MMS'2006*, 240–245, Genova, Italy, Sept. 2006.
6. <http://www.ergaerospace.com/>.
7. Paul, C. R., *Introduction to Electromagnetic Compatibility*, 2nd Edition, John Wiley & Sons Inc, Chapter 10, Jan. 2006.
8. Schulz, R. B., V. C. Plantz, and D. R. Brush, "Shielding theory and practice," *IEEE Transactions on Electromagnetic Compatibility*, Vol. 30, No. 3, 187–201, Aug. 1988.

Estimation and Validation of Soil Moisture Using PALSAR Onboard ALOS over Mongolian Plateau

T. Tadono¹, M. Shimada¹, H. Fujii¹, and I. Kaihotsu²

¹Earth Observation Research Center

Japan Aerospace Exploration Agency (JAXA), Japan

²Faculty of Integrated Arts and Sciences, Hiroshima University, Japan

Abstract— Soil moisture is important for fields not only hydrology but also meteorology. It plays important roles in the interactions between the land surface and the atmosphere, as well as in the partitioning of precipitation into runoff and ground water storage. In spite of its importance, soil moisture is not generally used for weather forecasting and water resources management because it is difficult to measure on a routine basis over large areas. The objective of this study is to develop algorithms to estimate spatial and temporal distributions of soil moisture using satellite remote sensing techniques. The Advanced Land Observing Satellite (ALOS, nicknamed “Daichi”) was successfully launched on January 24, 2006 from Tanegashima Space Center, Japan, and it is continuously working very well. ALOS has an L-band Synthetic Aperture Radar (SAR) called PALSAR. In this study, we applied existing algorithm to PALSAR data and generated surface soil moisture maps with 100 m spatial resolution. The test sites are located in the Mongolian Plateau, where is spatially homogeneous with basically flat terrain features, and three Automatic Weather Stations (AWSs) and twelve Automatic Stations for Soil Hydrology (ASSH) are installed.

1. INTRODUCTION

The Advance Land Observing Satellite (ALOS, nicknamed “Daichi”) was successfully launched on January 24, 2006 (Japan Standard Time, JST), and it continuously operating very well. Three mission instruments are mounted on ALOS i.e., an active microwave instrument called PALSAR, and two optical instruments called PRISM and AVNIR-2. PALSAR stands for the Phased Array type L-band Synthetic Aperture Radar which can be observed the Earth surface with high spatial resolution and multi polarizations even cloud cover conditions.

Soil moisture is a key parameter in numerous environmental studies, including hydrology, meteorology, and agriculture. It plays important roles in the interactions between the land surface and the atmosphere, as well as in the partitioning of precipitation into runoff and ground water storage. In spite of its importance, soil moisture is not generally used for weather forecasting because it is difficult to measure on a routine basis over large areas.

In this paper, 100 m-mesh soil moisture maps are derived using PALSAR polarimetry images with existing algorithm. Furthermore, estimated soil moisture values are compared with estimated one by using passive microwave instrument called AMSR-E onboard NASA’s AQUA satellite.

2. STUDY AREA AND DATA

The test sites of this study are located in the Mongolian Plateau, where is spatially homogeneous with basically flat terrain features. Figure 1 shows location of test sites in the Mongolian Plateau, and Figure 2 shows photographs of ground-based measuring systems. i.e., Automatic Weather Stations (AWSs) and Automatic Stations for Soil Hydrology (ASSH). We are setting up several test sites in southern part of Ulaanbaatar, Mongolia, and installing and maintaining three AWSs and twelve ASSH. Furthermore, we are carrying out intensive experiments in summer seasons.

PALSAR data used in this study were acquired on May 25 and August 25, 2006 by polarimetric observing mode over AWS site-DGS and ASSH sites-A3 and A6. I expected that these data can be identified seasonal changes of soil moisture during summer season. In winter season in the Mongolia is almost minus degree-C of soil temperature therefore soil is completely frozen and 0 percentage of soil moisture.

3. EXISING AROGORITHM TO ESTIMATE SOIL MOISTURE

We applied existing algorithm, which was developed by Shi et al. 1997 [1] that was based on regression analysis using single scattering IEM model [2] and applied to SIR-C/AIRSAT data. The

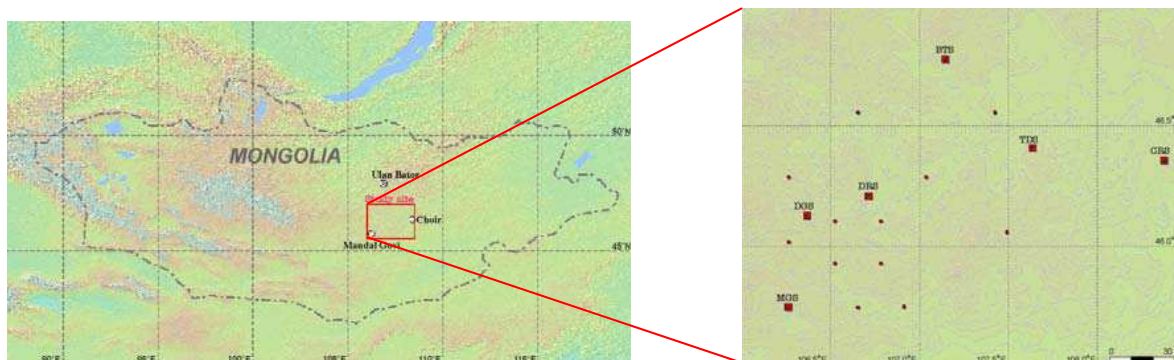


Figure 1: Location of test sites in the Mongolian Plateau (Red squares: AWS sites; red dots: ASSH sites right).



(a) Automatic Weather Station (AWS).

(b) Automatic Station for Soil Hydrology (ASSH).

Figure 2: Ground-based measuring systems in the Mongolian Plateau.

volumetric water content and surface roughness parameters can be separately retrieved using

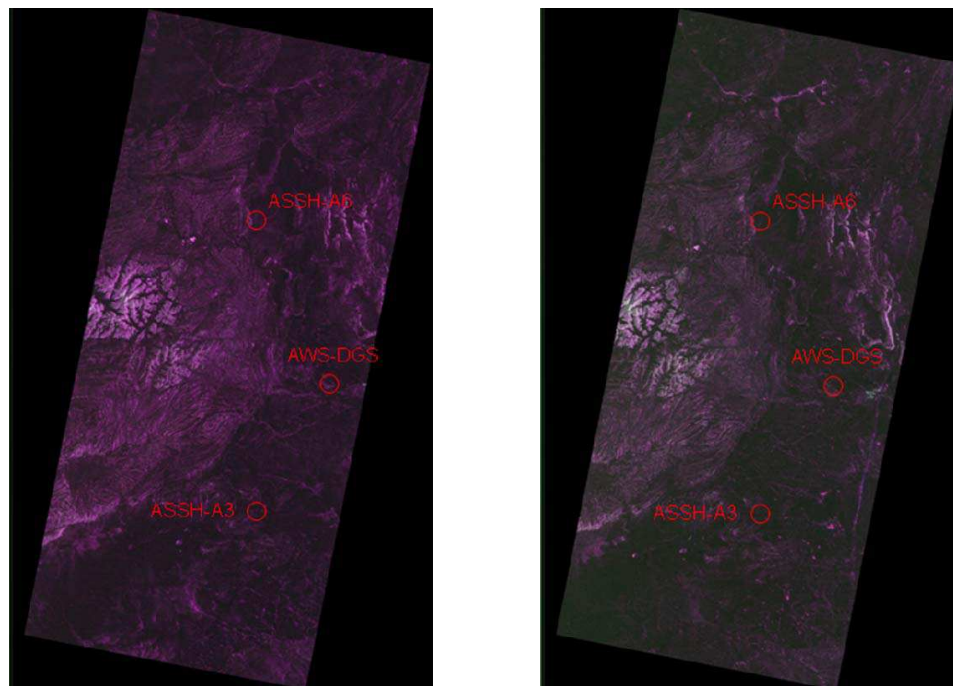
$$10 \log_{10} \left[\frac{|\alpha_{VV}|^2 + |\alpha_{HH}|^2}{\sigma_{VV}^0 + \sigma_{HH}^0} \right] = a_{VH}(\theta) + b_{VH}(\theta) \times 10 \log_{10} \left[\frac{|\alpha_{VV}| \cdot |\alpha_{HH}|}{\sqrt{\sigma_{VV}^0 \cdot \sigma_{HH}^0}} \right] \quad (1)$$

$$10 \log_{10} \left[\frac{|\alpha_{VV}|^2}{\sigma_{VV}^0} \right] = a_{VV}(\theta) + b_{VV}(\theta) \times 10 \log_{10} \left[\frac{1}{Sr} \right] \quad (2)$$

where, a : polarization amplitude, k : wave number, J : Bessel function, and coefficients a , b were defined. The validity range of the algorithm is 2 to 50 vol% of soil moisture, 0.2 to 3.6 cm of rms surface height, 2.5 to 35 cm of surface correlation length, 25 to 70 deg of incidence angle, and exponential, 1.2 power and 1.4 power correlation functions.

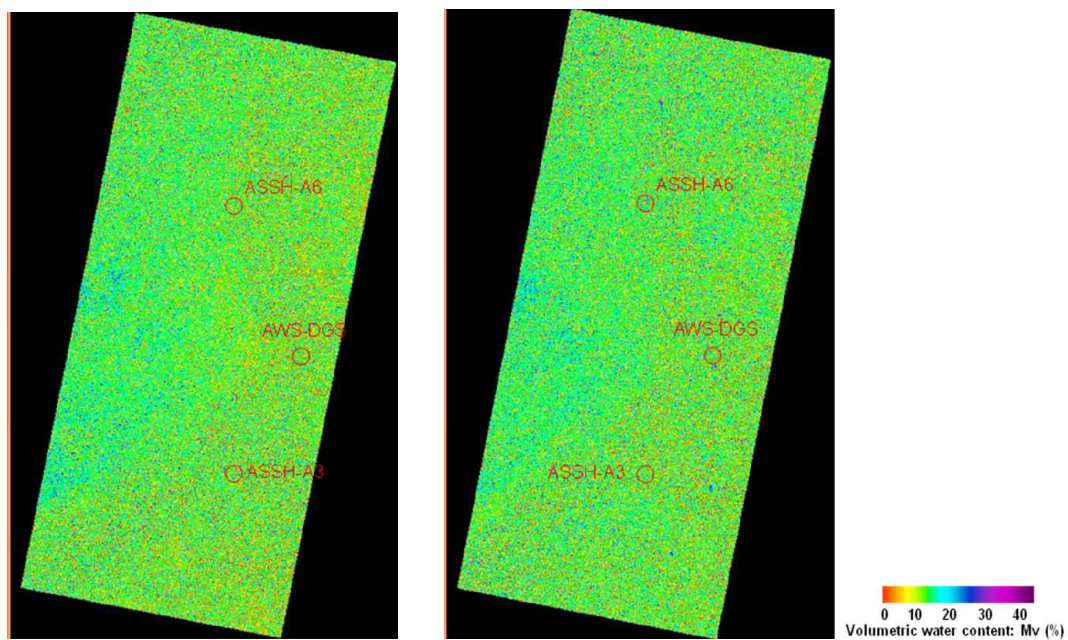
4. RESULTS AND DISCUSSION

Figure 3 shows browse images of PALSAR observed by polarimetric mode over the test sites on (a) May 25 and (b) Aug. 25, 2006. The red circles indicate location of the test sites. Figure 4 show results of soil moisture maps derived from Figure 3. The retrieval were carried out using original resolution than 8 by 8 pixels corresponding to 100 by 100 meters area averaged soil moistures to reduce effects of speckle noises and uncertainty of inversion processing. The spatial distributions of soil moisture can be identified from Figure 4 and estimated ranges from 0 to 28% of soil moisture. The distribution of soil moisture and its characteristics are important in the fields of hydrology and climatology. Figure 4(b) is looks like more wetter compared with (a) based on qualitatively comparison.



(a) 060525 Descending (ALPSRP017662680).

(b) 060825 Descending (ALPSRP031082680).

Figure 3: PALSAR images acquired by polarimetric observing mode ($R, G, B = VV, HV, HH$).

(a) 060525 Descending (ALPSRP017662680). (b) 060825 Descending (ALPSRP031082680).

Figure 4: 100-m-mesh (8×8 pixels averaged) estimated soil moisture maps applied by Shi et al. 1997.

Figure 5 shows estimated soil moisture using AMSR-E passive microwave radiometer onboard AQUA satellite on Aug. 25, 2006. It was derived by algorithm based on [3], and red square indicates location of study area corresponding to Figure 3. Figure 5 shows averaged soil moisture about 5% over the test site on August. Due to large gaps between both frequencies by PALSAR and AMSR-E, the depths of estimated soil moisture might be different between both estimations in Figures 4 and 5, especially in the case of dry soil.

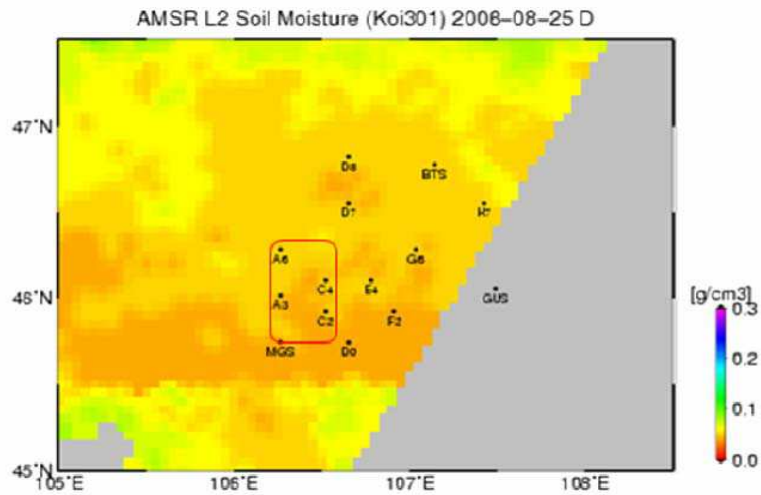


Figure 5: 0.01 degree-grid estimated soil moisture maps on August 25, 2006 derived by AMSR-E.

ACKNOWLEDGMENT

This research is conducting as a part of Research Announcement (RA) of ALOS Science Program.

REFERENCES

1. Shi, J., et al., "Estimation of bare soil moisture and surface roughness parameter using L-band SAR image data," *IEEE Trans. Geoscience Remote Sensing*, Vol. 35, No. 5, 1254–1266, 1997.
2. Fung, A. K., *Microwave Scattering and Emission Models and Their Applications*, Artech house, 1994.
3. Koike, T., Y. Nakamura, I. Kaihotsu, G. Davva, N. Matsuura, K. Tamagawa, and H. Fujii, "Development of an Advanced Microwave Scanning Radiometer (AMSR-E) algorithm of soil moisture and vegetation water content," *Annual Journal of Hydraulic Engineering, JSCE*, Vol. 48, No. 2, 217–222, 2004.

Classing and Extracting Information from Radar Images

G. Angiulli¹, V. Barrile¹, G. M. Meduri¹, R. Pucinotti², and S. Tringali¹

¹DIMET, University Mediterranea, Reggio Calabria 89100, Italy

²MECMAT, University Mediterranea, Reggio Calabria 89100, Italy

Abstract— GPR techniques had been successfully using for many years to examine structures and materials from inside. They are based on the possibility of sending electromagnetic pulses and registering the echo time and the amplitude of the signals eventually back-scattered by the interface between propagation media of different dielectric constants. The result consists of some radar images (the so-called radargrammes), where incidental targets generate distinctive hyperbolic plots or discontinuities, as an indirect evidence of either changes in the properties, nature and composition of the medium or the presence of internal breaks. The present note aims at expounding some tests and preliminary results drawn by the employment of specific algorithms for automatically interpreting, classing and extracting explicit information from radargrammes, once these have been traced from raw radar data by an ad hoc application designed in the MatLab framework.

1. INTRODUCTION

The advance following the introduction of new measurement instruments and methods and the development of more and more reliable techniques of data processing, has been allowing professional men and researchers to carry out accurate and fast investigations not even conceivable till some time ago. In the past decades non-invasive analysis [1] has been used with growing spread, both for inquiring the physical and mechanical properties of any sort of structural elements composing a work of engineering, and for the entry of detailed information about the internal geometry and composition. Moreover, these have revealed themselves indispensable when dealing with complex works or investigations of a different nature would entail an unavoidable interruption of vehicular traffic in areas where the structure is indeed an essential connection. On the other hand, the usage of radar technology (GPR) in structural surveys [2, 3] comes from its basic applications to underground investigations (namely, Georadar) and nowadays is mostly concerned with the problem of locating bars of armor and detect cavities or breaks inside structures [4], in such a way that is not invasive or destroying. The present note deals with preliminary results coming from the application of a classification algorithm for raster images to radargrammes (in a raster format) obtained from processing raw GPR data (concerning investigations on the girder of a bridge in armoured concrete) by means of a simple application designed and developed in Matlab. This algorithm permits to extrapolate the contour lines due to structural discontinuities or to draw the classical hyperboles produced by a certain signal in presence of reinforcement bars. Hence it is useful for the automatized location of such elements inside materials or buildings, once treated with suitable filtering routines (for example, able to remove noisy information), which we are still working on to optimize.

2. BASICS ON GPR IN CIVIL ENGINEERING

Localizing bars of reinforcement in concrete is one of the most important applications of GPR to Civil Engineering. In fact for a few years many researchers and practicers have been making intensively use of GPR technology in common applications, especially when dealing with structural inspections, testing and control or with the spotting of reinforcements and holes internal to ferroconcrete buildings. As known, the physical principle behind georadar techniques is founded on transmitting electromagnetic pulses and recording the time-stamp and the strength of eventually back-scattered signals produced at the interface between materials with different dielectric constants. This technology has turned out particularly effective in the surveys of non-electroconductive means and in reveling the presence of metallic objects inside the same materials. Due to relatively short survey times, this allows the survey of large structures. A GPR relief produces a radargram. These surveys are exploited on buildings for which it is practically difficult to get any information about internal structure. They allows to establish the number, the position and the diameter of all steel bars in the surveyed element. It is also possible to localize — whenever present — voids both in reinforced concrete and in masonry structures with some easiness. The electromagnetic pulse technique has the advantage of a portable equipment and the capability to detect large surfaces in

a fast nondestructive and non-invasive way. One of the main difficulties with the use of GPR is that the results are often difficult to be read and an expert technician is necessary to produce a reliable end result [5, 6].



Figure 1: The antennas employed in the survey and an overview of both the bridge and the reinforcement bars “checked” in our testings. In the photograph one of our researchers can be recognized while positioning the measurement instruments on the structure.

3. EXPERIENCING WITH GPR

Nowadays many reports exist proving the results are often very valuable. As a fact, the typical electromagnetic signals involved in effective inquiries exploiting GPR technology have a carrier frequency that normally ranges from 40 MHz to 2 GHz [4], depending on both the expected depth of penetration and the imaging resolution that one is actually interested to reach. As a rule of principle, low frequencies allow a deeper penetration at the price of a coarse resolution, whereas high frequencies improve the resolution, providing radar images of a superior quality, while being more advisable for superficial investigations. Moreover, high frequencies involves smaller antennas, hence not that heavy and easier to handle.

The electromagnetic signals are emitted and received by one or more antennas, running on the surface of a certain material, in order to return some radar images, in which precise targets correspond with characteristic hyperbolic curves. Generally, in the control of structures, antennas working with carrier frequencies greater than 1 GHz are employed, that warrant a depth of penetration lower than 0; 5 m on the one hand and a resolution less than 5 cm on the other. In our case, GPR has been used to survey the position of the metal reinforcements (some shaped longitudinal irons) and their brackets, with reference to a nearly four meters long portion of the bridge we are considering. The survey took advantage of two antennas working at different frequencies (precisely, 900 MHz and 2 GHz), running on the surface of interest (a beam) both in the cross and in the longitudinal directions. The former for the sake of locating the main reinforcements, the latter for spotting their brackets. The phase of post-processing for the drawing of the results has been based on the usage of a specific application developed in the framework of MatLab for the color display of the scanning outputs and the carrying out of different filters for reducing measurement noise. The final result is a classical radar image (see Figs. 2 and 3(a)), where the red hyperboles indicate the presence of the reinforcement bars [7].

4. THE PROCESSING ALGORITHM

Given it is still on trial, the algorithm we have designed and coded in Matlab with reference to our processing targets operates in two essential steps. First it carries out a classification of image elements (see Fig. 2(a)), performing an automated search of resemblances between contiguous groups of pixels. This task is accomplished by means of both a spectral analysis and the comparison with a prefixed set of color shades (after leaving through several ranges of color). Subsequently these very pixels are collected together by a standard algorithm of clustering, so forming homogeneous groups (see Fig. 2(b)) to be associated with a certain class (according to some initial parameters introduced by a human supervisor as well).

In the second step the classified image is segmented and vectorialized as a final result. Generally speaking, the vectorialization process is founded on the remarks that a pixel does not represent an

object by itself, but an area in the space taken up by an object, instead. Thus assembling contiguous pixels according to prefixed clustering rules allows to identify homogeneous regions within a given image (i.e., groups of pixels all sharing the very same features) and to draw the contour lines separating them from each other (see Fig. 3(a)). When dealing with classified images, pixels have been already subdivided into clusters, hence into disjoint regions. Hence the algorithm under consideration restricts itself to identify the boundary of each cluster, subsequently providing a way for tracing out the geometry of all structural elements generating the radar image (independently they are discontinuities in the propagation medium or hyperboles due to the presence of reinforcement bars). While still in course of development, actually the overall procedure succeeds in furnishing an integrated package (in fact, implemented in the framework of Matlab), capable to draw and vectorialize contours of radar images (see Fig. 3(b)) in an automatized fashion and to extract information about the accurate location of reinforcement bars as a consequence (seeking for the points of maxima associated with some selected hyperboles).

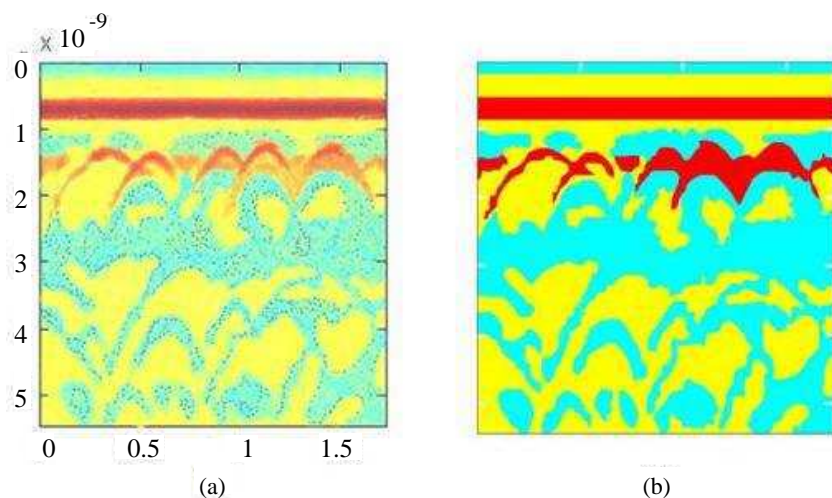


Figure 2: (a) Raw data are pre-processed to adjust brightness and contrast. (b) The output provided after the classification phase.

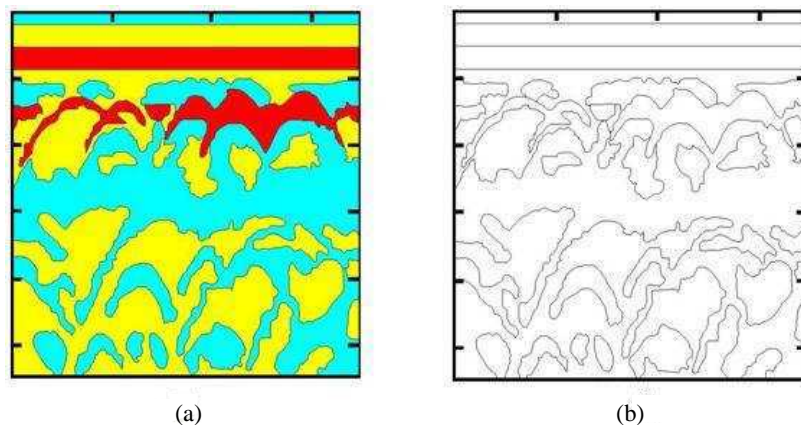


Figure 3: (a) The image produced as an intermediated processing result after the localization of contour lines. (b) The ultimate image obtained through segmentation and vectorialization.

5. CONCLUSIONS

Up till now, the algorithm we have proposed in the present note is giving satisfactory results in classifying radar images, in their segmentation and vectorial formatting and even in the automatic location of (both relative and absolute) maxima over characteristic curves (like canonical hyperboles) associated with the presence of peculiar structural elements. We are still managing some experiments for optimally improving the processing we have previously sketched out.

REFERENCES

1. Angiulli, G., V. Barrile, and M. Cacciola, “The GPR technology on the seismic damageability assessment of reinforced concrete building,” *PIERS Online*, Vol. 1, No. 3, 303–307, 2005.
2. Daniels, D. J., *Surface-penetrating Radar*, The Institution of Electrical Engineers, London, 1996.
3. Bungey, J. H. and S. G. Millard, “Radar inspection of structures,” *Proceeding International in Civil Engineering Structures & Buildings*, 173–178, 1993.
4. Hugenschmidt, J., “Concrete bridge inspection with a mobile GPR system,” *Construction and Building Materials*, No. 16, 147–154, 2002.
5. Bungey, J. H., M. R. Shaw, S. G. Millard, and T. C. K. Molyneaux, “Location of steel reinforcement in concrete using ground penetrating radar and neural networks,” In M. C. Forde, ed(s), *Structural Faults & Repair*, 8, Engineering Technics Press, London, 2003.
6. Concrete Society, *Guidance on Radar Testing of Concrete Structures*, Technical Report, No. 48, 88, 1997.
7. Noon, D. A., “Stepped-frequency radar design and signal processing enhances ground penetrating radar performance,” Ph.D. Thesis, University of Queensland, St. Lucia, Australia, 1995.

Sparse, Active Aperture Imaging

John K. Schindler

AFRL Sensors Directorate (RYHA) and the ARCON Corporation
80 Scott Drive, Hanscom AFB, MA 01731-2909, USA

Abstract— We describe an approach to radar imaging of an isolated, rotating target using coherent, sparse, or highly thinned arrays of transmit/receive elements. The array elements are assumed to be randomly positioned and accurately surveyed after placement. Further, the isolated target is assumed to occupy a limited angular sector such that there is no source of backscatter beyond the sector occupied by the target. Estimates of the resolution and image quality are provided when the array elements are widely separated and operate with coherent, multiple input/multiple output (MIMO) signaling, and inverse synthetic aperture radar (ISAR) processing at each MIMO element pair. The sparse array operation can provide superior resolution when compared to ISAR processing with a modest number of sparse array elements. Several important issues relating to feasibility remain to be investigated. These include establishing coherence and timing among the widely separated array elements, adaptive beamforming and processing requirements, and coherence of the scattering phenomena with the widely separated MIMO elements.

1. INTRODUCTION

We address the problem of radar imaging of an isolated, rotating target using coherent, sparse or highly thinned arrays of transmit/receive elements. The array elements are assumed to be randomly positioned and accurately surveyed after placement. Further, the target is assumed to occupy a limited angular sector and, because it is isolated, there is no source of backscatter beyond the sector occupied by the target.

It is well-known that highly thinned arrays provide enhanced imaging resolution determined by the extended aperture of the array. However, typically the random sidelobes of the sparse array are high and degrade the quality of the image due to leakage of scattering from elements of the target at other angles. In this work we examine whether the limited complexity of a linear, random, sparse array as expressed by the equivalent number of array elements is sufficient to control the array pattern over the limited angular extent of the isolated target with no requirements for pattern control elsewhere. Conversely, we examine the target angular extent that can be imaged with a given sparse array configuration and suggest radar signal processing techniques that can effectively limit the target angular extent to be imaged.

Sparse, active rf arrays for imaging have been studied extensively with emphasis on approaches for self cohering the arrays [1–4]. The work has been extended for communications applications using self organizing random arrays as a communications relay [5]. More recently, the concept of the coarray has been applied to the synthesis of active imaging systems [6, 7]. Coherent, multiple input/multiple output (MIMO) operation plays an important role in implementing the advantages of the extended coarray. Conveniently, recent advances in the theory of MIMO radar are summarized in two recent articles [10, 11].

2. PERFORMANCE ANALYSIS

Consider a linear, thinned array of coherent transmit/receive elements exciting a target which is rotating at an angular rate, ω . The elements are randomly positioned and accurately surveyed after placement and operate in a MIMO mode such that each receive element measures the complex transfer function of the array-target system from each transmit element. We assume that the transmit waveforms and matched receiver processing are of sufficient bandwidth that the range resolution of the waveform is small compared to target dimensions.

It is important to observe that as the angle subtended by the array elements increases, only a portion of the scattering from the range gate of each transmit/receive (T/R) pair is common to all pairs and has the potential to respond to coherent beamforming in the sparse array. The cross-range dimension of this common, coherent scattering zone y , normalized to the target diameter, is given by

$$\frac{y}{\text{Diameter}} = \frac{1}{2 \cdot BW_f \cdot \text{Diameter}_\lambda} \cdot \left(\frac{1 + \cos(\Delta\theta)}{\sin(\Delta\theta)} \right), \quad (1)$$

where $\Delta\theta$ is the angular separation between the bisectors of the T/R pairs and $BW_f = \Delta f/f_0 =$ waveform bandwidth/carrier or center frequency and Diameter_λ is the diameter of the target in carrier frequency wavelengths, λ . Scattering from outside this common zone appears as a kind of transmit-excited noise that is non-coherent to the beamforming and must be reduced by auxiliary, inverse synthetic aperture radar (ISAR) processing. Assuming that the ISAR coherent integration time is limited by the time it takes for the most rapidly rotating portion of the target to pass through a single range gate, the cross-range dimension of the ISAR processing, Δy , is

$$\frac{\Delta y}{\text{Diameter}} = BW_f. \quad (2)$$

Requiring that the ISAR resolution, Δy , be smaller than the cross range of the coherent scattering zone, y , places an upper bound on the allowable waveform bandwidth as well as a maximum angle, $\Delta\theta_{\max}$, subtended by the array when viewed from the target. Clearly, the limited angular extent of the array limits the array length and its physical resolution at the target. Elementary arguments provide the coherent sparse array spot size on the target as $\delta y = \lambda/\Delta\theta_{\max}$ providing a spot size compared to object diameter of

$$\frac{\delta y}{\text{Diameter}} = \frac{1}{\text{Diameter}_\lambda \cdot \Delta\theta_{\max}}. \quad (3)$$

Comparing this spot size (3) to the cross range dimension of the common scattering zone (1) reveals that the spot size is more than two orders of magnitude smaller for waveforms with 1% bandwidth and one order of magnitude smaller when the bandwidth is 10%. These results assume an object with a diameter of $10^4\lambda$. An important special case occurs when we require that the range resolution and the Doppler resolution achieved by the ISAR processing are equal. Under this condition we find that $BW_f = (2\text{Diameter}_\lambda)^{-1/2}$ and $\Delta\theta_{\max} = 90^\circ$. For an object which is 10^4 wavelengths in diameter, the resultant bandwidth is 0.7% giving a range and Doppler resolution of 70λ and a sparse array spot size of 0.64λ .

These results assume coherent processing of the sparse array element signals. In addition to establishing coherent reference and timing signals at all sparse array transmit and receive elements, coherent processing requires that the target scattering from the array focus point be coherent among the diverse bistatic and monostatic MIMO element pairs. This may be a reasonable assumption given that the spot size created by the sparse array is a fraction of a wavelength and any scattering from this limited area should have a broad scattering pattern. However, the validity of this assumption needs further investigation given that other phenomena may intervene, such as scattering center occlusion or translation with changes in the MIMO excitation/reception pairs.

Having established the potential for a substantial improvement in sparse array resolution with the use of MIMO operation and associated ISAR processing, there remains the question as to whether the sidelobe quality of the sparse array pattern is sufficient over the common, coherent scattering zone defined by (1) to avoid distortion of the scattering image from pattern leakage. Implicit in this question is the number of sparse array elements or the array fill factor necessary to achieve the required sidelobe levels.

MIMO operation of the array is of great value in introducing additional “virtual” elements that are useful in pattern control. With N real, sparse array elements, there are at most $\aleph = N(N+1)/2$ virtual MIMO elements or independent measurements of the transmit-scatterer-receiver system transfer function. The virtual elements form an extended aperture with a natural space taper since the virtual elements are located at positions given by the convolution of the physical elements positions with themselves. In effect, the array with virtual elements forms a linear system excited by the target scattering and with which the scattering reflectivity of the target is imaged.

We investigate the issue of pattern quality over the coherent scattering zone and physical array fill factor in two ways. First, we synthesize patterns with elements randomly positioned using maximum signal-to-interference ratio and minimum variance criteria. These synthesis techniques assume that scattering comes from a stationary, isolated scattering center when path length distances from transmit and receive elements are removed. Second, we estimate the scattered field in the vicinity of the coherent scattering zone using maximum a posteriori (MAP) and maximum likelihood (ML) estimation processing.

In the investigation of pattern quality, we assume that the sparse, random array with surveyed positions operates in a MIMO mode. The effective transmit-receive product pattern of the sparse

array is equivalent to a one-way array pattern from elements located at N virtual positions given from the convolution of physical array element positions with themselves. The reflected field from the target acts as an active source illuminating this equivalent one-way pattern. The transmit and receive element weights are determined assuming that they provide a limited, local scan from a common focus point for the array which is near the target to be imaged. This focus point is assumed to be determined adaptively from prior processing as has been demonstrated in earlier work [1–4].

In the first approach to evaluating pattern quality, we synthesize the transmit and receive patterns with a unique, iterative approach to maximize the signal to interference or minimize the variance of the output due to noise and scattering outside the common, coherent scattering zone. Initially, the interference is expressed as white receiver noise, independent between receive elements superposed with scattering from the coherent zone and non-coherent zones of the target. The non-coherent zones are assumed to have excess power distributed uniformly in position when compared to the uniform power scattered from the coherent zone. An isolated point target is assumed to exist in the coherent scattering zone. The iterative synthesis process begins by assuming a uniform, maximum gain transmit array with a pattern that shapes the interference within and beyond the coherent scatter zone. In the first stage of iteration, the receive pattern is synthesized according to the optimization criterion selected and the pattern further shapes the interference within and beyond the coherent scatter zone. In the next stage of iteration, the transmit pattern is synthesized with the same criterion. However, in this stage, the receiver noise power must be normalized by the constrained transmit power to insure that the criterion objective function is in the proper form for optimization. This iterative process continues until the value of the optimization criterion changes little between iterations.

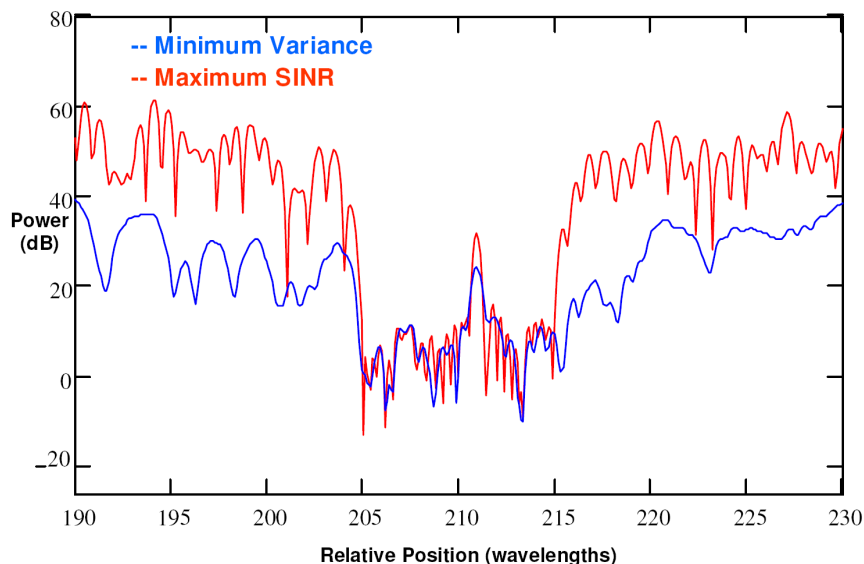


Figure 1: Synthesized transmit-receive patterns with maximum signal to interference ratio and minimum variance criteria.

The results of one such transmit-receive pattern synthesis are shown in Figure 1 for both the maximum signal-to-interference ratio and minimum interference variance criteria. The central region from relative position 205λ to 215λ is the coherent scatter zone where pattern control is desired. Outside this zone, little pattern control is required since here scatter is attenuated by the ISAR processing at each MIMO transmit-receive pair.

In this approach to pattern synthesis, we have implicitly assumed that the signal exciting the MIMO virtual array results from a single, isolated scatterer having a position which is fixed, independent of the MIMO transmit-receive pair exciting the scatterer. As discussed earlier, this may not be a universally valid assumption. A second approach to estimating the target reflectivity in the coherent scatter zone does not make this demanding assumption.

The second approach to sparse aperture imaging involves MAP and ML estimation of the scattered field in the vicinity of the coherent scattering zone. Here we expand the scattered field into an assumed finite series of orthogonal basis functions with expansion coefficients to be estimated. The

basis functions are propagated through each MIMO pair transfer function to yield \aleph observations from which estimation of the expansion coefficients is made.

There are at least two reasonable approaches to selecting the basis functions for expansion of the scattered field. The first assumes that the scattered field or reflectivity is a stationary random process such that each realization of the process can be expanded in the Karhunen-Loève expansion [9]. Here the basis functions are eigenfunctions of the process autocorrelation function and the expansion coefficients are statistically independent Gaussian random variables (assuming that the underlying reflectivity process is a complex Gaussian random process). While this approach is attractive, it requires assumptions regarding the statistical properties of the scattered field random process. An alternative expansion more closely tied to the electromagnetics of the scattering process seems preferable [8]. In this approach by Bucci and Franceschetti, the scattered field near a spatially bounded scatterer is expanded in cardinal sinc functions and the error in approximating the field with a finite series is bounded from considerations of the properties of the physical wave propagation of the scattered field. The spatial sampling frequency and hence the number of quantities to be estimated can be evaluated as a function of a bound on the error in approximating the scattered field near the coherent scatter zone of the object being imaged. Each basis function of this expansion is propagated through each MIMO pair transfer function to give the \aleph observations from which estimation is made. This approach is useful since it provides a numerical estimate of the number of parameters to be estimated for comparison with the number of independent space samples yielded by the sparse MIMO array. Application of this approach to our problem indicates that a minimum spatial sampling frequency of $\lambda/4$ is required. Quantitatively, an upper bound of 10% error in approximating the scattered field is expected when a 10% over-sampling rate is employed on a surface which lies 1.6λ from the scattering body. In this approximation it is assumed that the scattered field is determined most significantly by the structure of the scattering body after removal of the phase of the field introduced by the path lengths from the MIMO transmit and receive elements. Limitations of this assumption require further study.

An appropriate approach to estimating the scattered field expansion coefficients employs either the maximum a posteriori or maximum likelihood processing of the sparse MIMO array observations. Conventional maximization of the logarithm of the appropriate probability density functions results in the requirement to select the expansion coefficients that provide a least squares fit between the array observations and those provided from the MIMO array model. The relative value of the least squares fit as a function of the number of virtual array elements for a given size of the coherent scattering zone provides an estimate of the required sparse array fill factor which we can compare with heuristic estimate of the fill factor based on the requirement that quasi-grating lobes from a quasi-periodic sparse array remain outside the coherent scattering zone. These heuristic arguments require that the number of virtual MIMO array elements exceeds $1/BW_f$ for the fully extended sparse array.

3. CONCLUSIONS

We describe an approach to radar imaging of an isolated, rotating target using coherent, sparse arrays of transmit/receive elements. The isolated target is assumed to occupy a limited angular sector such that there is no source of backscatter beyond the sector occupied by the target. The array elements are assumed to be widely separated, randomly positioned, and accurately surveyed after placement. The array operates with coherent MIMO signaling and ISAR processing at each MIMO element pair. The sparse array operation can provide superior resolution comparable to the wavelength of the carrier frequency when compared to ISAR processing with a modest number of sparse array elements. Several important issues relating to feasibility remain to be investigated. These include establishing coherence and timing among the widely separated array elements, adaptive beamforming and processing requirements, and coherence of the scattering phenomena with the widely separated MIMO elements.

ACKNOWLEDGMENT

It is a pleasure to acknowledge the support of Dr. Arje Nachman of the Air Force Office of Scientific Research.

REFERENCES

1. Steinberg, B. D., et al., "First experiment results from the Valley Forge radio camera program," *Proceedings of the IEEE*, Vol. 67, No. 9, 1370–1371, 1979.

2. Steinberg, B. D., W. Whistler, and D. Carlson, “Two-dimensional imaging with a radio camera,” *Proceedings of the IEEE*, Vol. 71, No. 11, 1325–1326, 1983.
3. Tsao, J. and B. D. Steinberg, “Reduction of sidelobe and speckle artifacts in microwave imaging: The CLEAN technique,” *IEEE Transactions on Antennas and Propagation*, Vol. 36, No. 4, 543–556, 1988.
4. Attia, E. H. and B. D. Steinberg, “Self-cohering large antenna arrays using the spatial correlation properties of radar clutter,” *IEEE Transactions on Antennas and Propagation*, Vol. 37, No. 1, 30–38, 1989.
5. Vespoli, J. B., et al., “A Self-organizing random array communications relay,” *IEEE Transactions on Communications*, Vol. 31, No. 4, 484–492, 1983.
6. Hoor, R. T. and S. A. Kassam, “The unifying role of the coarray in aperture synthesis for coherent and incoherent imaging,” *Proceedings of the IEEE*, Vol. 78, No. 4, 735–752.
7. Hoor, R. T. and S. A. Kassam, “Array redundancy for active line arrays,” *IEEE Transactions on Image Processing*, Vol. 5, No. 7, 1179–1183, 1996.
8. Bucci, O. M. and G. Franceschetti, “On the spatial bandwidth of scattered fields,” *IEEE Transactions on Antennas and Propagation*, Vol. 35, No. 12, 1445–1455, 1987.
9. Van Trees, H. L., *Detection, Estimation and Modulation Theory, Part 1*, Wiley, New York, 1968.
10. Haimovich, A. M., R. S. Blum, and L. J. Cimini, “MIMO radar with widely separated antennas,” *IEEE Signal Processing Magazine*, Vol. 21, No. 1, 116–129, 2008.
11. Li, J. and P. Stoica, “MIMO radar with colocated antennas,” *IEEE Signal Processing Magazine*, Vol. 24, No. 5, 106–114, 2007.

Wavelet Based Synthesis of Multifractal Rough Surface

Zhaorui Wang and Shanwei Lv

School of Electronic and Information Engineering, Beihang University, Beijing, China

Abstract— In this work, a preliminary study is carried out to demonstrate the synthesis of one dimensional multifractal rough surface by means of discrete wavelet transform. The desired local regularity of the multifractal rough surface is obtained by controlling the weights of the wavelet expansion of the Gaussian white noise. The selling point is that roughness of the surface is allowed to vary from point to point. This approach is also appropriate for generating the multifractal rough surface that is non-Gaussian and autocovariance function unknown in advance. The validity and rationality are verified by numerical experiments.

1. INTRODUCTION

The problem of electromagnetic scattering from rough surface has been extensively studied in a wide variety of scientific and engineering applications, including electromagnetics, microwave remote sensing, integrated optics, underwater acoustics, radar cross section from sea and land surfaces, semiconductor packaging, computer vision and computer graphics, and other many potential applications [1]. For these problems the rough surface is either the primary target or the clutter. Although the understanding of interaction of electromagnetic waves with the rough surface is essential, the most definitely necessary thing is to generate needed rough surface profile.

Traditional Gaussian spectrum rough surface is single scale and the roughness is not time varying. During recent years, the fractal geometry is introduced to the study of rough surface. Since the fractal rough surface, as a multi-scale geometry, takes account of surface perturbations in large and small scales, such as the famous band limited Weierstrass-Mandelbrot roughness spectrum [2]. It seems better to describe some natural surfaces than traditional model. Whereas the limitation of the fractal model mentioned above is also obvious, its pointwise singularity describing the roughness remains the same all along the sample path. From a physical point of view, this may be too strong an idealization. Since many natural structures are determined by a large number of generating processes operating at different scales and the roughness is dynamic. For modeling these more realistic structures, multifractal rough surface is appropriate. In this paper, we preliminary investigate this subject with the wavelet for the first time. Presented algorithm is inspired by the work of J. F. Muzy and his coworkers [3], R. F. Peltier and J. L. Vehl, and our approach is close in spirit to that of Ayache [4].

2. MULTIFRACTAL AND WAVELETS

In practice, the roughness profile being analyzed are often very far from smooth, and these irregular surface usually have many nondifferentiable points, even nowhere differentiable. Mandelbrot coined the term “fractal” to characterize these irregular phenomena [5]. If the pointwise singularities of them are same along the sample path, then one can use a fractal process to model them. However, for other more complex physical surfaces whose pointwise singularity varies along the sample path, one usually models them with multifractal function. Fractal and multifractal signals all exhibit stochastically self-similarity, which inspires naturally us to investigate them with wavelets introduced firstly by Grossmann and Morlet [6].

The definition of discrete wavelet transform of $f(t)$ is as follows:

$$Wf(j, k) = \langle \psi_{j,k}(t), f(t) \rangle_{L^2(R)} = \int_R \bar{\psi}_{j,k}(t) f(t) dt \quad (1)$$

where $\psi_{j,k}(t) = 2^{j/2} \psi(2^j t - k)$ is the wavelet base. In terms of filtering operation, the t th element of wavelet approximate coefficient a_{j-1} can be reconstructed via following formula:

$$a_{j-1,t} = \sum_{l=0}^{L-1} h_l d_{j,t+l \bmod N_{j-1}}^\uparrow + \sum_{l=0}^{L-1} g_l a_{j,t+l \bmod N_{j-1}}^\uparrow \quad (2)$$

where $t = 0, \dots, N_{j-1} - 1$, and $x_{j,t}^\uparrow = \begin{cases} 0, & t = 0, 2, \dots, N_{j-1} - 2 \\ x_{j,(t-1)/2}, & t = 1, 3, \dots, N_{j-1} - 1 \end{cases}$ is the up-sampling operation (x stands for d or a), d is the detail coefficient [7].

Jaffard has proven that the decay of the detail coefficients amplitude across scales is related to the pointwise singularity of the fractal signal [8]. The wavelet coefficients give a necessary and sufficient characterization of local regularity of a fractal function.

The cone of influence of u_0 in the scale-space plane is the set of points (u, s) such that u_0 is included in the support of $\psi_{u,s}(t) = s^{-1/2}\psi((t-u)/s)$. Since the support of $\psi((t-u)/s)$ is equal to $[u - Ks, u + Ks]$, the cone of influence of u_0 is defined by

$$|u - u_0| \leq Ks \quad (3)$$

If u is in the cone of influence of u_0 then $Wf(u, s) = \langle \psi_{u,s}(t), f(t) \rangle_{L^2(R)}$ depends on the value of f in the neighborhood of u_0 . Since $|u - u_0|/s \leq K$, we have

$$|Wf(u, s)| \leq C' s^{h(u_0)+1/2} \quad (4)$$

3. SYNTHESIS ALGORITHM

Let N , an integer, denotes the desired size of an rough surface realization, and $h(t) : [0, \infty) \rightarrow [a, b] \subset (0, 1)$ is a Hölder function of exponent $\beta > 0$, then multifractal rough surface can be obtained by setting:

$$f_{h(t)}(t_i) = f_{h(t_i)}(t_i), \quad 1 \leq i \leq N \quad (5)$$

One can obtain the desired local regularity of the surface by controlling the weights of the wavelet expansion of the Gaussian white noise as follows

$$d_{h(t_i)}(j, k) = 2^{j(h(t_i)+1/2)}\theta_{j,k}, \quad j = 0, \dots, J, k = 1, \dots, N/2^j \quad (6)$$

where $\theta_{j,k}$ are i.i.d. $N(0, \sigma_0^2)$ random variables, and the σ_0^2 is the variance. So the simulated fractal surface can be written as a weighted summation of orthonormal wavelets adding a trend term, weights being samples of independent zero-mean Gaussian processes, whose variance is power-law scale dependent as described by Equation (6). The synthesis representation is following:

$$f_{h(t_i)}(t) = C \left(\sum_j \sum_k d_{h(t_i)}(j, k)\psi_{j,k} + \sum_k a_J(k)\phi_{J,k} \right) \quad (7)$$

with $\psi_{j,k} = 2^{j/2}\psi(2^j t - k)$, $j, k \in Z^+$ is the wavelet basis of $L^2(R)$, a_J is the J th level approximate coefficient of the wavelet representation of the Gaussian white noise process, $\phi_{J,k}$ is the scaling function. Note that the constant C , due to the right-hand side of (7) does not converge with the growth of $2^{j(h(t_i)+1/2)}$ as $j \rightarrow \infty$, so we use this constant to control the convergence. The value of C is taken as $2^{-JH(t_i)}$, and the validity is verified by the numerical experiments.

The complete procedures are presented as follows:

- 1) Generate a mean zero, variance σ_0^2 Gaussian white noise $W_0(n) \stackrel{d}{=} N(0, \sigma_0^2)$. Without loss of generality, the size is set as $N = 2^J$, $J \in Z^+$ due to using fast pyramid algorithm based on discrete time filters.
- 2) Perform the discrete wavelet transform to $W_0(n)$ to obtain the architecture (means different scale level) $j \in [0, J]$ and elementary bricks (means detail coefficients at each scale) $\theta_{j,k}$, $j = 0, \dots, J$, $k = 1, \dots, N/2^j$.
- 3) Calculate the weight $2^{j(h(t_i)+1/2)}$, $i = 1, \dots, N/2$.
- 4) Determine the relevant detail coefficients that correspond to the $f_{h(t_i)}(t_{2i-1})$ and $f_{h(t_i)}(t_{2i})$, and weighting these coefficients with $2^{j(h(t_i)+1/2)}$.
- 5) Perform inverse discrete wavelet transform to obtain $f_{h(t_i)}(t_{2i-1})$ and $f_{h(t_i)}(t_{2i})$.
- 6) Repeat step 3) to 5) for all other $h(t_i)$, $i = 2, \dots, N/2$ to obtain the rest $N - 2$ points multifractal signal.

As for the computation, due to the use of pyramid algorithm, the implementation is time saving. Suppose that N observations are needed, then the time complexity is $O(N^2)$. This approach is computationally faster and suited to building large traces, and also can be used for non-Gaussian case, and the autocovariance function of the simulated signal is not necessary known in advance.

4. NUMERICAL EXPERIMENTS

We generated 3 different kinds of one dimensional multifractal rough surface in terms of method described above. The length of these trajectories is $N = 4096$, and the corresponding Hölder function is $h(t) = 0.1 + 0.8t$, $0 < t < 1$ (linear), $h(t) = 0.1 + 0.01 \exp(4.4t)$, $0 < t < 1$ (exponential) and $h(t) = 0.5$ (constant), as shown in Figure 1 to Figure 3.

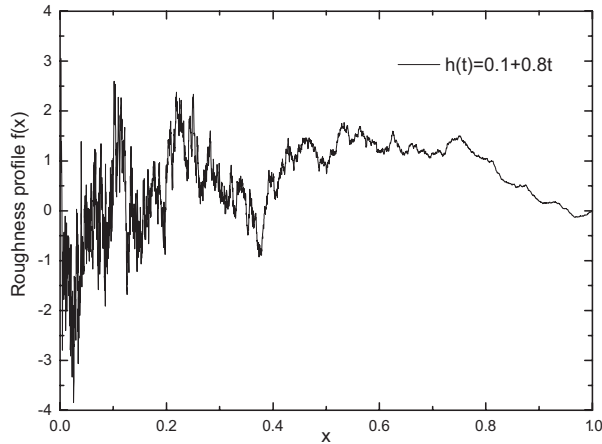


Figure 1: The multifractal rough surface with linear roughness.

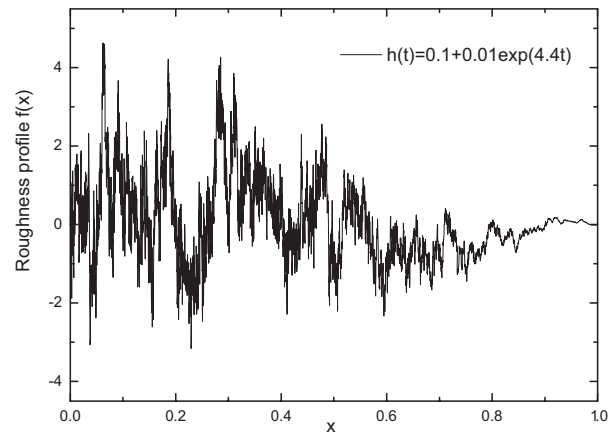


Figure 2: The multifractal rough surface with exponential roughness.

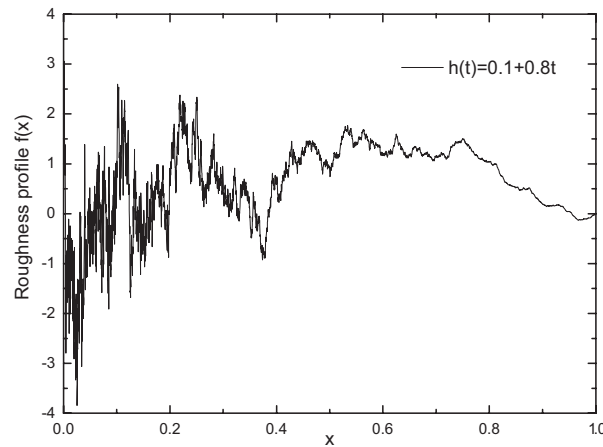


Figure 3: The degenerated multifractal rough surface.

In these figures we can see intuitively that the local regularity of the synthetic rough surface is controlled nearly exactly with the prescribed Hölder function, the larger (small) the value of $h(t)$, the rougher (smoother) the sample path, which is the behavior we are looking for. When $h(t)$ is set to a constant, then the synthesized multifractal rough surface degenerates to the ordinary fractal rough surface, as shown in Figure 3.

5. CONCLUSIONS

An approach for synthesis of multifractal rough surface in terms of discrete wavelet transform is proposed in this paper, which presents a new way for modeling the more realistic physical phenomenon. The numerical simulations demonstrate the validity. We hope this is a reproducible research and all source codes are available from the author upon request.

ACKNOWLEDGMENT

The authors are very grateful to financial support of 863 fund of China (2006AA12A110).

REFERENCES

1. Zahn, D., K. Sarabandi, K. F. Sabet, et al., “Numerical simulation of scattering from rough surfaces: A wavelet-based approach,” *IEEE Transactions on Antennas and Propagation*, Vol. 48, No. 2, 246–253, 2000.
2. Jaggard, D. L. and X. Sun, “Scattering from fractally corrugated surfaces,” *Journal of the Optical Society of America A*, Vol. 7, No. 6, 1131–1139, 1990.
3. Muzy, J. F., E. Bacry, and A. Arneodo, “Wavelets and multifractal formalism for singular signals: Application to turbulence data,” *Physical Review Letters*, Vol. 67, No. 25, 3515–3518, 1991.
4. Ayache, A., S. Cohen, and J. L. Vehele, “The covariance structure of multifractional Brownian motion, with application to long range dependence,” *Proceedings of the IEEE ICASSP’2000*, 3810–3813, Istanbul, Turkey, June 2000.
5. Mandelbrot, B. B., *The Fractal Geometry of Nature (Updated and Augmented)*, W.H. Freeman and Company, New York, 1983.
6. Grossmann, A. and J. Morlet, “Decomposition of hardy functions into square integrable wavelets of constant shape,” *SIAM Journal on Mathematical Analysis*, Vol. 15, No. 4, 723–736, 1984.
7. Percival, D. B. and A. T. Walden, *Wavelet Methods for Time Series Analysis*, Cambridge University Press, Cambridge, 2000.
8. Jaffard, S., “Functions with prescribed Hölder exponent,” *Applied and Computational Harmonic Analysis*, Vol. 2, No. 4, 400–401, 1995.

In-SiP Integration of Electromagnetic Shields

O. Alilou, J.-L. Lefebvre, and P. Descamps

NXP Semiconductors and Laboratoire de Microélectronique ENSI Caen-NXP (LAMIPS)
2 rue de la girafe, BP5120, 14079 Caen Cedex 5, France

Abstract— System-in-Package (SiP) is a growing trend of the electronic industry consisting in integrating one or several integrated circuits (ICs) together with discrete components of various technologies in a single package, resulting in one or several electronic systems. SiP allows for higher system miniaturisation, performance and offers higher system integration.

However, new electromagnetic compatibility challenges occur with: on the one hand, the constitutive sub-elements of the SiP within the package are closer than ever to one another. Circuits of heterogeneous technologies originally designed to function in their own packages are now placed together in a same confined environment separated by distances as small as a few tens of microns only. On the other hand, because of their smaller size, complete SiP systems are also closer to one another in the end equipment. Thus, they can suffer from significant noise from the neighbouring sub-systems. Each SiP may therefore need to be protected from external electromagnetic disturbances.

This paper addresses for the first time the need for electromagnetic shielding of sub-systems in a mobile phone. It will be shown that integration of electromagnetic shields within the SiPs against external incident disturbances not only offers more compliance to all types of electromagnetic environments, but also places SiP solutions higher in the system value chain.

Then, the SiP-specific boundary conditions are applied to the Maxwell equations for simplification, and a definition of shielding effectiveness formula applicable to SiP is proposed.

Tri-dimensional electromagnetic simulations of simplified shielding schemes are then presented. In order to assess the shielding effectiveness from thin-film deposited shields in SiP, and its influent variables, simulation results have shown that a 60 dB isolation from DC until 1.5 GHz, and a 30 dB from 1.5 GHz until 10 GHz can be fitted.

Finally, measurements of shielding effectiveness of a shielded SiP demonstrator are presented and compared to the initial simulations.

1. INTRODUCTION

Currently, most of the EMI (Electromagnetic Interferences) that computer motherboards cause result from emissions produced by the packaged integrated circuits (“ICs”) which are mounted, or coupled, into the motherboard. To reduce the emissions that those parts release, various types of Faraday cages (or other sealing/covering apparatus) may be placed over them. However, such devices increase the cost of the system, occupy more motherboard space, and may impose challenging signal routing requirements. As a consequence, using such devices to reduce the EMI that these packaged ICs cause is not a particularly attractive solution.

Therefore, there is a need for an improved technique for reducing IC generated EMI. There is a need for such a technique that can be integrated into standard component designs without requiring significant modification. The packaged IC of the present paper includes such a mechanism.

2. SHIELDING EFFECTIVENESS

The shielding effectiveness (SE) is the ratio between two EM power quantities, the incident power (P_i) and transmitted power (P_t):

$$SE(dB) = -10 \log \left(\frac{P_t}{P_i} \right) \quad (1)$$

In the far field case, it can be simplified as follows:

$$SE(dB) = -10 \log \left(\frac{P_t}{P_i} \right) = -20 \log \left(\frac{E_t}{E_i} \right) = -20 \log \left(\frac{H_t}{H_i} \right) \quad (2)$$

and

$$SE(dB) = S_a(dB) + S_r(dB) + M(dB) \quad (3)$$

with S_a : electromagnetic absorption, S_r : electromagnetic reflection and M : Multiple reflection.

Shielding theory is based on two fundamental mechanisms, reflection loss and absorption loss. In placing a metallic barrier in the path of an electromagnetic plane wave propagating with orthogonal E and H vectors. The E - and H -field components are related by the wave impedance, which is defined by the ratio of the tangential field components. This implies an impedance mismatch for the wave, which therefore causes reflections. The remaining field is transmitted through the barrier after partial absorption through the metal. The electric-field component is contrary reflected predominantly when it propagate into a medium with lower impedance (at the first surface), while the magnetic component is reflected when it must pass into a medium with higher impedance (the second surface). Between the two surfaces there will be multiple reflections, which may be overlooked if the absorption loss in the barrier is at least 10 dB.

To get a high efficient shield both in the low and high frequencies we should use a metal with high conductivity and high relative permeability (μ_r).

Our shield (Figure 1(a) and 1(b)) consists of a thin film metal deposition with chemical electrolyses process of Cooper, Nickel, and Gold flash respectively on the top of LCP (Liquid Crystal Polymer) package. The copper with a high conductivity at 588235 S/ohm ensures a good wave rejection in the HF, and Nickel with a relative permeability of 1240 has the capability to reject the magnetic wave in the low frequency ranges.

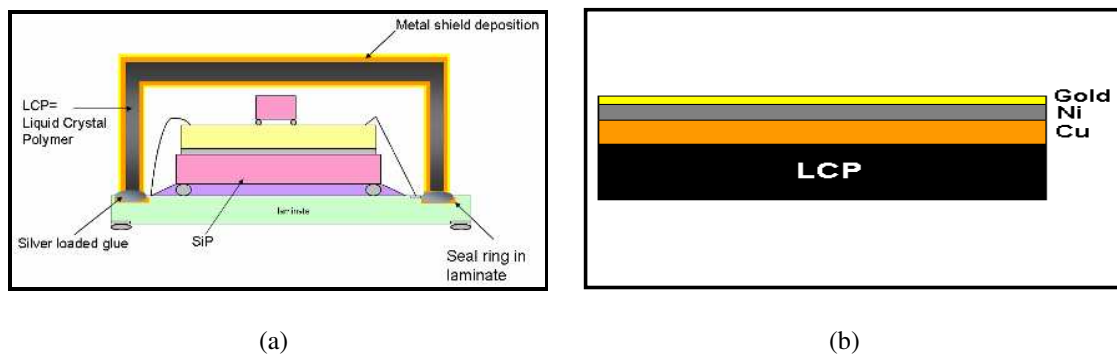


Figure 1: (a) Shield package structure; (b) Thin film metal deposition structure.

3. TRI-DIMENSIONAL ELECTROMAGNETIC SIMULATIONS

In order to estimate the shielding effectiveness of this technique, and to verify the influences of critical parameters such as the thickness of metal deposition or the ground connection, we have simulated a simplified structure (Figure 2) made with two half-wave antennas and a metal ground separation in copper:

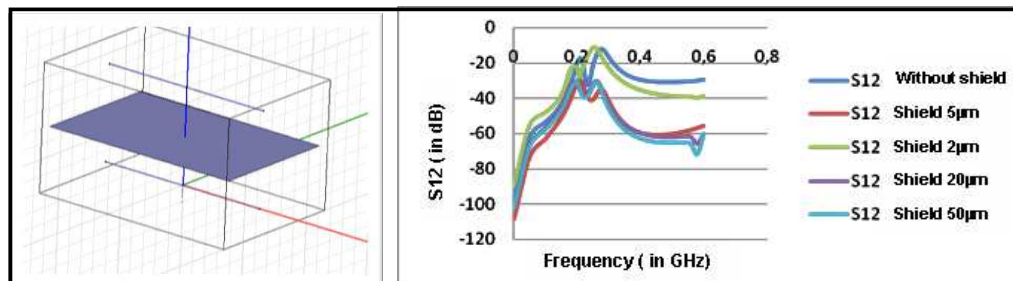


Figure 2: Transmission actor with different ground separation thickness.

Up to 300 MHz a ground copper separation with 5 μ m of thickness allows to obtain more than 30 dB of isolation. In the test chip demonstrator we have chosen a value of 8 μ m copper thickness, 3 μ m for Nickel and 0.2 μ m for gold. The package is reported on a laminate substrate, soldered with silver loaded glue into the ground ring. A passive inductance or a RF antenna is designed in the laminate, directly linked to a SMA connector through transverse Vias (Figure 3).

In the simulation we excite two wave port with Lamped wave in HFSS (Figure 4).

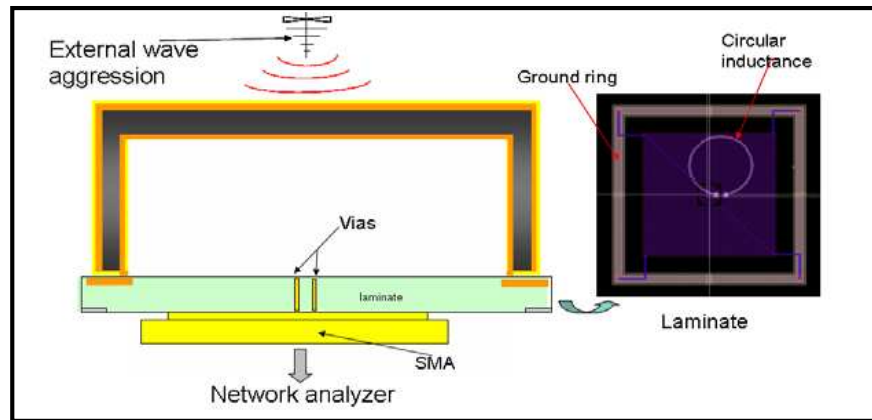


Figure 3: Measurement test chip.

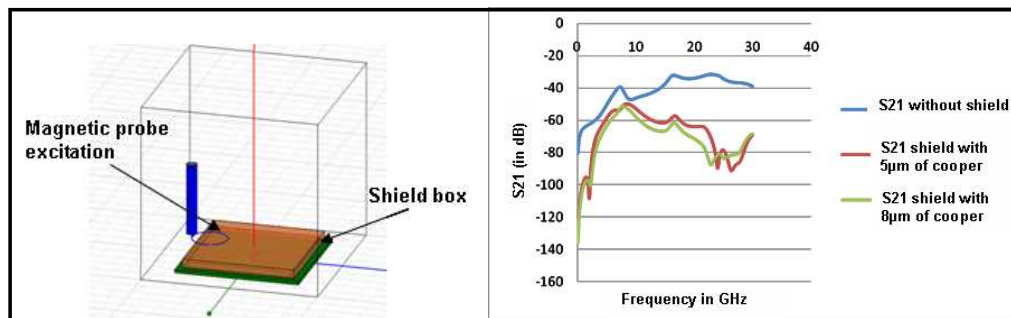


Figure 4: HFSS simulation of the test chip.

The transmission factor S_{21} between the external excitation probe and the laminate circular antenna give the power ratio between the emission power and the transmitted one.

The HFSS simulation shows that isolation obtained for a frequency range from 1Hz to 1.5 GHz is around 60 dB, and 30 dB until 10 GHz. Unfortunately, in the measurement, we cannot reproduce these levels because the noise levels of the network analyzer are too high, and it is difficult to model the silver loaded glue, and the irregularity of metal deposition (Figure 6), as well.

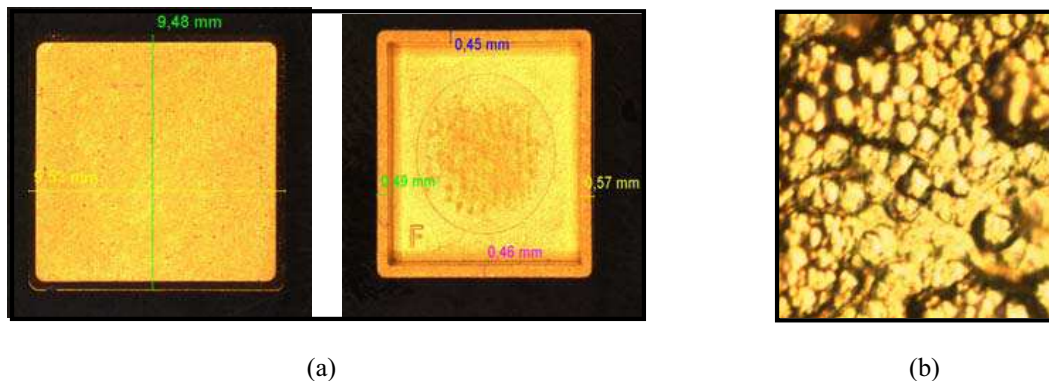


Figure 5: (a) Shielded package; (b) Optical surface observation with 50x magnification.

4. SHIELD PACKAGE

As we can see in Figures 5(a), 5(b) and 6, the electrolyses metal deposition of copper and Nickel is not regular and not homogeneous, the thickness values specification are very difficult to respect in this process. This non flatness is a key factor to generate a destructive resonance in the transmitted wave at high frequencies.

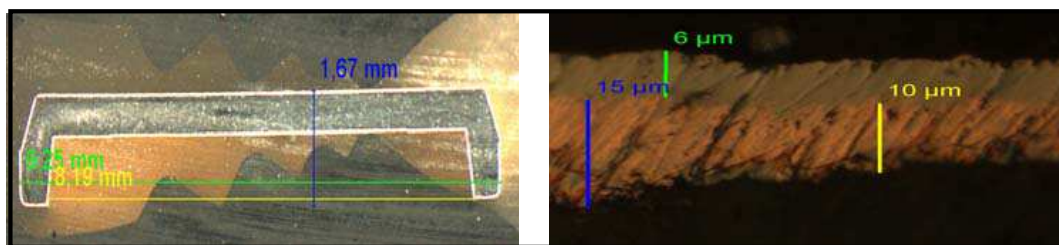


Figure 6: Shield package cross section.

5. MEASUREMENT

With the near field bench measurement (Figure 7(a) and 7(b)), at 2 mm upper the shield, the probe is directly connected to the power generator, and the SMA connector to the spectrum analyzer, this configuration is more realist than measurements for the rectangular cellule wave guide (Nicolson, Ross method [4]), because we have in real dimensions of ICs package, and also with near waves, the electrical and the magnetic field can be measured separately.

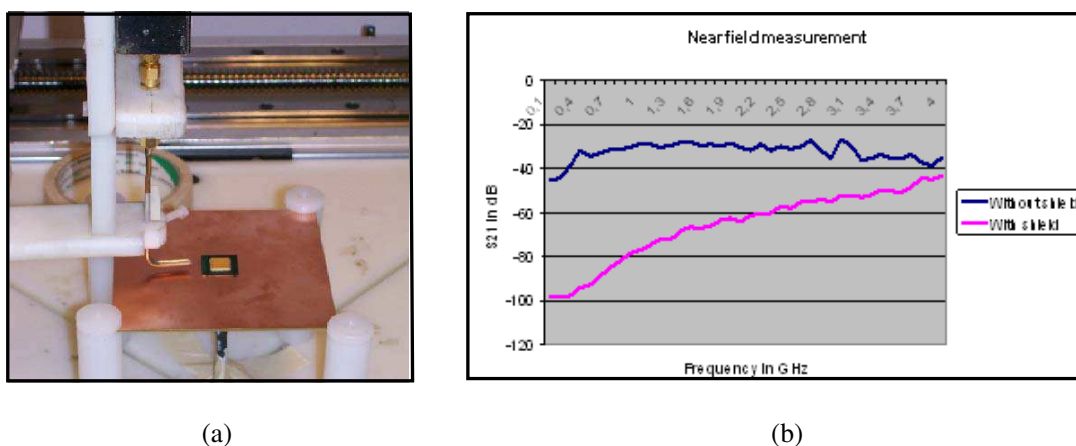


Figure 7: (a) Near field bench measurements; (b) Isolation comparison.

As shown in the Figure 7(a) and 7(b), isolation has a value higher than 35 dB until 1.5 GHz, and 15 dB until 3.5 GHz. Unfortunately after this frequency, box resonance degrades the shielding effectiveness.

6. CONCLUSIONS

The thin film metal deposition is a new shielding concept which has a lot of advantages, for ICs application, especially for Cellular and TV-front end circuits. This study gives a primary characterization of shielding effectiveness until 3.5 GHz, and simulation estimation in the higher frequencies.

The next step of our study will be focused to improve process deposition soldering and to test the package reliability. A technological demonstrator with TV-front end IC will be tested to evaluate its EMI immunity and emission.

ACKNOWLEDGMENT

We would like to acknowledge all people who are participants of this work, and especially the IRSEEM team, for its help in the measurements.

REFERENCES

1. Martin, N. and H. Pohjonen, "System-in-Package (SiP) modules for wireless multiradio," *Electronic Components and Technology Conference*, 2006.
2. Baudry, D., L. Bouchelouk, A. Louis, and B. Mazari, "Near-field bench for complete characterization of comonents radiated emissions," *EMC Compo*, 85–89, Angers, France, April 2004.

3. Miller, D. A. and J. E. Bridges, “Review of circuit approach to calculate shielding effectiveness,” *IEEE Transactions on Electromagnetic Compatibility*, 1968.
4. MIL-STD-285, Military Standard, Method of Attenuation Measurements for Enclosures, Electromagnetic Shielding, for Electronic Test Purposes.

Neural Network Modeling of Scattering Parameters from a Conducting Post in Rectangular Waveguide

Manidipa Bhattacharya¹, B. Gupta², K. Yasumoto³, and H. Jia³

¹SAMEER, Plot L2, Block GP, Sector-V, Salt Lake Electronic Complex, Kolkata 700091, India

²Department of Electronics and Telecommunication Engineering
Jadavpur University, Kolkata 700032, India

³Department of Computer Science and Communication Engineering
Kyushu University, Fukuoka-shi 812-8581, Japan

Abstract— Neural networks are popular as efficient alternatives to conventional computational models like numerical modeling or analytical methods for RF and Microwave modeling and design. Such models reduce both processing time and analytical complexity resulting in simpler computation process. Thus the technique has greater potential in the analysis of various problems in electromagnetism. In the present problem neural network technique has been used for non-linear modeling of the frequency response of the scattering properties of a long circular conducting cylinder in a three dimensional rectangular waveguide at X band. The scattering properties of the vertical posts are analyzed by semi analytical approach based on image theory and the scattered fields are calculated from the lattice sum and the transition matrices. Analysis results have been used to generate S parameter data for the configuration in order to train the proposed network.

1. INTRODUCTION

Neural network is a computational model based on biological neural networks. It consists of an interconnected group of artificial neurons and processes information by a weighted sum approach. In most cases an ANN works as an adaptive system that changes its structure based on external or internal information that flows through the network during the learning phase. Being a non-linear statistical data modeling tool neural networks can be used to model complex relationships between inputs and outputs and can be trained to learn from observation and generalize by abstraction [1]. A multi-layer perceptron model trained by a backpropagation algorithm [2] is a standard computational tool for any supervised-learning pattern recognition or function approximation process. A Multi Layer Perceptron (MLP) is a network of neurons with weighted interconnections where each neuron uses a nonlinear activation function. In our work, the neurons are properly trained to model the scattering reflectance and transmittance from a vertical conducting post embedded in rectangular waveguide. The universal approximation theorem [3] states that there always exists a three layer MLP neural network that can approximate any arbitrary nonlinear continuous multi-dimensional function to any desired accuracy. This forms a theoretical basis for employing neural networks to approximate RF/Microwave circuit/systems, as well for our work.

2. FORMULATION OF PROBLEM

Several analytical techniques [4] have been reported in the literature for studying the behavior of scattering properties of vertical conducting posts in a 3-D rectangular waveguide. The scattering properties of vertical posts placed in a rectangular waveguide can also be analyzed using numerical techniques [5]. The reflection and transmission matrices for a single scattering post can be derived in closed form [6] using the lattice sums and the T-matrix of a circular cylinder in free space. The geometry of the rectangular waveguide investigated with a full height conducting cylindrical post (radius r) is shown in the Fig. 1. TE_{10} mode is assumed to be propagating for which the frequency response of the power reflectance and transmittance are analytically obtained. The post dimensions are used as inputs of the proposed neural network model and the outputs are set as magnitude and phase of S_{11} and S_{21} .

For analysis of the structure the rigorous methods yield highly accurate results but they require considerable analytical efforts leading to complicated computer programming. But neural network method of modeling bypasses the repeated use of complex iterative process and hence the response of the model designed for desired response becomes fast.

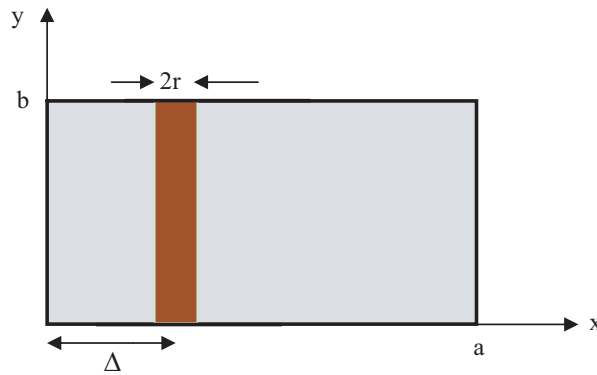


Figure 1: Cross sectional view of the circular post in rectangular waveguide.

3. NEURAL NETWORK CONFIGURATION

A typical neural network structure consists of neurons as processing elements and links/synapses as connection between neurons. Every link has a corresponding weight parameters associated with it and the neurons are grouped into layers. Three layer MLP network has input, hidden and output layers associated with it. The corresponding neurons produce outputs for each layer with weighted sum as the input of a non-linear activation function. Feed forward computation is a process used to compute the output vector from external inputs through neural network layers by keeping the weights fixed. To develop a neural network model we need to identify input and output parameters of the structure under consideration to generate and preprocess data for carrying out ANN training. Generally MLP weights are initialized by assigning the weights with small random values. The purpose of the neural network training is to adjust the weights such that the error function is minimized. As the error function is a nonlinear function of the adjustable weight parameters, iterative algorithms are used to update it with an appropriate learning rate. The back propagation training algorithm updates weights along the negative direction of the gradient of the training vector. Finally the quality of the neural network model is evaluated with an independent set of data and a quality measure has been performed based on average test error and standard deviation.

4. DESIGN OF NEURAL NETWORK

A three layer MLP as shown in Fig. 2 is used to model the scattering from conducting full height post in rectangular waveguide. For this purpose the post position relative to two axes of the waveguide

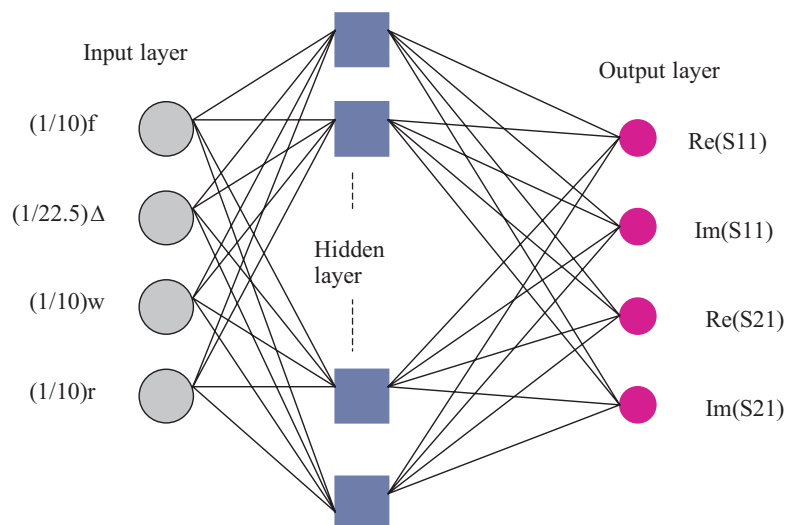


Figure 2: Neural network model for scattering post in rectangular waveguide (Δ and w are the post position along x and y direction respectively and r is the radius of the post).

and its radius are taken as inputs. The waveguide used here is WR-90 (22.5 mm \times 10.2 mm.) for the X band frequencies. The number of neurons taken for the hidden layer is 48. As the training data generated from the electromagnetic analysis has a normalized range from -1 to $+1$, the bipolar sigmoid function has been chosen as activation function. The ANN model is trained using 1025 data sets involving various combinations of normalized input parameters. The average error over the entire training data has been checked repeatedly till the training phase continues. The resulting mean-squared error between the network's output and the target value over all the training pairs are minimized. Here the gradient decent back propagation model is used for minimizing the error function. After proper training the average error is found to be 0.001 over a set of test data spanning the entire X band of frequencies and different values for the position and radius of the scattering post, which have not been used in the training process.

5. OBSERVATIONS

The learning rate has been set a small value initially and it has been set to decrease steadily with the average error function. The time taken for the network during training phase has been reduced by adding momentum factor. However the imaginary part of the reflectance (Fig. 3(b)) shows highly non-linear behavior as per our analysis and hence the corresponding neural network shows slower convergence compared to the others. The real part of the reflectance (Fig. 3(a)) also shows more deviation at lower frequency ranges that may be due to lack of uniform training data for the same. The smaller radius values (less than 0.5 mm) have not been taken into account for this modeling as they may generate a highly non-linear behavior due to inclusion of higher order modes in the lattice sum.

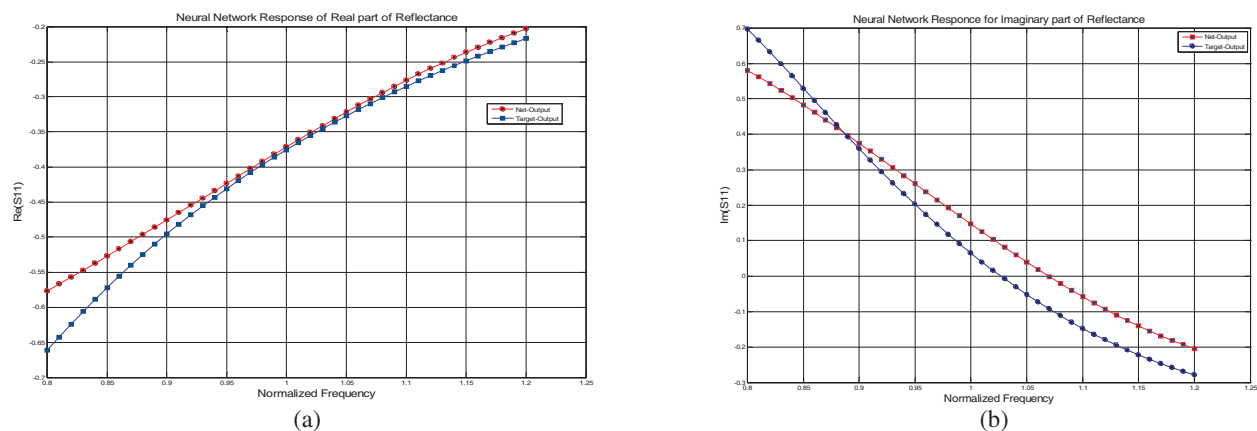


Figure 3: Comparison of neural network response with the computed values for real and imaginary part of reflectance of the scattering post embedded in rectangular waveguide.

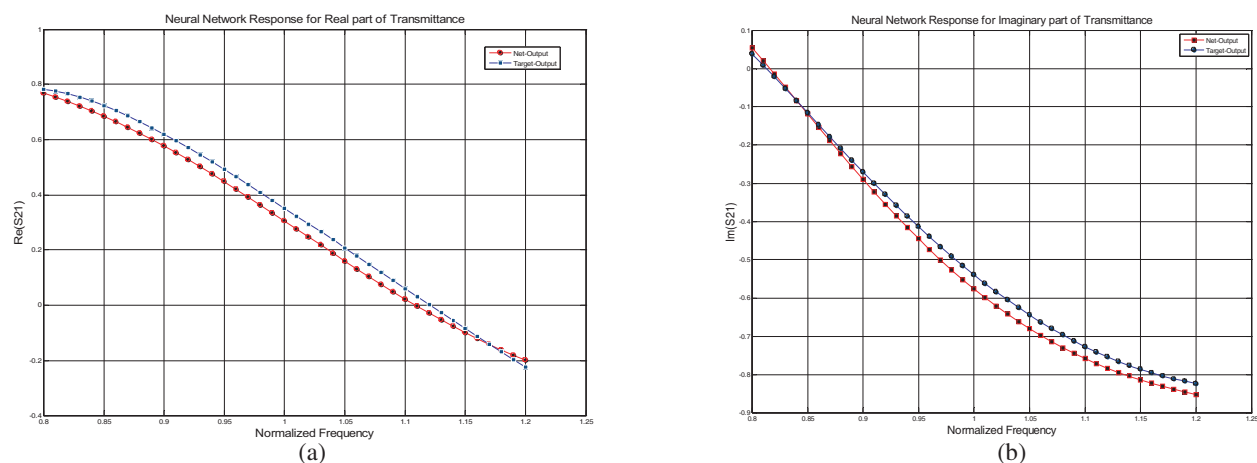


Figure 4: Comparison of neural network response with the computed values for real and imaginary part of transmittance of the scattering post embedded in rectangular waveguide.

6. CONCLUSION

In this work neural network technique has been used for non-linear modeling of the frequency response of the scattering properties of a long circular conducting cylinder in a three dimensional rectangular waveguide in X band. Analysis using Lattice sum and T-matrix method has been done to generate S_{11} and S_{21} data for the structure and 80% of them is used for proper training of the neural network. Rest of the data generated is used for testing the model for the required accuracy. This type of model is very useful in optimization problem [7] where a fast and accurate response is required which cannot be obtained from electromagnetic simulation.

ACKNOWLEDGMENT

The authors are grateful to SAMEER-Kolkata Centre and Indo-Jap Collaborative Project on ‘Infrastructural Communication Technologies Supporting Fully Ubiquitous Information Society’ for technical assistance rendered.

REFERENCES

1. Zhang, Q. J., K. C. Gupta, and V. K. Devabhakuni, “Artificial neural networks for RF and microwave design—from theory to practice,” *IEEE Trans. on MTT*, Vol. 51, No. 4, 1339–1350, April 2003.
2. Zhang, Q. J. and K. C. Gupta, *Neural Networks for RF and Microwave Design*, Chapter 3, Artech House.
3. Hornik, K., M. Stinchcombe, and H. White, “Multilayer feed forward networks are universal approximators,” *Neural Networks*, Vol. 2, 359–366, 1989.
4. Deshpande, M. D., “Analysis of discontinuities in a rectangular waveguide using dyadic Green’s function approach in conjunction with method of moments,” NASA Report, No. CR-201692, April 1997.
5. Yasumoto, K. and H. Jia, “Modeling of photonic crystals by multilayered periodic arrays of circular cylinders,” *Electromagnetic Theory and Applications for Photonic Crystals (Optical Science and Engineering Series*, Vol. 103), ed. K. Yasumoto, Chapter 3, 123–190, CRC Press, 2005.
6. Yasumoto, K., N. Koike, H. Jia, and B. Gupta, “Analysis of electromagnetic bandgap based filters in a rectangular waveguide,” *IETCE Trans. Electron.*, Vol. E89-C, No. 9, 1324–1329, September 2006.
7. Kabir, H., Y. Wang, M. Yu, and Q. J. Zhang, “Application of artificial neural network techniques in microwave filter modeling, optimization and design,” *PIERS Online* Vol. 3, No. 7, 1131–1135, 2007.

Preparation and Evaluation of Composite Electromagnetic Wave Absorbers Made of Fine Aluminum Particles Dispersed in Polystyrene Medium

Y. Wada, N. Asano, K. Sakai, and S. Yoshikado

Department of Electronics, Doshisha University, Japan

Abstract— We developed composite electromagnetic wave absorbers made of fine aluminum particles dispersed in a polystyrene medium and evaluated their properties in order to realize metal-backed single-layer electromagnetic wave absorbers with a good absorption property in the GHz region. Both the magnetization and the magnetic loss caused by the eddy current flowing on the surface of the aluminum particles increased proportionally to the volume mixture ratio of the aluminum particles for all samples. The magnetization was almost independent of frequency but the magnetic loss decreased with increasing frequency for all samples. These results were in agreement with qualitative theoretical predictions.

1. INTRODUCTION

It is necessary that electromagnetic wave absorbers can be produced easily and are lightweight with a low environmental impact. Furthermore, it is also important that the material used can be obtained cheaply and in large quantities, taking the problem of the depletion of resources into consideration. According to Snoek, electromagnetic wave absorbers made of magnetic materials, such as ferrite, exhibit an upper limit of absorbing center frequency [1]. Elements that are in increasingly short supply may also be included in ferrite. Moreover, the mass density of ferrite is large. On the other hand, according to Yamane et al., the magnetic dipole induced from an eddy current flowing on the surface of a metal particle, such as an aluminum particle, contributes to the absorption of an electromagnetic wave [2]. It is expected that there is no practical upper limit of the absorbing frequency, and it is possible to absorb waves with a wide frequency range if an appropriate size of aluminum particle is chosen. Moreover, aluminum is lightweight and comparatively cheap.

Aluminum is a paramagnetic substance, its nondimensional magnetic susceptibility is approximately 2.1×10^{-5} , and the real part μ'_r of the complex relative permeability μ_r^* of aluminum is almost 1. When an electromagnetic wave of high frequency enters an aluminum particle, an eddy current flows whose strength depends on the generated skin effect of the incident magnetic field on the particle surface [2–4], and a reverse magnetic moment appears. Then, the energy of the electromagnetic wave is converted into thermal energy by the eddy current, which flows on the surface of the aluminum particles. In a composite material, the real part ε'_r of the complex relative permittivity ε_r^* is not dependent on the frequency; however, the values of μ'_r , which determines the absorption of electromagnetic waves over a frequency range of several GHz, decreases with increasing frequency. Therefore, since the values of μ'_r smaller than 1 is required for absorption, the conditions under which the magnetic moment appears is an important factor when electromagnetic-wave-absorbent materials are developed. When the proportion of aluminum particles in the material increases, it is speculated that the magnetic moment increases and μ'_r becomes smaller than 1. However, if aluminum particles are in contact with each other, the total surface current of the particles decreases because the total surface area of the particles decreases. As a result, the loss μ''_r due to the eddy current will be small. Furthermore, because the conductivity of the electromagnetic-wave-absorbent materials increases upon the aluminum particles coming in contact and the reflection coefficient of the electromagnetic wave increases, it is difficult for the wave to pass through the materials inside. Eventually, the wave cannot be effectively absorbed, because the Joule loss becomes small. Therefore, in this study, electromagnetic-wave-absorbent materials made of aluminum particles coated with polystyrene resin, which is an insulator and ensures that the aluminum particles do not come in contact with each other, were fabricated and their characteristics were evaluated.

2. EXPERIMENTS

Particles of polystyrene resin with two different grain sizes (approximately 1 and 200 μm diameter) were prepared. First, chips of polystyrene resin were ground by a cutting mill into particles with an

average grain size of approximately several hundred μm . Polystyrene particles of 200 μm diameter were obtained by pulverization using a mortar. Polystyrene particles of 1 μm diameter were obtained by milling using a planetary ball mill (Fritsch P7) with a zirconia pot and zirconia balls of 1 mm diameter for 1.5 h with ethanol. The rotation speed of the turntable was 600 rpm. The ratio of the rotation speeds of the milling pot to the turntable was 2:1. Fine polystyrene particles and fine aluminum particles (average grain sizes of approximately 30, 50 and 180 μm) were mixed by the planetary ball mill using a polyacetal pot and nylon-6 balls of 15 mm diameter for 7 min to coat the aluminum particles with the polystyrene particles. The rotation speed was 500 rpm. The mixture was heated to above the melting point of polystyrene and then cooled naturally in the air and processed to a toroidal-core shape (outer diameter of approximately 7 mm, inner diameter of approximately 3 mm and thickness of 3 mm). The sample was loaded into a coaxial line, and the complex scattering matrix elements S_{11}^* (reflection coefficient) and S_{21}^* (transmission coefficient) were measured using a vector network analyzer (Agilent Technology 8722ES) by the full-two-port method. The values of μ_r^* ($\mu_r = \mu_r' - j\mu_r''$, $j = \sqrt{-1}$) and ε_r^* ($\varepsilon_r = \varepsilon_r' - j\varepsilon_r''$) were calculated from the data of both S_{11}^* and S_{21}^* . The return loss R for various sample thicknesses was calculated from the complex reflection coefficient Γ^* using the relation $R = 20 \log_{10} |\Gamma^*|$. The surface of the sample was observed using an optical microscope.

3. EFFECT OF ALUMINUM PARTICLES ON THE COMPLEX PERMEABILITY

The effect of aluminum particles on the complex permeability is qualitatively described in this section. The skin depth δ of a metal for an electromagnetic wave is

$$\delta = \sqrt{\frac{2}{\omega\sigma\mu_0\mu'_{Mr}}} . \quad (1)$$

Here, ω is the angular frequency of the electromagnetic wave, σ is the conductivity of the metal, μ_0 is the permeability in a vacuum and μ'_{Mr} is the real part of the complex relative permeability of the metal. The skin depth of aluminum which are from 0.9 μm to 2.6 μm in the frequency region from 1 GHz to 10 GHz is shorter than the diameter (approximately 30, 50 or 180 μm) of the aluminum particles used for experiments. Therefore, the eddy current flows in the region from the surface of the aluminum particles to the skin depth and generates a magnetic field in each aluminum particle. The dimensionless magnetic susceptibility of aluminum is very small (2.1×10^{-5}) and μ'_{Mr} is approximately 1. However, in the high-frequency region, the real part of the complex relative permeability of an aluminum particle is smaller than 1 because the magnetic field inside the aluminum particle is canceled by the magnetic field generated by the eddy current.

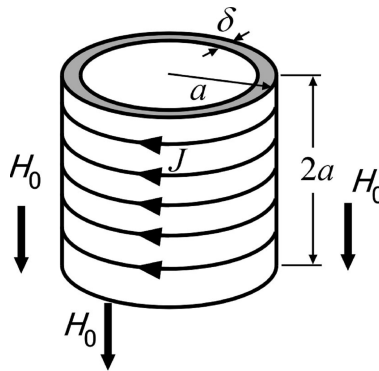


Figure 1: Model of magnetic moment with eddy current in thin metallic cylindrical shell.

To simplify the discussion, the shape of an aluminum particle is approximated as a cylinder of radius a and length $2a$. As shown in Fig. 1, a model in which current flows in the outer skin in a metal cylinder shell of thickness δ (equivalent to the skin depth) is used [4]. Here, $\delta \ll a$. In a vacuum, for an incident magnetic field strength of H_0 parallel to the central axis of the cylinder, the eddy current density is defined as J . Although the length of the cylinder is finite, we assume that J is uniform in the cylindrical shell. Thus, a uniform magnetic field H' parallel to the cylindrical central axis is generated by J . H' is given by Ampere's circuital law as

$$H' = \delta J. \quad (2)$$

Therefore, the magnetic field H inside the cylindrical shell is given by

$$H = H_0 + \delta J. \quad (3)$$

Because no magnetic field exists inside the cylindrical shell due to the skin effect, the following equation is obtained from Equation (3).

$$H_0 + \delta J = 0 \quad (4)$$

Therefore, J is given by

$$J = -H_0/\delta. \quad (5)$$

Therefore, the direction of the eddy current is opposite that shown in Fig. 1. The magnetic moment m generated by J is given by

$$m = 2\pi a^3 \delta J = -2\pi a^3 H_0. \quad (6)$$

The direction of m is opposite that of H_0 . If $2a$ is constant, the particle number N of aluminum particles per unit volume of the composite is given by

$$N = V/2\pi a^3. \quad (7)$$

Here, V is the volume mixture ratio of the aluminum particles in the composite. If it is assumed that the direction of all magnetic moments is the same and that the eddy current loss is zero, the magnetization M is given by

$$M = -VH_0. \quad (8)$$

M is independent of the frequency and the grain size of the aluminum particles according to Equation (8). Also, the following relation holds between the average magnetic flux density B and the magnetization M in the composite when M is proportional to H_0 .

$$M = B/\mu_0 - H_0 = (\mu_r^* - 1)H_0 = (\mu_r' - 1 - j\mu_r'')H_0 \quad (9)$$

Here μ_r^* is the complex relative permeability of the composite. μ_r'' is attributed to the eddy current loss. The following equation is obtained from Equations (8) and (9).

$$1 - \mu_r' = V \quad (10)$$

The value of $1 - \mu_r'$ is independent of the frequency, is proportional to V , and $0 < 1 - \mu_r' < 1$. The Joule loss P , caused by the eddy current loss, per unit volume of the composite is

$$P = N \frac{1}{2} (4\pi a^2 \delta) \frac{J^2}{\sigma} = \frac{VH_0^2}{a} \sqrt{\frac{2\omega\mu_0}{\sigma}}. \quad (11)$$

Therefore, for small values of V , μ_r'' is given by

$$\mu_r'' = \mu_r' \frac{P}{\omega \frac{1}{2} \mu_r' \mu_0 H_0^2} = \frac{2V}{a} \sqrt{\frac{2}{\omega \sigma \mu_0}} = \frac{2V\delta}{a}. \quad (12)$$

The value of μ_r'' increases proportionally to V and is inversely proportional to the square root of the frequency and a . Furthermore, it is expected that the above qualitative results are applicable to spherical aluminum particles.

4. RESULTS AND DISCUSSION

4.1. Dispersion State of Aluminum Particles in the Composite

Figures 2 and 3 show surface optical micrographs of the composite made of aluminum particles (180 μm average grain size) and polystyrene particles of 200 μm diameter and that made of aluminum particles (30 μm average grain size) and polystyrene particles of 1 μm diameter, respectively. As shown in Fig. 2, the aluminum particles were isolated in the polystyrene medium for the sample with a volume mixture ratio of 16.4 vol% for the aluminum particles. However, the aluminum particles were in contact with each other for that of 40.0 vol%. This result shows that both the aluminum particles and the polystyrene particles were uniformly dispersed when the volume mixture ratio of the aluminum particles was low. This result is also in agreement with percolation theory

(the particles are not in contact with each other up to the percolation threshold of 33.3 vol%) [5]. However, as shown in Fig. 3, the aluminum particles were isolated in the polystyrene medium in the sample with the volume mixture ratio of 40.0 vol%, which exceeded the percolation threshold. This result shows that fine polystyrene particles coated the surface of each particle of the aluminum and melted polystyrene resin enters between the aluminum particles, because the average grain size of the polystyrene particles was much smaller than that of the aluminum particles. Aluminum particles were in contact with each other in the sample with the volume mixture ratio of 50.0 vol% for the aluminum particles. However, if the grain size of the polystyrene particles is much smaller, the aluminum particles may not be in contact with each other.

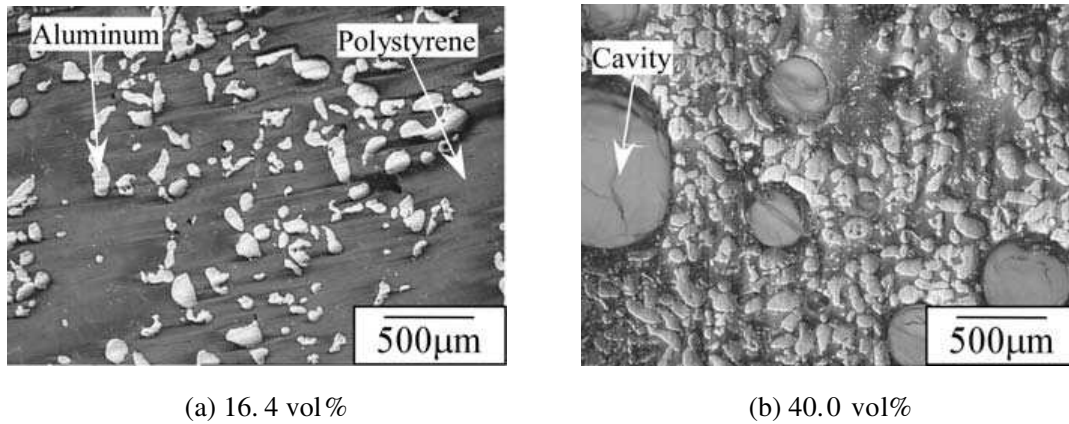


Figure 2: Optical micrographs of samples made of aluminum particles of 180 μm diameter and polystyrene particles of 200 μm diameter.

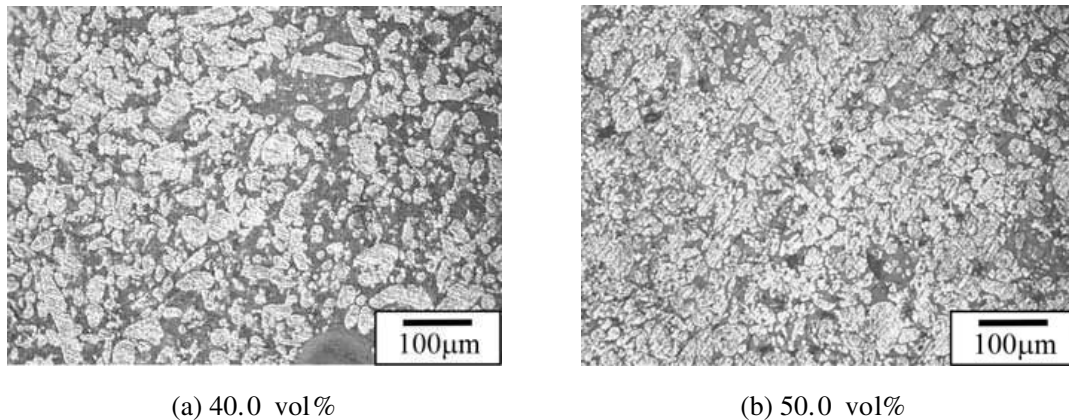


Figure 3: Optical micrographs of samples made of aluminum particles of 30 μm diameter and polystyrene particles of 1 μm diameter.

4.2. Dependences of $1 - \mu_r'$ and μ_r'' on Frequency and Volume Mixture Ratio of Aluminum

The frequency dependence of $1 - \mu_r'$ for the composite made of aluminum particles of 30 μm diameter and polystyrene particles of 1 μm diameter is shown in Fig. 4. Although the value of $1 - \mu_r'$ increased slightly with increasing frequency, it roughly agreed with the qualitative prediction of Equation (10).

Figure 5 shows the volume mixture ratio dependences of $1 - \mu_r'$ and μ_r'' for the composites made of aluminum particles of 30 μm diameter and polystyrene particles of 1 μm diameter. The measured values of both $1 - \mu_r'$ and μ_r'' increased proportionally to the volume mixture ratio of the aluminum particles up to the volume mixture ratio of approximately 40 vol%. In particular, the values of $1 - \mu_r'$ agreed well with those calculated ones Equation (10), as shown by thick solid line in Fig. 5(a). The values of μ_r'' also roughly agreed with those calculated using Equation (12), as shown in Fig. 5(b). As the frequency increased, μ_r'' for each volume mixture ratio decreased in inverse proportion to the square root of the frequency, which roughly agreed with the frequency dependence

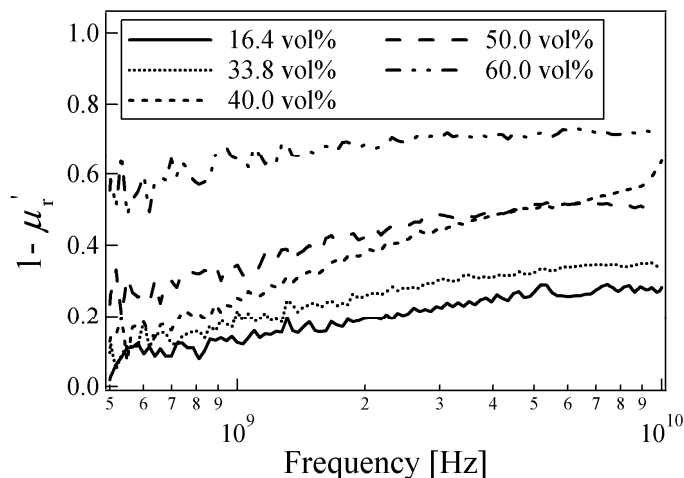


Figure 4: Frequency dependence of $1 - \mu_r'$ for composite materials made of aluminum particles of $30 \mu\text{m}$ diameter and polystyrene particles of $1 \mu\text{m}$ diameter.

estimated using Equation (12). The values of both $1 - \mu_r'$ and μ_r'' were saturated and decreased above approximately 40 vol%. As the volume mixture ratio exceeds approximately 40 vol%, it is speculated that clusters of aluminum particles are easily generated and that the aluminum clusters join to form a mesh like structure. For electromagnetic waves with wave lengths from 3 cm to 30 cm, it is possible that these clusters can be considered to be equivalent to spherical shells of aluminum. Therefore, it is speculated that the values of $1 - \mu_r'$ and μ_r'' decrease above 40 vol%, because the incident electromagnetic wave is reflected by the conductive mesh near the sample surface and the magnetic moments generated by the eddy current of the aluminum particles become small.

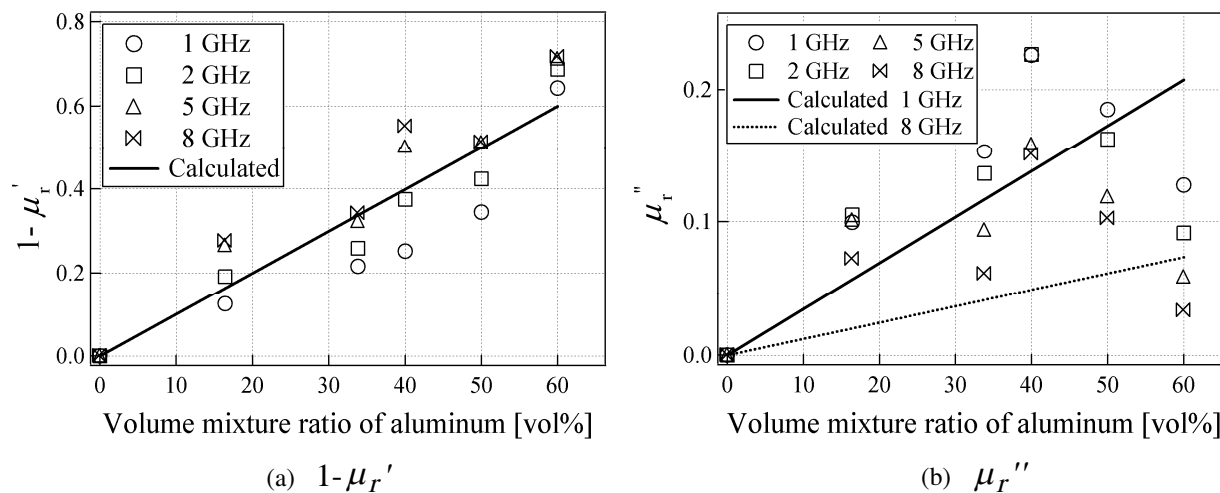


Figure 5: Dependences of $1 - \mu_r'$ and μ_r'' on mixture ratio of aluminum for composite materials made of aluminum particles of $30 \mu\text{m}$ diameter and polystyrene particles of $1 \mu\text{m}$ diameter.

Figure 6 shows the volume mixture ratio dependences of ϵ_r' and ϵ_r'' for the composites. The values of ϵ_r' and ϵ_r'' increased proportionally to the volume mixture ratio of the aluminum particles up to approximately 40 vol% and rapidly increased above approximately 40 vol%. This rapid increase is caused by the generation of clusters of aluminum particles; the melted polystyrene resin did not sufficiently penetrate between the aluminum particles. When the volume mixture ratio of the aluminum particles increases, the capacitance between the particles increases because the distance between the particles in the composite decreases. Because these capacitance elements are connected in series or parallel in the sample to form a 3-D network, the value of ϵ_r' of the sample is inverse proportional to the distance between the aluminum particles. If the particles are partially in contact with each other, the total capacitance rapidly increases. Therefore, it is estimated that the value

of ϵ_r' rapidly increases when the aluminum particles come in contact with each other.

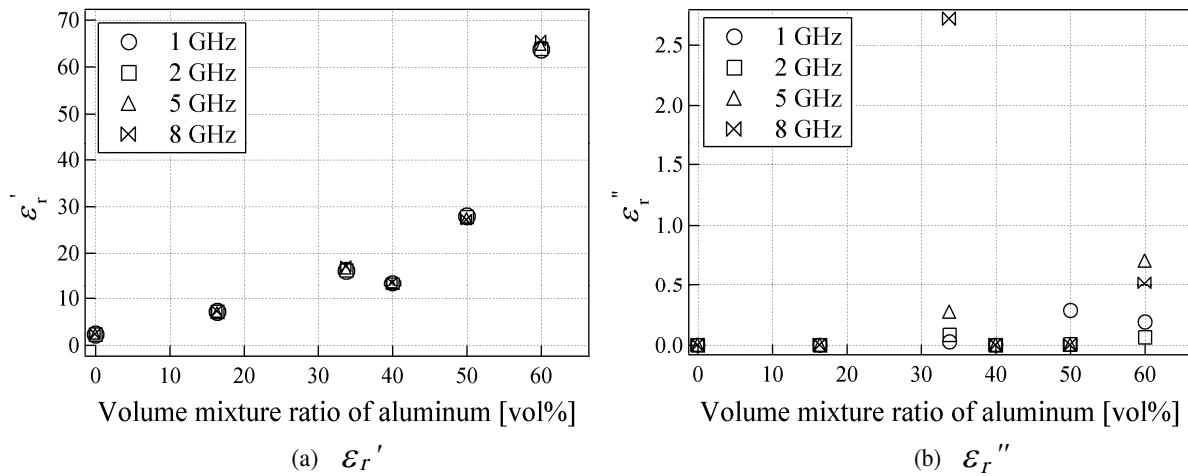


Figure 6: Dependence of ϵ_r' and ϵ_r'' on mixture ratio of aluminum for composite materials made of aluminum particles of 30 μm diameter and polystyrene particles of 1 μm diameter.

4.3. Dependences of $1 - \mu_r'$ and μ_r'' on Grain Size of Aluminum Particles

Figure 7 shows the dependences of $1 - \mu_r'$ and μ_r'' on the size of the aluminum particles for the composites made of aluminum particles and polystyrene particles of 1 μm diameter for the volume mixture ratio of 16.4 vol%. Although the value of $1 - \mu_r'$ was almost constant and μ_r'' was inversely proportional to the size of the aluminum particles, the values of neither $1 - \mu_r'$ nor μ_r'' agreed with those calculated using Equations (10) and (12), as shown by solid lines. The disagreement between the measured and calculated values of μ_r'' may be related to the low purity of the aluminum, because the conductivity of aluminum is dependent on its purity.

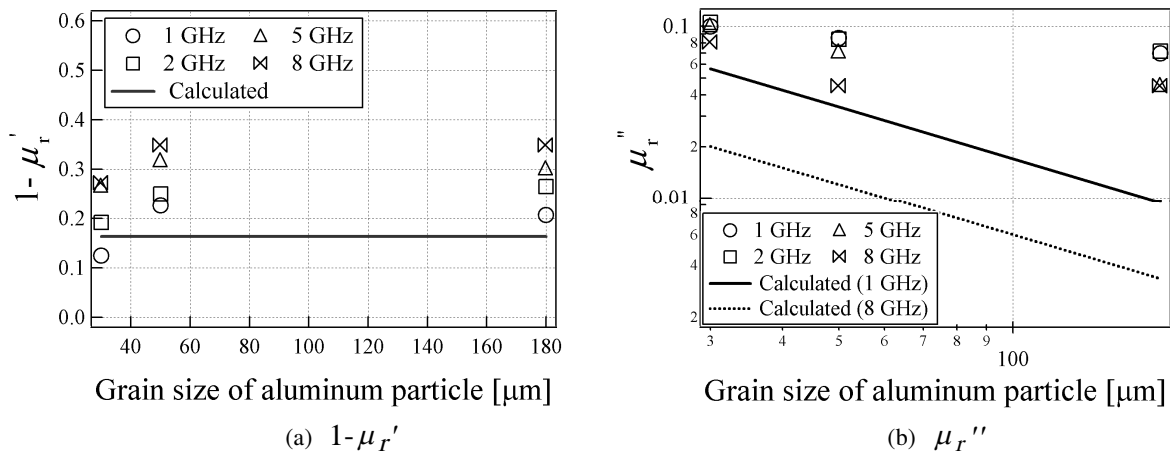


Figure 7: Dependences of $1 - \mu_r'$ and μ_r'' on particle size of aluminum for composite materials made of aluminum and polystyrene particles of 1 μm diameter with volume mixture ratio of 16.4 vol%.

4.4. Frequency Dependence of the Return Loss

The frequency dependence of the return loss was evaluated for all samples with the electromagnetic wave vertically incident to a metal-backed single-layer electromagnetic wave absorber. Fig. 8 shows the frequency dependence of the return loss for the composites made of aluminum particles of 30 μm diameter and polystyrene particles of 1 μm diameter for a volume mixture ratio of 40.0 vol%. The absorbing center frequency shifted to the high-frequency side as the thickness of the sample decreased. In comparison with composite electromagnetic wave absorbers made of ferrite particles dispersed in rubber, in the measuring frequency range, the absorption of -20 dB (99% of the electromagnetic wave power was converted into thermal energy) or less could be achieved using present composite. The thicknesses of the composite for which the absorption was largest were

approximately 6.9 and 19.2 mm and the absorbing center frequencies at which the absorption was largest were 4.0 and 1.2 GHz, respectively. The possibility of obtaining the absorption of -20 dB or less in the frequency range above 10 GHz was indicated, because the absorption center frequency shifted to the high-frequency side without adversely affecting the absorption characteristic as the thickness of the sample decreased. If the dispersion method is revised so that the aluminum particles cannot come in contact with each other, the absorption of -20 dB or less might be achieved above 10 GHz for a thickness of 6.9 mm or less. Although the electromagnetic absorber developed in this study is expected to be applicable to frequencies above 10 GHz, this cannot yet be confirmed for the following reasons. Processing the sample and loading it into the coaxial line are difficult for a coaxial line with outer diameter 7 mm and it is difficult to obtain high accuracy for the measurements of μ_r^* and ε_r^* above 10 GHz due to the generation of the higher modes other than the fundamental wave TEM (transverse electromagnetic) mode of the electromagnetic wave due to the distortion from the ideal toroidal-core shape and defects in the sample. In the future, the absorption property at frequencies above 10 GHz will be evaluated using a rectangular waveguide.

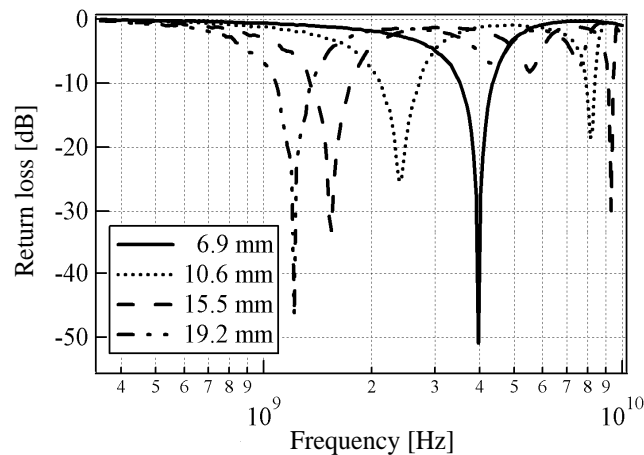


Figure 8: Frequency dependence of the return loss for composite material made of aluminum particles of $30\ \mu\text{m}$ diameter and polystyrene particles of $1\ \mu\text{m}$ diameter with volume mixture ratio of 40.0 vol%.

5. CONCLUSIONS

The complex relative permittivity did not increase rapidly, even when the volume mixture ratio of aluminum particles exceeded the percolation threshold, because fine polystyrene particles coated the surface of each aluminum particle and the aluminum particles were isolated in the polystyrene resin medium. The values of both $1 - \mu_r'$ and μ_r'' increased proportionally to the volume mixture ratio of the aluminum particles, the value of $1 - \mu_r'$ was almost independent of frequency, and the value of μ_r'' was inversely proportional to the size of the aluminum particles. Therefore, it was confirmed that the measured values of $1 - \mu_r'$ and μ_r'' roughly agreed with the qualitative theoretical prediction. Over 99% of electromagnetic wave power was absorbed below 10 GHz. Furthermore, the possibility of obtaining a good absorption characteristic in the frequency range above 10 GHz was indicated, because the absorption center frequency shifted to the high-frequency side without adversely affecting the absorption characteristic as the thickness of the sample decreased.

REFERENCES

1. Snoek, J. L., "Dispersion and absorption in magnetic ferrites at frequencies above one megacycle," *Physca XIV*, Vol. 4, 207–217, 1948.
2. Yamane, T., A. Nishikata, and Y. Shimizu, "Resonance suppression of a spherical electromagnetic shielding enclosure by conductive dielectrics," *IEEE Trans. on Electromagnetic Compatibility*, Vol. 42, 441–448, 2000.
3. Robert, P., *Electrical and Magnetic Properties of Materials*, 250–255, Artech House, Inc., Norwood, MA, 1988.
4. Misra, D. K., *Practical Electromagnetics*, 125–127, John Wiley & Sons, Inc., New York, 2007.
5. Stauffer, D. and A. Aharony, *Introduction to Percolation Theory*, 1–136, Taylor & Francis, London, 1994.

Composite Electromagnetic Wave Absorber Made of Permalloy or Sendust and Effect of Sendust Particle Size on Absorption Characteristics

K. Sakai, Y. Wada, and S. Yoshikado

Department of Electronics, Doshisha University, Japan

Abstract— The effects of the size and shape of sendust particles on the absorption characteristics of composite electromagnetic wave absorbers made of polystyrene resin and sendust were investigated. We also investigated the difference in the absorption characteristics between permalloy and sendust. The sendust particles were granular or flakes and those of permalloy were granular. The size of sendust particles was varied in the range from approximately 5 to 20 μm . A metal-backed single layer absorber made of a composite containing small sendust particles absorbed more than 99% of electromagnetic wave power in the frequency range from 1 to 3 GHz. The values of the real part μ'_r of the relative complex permeability μ_r^* for both magnetic materials became less than unity and had a minimum value at frequencies above 10 GHz. The composite made of small sendust particles exhibited a return loss of less than -20 dB at frequencies near 35 GHz for a suitable sample thickness.

1. INTRODUCTION

The development of an electromagnetic wave absorber suitable for frequencies higher than 1 GHz is required with the increasing use of wireless telecommunication systems. The frequencies used for these devices will shift to a high-frequency range in the future. To develop practical absorbers that operate in the frequency range above 1 GHz, the frequency dependences of the relative complex permeability μ_r^* and the relative complex permittivity ϵ_r^* and the absorption characteristics for a composite made of a soft magnetic material dispersed in an insulating matrix have been investigated [1–6]. Soft magnetic materials such as permalloy or sendust have high values of permeability at frequencies above 1 GHz. This characteristic makes it possible to fabricate an absorber that operates at these frequencies. In addition, sendust is a low-cost material because it does not contain any rare metals such as Ni, hence it is more suitable for use in a practical absorber than permalloy. Moreover, the value of μ'_r for a composite made of a soft magnetic material dispersed in an insulating matrix is expected to be less than unity [2]. This characteristic makes it possible to absorb 99% of the power of an electromagnetic wave because μ'_r should be less than unity to satisfy the absorption condition at frequencies above 10 GHz.

In this study, the particle-size dependence of the absorption characteristics of a metal-backed single layer composite absorber made of granular sendust particles and polystyrene resin and the absorption characteristics of granular permalloy, granular sendust and sendust flakes were investigated at frequencies below 40 GHz. If the amount of magnetic material particles dispersed in the polystyrene resin increases, they will be in direct contact with each other and the average conductivity of the composite will increase markedly. Thus, the reflection coefficient of the electromagnetic wave reflected by the composite will increase and its absorption characteristics will be degraded. To prevent this increase in conductivity, we attempted to uniformly disperse and isolate the soft magnetic material particles by dissolving polystyrene resin in an organic solvent and mixing the particles with the dissolved polystyrene resin.

2. EXPERIMENTS

Chips of polystyrene resin were dissolved in acetone. The dissolved polystyrene resin and permalloy (Ni 45%, Fe 55%) or sendust (Al 5%, Si 10%, Fe 85%) were mixed. The permalloy particles were granular and those of sendust were granular or flakes. The average particle size of the permalloy particles was approximately 10 μm and that of sendust flakes was approximately 20 μm . The average particle size of the granular sendust particles was approximately 5, 10 or 20 μm . After mixing, the mixture was heated to melt the polystyrene resin then hot-pressed at a pressure of 5 MPa into a pellet shape. Then, the pellet was cooled naturally to room temperature and processed into a toroidal-core shape (with an outer diameter of approximately 7 mm and an inner diameter of approximately 3 mm) for use in a 7 mm coaxial line in the frequency range from 50 MHz to 12.4 GHz, or into a rectangular shape for use in a waveguide in the frequency range from 12.4

to 40 GHz. The sample was loaded into the coaxial line or rectangular waveguide while ensuring that there was no gap between the coaxial line or the rectangular waveguide and the processed sample. The complex scattering matrix elements S_{11}^* (reflection coefficient) and S_{21}^* (transmission coefficient) for TEM mode (coaxial line) or TE₁₀ mode (rectangular waveguide) were measured using a vector network analyzer (Agilent Technology, 8722ES) by the full-two-port method. The values of μ_r^* ($\mu_r^* = \mu_r' - j\mu_r''$, $j = \sqrt{-1}$) and ε_r^* ($\varepsilon_r^* = \varepsilon_r' - j\varepsilon_r''$) were calculated from the data of both S_{11}^* and S_{21}^* . The return loss R for each sample thickness was calculated from the complex reflection coefficient Γ^* using the relation $R = 20 \log_{10} |\Gamma^*|$.

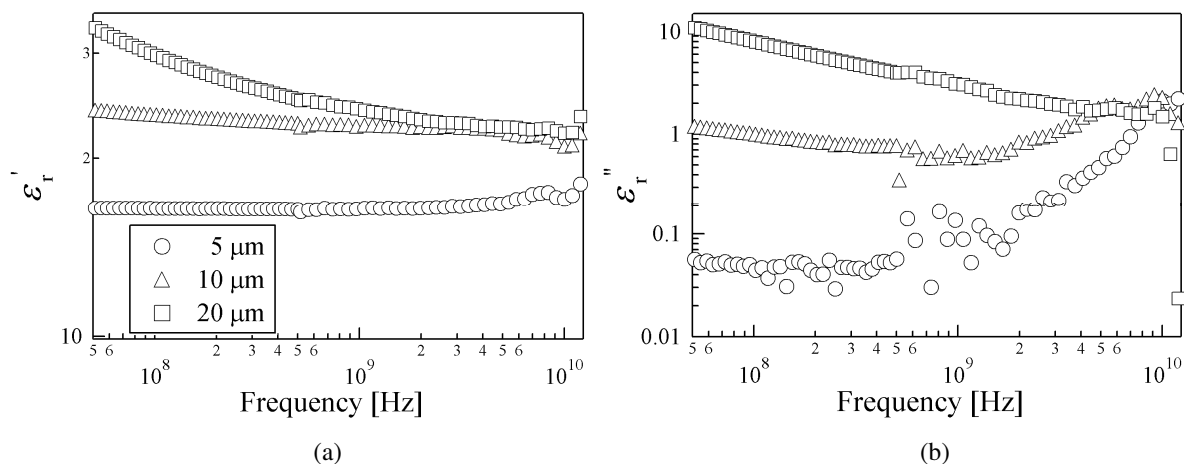


Figure 1: Frequency dependences of (a) ε_r' and (b) ε_r'' for composites made of polystyrene resin and sendust particles of various sizes.

3. RESULTS AND DISCUSSION

3.1. Frequency Dependences of μ_r^* and ε_r^* for the Composites Made of Sendust Particles of Various Sizes

Figure 1 shows the frequency dependences of ε_r' and ε_r'' for the composites made of granular sendust particles of 20, 10, or 5 μm diameter. The volume mixture ratio of sendust was fixed at 53 vol%. The values of ε_r' and ε_r'' decreased as the particle size decreased. This is because the sendust particles were more likely to be isolated from each other in the polystyrene resin as the particle size decreased. To investigate the dispersion of the sendust particles, the surfaces of the composites were observed using an optical microscope, as shown in Fig. 2. It is found from Figs. 2(a) and (b) that sendust particles of 20 and 10 μm diameter are partly in contact with each other and form clusters. On the other hand, sendust particles of 5 μm diameter were dispersed uniformly and isolated from each other in the polystyrene resin, and the contact between sendust particles decreased as shown in Fig. 2(c). Therefore, the values of ε_r'' were smaller, because the conductivity of the composite made of sendust particles of 5 μm diameter was lower. The values of ε_r' are determined by the capacitance

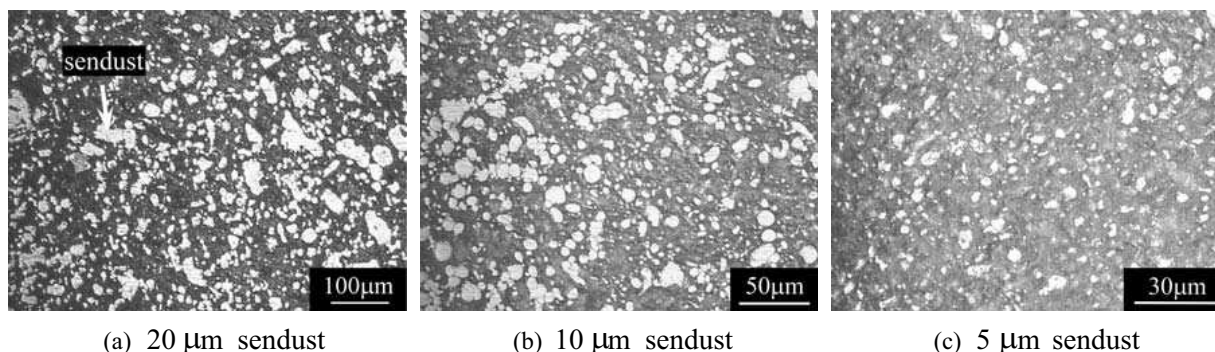


Figure 2: Surface optical microphotographs of composites made of polystyrene resin and granular sendust particles. The sizes of the sendust particles are approximately (a) 20 μm (b) 10 μm and (c) 5 μm .

between sendust particles. If the sendust particles are isolated, the distance between the particles becomes large and the capacitance between the particles decreases. Thus, the composite made of sendust particles of 5 μm diameter had low values of ε'_r due to the isolation of the particles.

Figure 3 shows the frequency dependences of μ'_r and μ''_r for the composite made of sendust particles of various sizes. In the low-frequency range, the values of μ'_r were largest for the composite made of sendust particles of 10 μm diameter and decreased in the order of particles with 20 and 5 μm diameter. Meanwhile, the frequency at which μ'_r begins to decrease increased as the particle size of sendust decreased. With relation to the frequency dependence of μ'_r , the frequency at which μ''_r was maximum increased as the particle size of sendust became small and the value of μ''_r increased rapidly with frequency for the composite made of sendust particles of 5 μm diameter. It is considered that the isolation of the sendust particles is one factor that explains the reason why the frequency dependence of μ_r^* is different for different sendust particle sizes [7, 8]. The scattering of an electromagnetic wave depend on the dispersion state of the sendust particles; thus, the frequency dependences of μ_r^* are different. This phenomenon has been reported for a composite made of ferrite particles isolated in a SiO_2 medium [8]. For this composite, μ'_r had low values in the low-frequency range, was almost constant with increasing frequency then decreased rapidly at high frequencies. Moreover, the value of μ''_r increased rapidly and the frequency at which μ''_r was maximum increased as the ferrite particles became increasingly isolated. This frequency dependence of μ_r^* is similar to that observed in the composite made of small sendust particles. Therefore, it is speculated that the difference in the frequency dependence of μ_r^* for the composites made of sendust particles of various sizes is due to the isolation of the sendust particles in the medium of polystyrene resin.

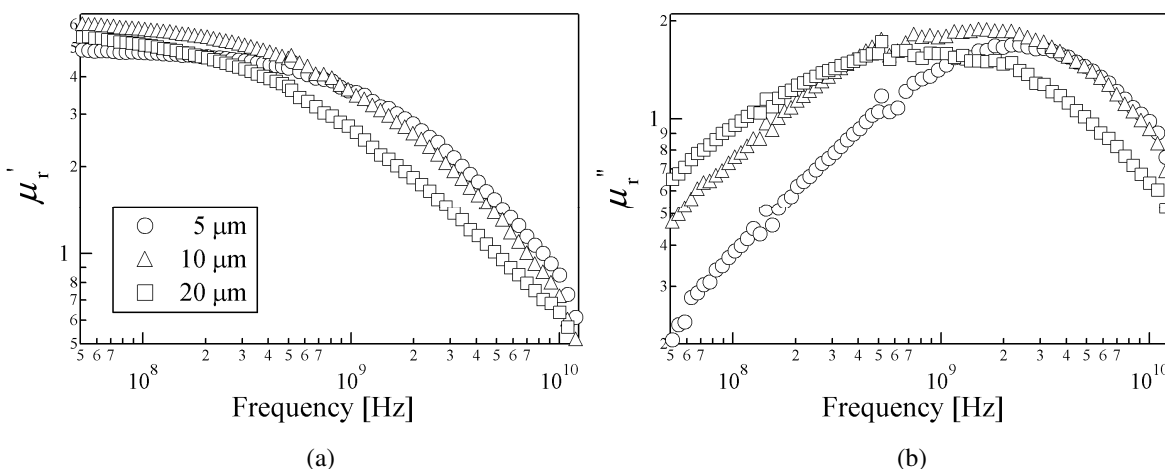


Figure 3: Frequency dependences of (a) μ'_r and (b) μ''_r for composites made of polystyrene resin and sendust particles of various sizes.

3.2. Frequency Dependences of μ_r^* and ε_r^* for the Composite Made of Granular Sendust, Sendust Flakes, or Granular Permalloy

Figures 4 and 5 respectively show the frequency dependences of ε_r^* and μ_r^* for the composites made of granular sendust, sendust flakes, or granular permalloy. The particle size and volume mixture ratio of the granular sendust and permalloy are 10 μm and 53 vol% and those of sendust flakes are 20 μm and 57 vol%, respectively. The values of ε'_r and ε''_r for the composite made of sendust flakes were larger than those of the granular sendust and granular permalloy, as shown in Fig. 4. This result shows that flake type particles easily coalesce, because flake type particles are in contact at planes while granular type particles are in contact at points. Therefore, the values of ε'_r and ε''_r for the composite made of sendust flakes increased for the same reason as discussed in Section 3.1.

The composite made of granular permalloy had higher values of μ'_r than that made of granular sendust at frequencies above 1 GHz. In addition, the frequency at which μ''_r for the composite made of granular permalloy has a maximum value was higher. However, the frequency dependence of μ_r^* for the composite made of granular permalloy roughly agreed with that for the composite made of granular sendust. On the other hand, the value of μ'_r for the composite made of sendust flakes decreased rapidly compared with that for the composite made of granular sendust. In addition, μ''_r had a local maximum at 150 MHz and 3.5 GHz for the composite made of sendust flakes, as

shown in Fig. 5(b). From the above results, it was found that the frequency dependence of μ_r^* is different between sendust flakes and granular sendust in spite of the magnetic material being same. This is because the magnetic properties of sendust flakes, such as the crystallomagnetic anisotropy, are different from those of granular sendust, and the response of the electromagnetic wave to the composite varies with particle shape. Therefore, the different frequency dependence of μ_r^* was observed for different particle shapes.

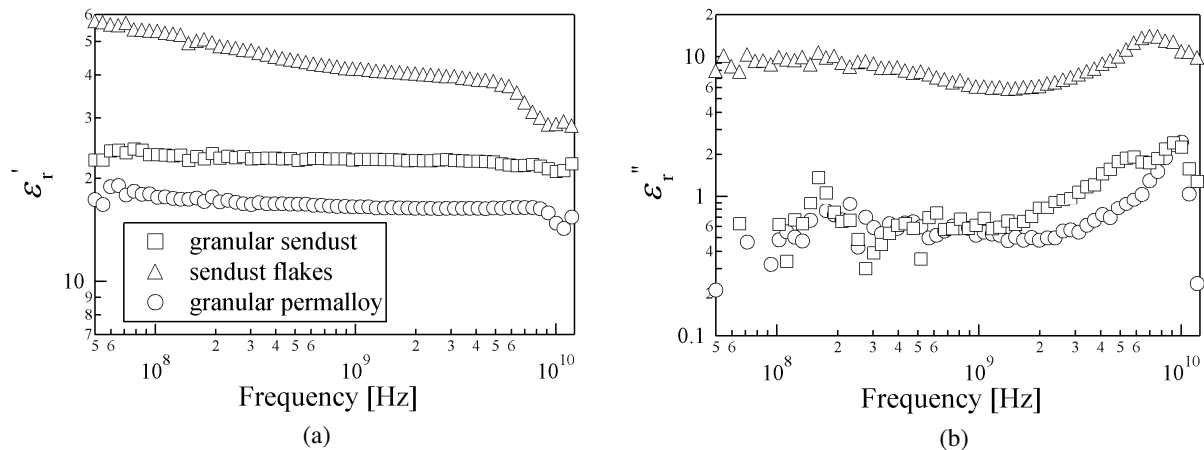


Figure 4: Frequency dependences of (a) ϵ'_r and (b) ϵ''_r for composites made of granular sendust, sendust flakes and granular permalloy.

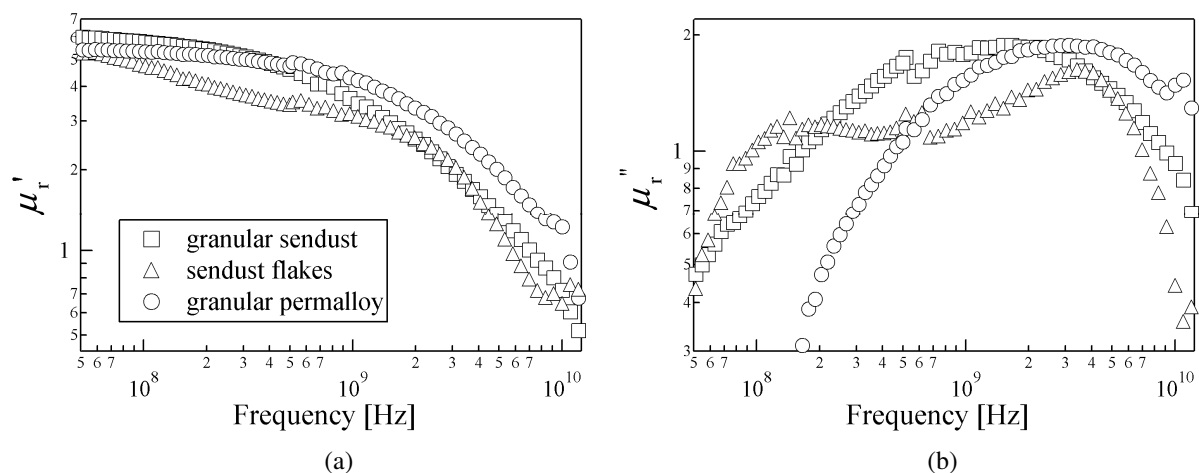


Figure 5: Frequency dependences of (a) μ'_r and (b) μ''_r for composites made of granular sendust, sendust flakes and granular permalloy.

3.3. Absorption Characteristics of Composites Made of Sendust or Permalloy

Figure 6 shows the absorption center frequency f_0 and the normalized -20 dB bandwidth (the bandwidth corresponding to the return loss of less than -20 dB divided by f_0) for the composites made of granular permalloy, granular sendust of $5 \mu\text{m}$ diameter, and that of $10 \mu\text{m}$ diameter. The value of -20 dB corresponds to the absorption of 99% of the electromagnetic wave power. These three composites had a return loss of less than -20 dB in the frequency range from 1 to 3 GHz. The sample thickness for which the return loss was less than -20 dB was relatively thin and both composites had a bandwidth of more than 10%. Compared with the composite made of sendust particles of $10 \mu\text{m}$ diameter, f_0 for the composite made of sendust particles of $5 \mu\text{m}$ diameter was high and the sample thickness was thin. Although f_0 for the composite made of granular permalloy was lower than that for the composite made of granular sendust at a sample thickness 4 mm, the composite made of granular permalloy exhibited a return loss of less than -20 dB at a sample thickness 3 mm, as shown in Fig. 6.

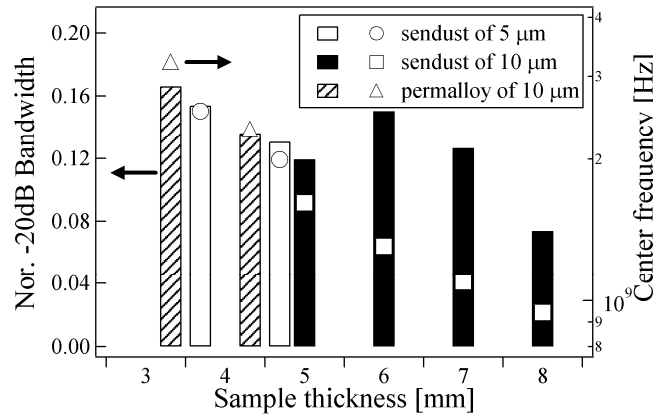


Figure 6: Values of normalized -20 dB bandwidth and center frequency f_0 for composites made of polystyrene resin and granular permalloy, granular sendust of $5 \mu\text{m}$ diameter, and granular sendust of $10 \mu\text{m}$ diameter.

To investigate the absorption characteristics for these three composites, the measured values of μ_r^* and the calculated values of μ_r^* that satisfy the nonreflective condition given by Equation (1) are shown in Fig. 7 [9].

$$1 = \sqrt{\mu_r^*/\varepsilon_r^*} \tanh\left(\gamma_0 d \sqrt{\mu_r^* \varepsilon_r^*}\right) \quad (1)$$

Here, γ_0 is the propagation constant in free space and d is the sample thickness. The value of ε_r' used for calculation is independent of frequency and the same as the measured value for each composite. ε_r'' is assumed to be zero. For the sample thickness of 4 mm, the lines showing the values of μ_r^* that satisfy the nonreflective condition moved to a higher frequency with decreasing value of ε_r' . Thus, f_0 for the composite made of sendust particles of $5 \mu\text{m}$ diameter with $\varepsilon_r' = 16$ was greater than that for the composite made of sendust particles of $10 \mu\text{m}$ diameter with $\varepsilon_r' = 23$. For the sample thickness of 3 mm, the calculated line for $\varepsilon_r' = 16$ and $d = 3$ mm intersected all the measured values of μ_r'' in the frequency range from 3 to 4 GHz, as shown in Fig. 7(b). However, the calculated line only intersected the measured values of μ_r' for the composite made of granular permalloy, as shown in Fig. 7(a). Thus, the composite made of granular permalloy exhibited a return loss of less than -20 dB for the sample thickness of 3 mm, because μ_r' for the composite made of granular permalloy had high values at frequencies above 1 GHz.

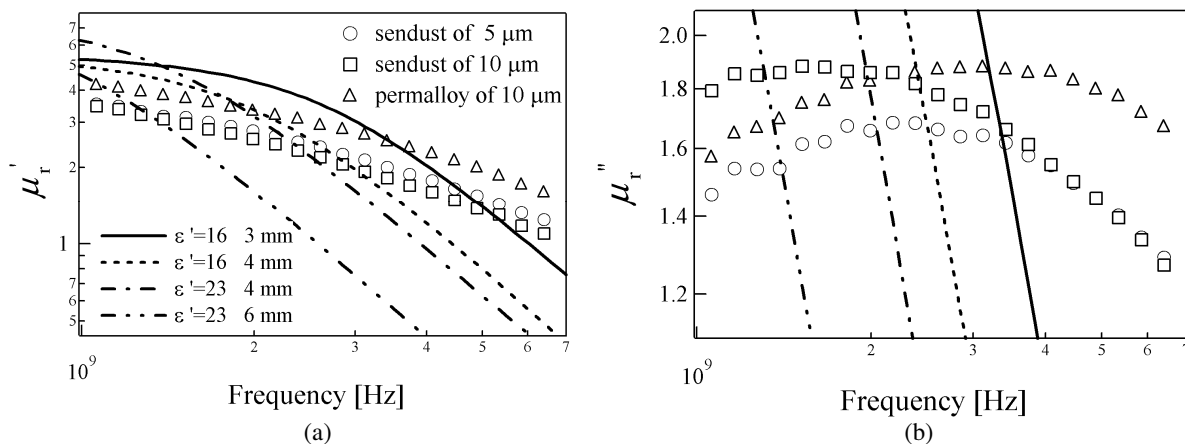


Figure 7: Measured and calculated values of (a) μ_r' and (b) μ_r'' . Plots show measured values for composites made of granular sendust and granular permalloy and lines show values calculated using Equation (1).

The composites made of sendust flakes and granular sendust particles of $20 \mu\text{m}$ diameter did not exhibit a return loss of less than -20 dB at frequencies above 1 GHz, although these two composites exhibited a return loss of less than -20 dB at several hundred MHz. This is because these composites had high values of ε_r' and ε_r'' and did not satisfy the nonreflective condition at frequencies above 1 GHz.

3.4. Frequency Dependence of μ_r^* and Absorption Characteristics at Frequencies above 10 GHz

Figure 8 shows the frequency dependences of μ_r' and μ_r'' for the composites made of polystyrene resin and sendust particles of 5 μm diameter or permalloy particles of 10 μm diameter in the frequency range from 12.4 to 40 GHz. The values of μ_r' for both composites decreased and became less than unity at frequencies above 10 GHz. The value of μ_r' for the composite made of sendust particles of 5 μm diameter was minimum near 14 GHz and increased with increasing frequency up to 40 GHz. Although the frequency dependence of μ_r' for the composite made of permalloy particles of 10 μm diameter was similar to that of the composite made of sendust particles of 5 μm diameter, its minimum value of μ_r' was lower and the frequency of the minimum μ_r' value was higher.

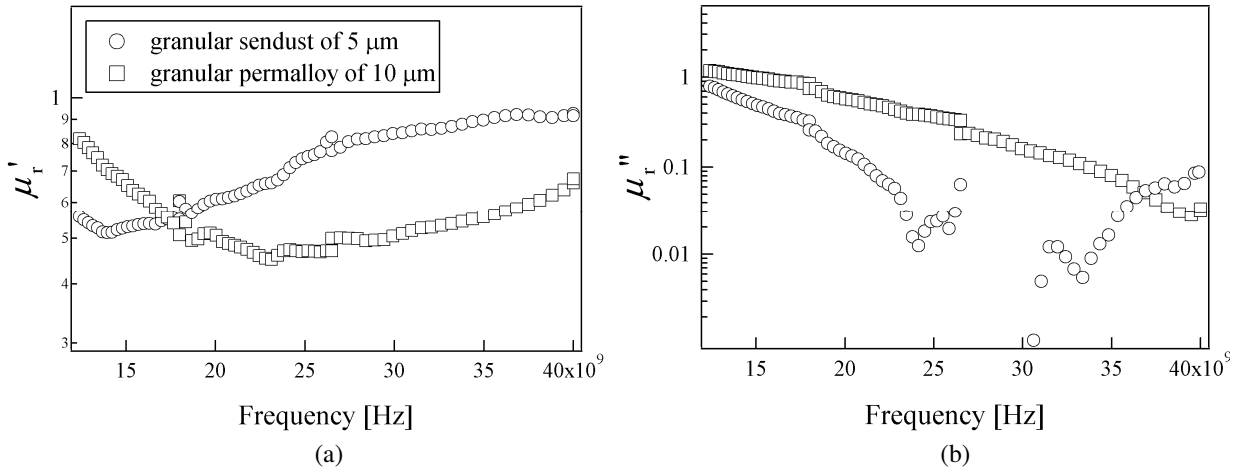


Figure 8: Frequency dependences of (a) μ_r' and (b) μ_r'' for composites made of granular sendust particles of 5 μm diameter and granular permalloy of 10 μm diameter.

To explain this frequency dependence of μ_r' , two reasons might be considered. The first reason is the natural magnetic resonance of soft magnetic materials. Soft magnetic materials have a resonance frequency in the frequency range from several hundred MHz to GHz, and the resonance frequency of a composite is higher than that of a pure magnetic material. The value of μ_r' decreases rapidly near the resonance frequency and becomes less than unity. Thus, the values of μ_r' for both composites are less than unity and increase as the frequency increases far from the resonance frequency. Another reason is the generation of magnetic moments by the eddy current flowing on the surface of soft magnetic material particles, because soft magnetic materials are conductive. The phenomenon that the values of μ_r' become less than unity has also been observed in composites made of polystyrene resin and conductive particles such as aluminum [10]. In this case, the value of μ_r' decreases upon increasing the volume mixture ratio of conductive particles and that of μ_r'' decreases in inverse proportion to the particle size of the conductive particles. These results were in approximate agreement with Equations (2) and (3) obtained by a qualitative theoretical estimation.

$$\mu_r' = 1 - V \quad (2)$$

$$\mu_r'' = \frac{2V\delta}{a} \quad (3)$$

Here, V is the volume mixture ratio of the conductive particles, δ is the skin depth and a is the radius of the conductive particles. It is found from Equation (2) that the value of μ_r' is independent of the skin depth and frequency and only depends on the volume mixture ratio of the soft magnetic material. Applying Equation (2) to the composites made of sendust particles and permalloy particles gives $\mu_r' = 0.47$ for $V = 0.53$. On the other hand, the minimum value of μ_r' for the composite made of sendust particles of 5 μm diameter is approximately 0.51 and that for the composite made of permalloy particles of 10 μm diameter is approximately 0.44. In addition, the value of μ_r'' for the composite made of sendust particles of 5 μm diameter was largest and decreased in inverse proportion to the particle size at frequencies above approximately 6 GHz, as shown in Fig. 3(b). This particle-size dependence of μ_r'' qualitatively agreed with Equation (3). These results suggest that the frequency dependence of μ_r^* in the high frequency range might be explained by

the generation of a magnetic moment. However, the reason for the frequency dependence of μ_r^* in the high-frequency range is uncertain and further investigation is necessary.

The composite made of sendust particles of 5 μm diameter exhibited a return loss of less than -20 dB in the frequency range from 33 to 39 GHz for sample thicknesses of 2.5, 2.8 and 2.9 mm, although the bandwidth was narrow (approximately 1.4%). It was found that the composite made of sendust particles of 5 μm diameter can operate in the frequency range of not only several GHz but also above 30 GHz.

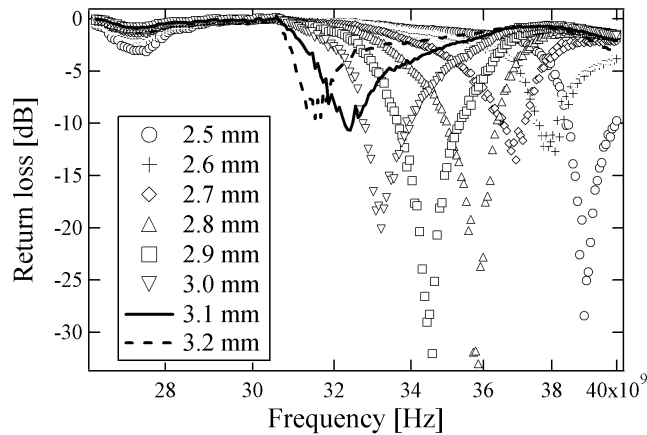


Figure 9: Values of return loss for the composite made of sendust particles of 5 μm diameter. The volume mixture ratio of sendust is 53 vol%.

4. CONCLUSIONS

The frequency dependences of μ_r^* and ε_r^* for composites made of polystyrene resin and granular sendust particles depended on the sendust particle size. Therefore, the absorption characteristics were different for sendust particles of different sizes, and the composite made of small sendust particles absorbed more than 99% of electromagnetic wave power in the frequency range from 1 to 3 GHz.

The frequency dependences of μ_r^* and ε_r^* and the absorption characteristics for the composite made of granular sendust particles were similar to those of the composite made of granular permalloy particles but were different from that made of sendust flakes.

The values of μ_r' for the composites made of granular sendust particles of 5 μm diameter and granular permalloy particles of 10 μm were minimum at frequencies above 10 GHz and increased with increasing frequency. The return loss of the composite made of granular sendust particles of 5 μm diameter was less than -20 dB in the frequency range from 33 to 39 GHz for a suitable sample thickness.

REFERENCES

1. Kasagi, T., T. Tsutaoka, and K. Hatakeyama, "Particle size effect on the complex permeability for permalloy composite materials," *IEEE Trans. Magn.*, Vol. 35, No. 5, 3424–3426, 1999.
2. Kasagi, T., T. Tsutaoka, and K. Hatakeyama, "Negative permeability spectra in permalloy granular composite materials," *Appl. Phys. Lett.*, Vol. 88, 17502, 2006.
3. Liu, J. R., M. Itoh, T. Horikawa, E. Taguchi, H. Mori, and K. Machida, "Iron based carbon nanocomposites for electromagnetic wave absorber with wide bandwidth in GHz range," *Appl. Phys. A*, Vol. 82, 509–513, 2006.
4. Lim, K. M., K. A. Lee, M. C. Kim, and C. G. Park, "Complex permeability and electromagnetic wave absorption properties of amorphous alloy-epoxy composites," *J. Non-Cryst. Solids.*, Vol. 351, 75–83, 2005.
5. Matsumoto, M. and Y. Miyata, "Thin electromagnetic wave absorber for quasi-microwave band containing aligned thin magnetic metal particles," *IEEE Trans. Magn.*, Vol. 33, No. 6, 4459–4464, 1997.
6. Olmedo, L., G. Chateau, C. Deleuze, and J. L. Forveille, "Microwave characterization and modelization of magnetic granular materials," *J. Appl. Phys.*, Vol. 73, No. 10, 6992–6994, 1993.

7. Nakamura, T., T. Tsutaoka, and K. Hatakeyama, “Frequency dispersion of permeability in ferrite composite materials,” *J. Magn. Magn. Mater.*, Vol. 138, 319–328, 1994.
8. Kusunoki, H., T. Kondo, K. Hiraki, K. Takada, and S. Yoshikado, “Grain-size dependence of the characteristics of electromagnetic wave absorbers of ferrite-SiO₂ composites,” *Key Eng. Mater.*, Vol. 248, 161–164, 2003.
9. Musal, Jr., H. M. and H. T. Hahn, “Thin-layer electromagnetic absorber design,” *IEEE Trans. Magn.*, Vol. 25, No. 5, 3851–3853, 1989.
10. Yamane, T., A. Nishikata, and Y. Shimizu, “Resonance suppression of a spherical electromagnetic shielding enclosure by conductive dielectrics,” *IEEE Trans. on Electromagnetic Compatibility*, Vol. 42, 441–448, 2000.

Stimulated Raman Scattering of Extraordinary Electromagnetic Waves in Weakly Magnetized Plasma

M. S. Bawa'aneh¹, H. M. EL-Nasser², Ghada Assayed¹, S. Alyones¹, A. M. Alsmadi¹
S. Al-Awfi³ and M. Al-Sughayer¹

¹Physics Department, The Hashemite University, Zarqa 13115, Jordan

²Physics Department, AL-al-Bayt University, Mafraq 25113, Jordan

³Physics Department, Taybah University, Medina Al-monawara, Saudi Arabia

Abstract— Stimulated Raman backscattering (SRBS) in a homogeneous, weakly magnetized plasma has been studied, where a system of coupled equations has been derived and solved for an analytical formula that describes SRBS instability. The presence of a static magnetic field is found to suppress the SRBS instability and increase the threshold. SRBS suppression increases as the density increases, where the instability growth rate drops to zero near the quarter critical density.

1. INTRODUCTION

A number of high-intensity, laser driven instabilities are known to exist in the corona of laser-produced plasmas. Such instabilities are of much current interest because of their relevance not only to inertial confinement fusion (ICF) [1], but also to various fields of plasma physics such as accelerator physics [2, 3], nonlinear optics [4] and physics of the atmosphere [5–8].

One important instability is stimulated Raman scattering (SRS) instability that is defined as the resonant decay of an incident electromagnetic wave with frequency ω_0 and wavenumber \vec{k}_0 into a scattered electromagnetic wave with frequency ω_1 and wavenumber \vec{k}_1 plus an electron plasma wave (ω, \vec{k}) , i.e., the decay of an incident photon into a scattered photon and a plasmon. The frequency and wave number matching condition are

$$\omega_0 = \omega_1 + \omega, \quad \text{and} \quad \vec{k}_0 = \vec{k}_1 + \vec{k}, \quad (1)$$

where from Equation (1) one can see that SRS could occur at densities up to quarter the critical density.

SRS has been thoroughly investigated both experimentally [9–13] and theoretically [14–28]. SRBS is a dominant process observed in laser-driven fusion experiments especially in high density plasma ($n > 0.1n_{cr}$) [9–11]. Controlling laser-plasma instabilities is of extreme importance especially for research on ICF because it is a source of high energy electrons, which penetrate the core resulting in the preheating of the fuel. Linear convective theory [14–18] predicts SRS instability with enormous gain levels, where backscattering is expected to have the highest spatial gain. Laser beam smoothing is an efficient way for the control of SRS level, however, high intensity laser speckles could be a source of enhanced SRS.

Initiated from noise level, unstable waves could develop a spacially growing amplitude. Also, laser hot spots affect the nature of SRS reflectivity, where convective amplification of thermal density fluctuations yields SRS reflectivity that is exponentially dependent of laser intensity and plasma size. Including beam diffraction and pump depletion can significantly decrease the spatial gain within a hot spot [19, 20].

Barr et al. [21, 22] examined the SRBS instability numerically in the presence of a transverse static density modulation. Enhancement in the instability was observed. An analytical formulation of SRS in laser filaments with density modulation was developed by Liu and Tripathi [23, 24]. They showed that density profiles strongly localize the plasma reducing the region of interaction and the instability. Two-dimensional simulation for nonlinear development of SRS from a laser hot spot was reported by David A. Russell et al. [25]. Their simulation includes many saturation mechanisms like pump depletion and ponderomotive density profile modulation. S. C. Wilks et al. [26] studied SRBS in ultraintense, short pulse laser-plasma interactions using linear theory and particle-in-cell (PIC) simulations. One thing they found is that maximum growth rate at the peak of the pulse is reduced from the homogeneous pulse value by a factor of $1/\sqrt{2}$. R. L. Berger et al. [27] studied the competition of SRS with stimulated Brillouin scattering (SBS) that are driven by nonuniform

laser beams. They found that SRS and SBS can be anticorrelated even when the total scattering is quite modest.

Kruer and Estabrook [28] showed the effect of self-generated magnetic fields on resonant absorption of light through the excitation of the upper hybrid oscillations. They used very simple linear equations for the X-mode inside the plasma and crudely estimated the components of the electric field of the light wave ignoring thermal and collisional effects and used a relativistic particle code to see that this effect is dominant on light absorption due to oblique incidence.

Self-generated magnetic fields in plasma were first detected in experiments using magnetic probes [29, 30]. Mega Gauss magnetic fields have been known to exist in laser-produced plasmas [31]. Such strong fields were first reported by Raven et al. [32], where they used the Faraday rotation as a field diagnostic in the plasma corona. Hundred mega Gauss fields are, also, known to exist in the context of ICF [33, 34]. Pukov related such strong fields to the generation of hot electrons [33], while Bawa'aneh and Boyd related them to thermoelectric generation [34], where non-aligned temperature and density gradients lead to the generation of toroidal fields in the underdense region that are advected then to the overdense region. Self generated fields are believed to have significant effects on the dynamics of the plasma channel bored by the intense laser.

In the present work, SRBS in magnetized homogeneous plasmas is investigated, where an ordinary electromagnetic wave decays parametrically into a backscattered electromagnetic wave which becomes extraordinary in magnetized plasma and an electron plasma wave which becomes an upper hybrid electron plasma wave in magnetized plasma. Here, the incident and scattered waves travel along a density gradient, which is perpendicular to a static magnetic field. In this work an expression for SRBS maximum growth rate in magnetized plasmas is obtained. The problem is formulated in Sec. 2 and a system of coupled equations is derived. The system of equations is solved in Sec. 3, where an extended dispersion relation for SRBS in magnetized plasma is derived. The dispersion relation is solved in Sec. 4 and a modified formula for maximum growth rate as a function magnetic field is derived and compared with that formula known in literature in nonmagnetized plasmas. Finally, comments and conclusions are stated in Sec. 5.

2. THE MODEL

Consider a large amplitude light wave incident on a plasma whose density is perturbed in the direction of propagation of the incident light wave. Using Ampere's and Faraday's laws and the electric current density in plasma due to electrons only, namely $\vec{J} = -en\vec{v}$, the following wave equation for the electric field of the scattered wave inside the plasma is obtained;

$$\frac{\partial^2 \vec{E}}{\partial t^2} + c^2 \vec{\nabla} \times (\vec{\nabla} \times \vec{E}) = \frac{e}{\epsilon_0} \frac{\partial}{\partial t} (n\vec{v}), \quad (2)$$

where e , n and \vec{v} represent the electron charge, density and velocity, respectively and ϵ_0 is the electric permittivity of vacuum. The electron density and velocity fluctuations are obtained from the electron continuity and force equations. These equations are given, respectively, by

$$\frac{\partial n}{\partial t} + \vec{\nabla} \cdot (n\vec{v}) = 0 \quad (3)$$

$$\frac{\partial \vec{v}}{\partial t} + (\vec{v} \cdot \vec{\nabla}) \vec{v} = -\frac{e}{m} \vec{E} - \frac{e}{m} \vec{v} \times \vec{B} - \frac{\gamma_e k_B T}{mn} \vec{\nabla} n, \quad (4)$$

where we consider an adiabatic equation of state for electrons, T , m and γ_e are the electron temperature, mass and specific heat ratio, respectively and k_B is the Boltzmann constant.

Let the electron density have the equilibrium part n_0 and a perturbation part n_1 . Also let the electric field be given by $\vec{E} = \vec{E}_0 + \vec{E}_1$ where \vec{E}_0 is the incident laser field and \vec{E}_1 is the total field of the induced waves, and let the electrons have a quiver velocity \vec{v}_{os} due to the \vec{E}_0 field and a perturbation \vec{v}_1 due to quivering in the induced wave field \vec{E}_1 . The linearized form of Equation (2) becomes

$$\frac{\partial^2 \vec{E}_1}{\partial t^2} - c^2 \vec{\nabla}^2 \vec{E}_1 + c^2 \vec{\nabla} (\vec{\nabla} \cdot \vec{E}_1) = \frac{e}{\epsilon_0} \frac{\partial}{\partial t} (n_0 \vec{v}_1 + n_1 \vec{v}_{os}) \quad (5)$$

We now consider a magnetic field such that $\vec{B} = \vec{B}_{dc} + \vec{B}_1$, where \vec{B}_{dc} is a constant dc-magnetic field that could be externally applied or self generated in the plasma and \vec{B}_1 is the space-time varying

magnetic field associated with the scattered electromagnetic wave. We, also, use the identities $(\vec{v}_e \cdot \vec{\nabla})\vec{v}_e = \frac{1}{2}\vec{\nabla}(\vec{v}_e \cdot \vec{v}_e) - \vec{v}_e \times (\vec{\nabla} \times \vec{v}_e)$ and $\vec{\nabla} \times \vec{v}_e = \frac{e}{m}\vec{B}_1$. The linearized continuity and force equations, namely Equations (3) and (4), respectively, become

$$\frac{\partial n_1}{\partial t} + n_0 \vec{\nabla} \cdot \vec{v}_1 = 0 \quad (6)$$

$$\frac{\partial \vec{v}_1}{\partial t} = -\vec{\nabla}(\vec{v}_{os} \cdot \vec{v}_1) - \frac{e}{m}\vec{E}_1 - \frac{e}{m}\vec{v}_1 \times \vec{B}_{dc} - \frac{\gamma_e k_B T}{mn_0} \vec{\nabla} n_1 \quad (7)$$

We now consider a geometry where $\vec{B}_{dc} = B_{dc}\hat{k}$, $\vec{\nabla} = \hat{i}\frac{\partial}{\partial x}$, a linearly polarized incident laser of $\vec{v}_{os} = v_{os}\hat{j}$, $\vec{E}_1 = (E_x^l + E_x^h)\hat{i} + (E_y^l + E_y^h)\hat{j}$ and $\vec{v}_1 = (v_x^l + v_x^h)\hat{i} + (v_y^l + v_y^h)\hat{j}$, where v_{os} is the high frequency quiver velocity due to the electric field of the pump wave and the superscripts “l” and “h” represent low and high frequency components, respectively. Note that although the incident laser is originally linearly polarized in the y -direction, the scattered wave develops a high frequency component of the electric field inside the plasma in the x -direction [28], v_x^h is the high frequency quiver velocities due to the electric field of the scattered wave E_x^h and v_y^l is a low frequency component that develops due to the presence of the magnetic field where electrons gyrate in the xy -plane, a plane perpendicular to the \vec{B}_{dc} direction. Accordingly, Equations (5), (6) and (7) give the following system of equations;

$$\frac{\partial n_1}{\partial t} = -n_0 \frac{\partial v_x^l}{\partial x} \quad (8)$$

$$\left(\frac{\partial^2}{\partial t^2} - c^2 \frac{\partial^2}{\partial x^2}\right) E_y^h = \frac{e}{\epsilon_0} \frac{\partial}{\partial t} (n_1 v_{os}) + \frac{en_0}{\epsilon_0} \frac{\partial v_y^h}{\partial t} \quad (9)$$

$$\left(\frac{\partial^2}{\partial t^2} - c^2 \frac{\partial^2}{\partial x^2}\right) E_y^l = \frac{en_0}{\epsilon_0} \frac{\partial v_y^l}{\partial t} \quad (10)$$

$$\frac{\partial^2 E_x^h}{\partial t^2} = \frac{en_0}{\epsilon_0} \frac{\partial v_x^h}{\partial t} \quad (11)$$

$$\frac{\partial v_x^l}{\partial t} = -\frac{\partial}{\partial x} (v_{os} v_y^h) - \frac{e}{m} E_x^l - \Omega v_y^l - \frac{V_e^2}{n_0} \frac{\partial n_1}{\partial x} \quad (12)$$

$$\frac{\partial v_x^h}{\partial t} = -\frac{\partial}{\partial x} (v_{os} v_y^l) - \frac{e}{m} E_x^h - \Omega v_y^h \quad (13)$$

$$\frac{\partial v_y^l}{\partial t} = -\frac{e}{m} E_y^l + \Omega v_x^l \quad (14)$$

$$\frac{\partial v_y^h}{\partial t} = -\frac{e}{m} E_y^h + \Omega v_x^h \quad (15)$$

$$\frac{\partial E_x^l}{\partial x} = \frac{-en_1}{\epsilon_0}, \quad (16)$$

where only resonant terms are kept and $\Omega = eB_{dc}/m$ is the electron gyrofrequency. This closed system of equations will be solved in Sec. 3 using Fourier transform.

Ignoring the dc-field in the system of equations, where the reduced form of Equation (15) is substituted in Equation (9), leaves us with two coupled equations, namely Equation (9) and the reduced form of Equation (8) that are widely known in literature for SRS in nonmagnetized plasmas [17].

3. DISPERSION RELATION

The system of equations obtained in Sec. 2 will now be solved to obtain a dispersion relation for SRBS in magnetized plasmas. The electric field of the incident wave appearing in the coupling terms via v_{os} , namely $\vec{E}_0(x, t)$, is assumed to be linearly polarized and to vary in space and time as follows;

$$\vec{E}_0(x, t) = \hat{j} E_0 \cos(k_0 x - \omega_0 t) = \frac{1}{2} \left(E_0 e^{i(k_0 x - \omega_0 t)} + c.c. \right) \hat{j},$$

where *c.c.* denotes the complex conjugate and E_0 is the amplitude of the incident wave. Fourier transforming the above system of equations and solving the low frequency velocities simultaneously, after excluding the upshift terms ($v_y^h(\omega + n\omega_0)$) for backscatter and ignoring all higher harmonics of $v_y^h(\omega - 2\omega_0)$ and above from the down shift terms as nonresonant, one obtains

$$v_x^l = \frac{\omega}{k} \frac{(k^2 V_{th}^2 + \omega_{pe}^2)}{\omega^2 - \Omega^2} \frac{n_1}{n_0} + \frac{1}{2} \frac{\omega k v_{os}}{\omega^2 - \Omega^2} v_y^h - \frac{e}{m} \frac{\Omega}{\omega^2 - \Omega^2} E_y^l \quad (17)$$

$$v_y^l = i \frac{\Omega}{k} \frac{(k^2 V_{th}^2 + \omega_{pe}^2)}{\omega^2 - \Omega^2} \frac{n_1}{n_0} + \frac{i}{2} \frac{\Omega k v_{os}}{\omega^2 - \Omega^2} v_y^h - \frac{ie}{m\omega} \left(1 + \frac{\Omega^2}{\omega^2 - \Omega^2}\right) E_y^l, \quad (18)$$

where $V_{th} = \sqrt{\gamma_e k_B T_e / m}$ is the electron thermal velocity. Also, solving the high frequency velocities simultaneously after dropping the nonlinear term on the right hand side of Equation (13), eliminating E_x^h using Equation (11), gives

$$v_x^h = \frac{-e}{m\omega_1} \frac{\omega_1 \Omega}{\omega_1^2 - \omega_h^2} E_y^h \quad (19)$$

$$v_y^h = \frac{-ie}{m\omega_1} \left(1 + \frac{\Omega^2}{\omega_1^2 - \omega_h^2}\right) E_y^h, \quad (20)$$

where $\omega_h^2 = \omega_{pe}^2 + \Omega^2$ is the upper hybrid frequency.

Upon the substitution of the velocities from Equations (17)–(20) in the Fourier transformed equations of the system, Equations (8), (9) and (10) will take the following forms;

$$\left[\omega_1^2 - c^2 k_1^2 - \omega_{pe}^2 \left(\frac{\omega_1^2 - \omega_{pe}^2}{\omega_1^2 - \omega_h^2} \right) \right] E_y^h - i \frac{e}{2\epsilon_0} \omega_1 v_{os} n_1 = 0 \quad (21)$$

$$\left[\omega^2 - V_{th}^2 k^2 - \omega_h^2 \right] n_1 + \frac{ien_0}{2m\omega_1} k^2 v_{os} \left(\frac{\omega_1^2 - \omega_{pe}^2}{\omega_1^2 - \omega_h^2} \right) E_y^h + \frac{en_0}{m\omega} k \Omega E_y^l = 0 \quad (22)$$

$$\left[\omega^2 - c^2 k^2 - \omega_{pe}^2 \frac{\omega^2}{\omega^2 - \Omega^2} \right] E_y^l - \frac{i}{2} k v_{os} \Omega \frac{\omega}{\omega_1} \frac{\omega_{pe}^2}{\omega^2 - \Omega^2} E_y^h + \frac{e}{\epsilon_0 k} \frac{\Omega \omega}{\omega^2 - \Omega^2} (k^2 V_{th}^2 + \omega_{pe}^2) n_1 = 0 \quad (23)$$

Note that ignoring the magnetic field, Equation (23) becomes excessive and we end up with two coupled equations, namely the reduced forms of Equations (21) and (22), that are well known in literature for SRS in a nonmagnetized plasma [17,18]. Note, also, that ignoring the pump wave ($v_{os} = 0$) and keeping the magnetic field in the system of equations results in the decoupling between Equations (21) and (22) and we end up with two decoupled linear modes; the first, that comes from the square bracket on the left hand side of Equation (21), describes an *X*-wave that is primarily a transversely polarized electromagnetic wave, while the second, that comes from the square bracket on the left hand side of Equation (22), is the upper hybrid electron plasma wave that is primarily electrostatic. However, this equation is coupled with the E_y^l equation that appears due to the presence of the magnetic field. The upper hybrid wave behaves like a langmuir wave with a frequency increase by $\omega_{ce}^2/(2\omega_{pe})$ in case of ignoring E_y^l as a small quantity.

One can, also, see that Equation (23) in it's primitive form is electromagnetic in nature with a frequency $\omega < \omega_1$ and wave number k . However, the presence of the pump and/or the magnetic field modifies the dispersion relation of this equation, and ignoring the pump and the magnetic field, this equation yields the *o*-wave.

Solving Equations (21), (22) and (23) simultaneously considering weakly magnetized plasma, i.e., $\Omega \ll \omega_0$, the following dispersion relation is obtained;

$$\begin{aligned} & \left[\omega^2 - V_{th}^2 k^2 - \omega_h^2 \right] \left[\omega_1^2 - c^2 k_1^2 - \omega_{pe}^2 \left(1 + \frac{\Omega^2}{\omega_1^2 - \omega_{pe}^2} \right) \right] \left[\omega^2 - c^2 k^2 - \omega_{pe}^2 \frac{\omega^2}{\omega^2 - \Omega^2} \right] \\ & - \omega_{pe}^2 \frac{\Omega^2}{\omega^2 - \Omega^2} (k^2 V_{th}^2 + \omega_{pe}^2) \left[\omega_1^2 - c^2 k_1^2 - \omega_{pe}^2 \left(1 + \frac{\Omega^2}{\omega_1^2 - \omega_{pe}^2} \right) \right] \\ & - \frac{1}{4} \omega_{pe}^2 k^2 v_{os}^2 \left(1 + \frac{\Omega^2}{\omega_1^2 - \omega_{pe}^2} \right) \left[\omega^2 - c^2 k^2 - \omega_{pe}^2 \frac{\omega^2}{\omega^2 - \Omega^2} \right] - \frac{1}{4} \omega_{pe}^2 k^2 v_{os}^2 \Omega^2 \frac{\omega_{pe}^2}{\omega^2 - \Omega^2} = 0 \quad (24) \end{aligned}$$

Ignoring the magnetic field in the dispersion relation of Equation (24) yields the following dispersion relation for SRS in nonmagnetized plasma [17, 18];

$$(\omega_1^2 - c^2 k_1^2 - \omega_{pe}^2) (\omega^2 - V_{th}^2 k^2 - \omega_{pe}^2) = \frac{1}{4} \omega_{pe}^2 k^2 v_{os}^2 \quad (25)$$

Equation (25) is analyzed in literature, where an expression for SRS instability growth rate in nonmagnetized plasma is obtained [see for example Ref. [17]]. Dispersion relation of Equation (24) is a generalization for that in Equation (25) for the case of magnetized plasmas. In Sec. 4, Equation (24) will be solved analytically to obtain an expression for SRBS growth rate in magnetized plasmas.

4. INSTABILITY GROWTH RATE

Following Ref. [17], we derived an approximate expression for the growth rate of SRBS instability using the system of Equations (21), (22) and (23). Let the low frequency ω be such that $\omega = \omega_r + i\gamma$, where γ is the instability growth rate, ω_r is the real part of ω and $\gamma \ll \omega_r$. Also, matching conditions of Equation (1) are considered and the following two approximations are made; $\frac{\Omega^2}{\omega_1^2 - \omega_{pe}^2} \approx \frac{\Omega^2}{\omega_{1r}^2 - \omega_{pe}^2} \left(1 + 2i \frac{\gamma}{\omega_{1r}} \frac{\omega_{1r}^2}{\omega_{1r}^2 - \omega_{pe}^2}\right)$ and $\frac{\omega^2}{\omega^2 - \Omega^2} \approx \frac{\omega_r^2}{\omega_r^2 - \Omega^2} - \frac{2i\omega_r \gamma \Omega^2}{(\omega_r^2 - \Omega^2)^2}$, where Ω , $\gamma \ll \omega_0$ and $\omega_{1r} = \omega_0 - \omega_r$. Now, considering these approximations and making use of the dispersion relation of the X -waves and the upper hybrid electron plasma waves, the following quantities may be simplified as:

$$I_1 = \omega_1^2 - c^2 k_1^2 - \omega_{pe}^2 \left(1 + \frac{\Omega^2}{\omega_1^2 - \omega_{pe}^2}\right) \approx -2i\gamma\omega_{1r} \left(1 + \frac{\omega_{pe}^2 \Omega^2}{(\omega_{1r}^2 - \omega_{pe}^2)^2}\right) \quad (26)$$

$$I_2 = \omega^2 - V_{th}^2 k^2 - \omega_h^2 \approx 2i\gamma\omega_r \quad (27)$$

$$I_3 = \omega^2 - c^2 k^2 - \omega_{pe}^2 \frac{\omega^2}{\omega^2 - \Omega^2} \approx 2i\gamma\omega_r \left(1 + \frac{\omega_{pe}^2 \Omega^2}{(\omega_r^2 - \Omega^2)^2}\right) + \omega_{pe}^2 \left(1 + \frac{\Omega^2}{\omega_r^2 - \Omega_{pe}^2} - \frac{\omega_r^2}{\omega_r^2 - \Omega^2}\right), \quad (28)$$

where in simplifying I_2 and I_3 , we have considered two different modes of a frequency ω and wave number k with two different natures; I_2 is an electrostatic mode being the upper hybrid electron plasma mode and I_3 is an electromagnetic mode following the extraordinary mode.

Solving the dispersion relation of Equation (24) making use of Equations (26) to (28), gives the following form for the growth rate instability of SRS in weakly magnetized plasma;

$$\gamma^2 = \frac{\gamma_0^2}{\alpha_1} \left(1 + \frac{\Omega^2}{\omega_{1r}^2 - \omega_{pe}^2} + \frac{\omega_{1r}}{\omega_r} \frac{\alpha_3}{\alpha_2} \frac{\omega_{pe}^2 \Omega^2}{(\omega_{1r}^2 - \omega_{pe}^2)^2} - \frac{\omega_{pe}^2 \Omega^2}{\alpha_2 (\omega_r^2 - \omega_{pe}^2)^2}\right) - \frac{1}{4} \frac{\omega_{pe}^2 \Omega^2}{\alpha_2 \omega_r^2}, \quad (29)$$

where

$$\alpha_1 = 1 + \frac{\omega_{pe}^2 \Omega^2}{(\omega_{1r}^2 - \omega_{pe}^2)^2}, \quad \alpha_2 = 1 + \frac{\omega_{pe}^2 \Omega^2}{(\omega_r^2 - \Omega^2)^2}, \quad \alpha_3 = 1 + \frac{\Omega^2}{\omega_r^2 - \omega_{pe}^2} - \frac{\omega_r^2}{\omega_r^2 - \Omega^2}$$

and γ_0 is the maximum growth rate known in literature [17, 18] for SRBS in nonmagnetized plasmas given by

$$\gamma_0 = \frac{1}{4} \frac{\omega_{pe} k v_{os}}{\sqrt{\omega_r (\omega_0 - \omega_r)}} \quad (30)$$

One can easily see that ignoring the dc-magnetic field ($\Omega_e \rightarrow 0$), Equation (29) reduces to γ_0 , the simple form of maximum growth rate for SRBS instability in nonmagnetized plasmas, namely Equation (30), where $\alpha \rightarrow 1$.

Note that the maximum growth rate for the backscattering case occurs when the scattered light is resonant [17]. According to our geometry, the scattered wave obeys the dispersion relation of extraordinary waves in magnetized plasmas. Using this dispersion relation one can obtain the value of k , say k_m , at which maximum growth occurs, namely

$$k_m = k_0 + \left(\frac{\omega_{1r}^2}{c^2} - \frac{\omega_{pe}^2}{c^2} \frac{\omega_{1r}^2 - \omega_{pe}^2}{\omega_{1r}^2 - \omega_h^2}\right)^{1/2} \quad (31)$$

A similar equation for k_m is obtained in [17] for the nonmagnetized plasma at $\omega_r = \omega_{pe}$.

For the rest of this section we will be looking at the effect of the modification obtained in this work on the growth rate. The figure shows the normalized SRBS growth rate given in Equation (29), namely γ/ω_0 , as a function of the normalized number density (n/n_{cr}), where SRS occurs at densities up to around quarter critical density. Curves in the figure represent values of Ω/ω_0 given by 0, 0.02, 0.04, 0.06 and 0.08, respectively, where the solid line represents the case of $B_{dc} = 0$, i.e., the nonmagnetized plasma case given by Equation (30). Other parameters are $I_0 = 10^{15}$ W/cm² and $\lambda_0 = 1.06$ microns, typical values for ICF. The introduction of a dc-magnetic field suppresses the SRBS instability. The peak value, for example, is suppressed by about 27% of its field-free value for $\Omega = 0.08\omega_0$. This suppression is stronger at higher density values.

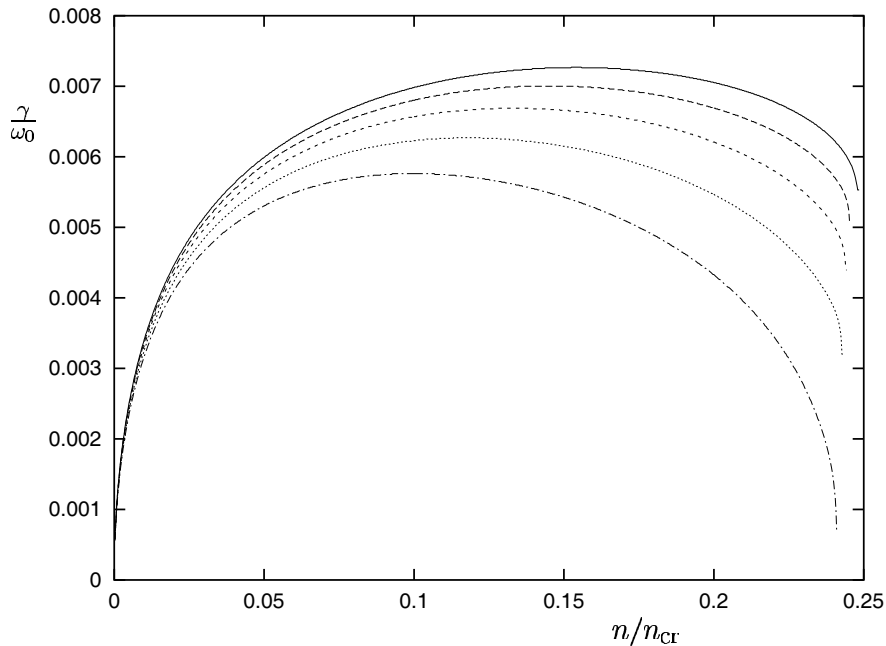


Figure 1: Normalized maximum growth rate versus normalized number density for $\Omega/\omega_0 = 0, 0.02, 0.04, 0.06, 0.08$, respectively, where solid line corresponds to $\Omega/\omega_0 = 0$. Other parameters are $I_0 = 10^{15}$ W/cm² and $\lambda_0 = 1.06$ microns.

5. CONCLUSION

The problem of stimulated Raman scattering of light waves in magnetized plasmas is considered. A system of coupled equations governing the electric field of the scattered light wave together with the electrostatic density fluctuations and other quantities coupled with them is derived for a plasma with a static magnetic field. The system of equations is Fourier transformed and a system of coupled linear equations is obtained, namely Equations (21), (22) and (23). In the absence of the dc-magnetic field, this system of three linear equations reduces to that of two linear equations known in literature. The coupled linear equations are solved, where a dispersion relation, modified for the presence of the dc-magnetic field, is derived, namely Equation (24). In the absence of the dc-magnetic field, the modified dispersion relation reduces into the corresponding expression known in literature for SRBS in nonmagnetized plasmas [17, 18], i.e., Equation (24) reduces to Equation (25) in case of zero static magnetic field. Dispersion relation of Equation (24) is solved analytically, where an expression for SRBS growth rate is obtained. Solution is presented in Equation (29). For zero magnetic field, Equation (29) reduces to that formula of SRBS growth rate known in literature for nonmagnetized plasmas [17, 18], namely Equation (30). In the derivation of Equation (29), the following approximations were used; $\gamma, \Omega \ll \omega_0$, limiting the validity of the formula obtained weakly magnetized plasma.

Numerical presentation of Equation (29) is obtained for typical plasma parameters found in ICF; $\lambda_0 = 1.06$ microns and $I_0 = 10^{15}$ W/cm² estimated for different Ω values ranging from zero to $0.08\omega_0$. The figure shows γ/ω_0 versus n/n_{cr} for $\Omega/\omega_0 = 0, 0.02, 0.04, 0.06, 0.08$, where the solid line corresponds to the nonmagnetized case. It shows suppression of the instability growth rate

as the magnetic field increases. This suppression becomes stronger as we get closer to the higher density side of the instability range, i.e., closer to $n \approx 0.25n_{cr}$. For $\Omega = 0.08\omega_0$, the peak value of the growth rate is suppressed by about 27%.

REFERENCES

1. Bawa'aneh, M. S., *Contrib. Plasma Phys.*, Vol. 43, 447, 2003.
2. Tajima, T. and J. M. Dawson, *Phys. Rev. Lett.*, Vol. 43, 267, 1979.
3. Umstadter, D., J. K. Kim, and E. Dodd, *Phys. Rev. Lett.*, Vol. 76, 2073, 1996.
4. Umstadter, D. and T. B. Norris, *IEEE J. Quantum Electron.*, Vol. 33, 1877, 1997.
5. Stenflo, L., *Phys. Scripta*, Vol. T30, 166, 1990.
6. Stenflo, L., *Phys. Scripta*, Vol. T50, 15, 1994.
7. Stenflo, L., *J. Geophys. Res.*, Vol. 83, 1154, 1978.
8. Stenflo, L. and J. Larsson, *Proc. of Noble-Symposium on Nonlinear Effects in Plasmas*, 152, edited by H. Wilhelmsson, Plenum Press, 1977.
9. Liu, C. S., M. N. Rosenbluth, and R. B. White, *Phys. Fluids*, Vol. 17, 1211, 1974.
10. Obenschain, S. P., et al., *Phys. Rev. Lett.*, Vol. 62, 768, 1989.
11. Rousseaux, C., et al., *Phys. Rev. Lett.*, Vol. 74, 4655, 1995.
12. Fernandez, J. C., et al., *Phys. Plasmas*, Vol. 4, 1849, 1997.
13. Alexandra, G., et al., *Appl. Opt.*, Vol. 37, 8453, 1998.
14. Rosenbluth, M. N., *Phys. Rev. Lett.*, Vol. 29, 565, 1972.
15. Goldman, M. V. and D. F. DuBois, *Phys. Fluids*, Vol. 8, 1404, 1965.
16. Bornatici, M., *J. Plasma Phys.*, Vol. 14, No. 1, 105, 1975.
17. Kruer, W. L., *The Physics of Laser Plasma Interaction*, Addison Wesley Publishing Company, 1988.
18. Baumgärtel, K. and K. Sauer, *Topics on Nonlinear Wave — Plasma Interaction*, Birkhäuser, Berlin, 1987.
19. Rose, H. A. and D. F. DuBois, *Phys. Rev. Lett.*, Vol. 72, 2883, 1994.
20. Eliseev, V. V., et al., *Phys. Plasmas*, Vol. 3, 3754, 1996.
21. Barr, H. C., T. J. M. Boyd, and A. P. Mackwood, *Phys. Fluids B*, Vol. 1, 1151, 1989.
22. Barr, H. C., T. J. M. Boyd, and Coutts, *Phys. Rev. Lett.*, Vol. 56, 2256, 1986.
23. Liu, C. S. and V. K. Tripathi, *Phys. Fluids*, Vol. 29, 4188, 1986.
24. Liu, C. S. and V. K. Tripathi, *Phys. Plasmas*, Vol. 3, No. 9, 3410, 1996.
25. Russell, D. A., et al., *Phys. Plasmas*, Vol. 6, No. 4, 1294, 1999.
26. Wilks, S. C., W. L. Kruer, E. A. Williams, P. Amendt, and D. C. Eder, *Phys. Plasmas*, Vol. 2, No. 1, 279, 1995.
27. Berger, R. L., C. H. Still, E. A. Williams, and A. B. Langdon, *Phys. Plasmas*, Vol. 5, No. 12, 4337, 1998.
28. Kruer, W. L. and K. Estabrook, *Phys. Fluids*, Vol. 20, No. 10, 1688, 1977.
29. Korobkin, V. V. and R. V. Serov, *JETP Lett.*, Vol. 4, 70, 1966.
30. Askar'yan, et al., *JETP Lett.*, Vol. 5, 93, 1967.
31. Nicolai, P., et al., *Phys. Plasmas*, Vol. 7, 4250, 2000.
32. Raven, A., et al., *Phys. Rev. Lett.*, Vol. 41, 554, 1978.
33. Pukov, A. and J. Meyer-ter-Vehn, *Phys. Rev. Lett.*, Vol. 79, 2686, 1997.
34. Boyd, T. J. M., M. S. Bawa'aneh, A. Tatarinov, and A. Dyson, *Proc. Int. Conf. Plas. Phys.*, 1714, Nagoya, 1996.

Plasmonic Effects in Dynamic Tunable Metal-dielectric Composites

Y. Y. Feng and M. Willatzen

Mads Clausen Institute for Product Innovation, NanoSyd, University of Southern Denmark, Denmark

Abstract— Sub-wavelength metal-dielectric-metal (MDM) composites support localized electromagnetic modes that are strongly confined in periodic structures. These modes can be controlled by tuning the shape of the composites as we demonstrated in previous works. Moreover, the Localized Surface Plasmon Resonance (LSPR) can be applied in new sensor applications. In this paper, we use the Finite-Difference Time-Domain (FDTD) method to study double-periodic metal-dielectric-metal composites and put emphasis to interactions with the dielectric cover layer. The numerical results demonstrate that variation of the refractive index (RI) of the cover layer as well as the layer thickness affect the LSPR response of the proposed MDM composite. The resonance-curve min/max groove period, the resonance-curve width, and the resonance-curve amplitudes from the MDM sensor output indicate that the proposed composite may find use as an effective sub-wavelength dielectric sensing optical component for photonic applications.

1. INTRODUCTION

The optical properties of metal films and composites with features of sub-micron dimensions are dominated by the surface plasmon modes and localized surface plasmon resonances. Light with appropriate frequency can excite spatially confined conduction electrons which undergo a coherent oscillation known as the Localized Surface Plasmon Resonance (LSPR) [1]. The spectral position and width of the LSPR is determined by the geometry of the fine structure, the dielectric functions of both the assay and surrounding media, inter-structure interactions and polarization of the light [2].

LSPR has been exploited in many sensing applications [3, 4], especially with triangular silver nano-particle arrays and detection of spectra shift [5, 6]. It has unique advantages compared to surface plasmon resonance (SPR) [7, 8], such as the *Kretschmann* SPR arrangement. First, the LSPR spectroscopy enables the development of large-scale sensing arrays composed of solid detectors that enable real-time, parallel monitoring of multiple species in chemical sensing or biotest. The LSPR sensing area is bigger than the SPP sensing area. The SPP sensing area is limited by several square micrometers due to the wavelength-dependent lateral propagation length of SPP [9]. Secondly, there is no need for automated goniometer angle detection or imaging devices as compared to the *Kretschmann* SPR arrangement. It is ideal for instrument applications in field portable or point-of-service medical diagnostic applications with UV-vis extinction spectroscopy in transmission or reflection geometry.

Most of the LSPR sensor progress are achieved with metal-particle array. It is well established that the peak extinction wavelength is associated with size, shape, inter-particle spacing, and dielectric properties. There are several LSP-based sensing mechanisms that enable the transduction of macromolecular or chemical binding events into LSP determined optical responses as summarized by Haes and Van Duyne [9], such as: (1) resonant Rayleigh scattering, (2) nano-particle aggregation, (3) charge-transfer interaction at nano-particle surfaces, (4) local refractive index changes. To extend the LSP applications, the LSPR can be excited with confined fields by different geometries other than particles. These structures can be mass produced by Nanoimprinting techniques with polymers [10]. In this work, we examine the polymer-metal film (MDM) composite [11, 12] and aim to find new sensing mechanisms.

2. DESIGN AND MODEL

Compared to metal particle based LSPR sensors, we consider the new (Metal-Dielectric-Metal Localized Surface Plasmon Resonance) MDM-LSPR with dielectric overlay as a survey for potential sensor approach. A MDM structure is comprised of periodic arrays of grooved dielectric material (e.g., flexible polymer film, poly-dimethylsiloxane (PDMS)) with thin metal films (See Figure 1). The tunable optical response with PDMS based material and MDM have been discussed in previous publications [12, 13].

With the MDM, the profile of the Gaussian-shaped narrow-grooves is defined by the total film thickness t , Gaussian-shaped groove depth d , the array period L , and the Gaussian full width at half maximum (FWHM) w . The parameters for the MDM structure are: $t = 300$ nm, $d = 50$ nm, $w =$

10 nm and metal-layer thickness 50 nm. The simulation is carried out with an in-house implemented FDTD package. This package applies periodic boundary conditions to simulate plasmonic structures with infinite periods in a unit cell (See Figure 1). The periodic boundary condition is implemented following the *Direct Field Methods* with *sine-cosine techniques* [14]. The metal dispersion is modeled employing a *Drude* dispersion model (See Equation (1)), and the auxiliary differential equation, with the *Drude* model addressed following the ADE-FDTD technique [14], is applied to model the *p*-polarized light interaction with the metal. Hence:

$$\varepsilon(\omega) = 1 + \frac{i\tau\omega_p^2}{\omega(1 - i\omega\tau)}. \quad (1)$$

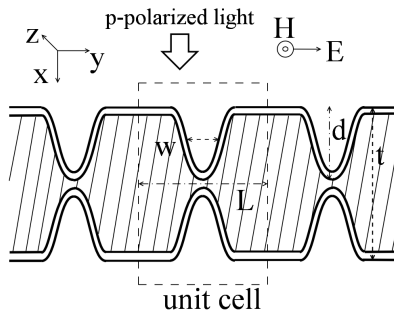


Figure 1: MDM structure.

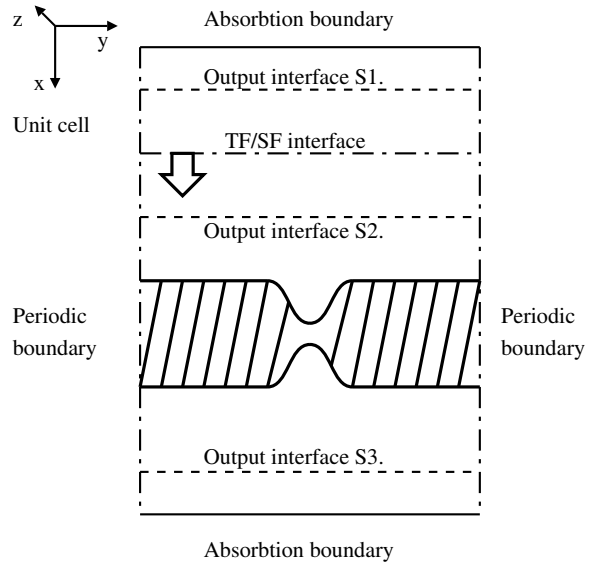


Figure 2: MDM structure.

The silver dielectric function in this work is described by the Drude model. For silver at room temperature we use the parameters [15]: $\omega_p = 1.32 \times 10^{16} \text{ s}^{-1}$ and $\tau = 1.45 \times 10^{-14} \text{ s}$. Liu et al. [16] applied similar values in their FDTD simulations with grooved metal film. A TFSF (Total Field Scatter Field) interface [14] introduces the incident plane wave (see Figure 2). In this paper, normal axis light incidence with *p*-polarization along the *x* axis is applied (i.e., E field parallel with the incident plane *x-y*). The normal direction intensity transmission coefficients and reflection coefficients are calculated by use of *time-averaged Poynting vectors* and energy fluxes.

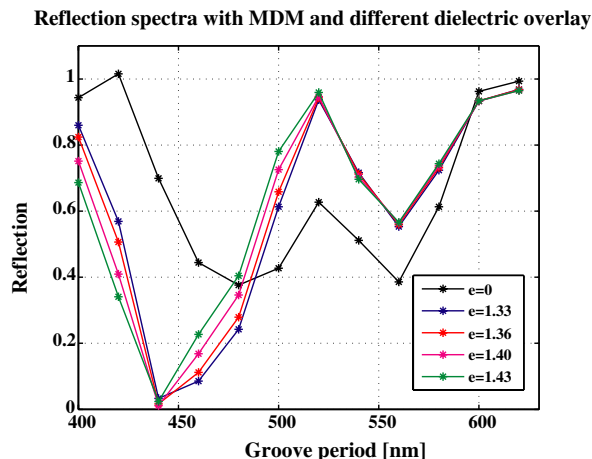


Figure 3: Reflection of MDM with cover layer RI variation.

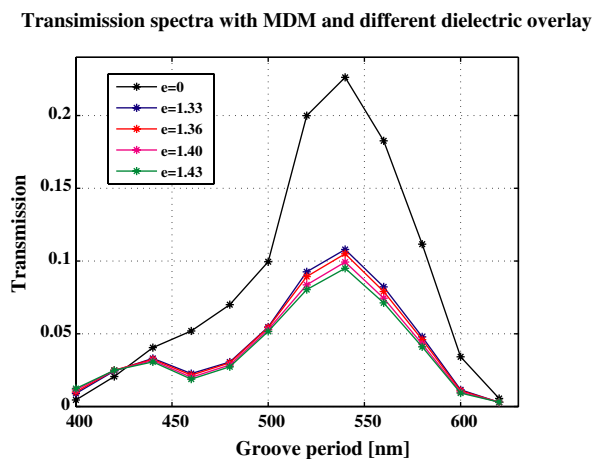


Figure 4: Transmission of MDM with cover layer RI variation.

3. SIMULATION AND ANALYSIS

For the FDTD simulation of the LSP with MDM, the grid FDTD cell size is chosen to be $1/300\lambda_{light}$. Hence, the grid consists of 1204×263 cells. The light wavelength is assigned as 630 nm. The FDTD time iteration is running for 15 period of cycles for a stable solution.

3.1. Response from Variation of Refractive Index:

The responses of different dielectric cover layer with the MDM from EM simulation are given in Figure (3 to 5) where 10 nm dielectric overlay with Refractive Index RI = 1.33, 1.36, 1.40 and 1.43 [RIU] are applied within the simulation. The figure indicates that the reflection, transmission, and extinction spectra with respect to the groove period L show responses with ambient RI changes.

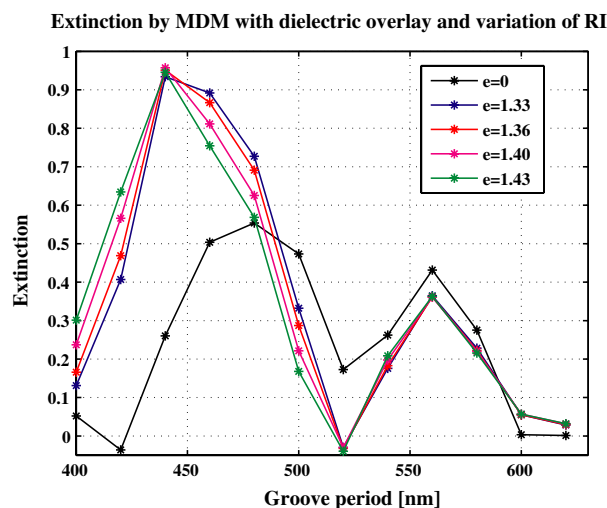


Figure 5: Extinction of MDM with cover layer RI variation.

It is interesting to plot the electrical field E_z as presented in Figure 6. The plots show the MDM exhibiting different resonant modes with its geometry. The tunneling of the light is at maximum when $L = 540$ nm (Figures 4 and 6(c)), where the groove in backside of MDM has its strongest resonance. The reflection minimum corresponds to a strong excitation of surface plasmons (SPs) for the top metal film (Figures 3 and 6(b)), while the extinction minimum corresponds to a strong

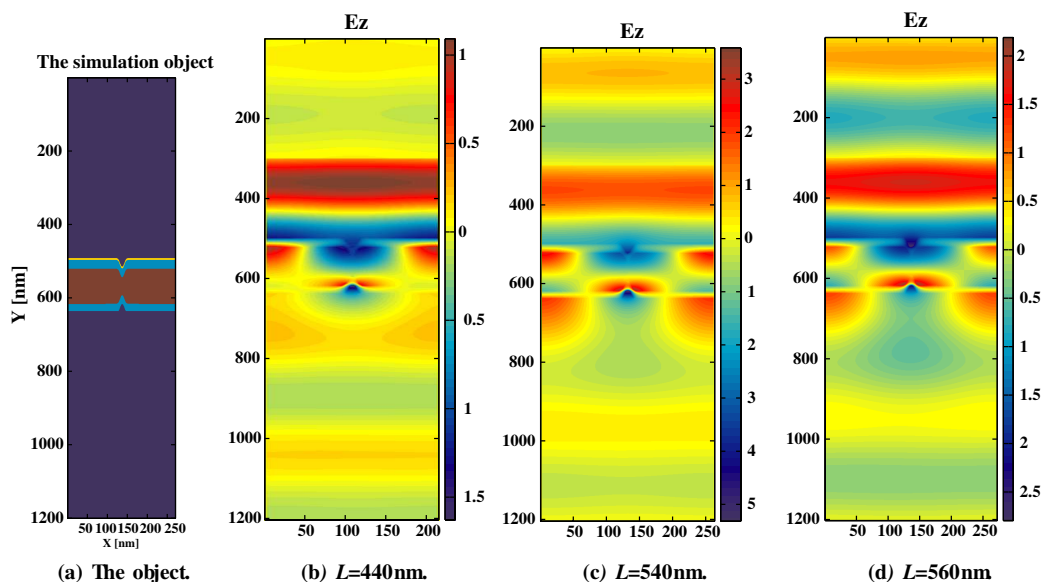


Figure 6: The E_z field plot with several groove periods L : 440, 540, and 560 nm. Figure 6(a) is the object for the simulation, where the MDM and dielectric overlay can be visualized (Dark red is the dielectric core with PDMS, light blue is the metal films and light yellow is the dielectric overlay (RI = 1.4, thickness = 10 nm).

excitation of SPs for the bottom metal film (Figures 5 and 6(d)). The confinement of the field inside the grooves can be clearly observed. Moreover, the plots show that the light tunneling shows dipole nature; the dipoles are oriented parallel to the x axis (Figure 1) and located between the groove pairs. The dipoles are coupled to each other in a chain along the MDM structure.

3.2. Response of Cover Layer with Different Refractive Index and Cover Layer Thickness

Figures (7 to 9) present the result of RI = 1.33, 1.40 and 1.43 with layer thickness of 5 nm, 10 nm and 15 nm, respectively. The figures demonstrate that the resonance periods shift toward shorter groove periods (460 nm with 5 nm thickness; 440 nm with 10 nm thickness and 420 nm with 15 nm thickness) with increased dielectric overlay thickness in the reflection spectrum and extinction spectrum (See Figures 7 and 9). The transmission spectrum does not show a shift with the groove period. It appears that the specific groove period for maximum light tunneling is governed by the MDM geometry instead of the ambient dielectric environment. The light-energy tunneling through the MDM-LSPR structure is decreased with more dielectric covering and increasing of RI (See Figure 8). The transmission spectrum shows a linear relationship between target thickness and transmission coefficients which is feasible for a quantitative representation. The sensitivity analysis for this approach will be present in future publications.

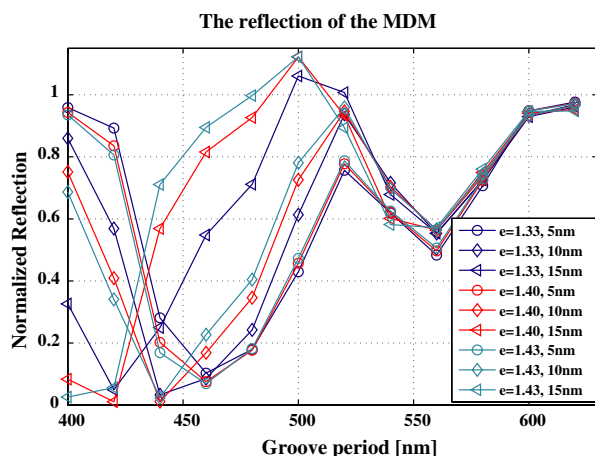


Figure 7: Reflection of MDM with cover layer RI variation.

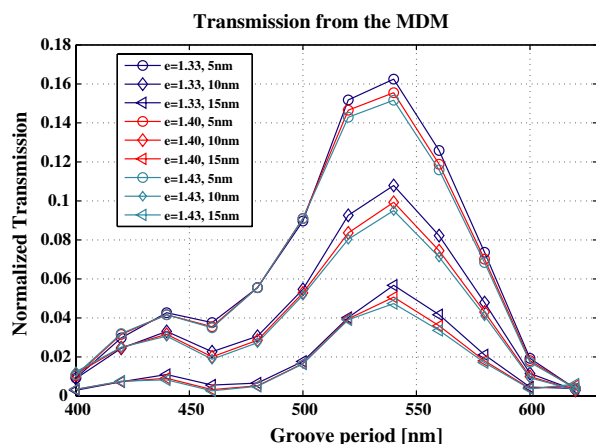


Figure 8: Transmission of MDM with cover layer RI variation.

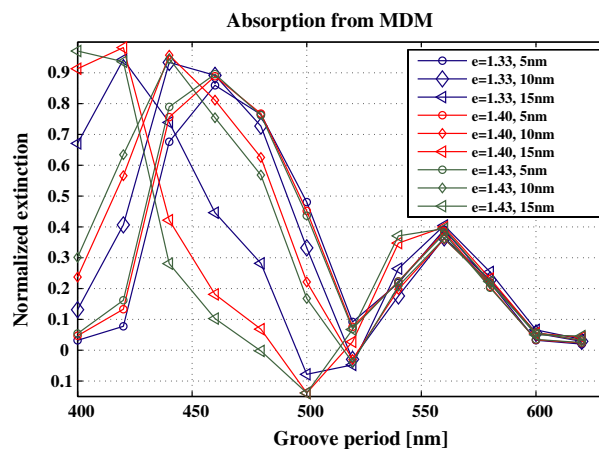


Figure 9: Absorption of MDM with cover layer RI variation.

4. CONCLUSION

We demonstrate the possibilities for sensing of RI variations and overlay changes based on MDM which can be used in chemical or bio-binding sensor applications. Compared to LSPR design based on noble metal particles, this MDM-LSPR approach has some particular advantages. Firstly, the MDM-LSPR based on grating periods works for monochromatic light such as a single LED or laser

diode. There is no demand for white-light and wavelength dispersion with a spectrograph setup. Cheap and compact design may thus be obtained. Secondly, the MDM-LSPR does not demand complex substrate patterns as in the case for nano-particle LSPR with NSL [17] and might be suitable for polymer-based device [10]. This allows possibilities for mass-production and low-cost applications. Thirdly, the principle may bring other applications in nano-photonics design as a component with tunable LSP composite [18]. Given our present knowledge with LSP design [5, 9], the tunable MDM-LSPR is a new approach for LSPR sensor and structure tuned composite. We hope it can bring new ideas for nano-photonics and sensor designs.

ACKNOWLEDGMENT

We would like to thank the support from Mads Clausen Institute for Product Innovation, NanoSyd, University of Southern Denmark.

REFERENCES

1. Murray, W. A., S. Astilean, and W. L. Barnes, "Transition from localized surface plasmon resonance to extended surface plasmon-polariton as metallic nanoparticles merge to form a periodic hole array," *Physical Review B*, Vol. 69, 165407, 2004.
2. Kreibig, U. and M. Vollmer, *Optical Properties of Metal Clusters*, Springer, 1995.
3. Okamoto, T., I. Yamaguchi, and T. Kobayashi, "Local plasmon sensor with gold colloid monolayers deposited upon glass substrates," *Opt. Lett.*, Vol. 25, 372–374, 2000.
4. Haes, A. J. and R. P. V. Duyne, "Nanoscale optical biosensors based on localized surface plasmon resonance spectroscopy," *Metallic Nanostructures and Their Optical Properties*, N. J. Halas, ed., *Proceedings of the SPIE*, Vol. 5221, 47, Plasmonics 5221, 2003.
5. Hutter, E. and J. H. Fendler, "Exploitation of localized surface plasmon resonance," *Advanced Materials*, Vol. 16, 1685–1706, 2004.
6. Zhao, J., X. Zhang, C. R. Yonzon, A. J. Haes, and R. P. V. Duyne, "Localized surface plasmon resonance biosensors," *Nanomedicine*, Vol. 1, No. 2, 219–228, 2006.
7. Xu, H. and M. Käll, "Modeling the optical response of nanoparticlebased surface plasmon resonance sensors," *Sens. Actuators B*, Vol. 87, 244–249, 2002.
8. Kreuzer, M. P., R. Quidant, G. Badenes, and M.-P. Marcoa, "Quantitative detection of doping substances by a localized surface plasmon sensor," *Biosensors and Bioelectronics*, Vol. 21, 1345–1349, 2006.
9. Haes, A. J. and R. P. V. Duyne, "A nanoscale optical biosensor: Sensitivity and selectivity of an approach based on the localized surface plasmon resonance spectroscopy of triangular silver nanoparticles," *J. Am. Chem. Soc.*, Vol. 124, 10599–10604, 2002.
10. Nishikawa, T., H. Yamashita, M. Nakamura, R. Hasui, T. Matsushita, and S. Aoyama, "Development of new localized surface plasmon resonance sensor with nanoimprinting technique," *Nano/Micro Engineered and Molecular Systems 2006. NEMS'06. 1st IEEE*, 2006.
11. Feng, Y., M. Willatzen, and N. L. Andersen, "Modeling localized surface plasmons in light tunneling and new optical sensing approach," *the Proceedings of ACES 2007*, Verona, Italy, 2007.
12. Feng, Y., M. Willatzen, and N. L. Andersen, "Metal-dielectric composite optical structures with novel dynamic tunable localized surface-plasmonic effects," *Metamaterials II*, V. Kuzmiak, P. Markos, and T. Szoplik, eds., *Proceedings of the SPIE 6581*, 65810G, 2007.
13. Park, W. and J.-B. Lee, "Mechanically tunable photonic crystal structure," *Appl. Phys. Letters*, Vol. 85, 4845–4847, 2004.
14. Tovlove, A., *Computational Electromagnetic: Finite-Difference Time-Domain Method*, Artech House, Boston, 2005.
15. Tan, W. C., T. W. Preist, and R. J. Sambles, "Resonant tunneling of light through thin metal films via strong localized surface plasmons," *Phy. Rev. B*, Vol. 62, No. 16, 11134–11138, 2000.
16. Liu, W. C. and D. P. Tsai, "Optical tunneling effect of surface plasmon polaritons and localized surface plasmon resonance," *Phys Rev. B*, Vol. 65, 155423, 1–6, 2002.
17. Malinsky, M. D., K. L. Kelly, G. C. Schatz, and R. P. V. Duyne, "Chain length dependence and sensing capabilities of the localized surface plasmon resonance of silver nanoparticles chemically modified with alkanethiol self-assembled monolayers," *J. Am. Chem. Soc.*, Vol. 123, 1471–1482, 2001.
18. Lèvêque, G. and O. J. Martin, "Tunable composite nanoparticle for plasmonics," *Optics Letters*, Vol. 31, 2750–2752, 2006.

Wave Scattering by Multi-valued Random Surfaces

Valerian I. Tatarskii

Radio-Hydro-Physics, LLC, USA

Abstract— We consider a scattering theory for multi-valued and multi-connected rough surfaces, which cannot be described by the conventional equation of the type $z = \zeta(x, y)$. Both Dirichlet and Neumann problems are analyzed. Starting with the Green's theorem we obtained representation of scattered field, the surface integral equation, and the extinction theorem for such surfaces. In contrast to conventional theory, these equations contain three random functions $x = x(u_1, u_2)$, $y = y(u_1, u_2)$, and $z = z(u_1, u_2)$, where u_1 and u_2 are the parameters describing the surface. The Kirchhoff approximation and the first Born approximation are derived and a general relation between these approximation was found. All final results are presented in the form of surface integrals, which are independent of choosing parameterization of surface.

1. INTRODUCTION

The conventional theory of wave scattering by random surfaces is developed for single-valued surfaces that may be described by the equation $z = \zeta(x, y)$. But some environmental and artificial random surfaces have more complicated structure, including multi-valued and multi-connected surfaces. As examples we can mention a water surface covered by foam or porous body. It is known that the scattering cross-section from a single-valued random surface in the first Born approximation is proportional to the surface spatial spectrum. But a priori it is unclear, how to define the spectrum of multi-valued surface. Thus, to analyze a wave scattering by multi-valued surfaces, it is necessary to describe such surfaces by more general manner, using the parametric equations of the type $\mathbf{R} = \mathbf{R}(u_1, u_2)$ where $\mathbf{R} = \{x, y, z\}$. In this paper, we use the general parametric form of surface equation. Assuming that the random surface may include multi-valued and isolated parts (such as air bubbles in water or water drops in air) we derive some basic equations for describing wave scattering: representation of scattered field in terms of surface sources, surface sources integral equation, and extinction theorem, both for Dirichlet and Neumann boundary conditions. We considered two approximate methods to solving these problems: Perturbation theory and Tangent Plane (Kirchhoff) approximation. The perturbation theory uses a small parameter, describing deviation of surface from a plane. This parameter is used for expansion both geometric parameters (surface metric tensor) and scattering parameters. The Kirchhoff approximation uses the doubled incident field or doubled normal derivative of the incident field at the surface as source functions. The results depend on the statistical properties of all three random functions $x(u_1, u_2)$, $y(u_1, u_2)$, and $z(u_1, u_2)$, i.e., on their joint probability density function and cross-correlation functions (spectra).

2. GEOMETRY OF MULTI-VALUED SURFACES

The multi-valued surfaces must be described by a parametric equations of the type

$$\Sigma : \mathbf{R} = \mathbf{R}(u_1, u_2) = \mathbf{R}(\mathbf{u}), \quad (1)$$

where $\mathbf{R} = \{x, y, z\} = \{\mathbf{r}, z\}$. Two (non-normalized) tangential to the surface vectors are defined by the equations

$$\bar{\tau}_\alpha(\mathbf{u}) = \frac{\partial \mathbf{R}(\mathbf{u})}{\partial u_\alpha}, \quad \alpha = 1, 2. \quad (2)$$

Four scalar products

$$g_{\alpha\beta}(\mathbf{u}) \equiv (\bar{\tau}_\alpha(\mathbf{u}) \cdot \bar{\tau}_\beta(\mathbf{u})), \quad \alpha, \beta = 1, 2 \quad (3)$$

form the metric tensor of surface. The vector product $[\bar{\tau}_1 \times \bar{\tau}_2]$ is a vector, which is perpendicular to the surface, and its modulus is equal to the area of the parallelogram based on vectors $\bar{\tau}_1$ and $\bar{\tau}_2$. It follows from this definition that the infinitesimally small element of the surface area $d\Sigma$ is determined by the formula

$$d\Sigma = \sqrt{g(\mathbf{u})} d^2u, \quad g(\mathbf{u}) = \det g_{\alpha\beta} = |g_{11}g_{22} - g_{12}^2|, \quad d^2u = du_1 du_2, \quad (4)$$

and the unit normal to the surface vector is determined by the formula

$$\mathbf{n}(\mathbf{u}) \equiv \frac{[\bar{\tau}_1 \times \bar{\tau}_2]}{||[\bar{\tau}_1 \times \bar{\tau}_2]||} = \frac{[\bar{\tau}_1 \times \bar{\tau}_2]}{\sqrt{g}}. \quad (5)$$

3. RANDOM MULTI-VALUED SURFACES

Now we consider random surfaces. In the case of single-valued surfaces the function $z = \zeta(\mathbf{r})$ is a random function of two independent variables x, y . It is known from the theory of rough-surface scattering from single-valued surfaces of the type $z = \zeta(x, y)$ that in the first Born approximation the scattering cross-section is proportional to the spatial spectrum of surface, which is the Fourier transform of the correlation function $\langle \zeta(\mathbf{r}')\zeta(\mathbf{r}'') \rangle$.¹ But in the case of multi-valued surfaces such function does not exist (because it is unclear, which of multiple values of a multi-valued function we must use) and it is unclear in advance, which quantity will replace the spectrum. For the Kirchhoff and small-slope approximations the scattering cross-sections are determined by the characteristic functions of the type $\langle \exp\{iq[\zeta(\mathbf{r}') - \zeta(\mathbf{r}'')]\} \rangle$ and this function also does not exist for multi-valued surfaces. Because of this, it is necessary to consider the rough-surface scattering by multi-valued surfaces from the beginning, starting with the first principles.

In the case of random multi-valued surfaces all 3 functions $x(\mathbf{u})$, $y(\mathbf{u})$, and $z(\mathbf{u})$ are random single-valued functions. They describe three random single-valued surfaces over the plane (u_1, u_2) . If these functions are Gaussian random functions,² they are completely determined by the first and second moments.

$$\langle \mathbf{R}(\mathbf{u}) \rangle = \bar{\mathbf{R}}(\mathbf{u}), \quad \langle \tilde{R}_i(\mathbf{u}') \tilde{R}_j(\mathbf{u}'') \rangle \equiv B_{ij}(\mathbf{u}', \mathbf{u}''), \quad \text{where} \quad \tilde{\mathbf{R}}(\mathbf{u}) \equiv \mathbf{R}(\mathbf{u}) - \bar{\mathbf{R}}(\mathbf{u}). \quad (6)$$

If these functions are non-Gaussian, their full description includes the infinite number of highest moments or cumulants.

Some examples of surfaces described by the parametric equations are shown below in Figures 1 and 2:

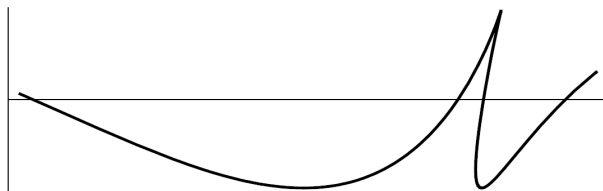


Figure 1: The profile described by equations $x(\mathbf{u}) = u + 0.000365 \sin(1000\pi u)$, $z = 0.000365 \cos(2400\pi u)$.

Taking into account more Fourier harmonics in $x(\mathbf{u})$, $y(\mathbf{u})$, and $z(\mathbf{u})$ than in Figure 1 makes it possible to model a pseudo-chaotic surface. An example of such modeling is presented in the Figure 2:



Figure 2: Modeling of pseudo-chaotic surface. Each of $x(\mathbf{u})$ and $z(\mathbf{u})$ contains 5 Fourier harmonics.

Physically such complicated surfaces may model, for example, appearance of foam, bubbles or drops near the air-water interface.

Considering the perturbation theory of wave scattering, we will work with the special class of functions $\mathbf{R}(\mathbf{u})$, which have the form

$$x(\mathbf{u}) = u_1 + \varkappa \xi(\mathbf{u}), \quad y(\mathbf{u}) = u_2 + \varkappa \eta(\mathbf{u}), \quad z(\mathbf{u}) = \varkappa \zeta(\mathbf{u}). \quad (7)$$

Here, \varkappa is a small parameter $|\varkappa| \ll 1$. In spite of \varkappa is small, the surface, described by (7) may be multi-valued. If the function $\zeta(\mathbf{u})$ is very steep near the point \mathbf{u}_0 , even very small displacement of

¹The angle bracket $\langle \dots \rangle$ denotes the statistical averaging.

²The random function $f(t)$ is Gaussian if for any N the joint PDF for the set $\{f(t_1), f(t_2), \dots, f(t_N)\}$ is a N -dimensional Gaussian distribution.

x or y may lead to multi-valuity of surface. The example of multi-valued profile for $\varkappa = 0.000365$ was shown above in Figure 1.

In the following we assume that the equation $\mathbf{R} = \mathbf{R}(\mathbf{u})$ describes the entire surface Σ , including all its isolated parts.

4. BASIC SCATTERING EQUATIONS

By the usual method it is easy to derive the basic equations for the scattering problem. These equations, if written in the parameterization-independent form of surface integrals, have the same form as in the case of single-valued surfaces. It is possible to derive the representations for the scattered field, the surface integral equation, and the extinction theorem.

For the Dirichlet problem the resulting equations in terms of surface source $F(\mathbf{R})$ (which is a normal derivative of the field at the surface) have the form

$$E_{sc}(\mathbf{R}) = \iint_{\Sigma} G_0(\mathbf{R}, \mathbf{R}_{\Sigma}) F(\mathbf{R}_{\Sigma}) d\Sigma; \quad \text{arbitrary } \mathbf{R}; \quad \text{scattered field} \quad (8a)$$

$$E_{inc}(\mathbf{R}) + E_{sc}(\mathbf{R}) = 0; \quad \mathbf{R} \in M_2; \quad \text{extinction theorem} \quad (8b)$$

$$E_{inc}(\mathbf{R}_{\Sigma}) + E_{sc}(\mathbf{R}_{\Sigma}) = 0; \quad \mathbf{R}_{\Sigma} \in \Sigma; \quad \text{surface integral equation.} \quad (8c)$$

Here, $G_0(\mathbf{R}, \mathbf{R}_{\Sigma})$ is a free-space Greens function. The unknown function $F(\mathbf{R})$ must be determined either from the extinction theorem (8b) or from the surface integral Equation (8c).

For the Neumann problem, the function F_0 (the normal derivative of G_0 at the surface) is known but the field $E(\mathbf{R}_{\Sigma})$ must be determined either from the extinction theorem (9b) or from the surface integral Equation (9c).

$$E_{sc}(\mathbf{R}) = - \iint_{\Sigma} F_0(\mathbf{R}, \mathbf{R}_{\Sigma}) E(\mathbf{R}_{\Sigma}) d\Sigma; \quad \text{arbitrary } \mathbf{R}; \quad \text{scattered field} \quad (9a)$$

$$E_{sc}(\mathbf{R}) + E_{inc}(\mathbf{R}) = 0; \quad \mathbf{R} \in M_2; \quad \text{extinction theorem} \quad (9b)$$

$$E(\mathbf{R}_{\Sigma_0}) = 2E_{inc}(\mathbf{R}_{\Sigma_0}) + 2 \iint_{\Sigma} E(\mathbf{R}_{\Sigma}) F_0(\mathbf{R}_{\Sigma_0}, \mathbf{R}_{\Sigma}) d\Sigma; \quad \mathbf{R}_{\Sigma_0} \in \Sigma; \quad \text{surface integral equation.} \quad (9c)$$

In (8) and (9) the value $E_{inc}(\mathbf{R})$ is the incident wave.

Equations (8) and (9) take a simple form if written in terms of the scattering amplitude, which is determined as

$$S_{\pm}^{(D)}(\mathbf{q}, z) = \frac{k}{8i\pi^2} \iint \exp\{-i\mathbf{q}\mathbf{r}(\mathbf{u}) + i\nu(q)[|z - z(\mathbf{u})| \mp z]\} F(\mathbf{R}(\mathbf{u})) \sqrt{g(\mathbf{u})} d^2u \quad (10)$$

for the Dirichlet problem and as

$$S_{\pm}^{(N)}(\mathbf{q}, z) = - \iint \frac{k\mathbf{n}(\mathbf{u})}{8\pi^2} \left(\mathbf{q} + \mathbf{e}_3 \nu(q) \frac{z(\mathbf{u}) - z}{|z(\mathbf{u}) - z|} \right) E(\mathbf{R}(\mathbf{u})) \\ \times \exp\{i\mathbf{q}\mathbf{r}(\mathbf{u}) + i\nu(q)[|z(\mathbf{u}) - z| \mp z]\} \sqrt{g(\mathbf{u})} d^2u \quad (11)$$

for the Neumann problem (we denote \mathbf{e}_3 the vertical unit vector). If we take the upper sign in $S_{\pm}^{(D, N)}(\mathbf{q}, z)$, dependence on z vanish for $z > \max z(\mathbf{u})$. If we take the lower sign, dependence on z vanish for $z < \min z(\mathbf{u})$. In (10) and (11) \mathbf{q} denotes the horizontal projection of a wave vector and $\nu(q) = \sqrt{k^2 - q^2}$ is the vertical component of a wave vector.

5. KIRCHHOFF APPROXIMATION FOR THE SCATTERED FIELD

For the Neumann problem, in the Kirchhoff approximation we neglect the integral term in (9c) and set $E(\mathbf{R}_{\Sigma_0}) = 2E_{inc}(\mathbf{R}_{\Sigma_0})$. Substituting this value in (9a) it is possible to obtain, in terms of the scattering amplitude $S_{+}^{(N)}$,

$$S_{+}^{(N, K)}(\mathbf{k}_{sc}, \mathbf{k}_{inc}) = - \frac{k\mathbf{k}_{sc}\mathbf{Q}(\mathbf{k}_{inc} - \mathbf{k}_{sc})}{4\pi^2} \quad (12)$$

where we denote $\mathbf{k}_{sc} = \mathbf{q}_{sc} + \mathbf{e}_3\nu(q_{sc})$, $\mathbf{k}_{inc} = \mathbf{q}_{inc} - \mathbf{e}_3\nu(q_{sc})$ and

$$\mathbf{Q}(\mathbf{k}_{inc} - \mathbf{k}_{sc}) = \iint_{\Sigma} \exp\{i(\mathbf{k}_{inc} - \mathbf{k}_{sc})\mathbf{R}_{\Sigma}\} \mathbf{n}(\mathbf{R}_{\Sigma}) d\Sigma. \quad (13)$$

For the Dirichlet problem in the Kirchhoff approximation we have

$$F(\mathbf{R}_{\Sigma_0}, \mathbf{R}_0) = 2 \frac{\partial G_0(\mathbf{R}_0, \mathbf{R}_{\Sigma_0})}{\partial n(\mathbf{R}_{\Sigma_0})}$$

and by the similar way it is possible to obtain

$$S_+^{(D,K)}(\mathbf{k}_{sc}, \mathbf{k}_{inc}) = \frac{k\mathbf{k}_{inc}\mathbf{Q}(\mathbf{k}_{inc} - \mathbf{k}_{sc})}{4\pi^2}. \quad (14)$$

It follows from (12) and (14) that in the back-scattering case, for which $\mathbf{k}_{sc} = -\mathbf{k}_{inc}$, the scattering amplitudes for the soft and rigid interfaces coincide:

$$S_+^{(D,K)}(-\mathbf{k}_{inc}, \mathbf{k}_{inc}) = S_+^{(N,K)}(-\mathbf{k}_{inc}, \mathbf{k}_{inc}) = \frac{k\mathbf{k}_{inc}\mathbf{Q}(2\mathbf{k}_{inc})}{4\pi^2}. \quad (15)$$

6. THE FIRST BORN APPROXIMATION

In this case, we consider the surface as close to plane and describe it by the Equation (7) where $|\varkappa| \ll 1$. We expand $g_{\alpha\beta}$ and the unknown quantities $F(\mathbf{R})$ and $E(\mathbf{R})$ in powers of \varkappa and obtain the equations of the zero-order and first-order in \varkappa . The resulting formulae for the Dirichlet scattering amplitude have the form

$$\varkappa S_+^{(D,1)}(\mathbf{q}) = 2i\varkappa k\nu(q_{inc})\nu(q)\hat{\zeta}(\mathbf{q} - \mathbf{q}_{inc}), \quad (16)$$

where $\hat{\zeta}(\mathbf{q})$ is the Fourier component of the $\zeta(\mathbf{u})$ with respect to \mathbf{u} :

$$\varkappa\hat{\zeta}(\mathbf{q}) = \frac{\varkappa}{4\pi^2} \iint \exp(-i\mathbf{q}\mathbf{u})\zeta(\mathbf{u})d^2u. \quad (17)$$

This formula looks similarly to the conventional result for single-valued surfaces, excluding a significant difference: (16) contains the Fourier component with respect to \mathbf{u} , whereas the conventional formula contains the Fourier component with respect to \mathbf{r} . The result given by the formula (17) depends on chosen parameterization. But it is possible to show that with the accuracy of $O(\varkappa^2)$ the value $\varkappa\hat{\zeta}(\mathbf{q})$ may be presented in the form of surface integral

$$\varkappa\hat{\zeta}(\mathbf{q}) = \frac{1}{4\pi^2} \iint \exp\{i(\mathbf{k}_{inc} - \mathbf{k}_{sc})\mathbf{R}_{\Sigma}\} \mathbf{n}(\mathbf{R}_{\Sigma}) \cdot \mathbf{R}_{\Sigma} d\Sigma \quad (18)$$

as follows:

$$\varkappa\hat{\zeta}(\mathbf{q}_{sc} - \mathbf{q}_{inc}) = \varkappa\hat{\zeta}(\mathbf{k}_{inc} - \mathbf{k}_{sc}) + O(\varkappa^2). \quad (19)$$

The integral in the right-hand side of (18) is independent of chosen parameterization. Substituting (19) in formula (16) we obtain

$$\varkappa S_+^{(D,1)}(\mathbf{q}_{sc}) = 2ik\nu(q_{inc})\nu(q_{sc})\varkappa\hat{\zeta}(\mathbf{k}_{inc} - \mathbf{k}_{sc}). \quad (20)$$

We call this approximate formula modified first Born approximation. The exponent in (18) contains the terms of the order of \varkappa , which seems to be an excess of accuracy of calculations; but this is the only way to obtain the parameterization independent result.

The similar formula for the Neumann problem has the form

$$\varkappa S_+^{(N,1)}(\mathbf{q}_{sc}) = 2ik [k^2 - \mathbf{q}_{inc}\mathbf{q}_{sc}] \varkappa\hat{\zeta}(\mathbf{k}_{inc} - \mathbf{k}_{sc}) \quad (21)$$

7. RELATION BETWEEN THE KIRCHHOFF AND MODIFIED FIRST BORN APPROXIMATIONS

Let us compare the Kirchhoff approximate solutions and the modified first Born approximations. The Kirchhoff approximation is expressed in terms of $\mathbf{Q}(\mathbf{k}_{inc} - \mathbf{k}_{sc})$, whereas the modified first Born approximation is presented in terms of $\mathfrak{T}(\mathbf{k}_{inc} - \mathbf{k}_{sc})$.

Let us find a relation between $\mathbf{Q}(\mathbf{k}_{inc} - \mathbf{k}_{sc})$ and $\mathfrak{T}(\mathbf{k}_{inc} - \mathbf{k}_{sc})$. If we denote the scattering vector $\mathbf{k}_{inc} - \mathbf{k}_{sc} = \mathbf{K}$, it is easy to obtain from (18) and (13):

$$\operatorname{div}_{\mathbf{K}} \mathbf{Q}(\mathbf{K}) \equiv \sum_{i=1}^3 \frac{\partial Q_i(\mathbf{K})}{\partial K_i} = -i \iint_{\Sigma} \exp\{-i\mathbf{K}\mathbf{R}_{\Sigma}\} \mathbf{n}(\mathbf{R}_{\Sigma}) \mathbf{R}_{\Sigma} d\Sigma = -4i\pi^2 \mathfrak{T}(\mathbf{K}) \quad (22)$$

Thus,

$$\mathfrak{T}(\mathbf{K}) = \frac{i}{4\pi^2} \operatorname{div}_{\mathbf{K}} \mathbf{Q}(\mathbf{K}) \quad (23)$$

Formula (23) establishes a parametric relation between the Kirchhoff and the modified first Born approximations. Using (23) we may obtain the modified first Born approximation from the Kirchhoff approximation.

8. MEAN SCATTERING CROSS-SECTION

The mean scattering cross-section in the Kirchhoff approximation is proportional to $\mathfrak{Q}_{ij} = \langle Q_i(\mathbf{K}) Q_j^*(\mathbf{K}) \rangle$. From (13) we have

$$\mathfrak{Q}_{ij} = \iint_{\Sigma} d\Sigma \iint_{\Sigma} d\Sigma' \langle \exp [i\mathbf{K}(\mathbf{R}_{\Sigma} - \mathbf{R}'_{\Sigma})] n_i(\mathbf{R}_{\Sigma}) n_j(\mathbf{R}'_{\Sigma}) \rangle. \quad (24)$$

If \mathbf{R}_{Σ} is a Gaussian random variable, the mean value (24) will be determined by the following second moments:

$$\langle (\mathbf{R}_{\Sigma} - \mathbf{R}'_{\Sigma})_m (\mathbf{R}_{\Sigma} - \mathbf{R}'_{\Sigma})_l \rangle, \quad \left\langle (\mathbf{R}_{\Sigma} - \mathbf{R}'_{\Sigma})_m \left(\frac{\partial \mathbf{R}_{\Sigma}}{\partial u_{\alpha}} \right)_l \right\rangle, \quad \left\langle \left(\frac{\partial \mathbf{R}_{\Sigma}}{\partial u_{\alpha}} \right)_l \left(\frac{\partial \mathbf{R}'_{\Sigma}}{\partial u_{\beta}} \right)_m \right\rangle. \quad (25)$$

These moments include not only vertical elevations of surface, but also horizontal displacements. For non-Gaussian \mathbf{R}_{Σ} the highest cumulants also will be important.

Investigation of Pear-shaped Monopole Antenna

G. N. Ghvedashvili, D. G. Kakulia, K. N. Tavzarashvili, and T. L. Gogua
3 Chavchavadze Ave., Laboratory of Applied Electrodynamics, Tbilisi State University
Tbilisi 0128, Georgia

Abstract— The Pear-Shaped Monopole Antenna (PSMA) for Personal Communication Systems (PCS) presented together with a user-friendly program package for dielectric coatings antennas analysis. PSMA contains a Pear-Shaped metallic core covered by a thin dielectric layer. The proposed antenna utilizes the advantages of the simple design to matched antenna structure with feeding cable and free space. A special shape of metallic part helps to match it with feeding cable and dielectric layer keeps antenna size small. The Method of Auxiliary Sources (MAS) is used to study PSMA. Experimental data is provided for several PSMA configurations to validate the MAS results.

1. INTRODUCTION

The performance of Personal Communication Systems (PCS) directly depends on the quality of the antennas used. Besides very low input return loss over a large bandwidth, antennas must also comply with additional requirements imposed by geometrical, directional, and compatibility restrictions [1]. Specifically, PCS Antennas should be well matched with their feed and with free space, and they should exhibit wide-band characteristics. Also, they are desired to be as small as possible. Moreover, Antenna's radiation characteristics should satisfy the modern ecological and safety standards, i.e., Antenna is desired to have directed radiation for minimizing SAR in user head and should operate with low electromagnetic (EM) energy emitted by batteries [2]. That is why, research, development, and fabrication of new types of Antenna for PCS is an important technical, compatibility, ecological, and health safety problem.

In the following, Pear-Shaped Monopole Antenna (PSMA) is introduced to address most of the above mentioned problems. The Method of Auxiliary Sources (MAS) [5] is used as a numerical technique to simulate the PSMA radiation. Two types of antennas are considered: 1) axisymmetric PSMA that provides uniform radiation for non-directional applications and 2) directional PSMA. The near field distribution, radiation field pattern, and S11 are computed for both types of PSMA and experimental data is provided to validate the MAS.

2. ANTENNA MODEL AND SOLUTION

One of the promising, efficient and powerful ways to solve the above-mentioned problems is computer simulation of electromagnetic waves of promising Antenna types. Monopole antennas are fed by a coaxial line with an inner radius equal to the monopole radius. It is well known that although the larger monopole radius can improve the monopole performance, the simultaneous increase of feeding coaxial line radius leads to existence of higher order coaxial modes [3, 4]. Therefore it is common to feed monopole antennas by low-impedance coaxial lines that do not support higher order modes. However, this causes different practical problems, as it is difficult to match antennas at microwave frequencies to such low impedance lines. To overcome this problem, Al Badwaihy [3, 4] introduced a conical feed section between the monopole with larger radius and the feeding coaxial line with smaller radius. With this measure it was possible to improve the overall properties of the monopole. In the following work this idea is extended, so that the conical taper is now included in the antenna geometry and becomes a part of the radiating structure. This results in a Pear-Shaped structure of the antenna as illustrated in Fig. 1. While in [3] the monopole is limited to having a lower cone angle of 60 degrees and a radii ratio of $R/R_c = 0.5$, there is no limitation for the PSMA introduced in this paper. The metallic part of the PSMA is covered with a thin dielectric layer in order to decrease the Q-factor for broader operating bandwidth. Utilizing a high permittivity layer the antenna size may be reduced. For prototyping antennas dielectric materials with permittivity between 4 and 5 were used. Furthermore, to obtain directivity, a metallic strip line is introduced on one side of the PSMA dielectric layer (Fig. 1). A 50Ω transmission line is used to excite the monopoles and a metallic disk with 3 cm radius is used to avoid influence from the cable.

In [3] the MAS were proposed as numerical method that provides both computational efficiency and modeling versatility.

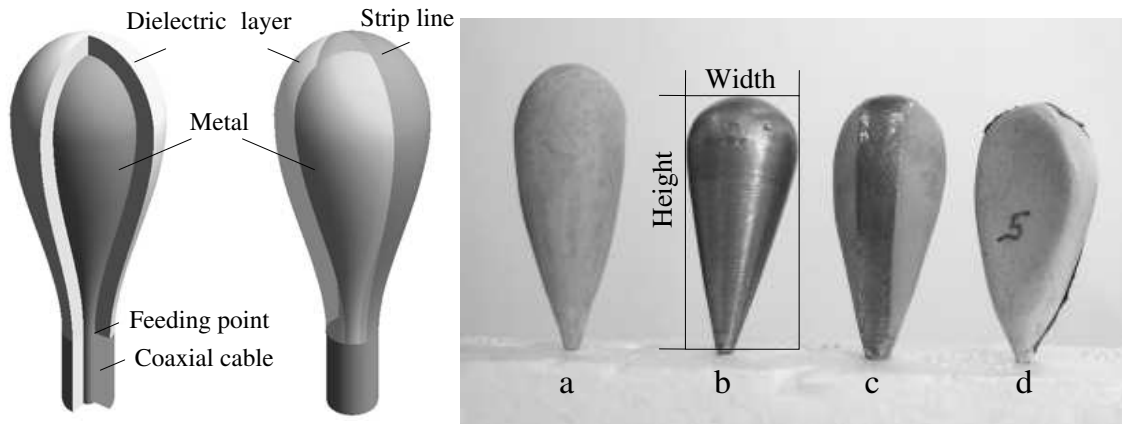


Figure 1: Antenna models and prototypes: Symmetrical and directed Pear-Shaped antenna.

The software package “Pear-Shaped Antenna Designer” was developed based on the MAS with a user-friendly interface that provides fast parametric optimization of the Antenna and the analysis of the Antenna together with the feeding cable. Management of this software does not require from the user a deep knowledge of mathematical apparatus and the employed solution method.

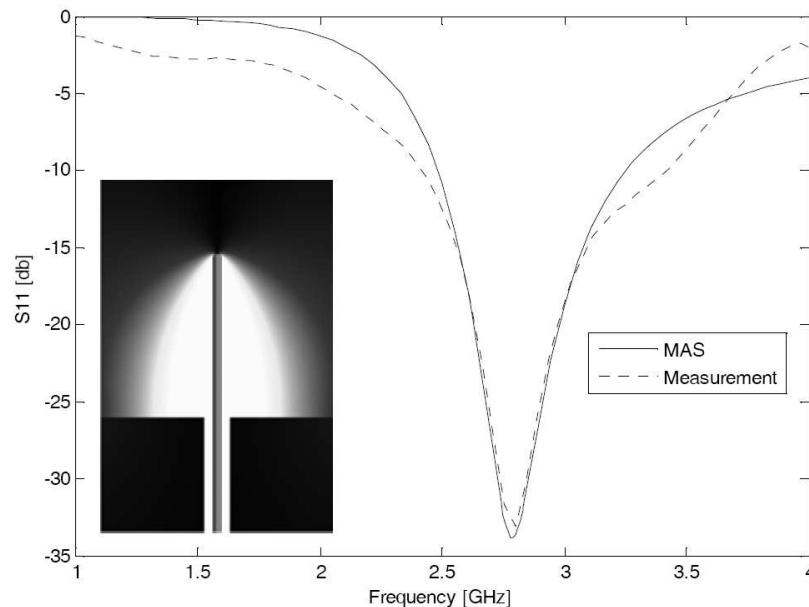


Figure 2: Return loss versus frequency for a single wire antenna. Experimental and numerical measurements. Monopole height = 2.8 cm.

3. RESULTS

The PSMA investigation considers first a simple monopole antenna model. A 2.8 cm high thin wire antenna is connected to a $50\ \Omega$ coaxial line as illustrated on Fig. 2. The numerical results as well as the measurements of S_{11} are shown in the frequency range of 1 to 4 GHz. Good agreement between MAS and measurements are obtained. It is well known that the size of a resonance antenna is comparable to the operating wavelength. For example, the first resonance of the thin wire antenna appears when its height equals a quarter of wavelengths. Thus, communication applications in the 0.9–1.8 GHz range the antenna height should be at least 6.5 cm. This is quite large for handset antennas, for example. To reduce the size of the antenna while keeping its electrical size constant, a high permittivity layer material can be used [6–8]. This causes matching problems between the feeding cable, the antenna, and free space due to the differences between wave impedances in the different media. One can alleviate this problem to a large extent by using materials with high

permittivity and high permeability that have the same wave impedance as in the coaxial line or the free space. Such materials can be made with composites of ferrites. This increases the freedom to design antennas with small size. Fig. 3 shows the return loss versus the frequency for different values of permittivity and permeability. From this result it is clear that even small antennas can operate at relatively low frequencies with good matching conditions.

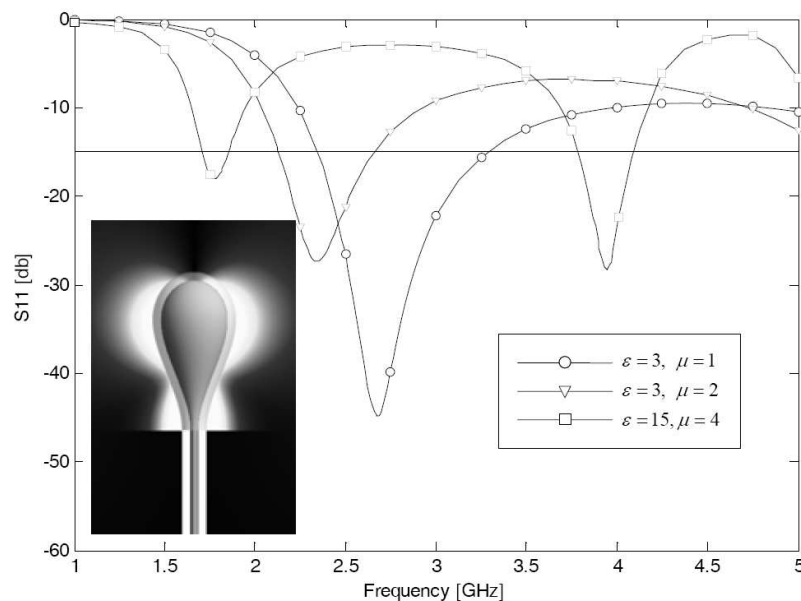


Figure 3: Return loss versus frequency for different values of the permittivity and permeability of the dielectric layer: $\epsilon = 3, \mu = 1$; $\epsilon = 3, \mu = 2$; $\epsilon = 15, \mu = 4$; near field distribution for $\epsilon = 15, \mu = 4$ at the $f = 4.18$ GHz. PSMA height = 2.7 cm, width = 1.5 cm.

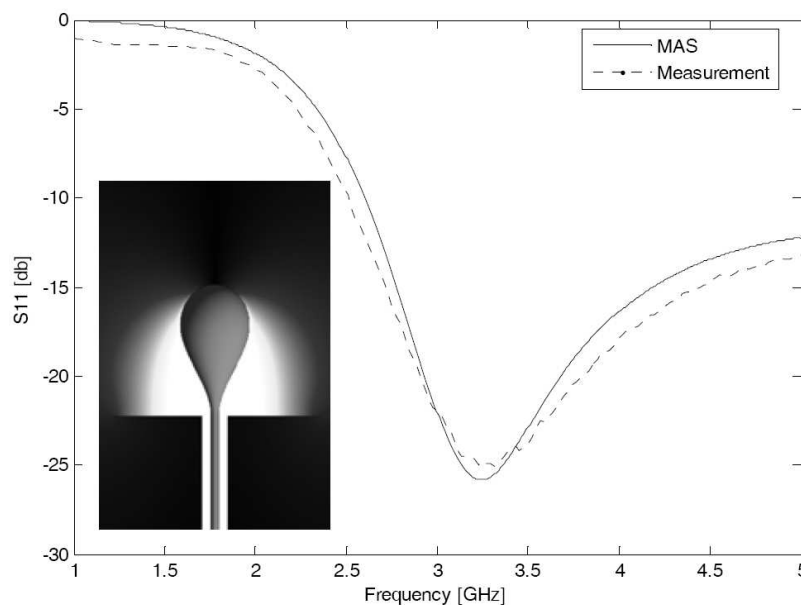


Figure 4: Return loss versus frequency. Experimental and numerical measurements. Antenna height — 2.3 cm, width — 1 cm, resonance frequency — 3.23 GHz.

Several Antenna prototypes were fabricated and characterized (Fig. 1, a, b, c, d), based on optimal geometrical and electrodynamic parameters obtained from the numerical experiments [6–8]. The measured return loss curves together with the corresponding numerical results are shown on Fig. 4 and Fig. 5 with corresponding near field distributions at the resonance frequency. Fig. 4 shows the measured and numerical return loss versus frequency for the 2.3 cm height Pear-Shaped Antenna

prototype without any dielectrical layer. The resonance frequency occurs at $f = 3.23$ GHz with a good matching condition. The impedance bandwidth, determined from -15 dB level is 46%. A good agreement is observed between the simulation and the measurement. Another picture (Fig. 5) shows the measured and numerical return loss for another 1.77 cm height prototype with dielectric layer. In this case resonance occurs at frequency $f = 3.95$ GHz. The impedance bandwidth, determined from 15-dB level is 38%. Also a good agreement is observed in this case between the simulation and the measurement.

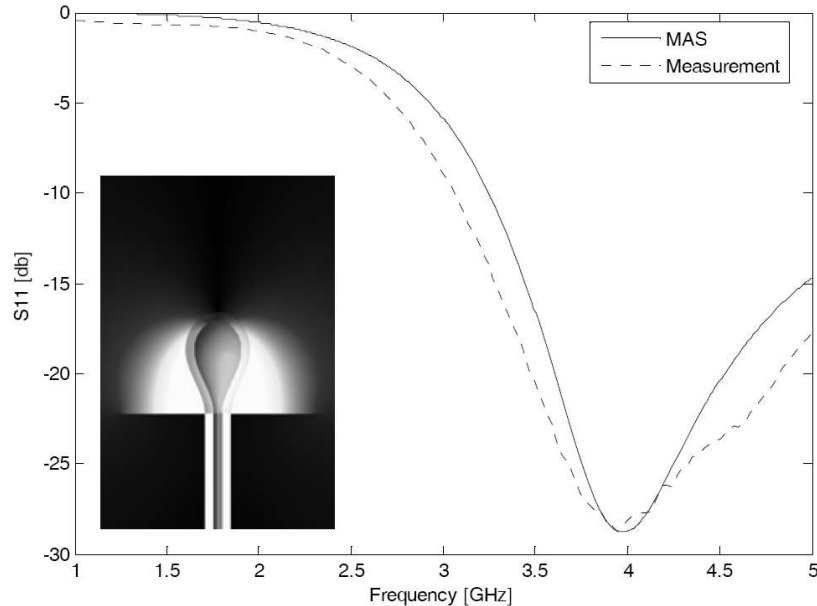


Figure 5: Return loss versus frequency. Experimental and numerical measurements. Antenna height — 1.77 cm, width — 1 cm, resonance frequency — 3.95 GHz.

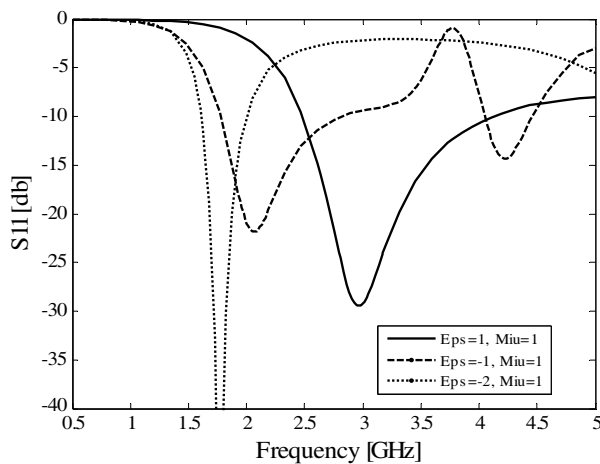


Figure 6: Return loss versus frequency for different values of the permittivity and permeability of the dielectric layer: $\epsilon = 1$, $\mu = 1$; $\epsilon = -1$, $\mu = 1$; $\epsilon = -2$, $\mu = 1$; PSMA height = 2.5 cm, width = 1.2 cm.

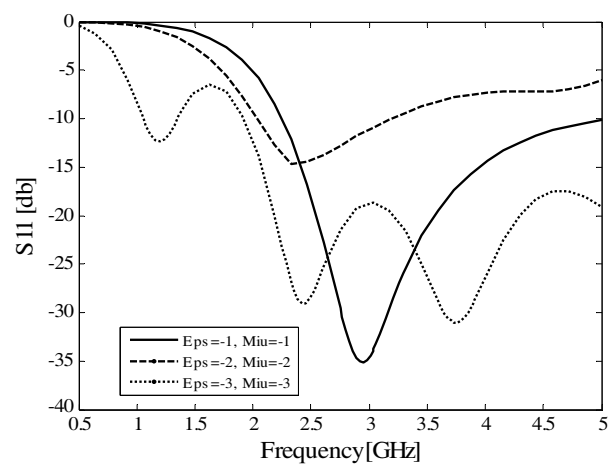


Figure 7: Return loss versus frequency for different values of the permittivity and permeability of the dielectric layer: $\epsilon = -1$, $\mu = -1$; $\epsilon = -2$, $\mu = -2$; $\epsilon = -3$, $\mu = -3$; PSMA height = 2.5 cm, width = 1.2 cm.

From the theoretical point of view it is interesting to investigate the performance of antenna made of materials with negative index of reflection. The theoretical aspects of such kind of materials were proposed by Prof. Veselago [9] and later the negative reflection was observed in some metamaterials [10]. We just try to use negative permittivity and permeability in order to see the behavior of PSMA antenna made with negative materials. Some preliminary results are shown on

Fig. 6 and Fig. 7 for different values of permittivity and permeability of PSMA dielectric layer.

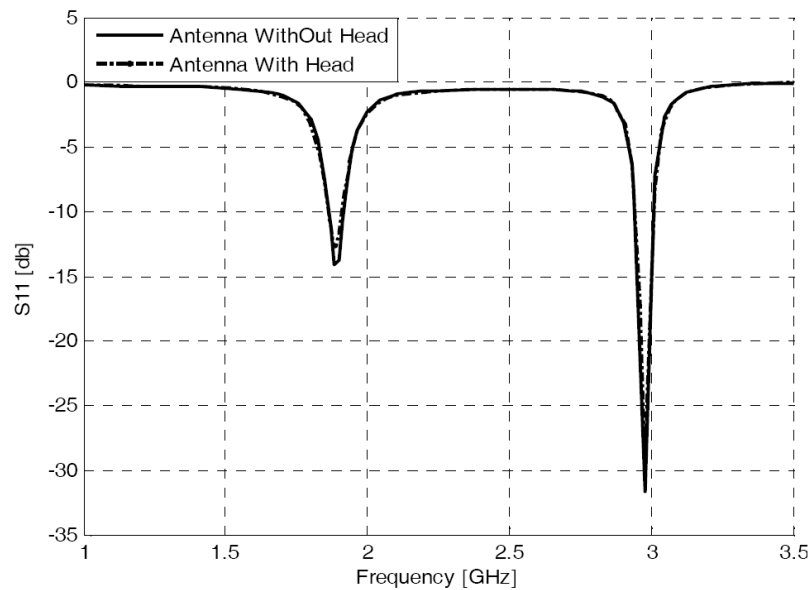


Figure 8: Return loss versus frequency for antenna field interaction with the user's head; Antenna height — 2.5 cm, width — 1 cm; without head: $f_1 = 1.9$ GHz, $f_2 = 976$ GHz; with head: $f_1 = 1.885$ GHz, $f_2 = 2.979$ GHz; head permittivity $\varepsilon = (30, 3)$.

Investigation of Antenna characteristics taking into consideration its field interaction with the User body has been performed to study variability and instability it brings to Antenna properties. On Fig. 8 presented return loss versus frequency for Antenna field Interaction with User's Head at the 5 cm distance from antenna; Resonance frequency and efficiency of Antenna significantly not changed, but radiation pattern and SAR distribution show that large portion of EM energy absorbed by User Head (Fig. 9).

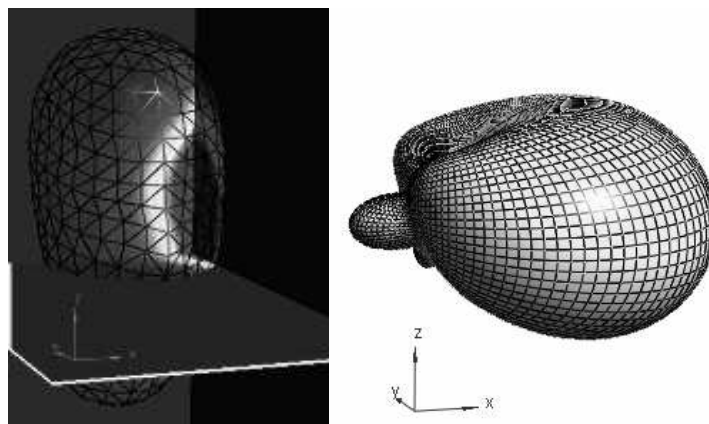


Figure 9: SAR distribution and radiation pattern at 1.885 GHz.

In many PCS devices it is important to have a directional antenna. For example, in mobile handsets it is important to avoid undesirable influence of the antenna radiation on the user [6–8]. Also it is not necessary to radiate energy uniformly in free space. It is sufficient to radiate energy in the direction of the receiver. There are also many other applications that require directional antennas. For this propose, the PSMA was modified by introducing a metallic strip that partially covers the dielectric layer of the PSMA (Fig. 1). The metallic strip changes the polarization of the radiated field partially and reflects some portion of the energy. As a result, the antenna becomes a directional radiator. The measured return loss for this PSMA prototype is presented in Fig. 10. According to measurements, the bandwidth is 16% at the -10 dB level and the resonance frequency is 3.0 GHz while the numerical calculation provides a bandwidth of 20% at -10 dB

level and resonance frequency at 2.7 GHz. One can see that there are certain differences between measured and simulated data: mainly, there is a shift of resonance frequency. It is due to the differences between computer model and experimental PSMA prototypes (caused, mainly, by the manufacturing inaccuracies of the prototypes built in our laboratory). The radiation patterns in two planes (XOZ and XOY planes) are shown in Fig. 11, illustrating directional behavior of this antenna.

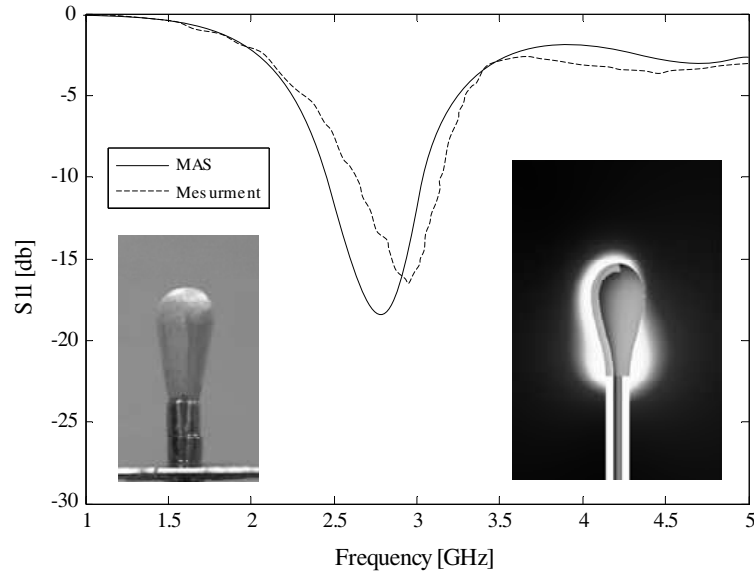


Figure 10: Return loss versus frequency. Measured bandwidth is 16% at 3.0 GHz while simulated bandwidth is 20% at 2.7 GHz; PSMA height = 2 cm; width = 0.9 cm; strip angular aperture = 180.

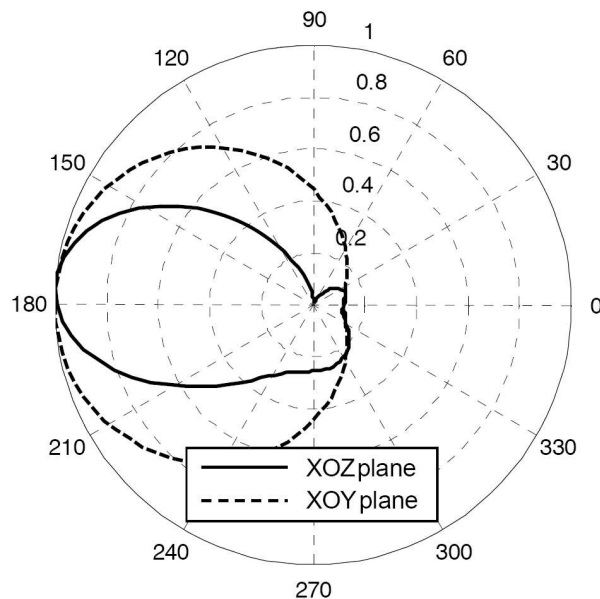


Figure 11: Radiation patterns in the XOY and XOZ planes at resonance frequency $f = 2.9$ GHz.

4. CONCLUSIONS

A class of Pear-Shaped Monopole Antennas (PSMA) covered by a thin dielectric layer has been introduced. Two types of PSMA antennas were considered 1) axisymmetric PSMA and 2) directional PSMA. A software package “PSMA Designer” was developed based on the MAS and applied to characterize the PSMA performance. Results of the simulations were presented in the frequency

range from 1 GHz to 5 GHz. Prototypes of several PSMA were fabricated and characterized. The measured results were found to be in reasonable good agreement with the simulations. “PSMA Designer” helps the antenna designer to simulate the operation of antennas in different environments, to study their EM characteristics, and to optimize the geometry of the antenna.

ACKNOWLEDGMENT

The designated project has been fulfilled by financial support of Georgian National Science Foundation (Grant #GNSF/ST06/4-016). Any idea in this publication is possessed by author and may not represent the opinion of Georgian National Science Foundation itself.

REFERENCES

1. Skrivervik, A. K., J.-F. Zurcher, O. Staub, and J. R. Mosig, “PCS antenna design: The challenge of miniaturization,” *IEEE Antennas and Propagation Magazine*, Vol. 43, No. 4, 12–27, August 2001.
2. Bernardi, P. and S. Pisa, “Specific absorption rate and temperature increases in the head of cellular-phone user,” *IEEE Trans. Microwave Theory Tech.*, Vol. 48, 1118–1126, 2001.
3. Al-Badwaih, K., “Duoconical monopole,” *Electron. Lett.*, Vol. 10, No. 10, 199–201, May 1974.
4. Al-Badwaih, K. and J. Yen, “Hemispherically capped thick cylindrical monopole with a conical feed section,” *IEEE Trans. on Antennas and Propagation*, Vol. 22, No. 3, 477–481, May 1974.
5. Zaridze, R., G. Bit-Babik, K. Tavzarashvili, N. Uzunoglu, and D. Economou, “Wave field singularity aspects large-size scatterers and inverse problems,” *IEEE Trans. on Antennas and Propagation*, Vol. 50, No. 1, 50–58, January 2002.
6. Ghvedashvili, G. N., G. G. Kajaia, G. S. Sapparishvili, and R. S. Zaridze, “Analyze of dielectric coated Personal Communication Systems (PCS) antenna and study of its field interaction with the user,” *Proceedings of 17th International Zurich Symposium on Electromagnetic Compatibility*, 517–520, Singapore, February 27–March 3, 2006.
7. Ghvedashvili, G. N., G. G. Kajaia, G. Sh. Sapparishvili, D. G. Kakulia, and R. S. Zaridze, “Numerical and experimental analysis of Pear-Shaped monopole antenna and study of its field interaction with the user,” *Proceedings of the 11th International Conference on Mathematical Methods in Electromagnetic Theory (MMET-2006)*, 115–117, Kharkiv, Ukraine, June 26–29, 2006.
8. Ghvedashvili, G. N., K. N. Tavzarashvili, D. G. Kakulia, and R. S. Zaridze, “Personal Communication Systems (PCS) antenna with managed radiation characteristics and study of its interaction with the user,” *Journal of Telecommunications and Radio Engineering*, Vol. 66, No. 14, 1265–1272, 2007.
9. Veselago, V. G., *Soviet Physics — Uspekhi*, Vol. 10, 509, 1968.
10. Pendry, J. B., A. J. Holden, D. J. Robbins, and W. J. Stewart, *IEEE Trans. Microwave Theory Tech.*, Vol. 47, 2075, 1999.

Design of Multiband Balanced Folded Dipole Antenna Based on a Dual-arm Structure for Mobile Handsets

D. Zhou, R. A. Abd-Alhameed, C. H. See, and P. S. Excell

Mobile and Satellite Communications Research Centre, University of Bradford
Bradford, West Yorkshire, BD7 1DP, UK

Abstract— In this paper, a balanced antenna for mobile handset applications with enhanced bandwidth performance, that covers four bands (GSM1800, GSM1900, UMTS and 2.4-GHz WLAN), is investigated. The antenna is a slot planar dipole with folded structure and a dual-arm on each monopole. A wide bandwidth planar balun is employed to feed the wideband balanced antenna from an unbalanced source. A prototype of the proposed antenna is fabricated and tested. The performance of the antenna is verified and characterized in terms of return loss, radiation patterns and power gain. The calculated and measured results show good agreement and also confirm good wideband characteristics for the proposed antenna with multiband operation.

1. INTRODUCTION

Over the recent years, the need to expand the bandwidth of antennas in mobile handheld devices follows from the ever-increasing data rates, and hence spectrum requirements, of mobile devices. The implementation of antenna designs causing minimised coupling with the human head and hand and hence minimised SAR would be attractive to many consumers, thus increasing the market acceptance of devices using such antennas.

A good candidate is a balanced antenna [1]. An antenna with symmetrical structure that is fed with balanced currents to make it electrically symmetrical is said to be a balanced antenna. Dipoles and loops are the most commonly encountered balanced antennas [2, 3]. In this type of antenna, balanced currents only flow on the antenna element, thus dramatically reducing the effect of current flow on the ground plane. As a result, balanced antennas should have good efficiency and more important to maintain their performance when in use adjacent to the human body.

Narrow band nature for balanced antennas, however, is a limitation for handset applications; even though they were designed and operated in the higher band. Some novel techniques have been proposed for the enhancement of impedance bandwidth for balanced antennas. For example, a genetic algorithm technique has been implemented to improve the impedance bandwidth [4].

In this paper, characteristics of a built-in balanced folded slotted dipole antenna with a novel dual-arm structure for mobile handsets are introduced and analysed in order to realise multiple-band operation, including GSM1800, GSM1900, UMTS and WLAN (2.4 GHz). A planar balun with corresponding wide bandwidth for feeding the proposed antenna was implemented in a hardware realization. In the analysis, an electromagnetic simulator based on the finite integration technique (FIT) was applied to calculate return loss and radiation patterns [5].

2. ANTENNA DESIGN CONCEPT AND STRUCTURE

The first antenna design attempted was designed in free space and then modifications were introduced to achieve wideband operation for mobile handset applications. The antenna, as shown in Fig. 1(a), is mounted on the top of a rectangular conductor plate (120×50 mm), which can be regarded as the mobile handset chassis or ground plane of a practical mobile phone.

Planar metal-plate monopole antennas have been investigated in the past as good candidates for ultrawide-band applications [6, 7]. A pair of such wideband monopole antennas can be integrated together to configure a dipole and still remain a wide bandwidth feature. Following this principle, a wideband planar dipole antenna in free space can be developed. Moreover, like most balanced antennas, the planar dipole antenna works best in free space and, on the contrary, performs badly when placed in the vicinity of other conductors (e.g., mobile phone ground plane). Thus, in order to mitigate the effects of the ground plane causing degradation of antenna performance, a technique was applied by inserting a slot in each one of the arms of the planar dipole to reduce the effects of the induced current on the ground plane. Consequently, a ground plane in which current is induced may have less mutual effect on the proposed mobile antenna. In this way, the antenna may be able to be placed close to the ground plane of the handset (e.g., 1 mm away). In order to achieve a built-in low profile feature, two arms of dipole antenna were required to be folded.

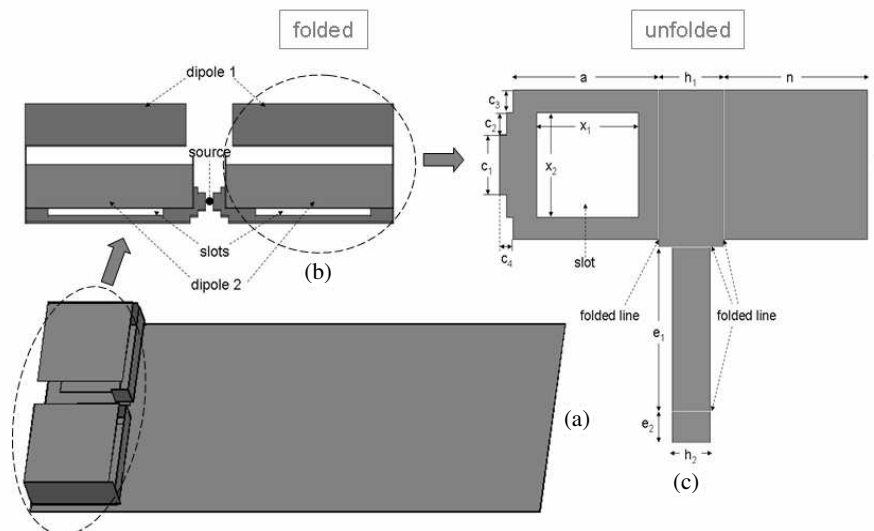


Figure 1: Antenna configuration studied. (a) Balanced folded dipole antenna with conducting plate; (b) Front view of the antenna model; (c) Unfolded structure of the proposed antenna.

The foregoing design concept for balanced mobile antennas was applied and implemented in the authors’ previous work, as illustrated in [8]. In this work, a further improvement on the impedance bandwidth for the antenna was investigated, in order to cover an additional band at 2.4 GHz for WLAN as a new achievable multiple-band operation, since most mobile phones available in the market have such a feature. Therefore, in order to meet and fulfil the mobile market demands, the proposed balanced mobile antenna was investigated as tailored for multi-band operation.

Initially, an antenna (referring as ‘dipole 1’ in Fig. 1(b)), operating at around 2 GHz, was designed and optimized using the CST simulation package. In addition, a new technique was applied by inserting an additional thin-strip arm (referring as ‘dipole 2’ in Fig. 1(b)) in one of the arms of the planar dipole to generate another resonant frequency for 2.4 GHz band (see Fig. 1(c)). Using this technique, the single resonant antenna was modified and developed as a wideband dual-resonant variant for multi-band operation. It is notable that a symmetrical structure was exploited at the monopole edge near the feed point, as shown in Fig. 1(c), replacing the symmetrical triangle trimming structure as used in [8]. This is because the current configuration has better control on the impedance bandwidth as found in the analysis.

The slot size and location on the antenna, together with the length and location of arm for ‘dipole 2’, including other parameters of the proposed antenna, were adjusted and further optimised to ensure that the design entirely covered the required frequency bands (1710–2485 MHz) at $VSWR \leq 3$.

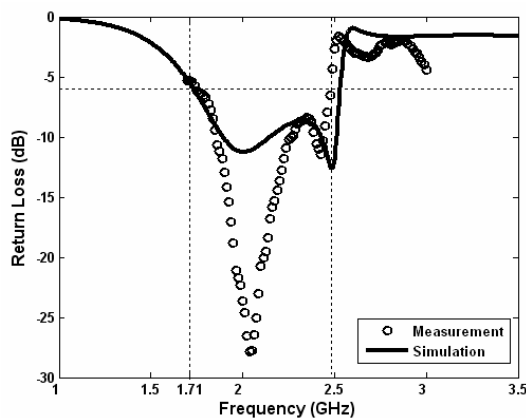


Figure 2: The simulated and measured return loss versus the operating frequency.

3. RESULTS AND DISCUSSION

For a balanced antenna (e.g., dipole) system, a balun is required as a support feeding network, to provide a balanced feed from an unbalanced source. In this study, a wideband planar balun was adopted [9] and modification was applied to it by rearrangement of the element locations for the purpose of the required practical measurement. Agilent ADS [10] was used to simulate and analyse the characteristic performance of this modified balun. It was found the balun is operated from 1.7 GHz to 3 GHz with maximum 0.9 dB insertion loss in which the amplitude and phase imbalance are ± 0.1 dB and $\pm 2^\circ$, respectively. The balun structure was mounted on Duroid material ($\epsilon_r = 3.48$, $h = 0.8$ mm, and $\tan \delta = 0.0019$).

The optimal antenna configuration studied in terms of return loss, radiation patterns and power gain was found with aid of CST simulator ($a = 21.5$, $b = 20$, $h_1 = 9.5$, $h_2 = 5.5$, $n = 21$, $c_1 = 8$, $c_2 = 3$, $c_3 = 3$, $c_4 = 2$, $x_1 = 15$, $x_2 = 14$, $e_1 = 22$ and $e_2 = 4$; dimensions are in mm). For the hardware realisation, copper sheet of thickness 0.15 mm was used for fabricating the proposed balanced antenna. The ground plane (0.035 mm copper thickness) of the proposed antenna was printed on one side of the dielectric substrate and planar balun was placed on the other side of the substrate. The non-conductive material was used to suspend the antenna from the ground plane with 1 mm distance. The position of the two balanced outputs from the balun was carefully located right beneath the feed point of the balanced antenna on the top layer of the substrate. Two thin wires were employed to connect the antenna feed point with the balun through two holes. In this way, the prototype balanced antenna and its feeding network virtually share the same ground plane as one whole system with close integration.

Figure 2 presents the measured and simulated return loss of the prototype antenna. As can be

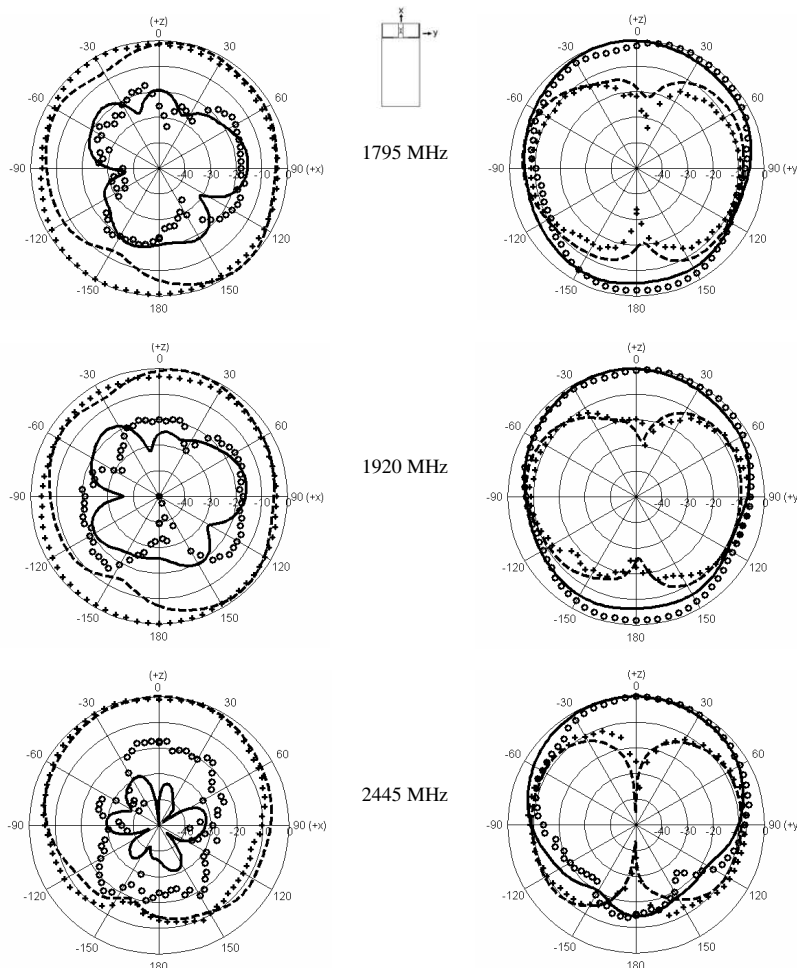


Figure 3: Radiation patterns of the proposed antenna for 1795 MHz, 1920 MHz and 2445 MHz at: (left) zx plane; (right) zy plane; ('ooo' measured E_θ , '—' simulated E_θ , '+++ measured E_ϕ , and '- - - -' simulated E_ϕ).

seen, taking into account the errors caused by manufacturing the proposed antenna, a fairly good agreement between the calculated and measured return loss was observed.

Measurements of the radiation patterns of the prototype were carried out in a far-field anechoic chamber. Two pattern cuts were taken for three selected operating frequencies that cover the designated whole bandwidth in this study. The radiation patterns in the zx plane and zy plane for the balanced folded dipole at 1795, 1920 and 2445 MHz were measured. The results were verified and plotted against the prediction in Fig. 3, in which the patterns of the prototype antenna are seen to be quite similar to each other for the first two cases. Moreover, the zx plane presents a nearly omni-directional radiation pattern in all intended three frequency bands; whereas, the proposed antenna at 2445 MHz tends to radiate at the $+z$ direction in both plane cuts. In this case, the ground plane in this band acts as a good reflector.

Measured broadside antenna power gain for the frequencies across the GSM1800, GSM1900, UMTS and 2.4-GHz WLAN bands were also performed. It is notable that the insertion loss of the feeding network was subsequently compensated for each measured power gain over all bands. It was found that the measured antenna gain was varied between 3.7 dB and 4.8 dB over the entire bandwidth considered. For the whole four bands, the peak antenna gain variations are less than 1 dBi, as compared with the prediction.

4. CONCLUSIONS

A new wideband balanced folded dipole antenna, together with its feeding network (a planar wide-band balun), operated over GSM1800, GSM 1900, UMTS and 2.4-GHz WLAN bands, has been presented. The proposed antenna model was experimentally verified in terms the input impedance, radiation pattern and power gain. The simulated and measured results over all frequency bands considered, show a good agreement and this made the proposed antenna an attractive candidate for mobile handset applications.

ACKNOWLEDGMENT

The authors would like to gratefully acknowledge the support by the Engineering and Physical Sciences Research Council (EPSRC) in the UK under grant EP/E022936.

REFERENCES

1. Morishita, H., H. Furuuchi, and K. Fujimoto, "Performance of balance-fed antenna system for handsets in vicinity of a human head or hand," *IEE Proc.-Microw. Antennas Propag.*, Vol. 149, No. 2, 85–91, April 2002.
2. Abd-Alhameed, R. A., P. S. Excell, K. Khalil, R. Alias, and J. Mustafa, "SAR and radiation performance of balanced and unbalanced mobile antennas using a hybrid formulation," *IEE Proceedings-science, Measurement and Technology Special Issue on Computational Electromagnetics*, Vol. 151, No. 6, 440–444, November 2004.
3. Hayashida, S., H. Morishita, Y. Kim, Y. Koyanagi, and K. Fujimoto, "Wideband folded loop antenna for handsets," *IEEE AP-S Proc.*, Vol. 3, 2–5, June 2002.
4. Zhou, D., R. A. Abd-Alhameed, and P. S. Excell, "Bandwidth enhancement of balanced folded loop antenna design for mobile handsets using genetic algorithms," *PIERS Online*, Vol. 4, No. 1, 136–139, 2008.
5. Computer Simulation Technology Corporation, CST Microwave Studio, Version 5.0, Germany.
6. Ammann, M. J. and Z. N. Chen, "Wideband monopole antennas for multi-band wireless systems," *IEEE Antennas and Propagation Magazine*, Vol. 45, No. 2, 146–150, April 2003.
7. Wong, K.-L., C.-H. Wu, and S.-W. Su, "Ultrawide-band square planar metal-plate monopole antenna with a trident-shaped feeding strip," *IEEE Transaction on Antennas and Propagation*, Vol. 53, No. 4, 1262–1269, April 2005.
8. Zhou, D., R. A. Abd-Alhameed, and P. S. Excell, "Wideband balanced folded dipole antenna for mobile handsets," *The 2nd European Conference on Antennas and Propagation*, No. 39, Session MoPA, Edinburgh, UK, November 11–16, 2007.
9. Zhang, Z. Y., Y. X. Guo, and L. C. Ong, "A new wideband planar balun on a single-layer PCB," *IEEE Microwave and Wireless Components Letters*, Vol. 15, No. 6, 416–418, June 2005.
10. Advanced Design System, Version ADS2005A, Agilent Technologies.

Wideband Loaded Wire Bow-tie Antenna for Near Field Imaging Using Genetic Algorithms

S. W. J. Chung, R. A. Abd-Alhameed, C. H. See, and P. S. Excell
 Mobile and Satellite Communications Research Centre, University of Bradford
 Bradford, West Yorkshire, BD7 1DP, UK

Abstract— The potentially broad application area in engineering design using Genetic Algorithm (GA) has been widely adopted by many researchers due to its high consistency and accuracy. Presented here is the initial design of a wideband non-dispersive wire bow-tie antenna using GA for breast cancer detection applications. The ultimate goal of this design is to achieve minimal late-time ringing but at higher frequencies such as that located from 4 to 8 GHz, in which is desire to penetrate human tissue for near field imaging. Resistively loading method to reduce minimal ringing caused by the antenna internal reflections is implemented and discussed when the antenna is located in free space and surrounded by lossy medium. Results with optimised antenna geometry and different number of resistive loads are presented and compared with and without existence of scatterers.

1. INTRODUCTION

Due to the non-dispersive and ultra-wideband characteristics, the bow tie antenna has been applied on various applications; from Ground Penetrating Radar (GPR) to biomedical imaging tools. The bow-tie antenna play crucial roles in these applications by transmitting and receiving a relatively short transient pulse with minimum distortion and a low level of late time ringing. The lack of adaptive characteristic on the solid bow-tie antenna have motivated [1] to represent it in wire form in order to make it more suitable for GPR application. Drastic improvement is later been made by [2] by representing the typical solid bow tie antenna with a series of wires by means of Genetic Algorithm (GA). The Wire Bow-Tie (WBT) antenna is found more adaptive and advantageous as it is easily loaded with lumped elements to accommodate certain applications need while preserve its characteristics [3, 4]. Further improvement has also been done by the same group by resistively loading the design to minimize late-time ringing. Nevertheless, loading lump elements on wires is somehow impractical and difficult to achieve.

In this paper, a WBT antenna design is reported using GA as the main optimization tool. The antenna is designed based on the fundamental requirement for near field imaging tools such as for microwave breast cancer detector. This can be done by specify certain crucial goals on GA in order to obtain the optimum results. The design is then been analysed in time domain for further inspection using efficient and accurate computational software package where the resistive loading will also be implemented. For the sake of practical measurement, the design will then be transformed to microstrip to realize resistive loading method by using Surface Mount Resistors (SMR). Ideally, the successful antenna design should satisfy the following:

1. Operate at large bandwidth (4 to 8 GHz) to accommodate short pulses.
2. Late-time ringing less than 10^{-4} dB.

2. ANTENNA DESIGN USING GENETIC ALGORITHM

Figure 1 shows the general flow chart of the GA tools being implemented. Notice that the GA is incorporated with the electromagnetic code as the simulator. In this paper, the antenna wing is represented by 3 wires on each side with the radii of 0.5 mm. The total length is initially ranging from 50 to 120 mm while the flare angle is set to be 70° . These parameters will be computed in order to satisfy the pre-defined goal. Both wings are connected to a common feed point at the center of the antenna. The differential Gaussian pulse is adopted from [5] which has the following property:

$$V(t) = V_o \sin(2\pi f_o(t - t_o))e^{-((t-t_o)/\tau)^2} \quad (1)$$

where $f = 6$ GHz, $\tau = 0.133$ ns, $t_o = 4\tau$ and V_o is the voltage amplitude. In frequency domain the following equations is defined:

$$V(j\omega) = -j\tau\sqrt{\pi}e^{-j\omega t_o} \cdot e^{-\tau^2(\pi^2 f_o^2 + 0.25\omega^2)} \sinh(\pi\omega f_o\tau^2) \quad (2)$$

$$I(j\omega) = V(j\omega)/Z(j\omega) \quad (3)$$

$$I(t) = IFFT(I(j\omega), n) \quad (4)$$

where $n =$ number of frequency samples proposed in GA.

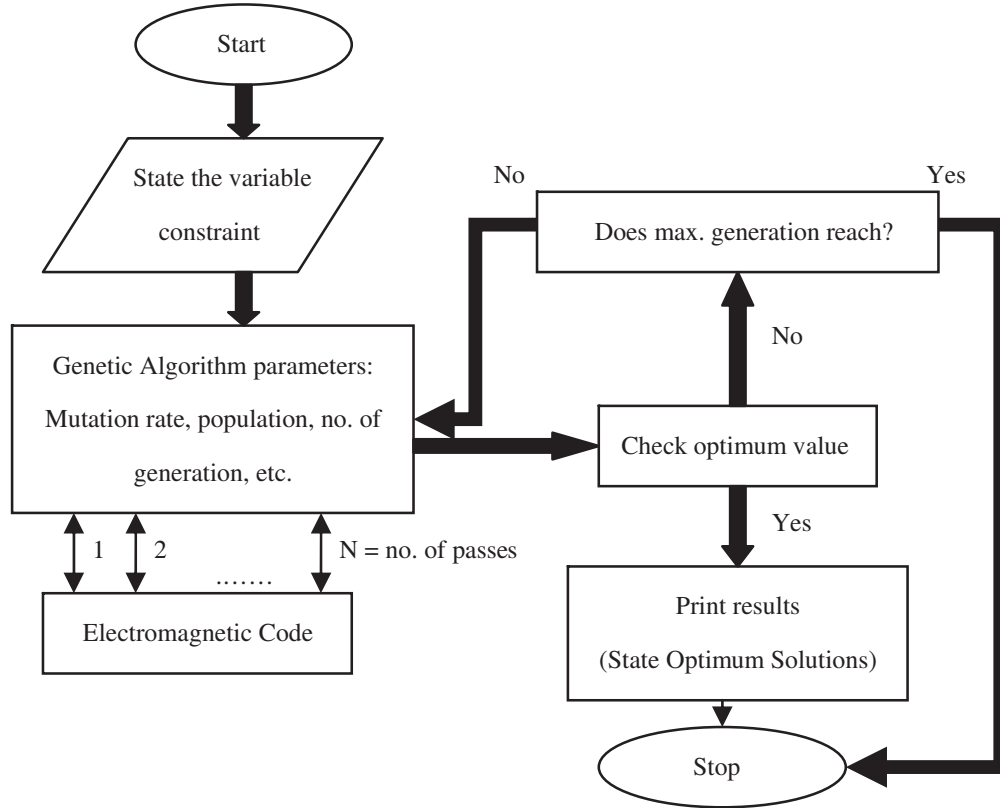


Figure 1: Flow chart of the GA tools applied to optimize the WBT antenna design.

Here, the GA has been pre-defined to optimize the matching impedance over the operating frequency bandwidth. The goal or the cost function is expressed as the following:

$$F = \sum_{i=1}^n \left(w_1 \frac{1}{VSWR(f_i)} + w_2 \frac{1}{1 + (\zeta(f_i) - \zeta_c)^2} \right) \quad (5)$$

where:

$$VSWR(f_i) = \frac{1 + |\Gamma(f_i)|}{1 - |\Gamma(f_i)|} \quad (6)$$

$$\Gamma(f_i) = \frac{Z_L(f_i) - Z_o}{Z_L(f_i) + Z_o} \quad (7)$$

Note that w_1 and w_2 are the weighted coefficients, $Z_L(f_i)$ is the input impedance at the operating frequency f_i , Z_o is the reference load, $\zeta(f_i)$ is the radiation efficiency at operating frequency f_i and ζ_c is the reference radiation efficiency.

3. NUMERICAL RESULTS

Table 1 shows the properties of the applied genetic algorithm while Table 2 shows the optimum values of the antenna design's parameters in free space. The optimum total length of the antenna

as well as the load impedance acquired from the GA is to be 77.2 mm at 188 Ohm. The antenna design is depicted in Fig. 2 in which each radiating element (single arm) is loaded with resistors acquired from genetic algorithm. Note that the position of these resistors has been identified prior to optimization process.

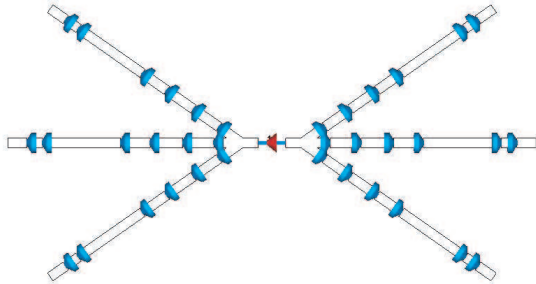


Figure 2: Geometry of the resistive loaded antenna design model.

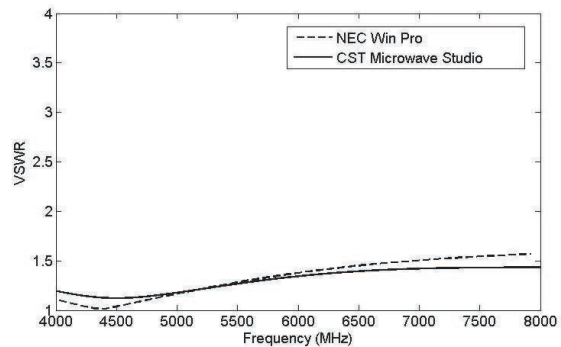


Figure 3: Voltage standing wave ratio (VSWR) versus the operating frequency of two computational tools.

Table 1: Properties of the applied Genetic Algorithm.

GA parameters	
Population size	4
Maximum number of parameters	8
Probability of mutation	0.02
Maximum generation	100
Number of possibilities	2^{15}

Table 2: Input load parameters, their associated locations and optimum values in free space.

No. of resistors	Min.	Max.	Location of resistors (segment number)	Resistors value (Ohm)	Maximum fitness
1	5	300	8	280	4.00
2	5	300	7, 9	6, 260	4.11
3	5	300	3, 8, 9	297, 150, 165	5.18
4	5	300	2, 3, 8, 9	300, 300, 133, 157	6.06
5	5	300	2, 3, 7, 8, 9	300, 297, 116, 65, 40	6.09
6	5	300	2, 3, 6, 7, 8, 9	295, 296, 43, 66, 69, 130	6.08

The antenna is later being optimised inside a medium that is characterized by relative dielectric permittivity $\epsilon_r = 9.0$, and conductivity $\sigma = 0.4 \text{ S/m}$ for further investigation and the results are tabled in Table 3. The optimum length of each antenna arm and the match load were found to be 35 mm and 190 ohms respectively.

The respective voltage standing wave ratio and the input impedance of the antenna in free space are computed using different simulation tools and plotted as shown in Fig. 3 and Fig. 4 respectively. Both results show good agreement in terms of input impedance stability across the operating frequency and optimised matched load of 188 ohms (found by GA).

Further free space investigation involving a scattered object placed at various distances below the antenna along the z -axis. The scatterer was considered as cross short dipoles of length 5 mm, parallel to the WBT and both having the conductivity of 9 S/m . Fig. 5 shows the frequency spectrum of the received signal with and without the presence of the scatterer where as Fig. 6 shows

Table 3: Input load parameters, their associated locations and optimum values within the medium $\epsilon_r = 9.0$, and $\sigma = 0.4\text{S/m}$.

No. of resistors	Min.	Max.	Location of resistors (segment number)	Resistors value (Ohm)	Maximum fitness
1	5	300	8	300	3.86
2	5	300	7, 9	8, 298	4.02
3	5	300	3, 8, 9	5, 278, 7	4.32
4	5	300	2, 3, 8, 9	110, 6, 84, 184	4.96
5	5	300	2, 3, 7, 8, 9	164, 8, 37, 260, 173	5.23
6	5	300	2, 3, 6, 7, 8, 9	109, 7, 11, 113, 120, 219	5.22

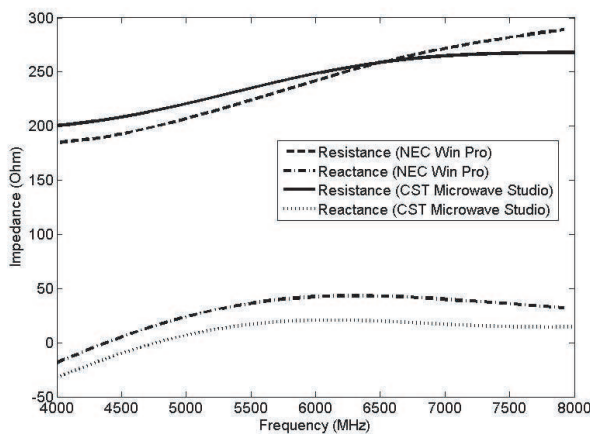


Figure 4: Input impedance of the antenna.

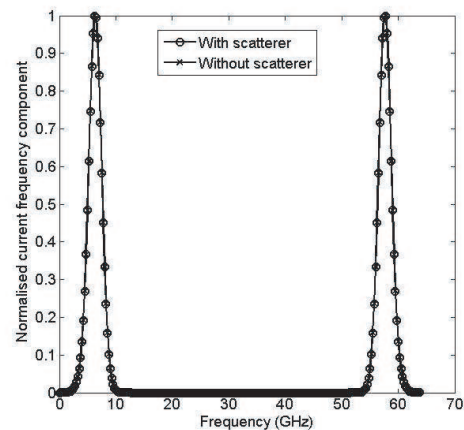


Figure 5: The frequency spectrum of the current component.

the time variations of the normalised difference current components (i.e., the components associated with and without scatterer) observed when the object is placed at 3 cm, 6 cm and 9 cm below the antenna geometry. An enlargement figure time response of the normalised current component due to a scatterer object placed at 9 cm below the antenna is depicted in Fig. 7, in which, a clear indication can be observed the present of the scatterer.

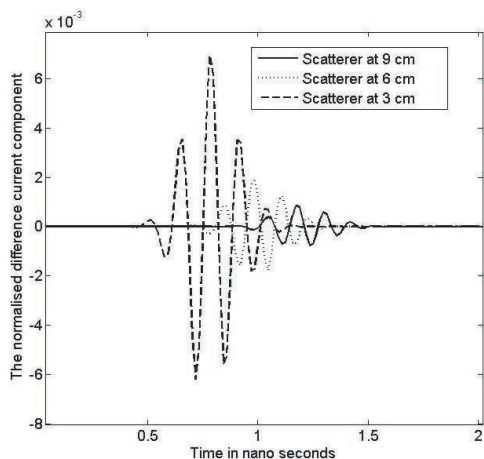


Figure 6: Time variations of the normalised difference current component subject to various scatterer distances along z axis.

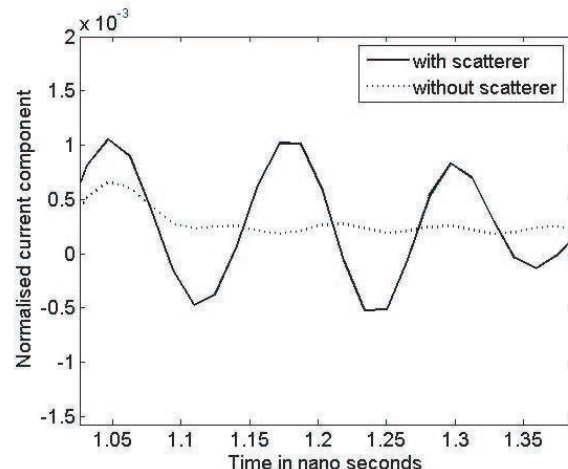


Figure 7: Time variations of the normalised current component observed from a scatterer object placed at 9 cm along z -axis below the antenna.

Finally, the optimised antenna configurations surrounded by lossy medium was tested with the presence of scatterer located below the antenna at different distances as shown in Fig. 8. The scatterer (or target) has spherical geometry of radius 5 mm and characterized by relative dielectric permittivity of 36 and conductivity of 9 S/m. Fig. 9 shows the normalised difference current components for two scatterer distances in which each antenna arm loaded by six resistors as stated in Table 3. The variations effects of the back scattered fields from the scatterer on the currents values clearly indicated the expected position of the target. The relative peak values (that represents the maximum normalised reflections) of these variations normalised to the maximum current component were found to be 68 to 60 dBs respectively to 1.5 cm and 3 cm scatterer distances.

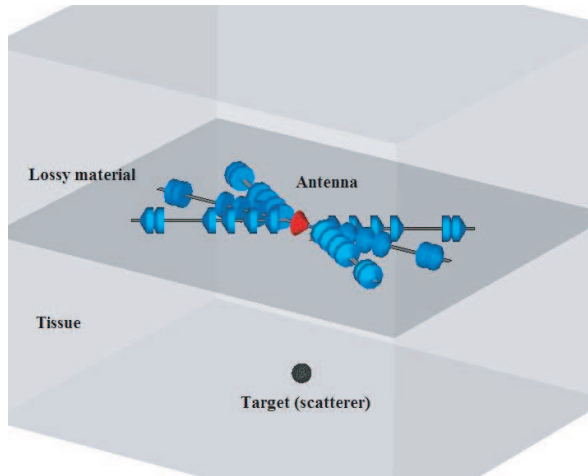


Figure 8: Resistive loaded BTW with scatterer surrounded by a lossy medium.

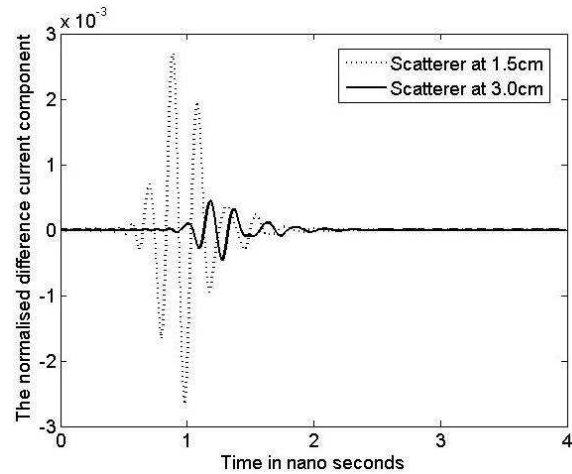


Figure 9: Time variations of the normalised difference current components when the antenna and scatterer surrounded by a lossy medium.

4. CONCLUSION

A WBT antenna design for near field imaging using GA as the primary optimization tools has been presented. The design concept of resistively loaded WBT in free space and when surrounded by lossy medium was discussed. The optimum load values and their locations for each space medium were addressed. The computational results of two softwares using the optimum design were found in good agreement in terms of the variations of the input impedance and the VSWR across the frequency range considered. A reasonable reflection levels that describe the back scattered fields from scatterer located underneath the antenna were also recorded. More improvements are still in progress where it involves increment the number of radiating elements on both arms and matched to a lower system load. Enhancing the antenna by placing two WBT in a cross polarization position is also being considered to improve its imaging capability.

REFERENCES

1. Lestari, A. A., A. G. Yarovoy, and L. P. Lightart, "Adaptive antenna for ground penetrating radar," *Proceedings of the Tenth International Conference on Ground Penetrating Radar*, Vol. 1, 121–124, 2004.
2. De Jong van Coevordon, C. M., A. R. Bretones, M. F. Pantoja, F. J. G. Ruiz, and R. G. Martin, "GA Design of a thin-wire bow-tie antenna for GPR applications," *IEEE Trans. Geosci. Remote Sensing*, Vol. 44, No. 4, 1004–1010, April 2006.
3. Uduwawala, M. N. D., P. Fuks, and A. W. Gunawardena, "A deep parametric study of resistor-loaded bow-tie antennas for ground-penetrating radar applications using FDTD," *IEEE Trans. Geosci. Remote Sensing*, Vol. 42, 732–742, April 2004.
4. Lestari, A. A., A. G. Yarovoy, and L. P. Lightart, "Adaptive wire bow-tie antenna for GPR applications," *IEEE Trans. Antenna Propagat.*, Vol. 53, 1745–1754, May 2005.
5. Hagness, S. C., A. Taflove, and J. E. Bridges, "Three-dimensional FDTD analysis of a pulsed microwave confocal system for breast cancer detection: Design of an antenna-array element," *IEEE Trans. Antennas Propagat.*, Vol. 47, 783–791, May 1999.

A Novel CPW-fed Bow-tie Slot Antenna for 5.8 GHz RFID Tags

Fei Lu, Quanyuan Feng, and Shiyu Li

Microelectronic Technology Lab of Southwest Jiaotong University, China

Abstract— A Novel Bio-Tie slot antenna with CPW-fed structure is presented. The designed antenna, which is fabricated on a 35×25 mm substrate can operate at the 5.8 GHz band with 51% broad bandwidth ($s_{11} < -10$ dB) and gain 3.9 dBi, respectively. The radiation patterns are almost omni-directional in H -plane. All these properties and the uniplanar structure make the antennas suitable for 5.8 GHz Radio Frequency Identification applications.

1. INTRODUCTION

In recent years, Radio Frequency Identification (RFID) technology has been extensively utilized in modern supply chain management to identify and track goods. Usually, a basic RFID system is made up of two components: one is the transponder, which is located on the object to be identified and the other is the reader, which, depending upon the design and the technology used, may be a read or write/read device [1]. The tag's antenna receives signals from an RFID reader and then sends back the signals, usually including some additional data, including a unique serial number or customized information.

The frequency bands assigned to RFID application are less than 135 KHz, 13.56 MHz, UHF band, and microwave band, including 2.45 GHz and 5.8 GHz. As the operating frequency for RFID system raises into microwave region, the tag antenna design becomes more acute and essential [2]. The tag antennas must be small enough to be attached to the required object and have omni-directional or hemispherical coverage. Besides, the cheap cost and proper impedance are also required.

Some kinds of tag antenna have been presented these years, like folded dipole antenna, Inverted-F antenna, CPW-fed Folded-slot Antenna [3–5]. However, those antennas are either too large in size or too complex in structure, and also have narrow band. In this letter, a broad bandwidth slot antenna with RF performance suitable for RFID tag use at 5.8 GHz is presented, and the details of the antenna design and simulated results are presented and discussed.

2. ANTENNA CONFIGURATION

The basic geometry of the proposed antenna is shown in Fig. 1. The designed antenna is only one layer of RF4 dielectric substrate which is 45×30 mm in dimension. The antenna is symmetrical with respect to the longitudinal direction, whose main structure is a bowtie-shaped slot and a balance-shaped strip with Co-planar waveguide (CPW) fed line. For the first approximate design and according to the [7], the antenna's dimension could be decided.

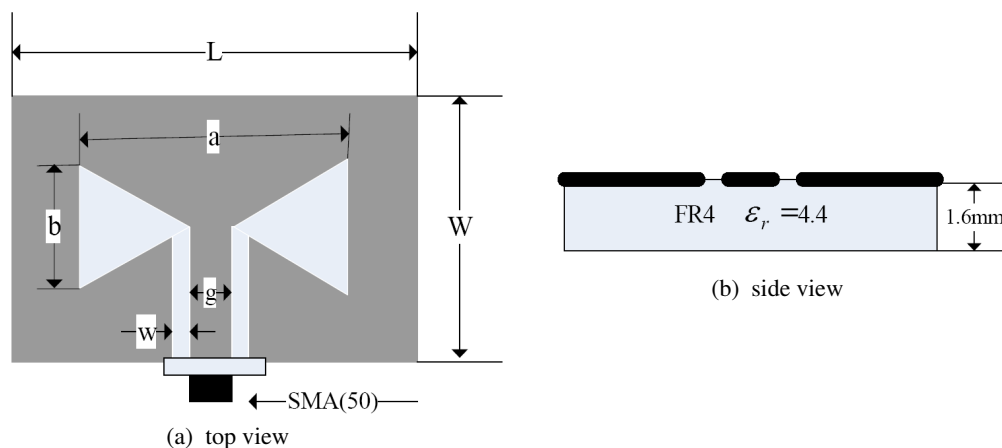


Figure 1: The basic geometry of proposed antenna for 5.8 GHz RFID application $a \times b = 36.2 \times 16.4$ mm, $L \times W = 45 \times 35$ mm, $w = 0.6$ mm, $g = 1$ mm.

$$a = 1.6\lambda_0/\sqrt{\varepsilon_r} \quad b = 0.5\lambda_0/\sqrt{\varepsilon_r} \quad (1)$$

where λ_0 is the wavelength of 5.8 GHz in free space, and ε_r is the dielectric constant of the FR4 substrate. However, this paper emphasizes a novel bow-tie slot antenna which could decrease the antenna's dimension to 35×20 mm. the improved antenna can not only make the antenna's radiation pattern performs better but broaden the bandwidth. The advanced bow-tie antenna is showed in Fig. 2. Different from the basic antenna, the improved antenna adopts dual bow-tie structure.

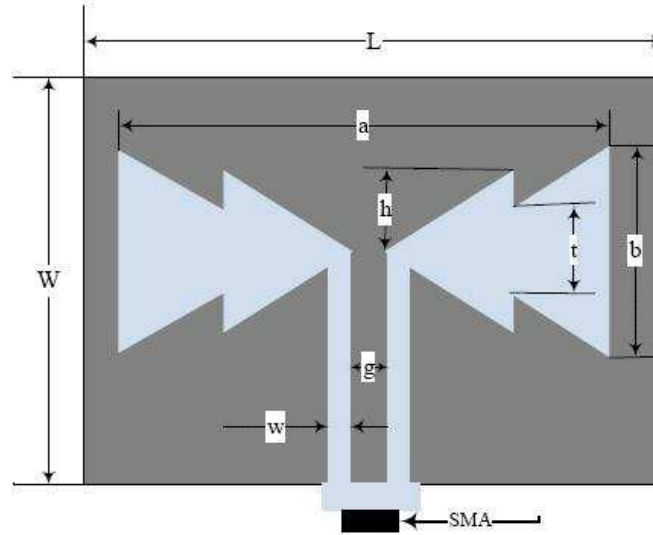
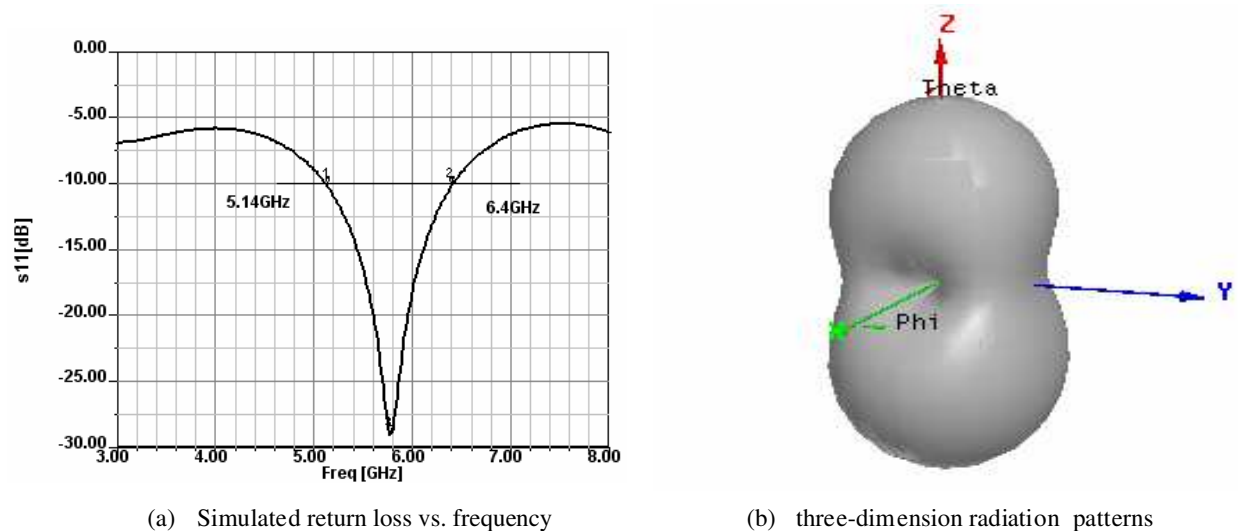


Figure 2: The geometry of novel antenna for 5.8 GHz RFID application.

3. RESULT AND DISCUSSION

Prototypes of the proposed CPW-fed bow-tie slot antennas showed in Fig. 1 and Fig. 2 were both constructed and analyzed, and the performance of both antennas is simulated with the aid of HFSS v10.0 software. Fig. 3 shows the simulated results of the basic geometry of proposed antenna, of which (a) presents the return loss at 5.8 GHz while (b) shows the simulated radiation patterns at the centre operating frequency (5.8 GHz). From the simulated results, it is seen that, in the H -plane, the radiation patterns are almost omni-directional radiation. Besides, the antenna gains 4.5 dBi gain and 21.7% bandwidth. All these properties are suitable for RFID application.



(a) Simulated return loss vs. frequency

(b) three-dimension radiation patterns

Figure 3: The properties of the basic bow-tie antenna for 5.8 GHz RFID application.

Though the basic CPW-fed bow-tie antenna could answer for RFID system, the size is big in some sort and the radiation patterns could be better. So the novel antenna adopts dual bow-tie

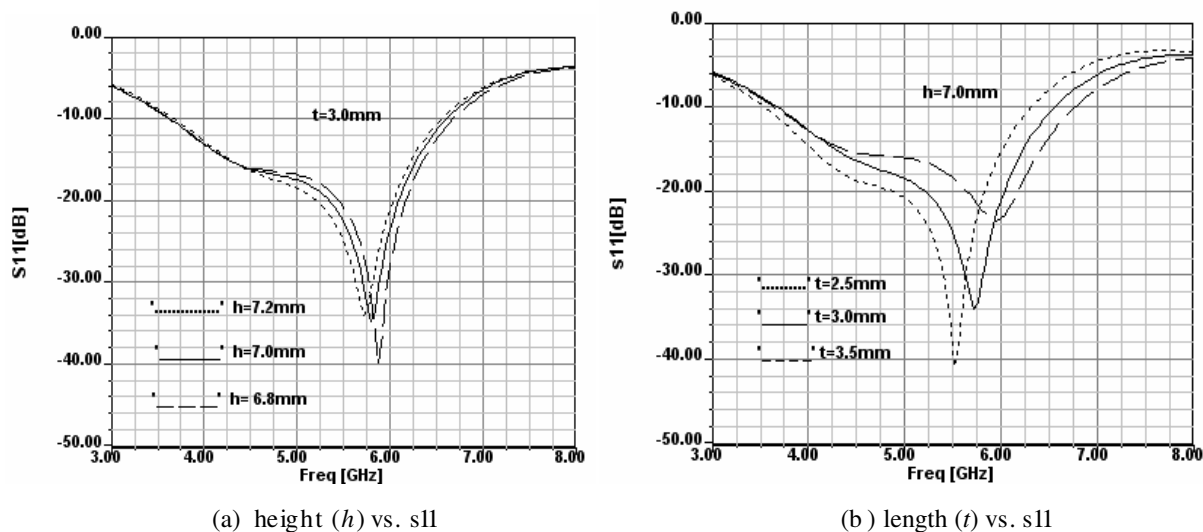


Figure 4: The dimension of dual structure vs. return loss.

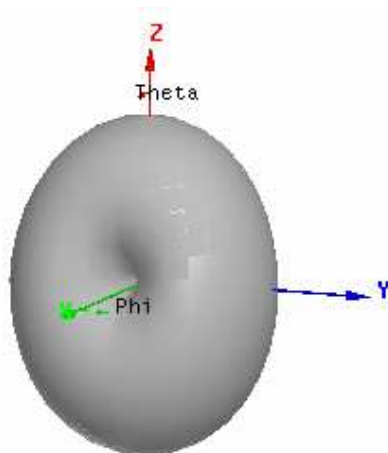


Figure 5: Three-dimension radiation patterns of the novel RFID antenna.

structure to get over these disadvantages. Tab. 1 shows how the dimension of dual bow-tie structure affects the antenna’s properties. From the table we could find the proper dual bow-tie structure dimension. Fig. 5 shows the simulated results of the novel CPW-fed bow-tie antenna with the proper dual bow-tie structure dimension which is $a \times b = 33 \times 13.6$ mm, $L \times W = 35 \times 25$ mm, $w = 0.6$ mm, $g = 1$ mm and $t = 6.0$ mm, $h = 7$ mm. Compare to the basic bow-tie antenna, as shown in Fig. 5 the three-dimension radiation patterns of the novel antenna performs better. Besides, the bandwidth could expand to 51%. Because of the dual structure, the gain is decreased

Table 1: The affection of different dual structure dimension (h and t).

h, t (mm)	Centre frequency (GHz)	Bandwidth(GHz), percentage
$t = 5.0 \quad h = 7.0$	5.64	2.80, 48.2%
$t = 6.0 \quad h = 7.0$	5.80	2.96, 51.0%
$t = 7.0 \quad h = 7.0$	5.96	3.08, 53.1%
$h = 7.2 \quad t = 6.0$	5.72	2.80, 48.2%
$h = 7.0 \quad t = 6.0$	5.80	2.96, 51.0%
$h = 6.8 \quad t = 6.0$	5.88	3.00, 51.7%

slightly. However, all these proprieties could answer for the RFID application well.

4. CONCLUSIONS

A CPW-fed bow-tie slot antenna for RFID system has been designed and simulated. On the basis of this kind of antenna, a novel bow-tie slot antenna for RFID is presented emphatically. This kind of antennas can be easily fabricated and has considerable cheap price. Its broadband property should be more robust to deal with environmental factors, which may shift its resonant frequency in designing. Also, the antenna has very small dimension. This novel kind of antenna can be used not only in RFID system, but also in WLAN communication system for 5.80 GHz.

REFERENCES

1. Finkenzeller, K., *RFID Handbook [M]*, 2nd edition, Wiley, London, 2004.
2. Foster, P. and R. Bueberry, "Antenna problems in RFID systems," *IEE Coll. on RFID Technology*, 3/1–3/5, 1999.
3. Qing, X. and N. Yang, "A folded dipole antenna for RFID," *Proceedings of Antennas and Propagation Society International Symposium*, 97–100, 2004.
4. Ukkonen, L. and L. Sydanheimo, "A novel tag design using inverted-F antenna for radio frequency identification of metallic objects," *Proceedings of Advances in Wired and Wireless Communication, 2004 IEEE/Sarnoff Symposium*, 91–94, 2004.
5. Chen, S. Y. and P. Hsu, "CPW-fed folded-slot antenna for 5.8 GHz RFID tags," *Electron Letter*, Vol. 40, No. 24, 1516–1517, 2004.
6. Bhohe, A. U., C. L. Holloway, and M. Pikeet-May, "CPW fed wide-band hybrid slot antenna," *Proceedings of IEEE Antennas and Propagation Society International Symposium*, Vol. 2, 636–639, US, 2000.
7. Li, K., C. H. Cheng, T. Mastui, and M. Izusu, "Coplanar patch antennas," *Proceedings of IEEE MTT-S Int. Microwave Sym.*, 402–405, 2001.

A Mode Based Model for Radio Wave Propagation in Storm Drain Pipes

Ivan Howitt, Safeer Khan, and Jumanah Khan

Department of Electrical and Computer Engineering

The University of North Carolina at Charlotte, Charlotte, NC 28223, USA

Abstract— In this paper, we analyze the behavior of Storm Drain Pipes (SDPs) as multi-mode leaky waveguides for radio wave transmissions between 2.4–2.5 GHz within the Industrial, Scientific and Medical (ISM) band. The previous research on analyzing RF propagation inside underground structures focused on auto, railroad, subway, mine and sewer tunnels of diameters greater than 1.05 m. Our research provides a novel contribution by characterizing RF propagation inside narrow SDPs of diameter as low as 0.30 m. Understanding the behavior of SDPs as communication channels is not only important for designing portable military communication equipment, but also for other civil applications. We study the modal content of propagating waves and derive a mode based model (MBM) for predicting the received power. Empirical data gathered at selected sites in Charlotte, North Carolina is used to validate the MBM. Based on analysis of nonlinear curve fitting through the measured data, close agreement is found between the predicted and measured power. We also highlight the requirement of further work to improve the fitting of measured data with the predicted results.

1. INTRODUCTION

In this paper, we present an analytical model for characterizing RF propagation in SDPs. The model provides an estimate of the received power at some distance d from the source and also provides an estimate for the contribution of propagating modes to the received power. Historically, research and experimentation into RF propagation through underground structures has examined ultra high frequency (UHF) propagation through coal mines for addressing communication needs of the coal mining industry [1]. Demands of mobile communications expanded research into RF propagation in railroad, auto and subway tunnels [2].

Holloway, et al. in [3] have numerically evaluated the frequency dependence of attenuation for various modes in underground, lossy wireless communication channels such as mines, tunnels, boreholes and shafts. This area was further investigated by Dudley [4]. He studied models for propagation in circular tunnels using excitation from a circular magnetic or circular current loop. In [5], he proposed a parsimonious model for field intensity in a tunnel as a function of axial distance. Multimode waveguide behavior of heating, ventilation and air conditioning (HVAC) ducts is proposed for high data rate wireless networks [6] and provided insight into developing the model presented in this paper.

To date there is limited research into propagation issues associated with networked pipes such as storm drain pipes (SDPs). The closest parallel to such work is testing done for inspecting, repairing and cleaning of water reclamation tunnels [7]. Also, in 2006, Kjeldsen, et al. conducted experiments on RF propagation through concrete tunnels at Military Operations and Urban Terrain (MOUT) facility at Camp Lejuene, NC [2]. Their aim was to conduct path loss measurements in order to gain better comprehension of critical propagation factors for designing an effective communication system for military operations in subterranean cavities.

Our work focuses on understanding RF propagation inside concrete SDPs of diameters 1.37 m, 1.06 m, 0.76 m, 0.61 m, 0.46 m and 0.30 m. The aim is to formulate a reliable propagation model that can be used to predict received power at distance d from the source. We, therefore, propose a mode based model (MBM) for radio wave propagation inside SDPs and carry out experimental measurements at selected locations in Charlotte, North Carolina. We use the results from the measurement campaign to validate the MBM.

2. PROPOSED MODEL

For RF propagation through lossy circular waveguides, the electromagnetic modes generated at the transmitter have varying levels of contribution to the transmitted signal [3]. Evanescent or stationary modes have exponential attenuation and suffer a rapid decay whereas propagating modes are the main source of power transfer from transmitter to the receiver. It is, therefore, of interest to understand properties of propagating modes.

For modal analysis of electromagnetic wave propagation in circular waveguides, propagation constant, γ , is complex given by $\alpha + j\beta$, where α represents modal attenuation constant and β is phase constant for a particular mode. Phase constant is defined in [8] as

$$\beta_n = \frac{2\pi f}{c} \sqrt{1 - \left(\frac{f_c}{f}\right)^2} \quad (1)$$

where f_c is cut-off frequency for mode n . For cylindrical waveguides, the modal cut-off frequency is

$$f_c = \frac{cg}{2\pi a} \quad (2)$$

where c is velocity of light, a is the waveguide radius and $g = p_{nm}$ is the m th zero of the Bessel function $J_n(x)$ for Transverse Magnetic (TM) modes, and $g = p'_{nm}$ is the m th zero of the Bessel function derivative $J'_n(x)$ for Transverse Electric (TE) modes. The attenuation coefficient α_n is dependent upon the cut-off frequency for a particular mode. The attenuation coefficient is given by

$$\alpha_n = \frac{BR_s}{\eta_0 a \sqrt{1 - \left(\frac{f_c}{f}\right)^2}} \quad (3)$$

where $B = 1$ for TM Modes and $B = (f_c/f)^2 + (n^2/(p'_{nm}{}^2 - n^2))$ for TE Modes; η_0 is the intrinsic impedance of free space and is equal to 120π when the medium inside the waveguide is air; R_s is the real part of the intrinsic impedance of the waveguide walls given by $R_s = \sqrt{\mu_0 \pi f / \sigma}$, where μ_0 is the permeability of air, i.e., $4\pi \times 10^{-7}$ H/m, and σ is the conductivity.

The RF propagation model for HVAC proposed in [6] defines the total received power at distance d from the source, $P_R(d)$, as the sum of powers excited in propagating modes, i.e.,

$$P_R(d) = \sum_{n=1}^N p_n e^{-2\alpha_n d} \quad (4)$$

where p_n represents the power excited by the transmitting antenna in mode n . The value of p_n is dependent upon the current distribution inside the source antenna and the impedance of the antenna.

The model in (4) is based on modeling RF propagation through a galvanized steel duct and therefore assumes a lossless waveguide. The concrete SDPs can be modeled based on a lossy waveguide model, similar to circular underground concrete tunnels [5]. Therefore, the form of the SDP model is the same as (4) where the received RF signal power in the SDP is based on the summation of powers contained in each mode. The power contained in the n th mode is

$$P_n = \frac{1}{2} A_n^2 \quad (5)$$

where the voltage amplitude A_n can be expressed as

$$A_n = A_{CL_n} \times e^{-\alpha_n d} \quad (6)$$

where α_n is expressed in Nepers/m (Np/m) and A_{CL_n} is the coupling factor. Combining (5) and (6), the MBM can be expressed as

$$P_R(d) = \sum_{n=1}^N P_n = \frac{1}{2} \sum_{n=1}^N A_{CL_n}^2 \times e^{-2\alpha_n d} \quad (7)$$

where $P_R(d)$ is in Watts.

To analyze the MBM, the modal cutoff frequencies and the attenuation coefficients are computed using (2) and (3). Values are provided in Table 1 based on a 2.5 GHz operating frequency and for various SDPs diameters. In evaluating these values the following constants were used: concrete permeability $4\pi \times 10^{-7}$ H/m; concrete conductivity, σ , 0.06 S/m; and the dielectric constant, κ , 4.5 [9].

In the next section a 1.07 m diameter SDP is chosen to illustrate the utility of the MBM. From Table 1, 196 modes are excited in the 1.07 m diameter SDP and in Table 2 the modal attenuation constants for the ten lowest attenuation constants are provided in rank order from lowest to highest.

Table 1: Modal analysis of SDPs as a function of pipe diameter.

Diameter (m)	Number of modes TE+TM modes at $f= 2.5$ GHz	Lowest cut-off frequency (MHz)	Minimum Attenuation (TE ₀₁) (dB/m)
0.30	17	577	16.12
0.46	40	385	4.42
0.61	66	288	1.82
0.76	104	231	0.92
1.07	196	165	0.33
1.37	278	128	0.16

Table 2: Modal attenuation constants for 1.07 m diameter SDP at 2.5 GHz.

Mode	Attenuation Constant (dB/m)	Cut-off Frequency (GHz)
TE ₀₁	0.33	0.343
TE ₀₂	1.14	0.628
TE ₁₂	1.30	0.477
TE ₁₃	1.97	0.764
TE ₀₃	2.49	0.910
TE ₂₂	2.80	0.600
TE ₂₃	3.17	0.892
TE ₁₄	3.53	1.047
TE ₃₂	4.48	0.717
TE ₀₄	4.53	1.192

3. EMPIRICAL MEASUREMENTS AND MODEL VALIDATION

For the empirical measurements, an Agilent CSA Spectrum Analyzer N1996A-506 was used to measure the received power and an Agilent E4428C analog signal generator was used as the signal source. Two GigaAnt dipole antennas with a nominal gain of 2 dBi were used. The equipment set up used in the measurement campaign is illustrated in Figure 1.

A CW signal at 20 dBm was generated between 2.4–2.5 GHz at 10 MHz steps. Coaxial cables were used to connect antennas to the transmitter and receiver. At each measurement location the received power was recorded at the eleven points over the frequency range and the mean and standard deviations were evaluated based on the eleven measurements. The measured data for the 1.07 m SDP is given in Table 3. To evaluate the MBM based on (7), the coupling loss parameter $A_{CL_n}^2$ was estimated for all modes to be evaluated in the sum. This provides the mechanism by which we can gain insight into the possible modes present in the received power solution. By varying the number of modes used in evaluating (7) and accessing the quality of the curve fit to the empirical data provides this insight. To achieve this, we employed a nonlinear least square curve fitting algorithm using the following procedure:

- (1) Modal cutoff frequencies and attenuation coefficients were computed as given in Table 2.
- (2) Analysis was based on 1, 2, 3, 5 and 7 modes with the lowest attenuations.
- (3) The parameters A_{CL_n} were estimated based on best fit coefficients for the MBM to minimize the error between the measured and the MBM model.

The values for $P_R(d)$ were estimated based on (7) using the coefficients obtained for A_{CL_n} . The measured and estimated values of the received powers are plotted in Figure 2. The mean errors

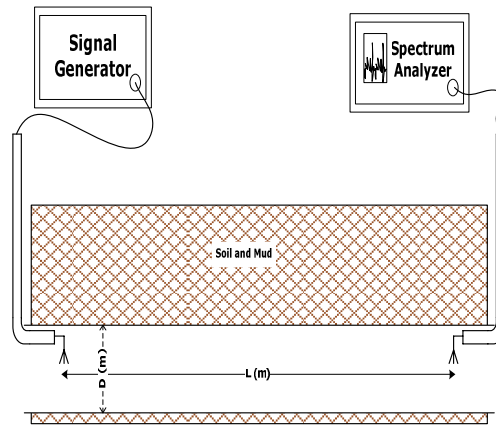


Figure 1: Equipment setup.

between the estimated and measured values are given in Table 4.

From Figure 2 we can observe the impact of varying the number of modes in evaluating $P_R(d)$. If only mode 1 is considered, then the estimated power does not fit the measured received power and the error is relatively large. Note mode 1 is the dominant mode due to its lowest attenuation constant of 0.33 dB/m. In contrast, when 2, 3, 5 and 7 modes are considered, the estimated power plot fits well to the measured power plot.

To further elaborate this aspect, we have analyzed the individual contribution of each coefficient to the received power considering the 3 mode case. In Figure 3, individual graphs are provided indicating the contribution from each mode based on its estimated coupling loss coefficient. From the graphs, it is clear that $A_{CL_2}^2$ contributes very little to the overall received power. Nearly equal contribution comes from $A_{CL_1}^2$ and $A_{CL_3}^2$. The contribution from these two coefficients results in the overall estimated power.

Table 3: Measured received power data for 1.07 m diameter SDP.

Distance (m)	Mean Power (dBm)	Standard. Deviation (dB)
3.64	-23.16	1.82
6.38	-22.45	1.82
11.96	-21.82	0.81
15.14	-33.77	3.25
17.62	-41.86	2.82
20.24	-47.13	4.40
28.48	-40.42	1.48

Table 4: Estimated power and mean error in evaluating the MBM received power.

Modes	Estimated Powers (dBm)							Mean Error (dB)	
	Distance (m)	3.64	6.38	11.96	15.14	17.62	20.24		28.48
1 Mode		-19.4	-20.3	-22.2	-23.2	-24.1	-24.9	-27.7	9.8
2 Modes		-21.4	-24.5	-30.6	-33.9	-36.3	-38.8	-44.8	4.4
3 Modes		-20.3	-23.8	-30.7	-34.3	-36.9	-39.4	-44.9	4.3
5 Modes		-20.3	-23.8	-30.7	-34.3	-36.9	-39.4	-44.9	4.3
7 Modes		-20.3	-23.7	-30.6	-34.2	-36.8	-39.2	-49.8	4.3

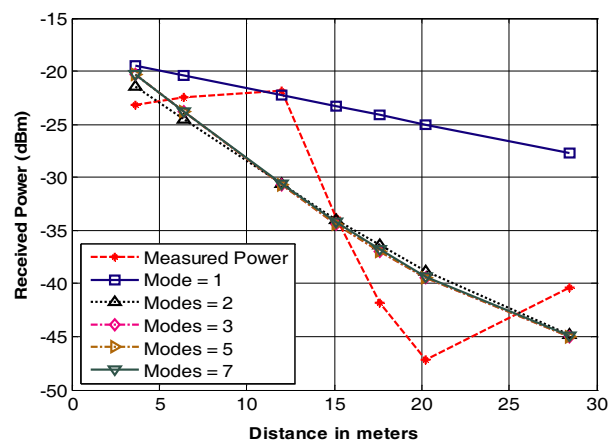


Figure 2: Measured and estimated received power for 1.07 m diameter SDP for 1, 2, 3, 5 and 7 modes.

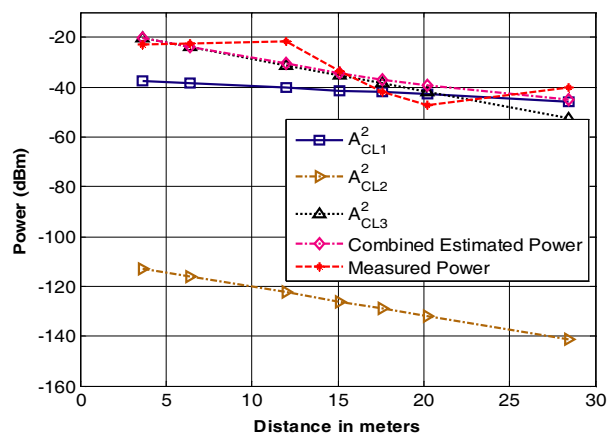


Figure 3: Contribution of modal coefficients in total received power using 3 modes.

The above discussion indicates that the received power at distance d from the source can be specified by evaluating and combining the powers contained in individual modes. By evaluating the individual contributions of each mode, insight can be gained on the relative strength of the modes likely to contribute to the received power within the SDP.

4. CONCLUSION

In this paper, we have proposed a mode based model to evaluate received power at distance d within the SDP. We undertook a measurement campaign to validate the MBM with empirical data. Our results indicate that evaluation of received power as sum of power contributions from propagating modes provides a good estimate of the actual measured power. The fitting of estimated data with the measured results can be further improved if the accuracy of measurements and size of the observations are increased. Also precise measurement of electrical conductivity values for SDP material can enable accurate evaluation of modal attenuation that can further improve the received power estimate. Within these limitations, we have found that the proposed model is a good approximation for estimating the received power at a particular distance in the SDP and provides insight into the modal content of the propagating signal.

REFERENCES

1. Emslie, A., R. Lagace, and P. Strong, "Theory of the propagation of UHF radio waves in coal mine tunnels," *IEEE Trans. Antennas and Propag.*, Vol. 23, No. 2, 192–205, March 1975.
2. Kjeldsen, E. and M. Hopkins, "An experimental look at RF propagation in narrow tunnels," *Proc. IEEE Military Communications Conf. (MILCOM06)*, Washington D.C., October 23–25, 2006.
3. Holloway, C. L., D. A. Hill, R. A. Dalke, and G. A. Hufford, "Radio wave propagation characteristics in lossy circular waveguides such as tunnels, mine shafts, and boreholes," *IEEE Trans. Antennas Propag.*, Vol. 48, No. 9, 1354–1365, September 2000.
4. Dudley, D. G., "Wireless propagation in circular tunnels," *IEEE Trans. Antennas Propag.*, Vol. 53, No. 1, 435–441, January 2005.
5. Dudley, D. G. and H. Y. Pao, "Wireless propagation in circular tunnels," *IEEE Trans. Antennas Propag.*, Vol. 53, No. 8, 2400–2405, August 2005.
6. Nikitin, P., D. D. Stancil, O. K. Tonguz, A. Cepni, A. Xhafa, and D. Brodtkorb, "Propagation model for the HVAC duct as a communication channel," *IEEE Trans. Antennas Propag.*, Vol. 51, 945–951, May 2003.
7. DeHaan, J. and M. Jacobs, "Tunnel communication test results," Project Notes 8450-98-06, Hydroelectric Research and Technical Services Group, Bureau of Reclamation, U.S. Dept. of Interior, September 1998.
8. Collin, R. E., *Field Theory of Guided Wave*, IEEE Press, New York, 1990.
9. Ghuniem, A. M., "Modes of electromagnetic wave propagation in circular concrete tunnels," *Journal of Electromagnetic Waves and Applications*, Vol. 19, No. 1, 95–106, 2005.

Handset Beamforming Synthesis Using PSO for 4G Mobile Communication Systems

K. R. Mahmoud^{1,2}, M. El-Adawy¹, Sabry M. M. Ibrahim¹
R. Bansal², and S. H. Zainud-Deen³

¹Faculty of Engineering, Helwan University, Cairo, Egypt

²Department of Electrical and Computer Engineering, University of Connecticut, CT, USA

³Faculty of Electronic Engineering, Menoufiya University, Menoufiya, Egypt

Abstract— In this paper we investigate the integration of monopole-antenna arrays into hand-held devices in the 5.0-GHz band and study their capability for beamforming synthesis. Two different antenna array configurations integrated into the handset are considered. The first geometry is a 4-element linear array, but due to its inability to maximize the electric field in a broadside direction and simultaneously minimize in the opposite direction, it has limited applications. The second geometry consists of a 5-element array; four elements located at handset corners and the fifth-element located at the center. The particle swarm optimization (PSO) algorithm is used to optimize the complex excitations of the adaptive arrays elements in a mutual coupling environment for beamforming synthesis. All numerical simulations are performed using the FEKO Suite 5.3 software. To verify the validity of numerical simulations we first perform two validation tests (one-element monopole on a handset) and compare their results with published simulated and measurement results.

1. INTRODUCTION

Mobile communication is currently one of the hottest areas that are developing at a rapid speed. The approaching 4G (fourth generation) mobile cellular systems are projected to solve still-remaining problems of 3G (third generation) systems and to provide a wide variety of new services, from high quality voice to high definition video to high-data-rate wireless channels. The most promising frequency band for these systems is the 4–5 GHz band because of spectrum availability, wide-area coverage, mobility, and low cost for the associated RF equipment [1].

Smart antenna arrays with adaptive beamforming capability are very effective in the suppression of interference and multipath signals. Therefore, applying smart antenna technology on a handset would help enhance the system capacity and quality. Much attention has been paid to the base-station design [2–5]. However, sufficient discussion has not yet been made at handset especially in the 5.0 GHz band [6].

In the array pattern synthesis, the objective function and the constraints are often highly nonlinear and nondifferentiable. Therefore, analytical methods, such as the Taylor method and the Chebyshev method, are not applicable any more. Rather, stochastic methods are necessary to deal efficiently with large nonlinear search spaces. Compared with other evolutionary algorithms such as the genetic algorithm (GA), the particle swarm optimization (PSO) algorithm is much easier to understand and implement and requires minimum mathematical processing. Therefore, in this paper the PSO is used to adjust the relative phase shifts and the amplitudes of the excitations of the array elements for beam synthesis. In particular, we investigate the appropriate integration of monopole-antenna arrays into handheld devices and study their capability for beamforming synthesis in a mutual coupling environment using the PSO algorithm. The total power delivered to all antenna elements for all cases is held constant. All numerical simulations are performed using the FEKO Suite 5.3 software. The core of the FEKO programs is based on the method of moments (MoM).

The organization of the present paper is as follows. In Section 2, a brief introduction to the particle swarm optimization algorithm is introduced. In Section 3, the validation of numerical simulations is presented. Handsets design and simulation results are discussed in Section 4. Finally, Section 5 presents the conclusions.

2. PARTICLE SWARM OPTIMIZATION (PSO) ALGORITHM

PSO is a population based optimization tool, where the system is initialized with a population of random particles and the algorithm searches for optima by updating generations [7]. Suppose

that the search space is D -dimensional. The current position of the i -th particle can be represented by a D -dimensional vector $X_i = (x_{i1}, x_{i2}, \dots, x_{iD})$ and the velocity of this particle is $V_i = (v_{i1}, v_{i2}, \dots, v_{iD})$. The best previously visited position of the i -th particle is represented by $P_i = (p_{i1}, p_{i2}, \dots, p_{iD})$ and the global best position of the swarm found so far is denoted by $P_g = (p_{g1}, p_{g2}, \dots, p_{gD})$. The fitness of each particle can be evaluated through putting its position into a designated objective function. The particle's velocity and its new position are updated as follows:

$$v_{id}^{k+1} = \omega v_{id}^k + c_1 r_1^k (p_{id}^k - x_{id}^k) + c_2 r_2^k (p_{gd}^k - x_{id}^k) \quad (1)$$

$$x_{id}^{k+1} = x_{id}^k + v_{id}^{k+1} \Delta t \quad (2)$$

where $d \in \{1, 2, \dots, D\}$, $i \in \{1, 2, \dots, N\}$, N is the population size, the superscript k denotes the iteration number, ω is the inertia weight, r_1 and r_2 are two random values in the range $[0, 1]$, c_1 and c_2 are the cognitive and social scaling parameters which are positive constants ($c_1 = 2.8$ and $c_2 = 1.3$). In this paper, the PSO algorithm is employed with a population size of 20 and 500 iterations. For beamforming synthesis, the amplitude was allowed to vary between 1.0 and 3.0 and the phase was allowed to vary between $-\pi$ and π .

A very simple objective function for the antenna array is used for maximizing the output field toward the desired signal at φ_i and minimizing the total output field in the direction of the interfering signals at φ_j .

$$\text{Objective_function} = \sum_{i=1}^N a_i E_\theta(\varphi_i) - \sum_{j=1}^M b_j E_\theta(\varphi_j) \quad (3)$$

where E_θ is the vertical field component and the constants a_i and b_j are the weights that control the contribution from each term to the overall objective function. The emphasis on E_θ is related to using vertical monopole-elements in our design. The constants N and M represent the number of desired signals and interferers respectively. In our analysis, we take the weights $a_i = 2$ and $b_j = 1$ to give some priority to maximizing the output field toward the desired signal rather than minimizing the output field in the direction of the interfering signals.

3. VALIDATION OF NUMERICAL SIMULATIONS

To verify the validity of numerical simulations we first perform two validation tests (single monopole on a handset) and compare their results with published computed and measured results. In the

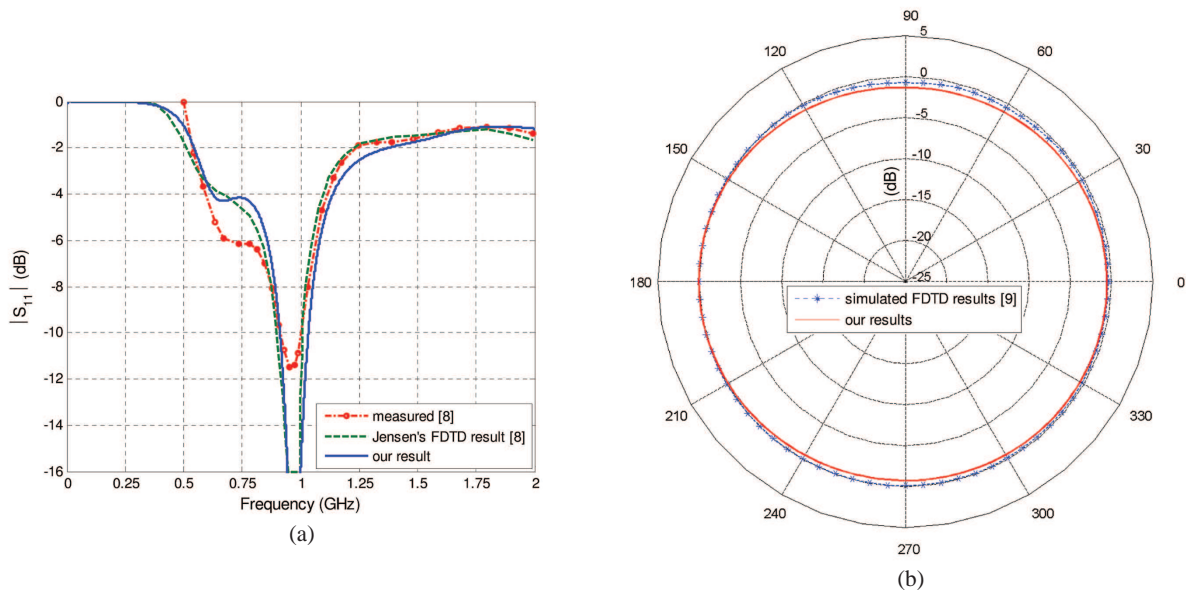


Figure 1: Comparison between our results and the published simulated and measured results. (a) Comparison between the resulting values of $|S_{11}|$ and the results obtained via FDTD technique and measurements in reference [8] for the $\lambda/4$ monopole on the handset. (b) Radiation pattern comparison between our result and the simulated pattern obtained in [9] for the $\lambda/4$ monopole on the handset at 1.9 GHz.

first validation example test, the cellular phone was modeled as a metallic box (perfect conductor), having external dimensions $1.31 \times 5.25 \times 15.1$ cm. The monopole antenna was modeled by a $\lambda/4$ metallic wire fixed on top of the metal box [8]. Figure 1(a) shows a comparison between the resulting values of $|S_{11}|$ employing the MoM-based Feko technique and the results obtained via the FDTD technique and the measurements from Ref. [8]. It can be seen that, our numerical simulation results are in good agreement with the published simulated and measured results.

In the second example, the mobile phone was modeled as a metallic box, covered with a 1.8 mm thick dielectric coating ($\epsilon_r = 2.1$), having external dimensions $45 \times 19.8 \times 117$ mm. the monopole antenna was modeled by a $\lambda/4$ metallic wire fixed on top of the metal box [9]. Figure 1(b) shows the comparison between the computed radiation pattern (horizontal plane) and the simulated pattern obtained in [9] for the $\lambda/4$ monopole on the handset at 1.9 GHz; once again good agreement is obtained.

4. HANDSETS DESIGN AND SIMULATION RESULTS

In this section, the handset has been modeled as a metallic box with the dimensions $46.4 \times 16.4 \times 96.4$ mm. These dimensions are large enough to let us design the array with a $\lambda/4$ spacing without making the overall size too large. The monopole antennas were modeled by a $\lambda/4$ metallic wire fixed on top of the metal box and fed with voltage sources. The quarter wavelength monopoles were chosen to be of radius 0.2 mm. The metal box with the attached monopoles is covered with a dielectric material ($\epsilon_r = 2.1$), having external dimensions $50 \times 20 \times 114.7$ mm. Two different antenna arrays configurations integrated into the handset will be considered and their capability for beamforming will be studied. The first geometry is a 4-element linear array and the second one consists of a 5-element array.

4.1. Four-element Monopole Array on the Handset

For the purpose of beamforming applications, an antenna array should be used. In this section, a 4-element linear array of $\lambda/4$ monopole is used. The elements are mounted on top of the metal box as shown in Figure 2.

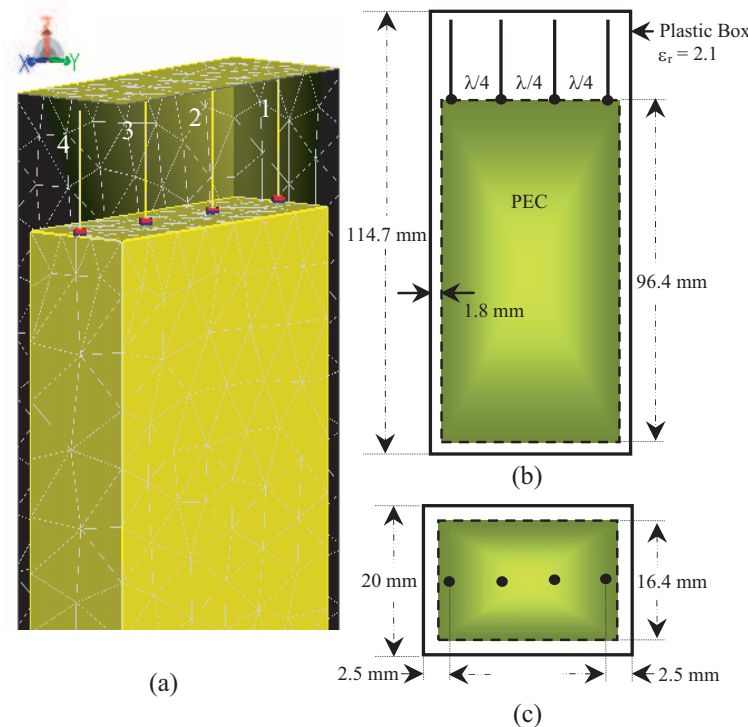


Figure 2: Geometry of four-element monopole array on mobile handset. (a) Numerical model. (b) Elevation view. (c) Top view.

As an example of adaptive beamforming, we considered two scenarios as shown in Table 1. Figures 3(a) and 3(b) show the optimized radiation patterns in the x - y plane for scenario 1 and 2 respectively. Table 2 shows the required amplitude and phase excitations of the elements to

obtain the beam patterns. Figure 3(a) shows the capability of the 4-element linear array geometry to achieve scenario 1, but Figure 3(b) shows the expected inability of a linear array to maximize the electric field in a broadside direction and simultaneously minimize in the opposite direction. Therefore, another geometry is considered.

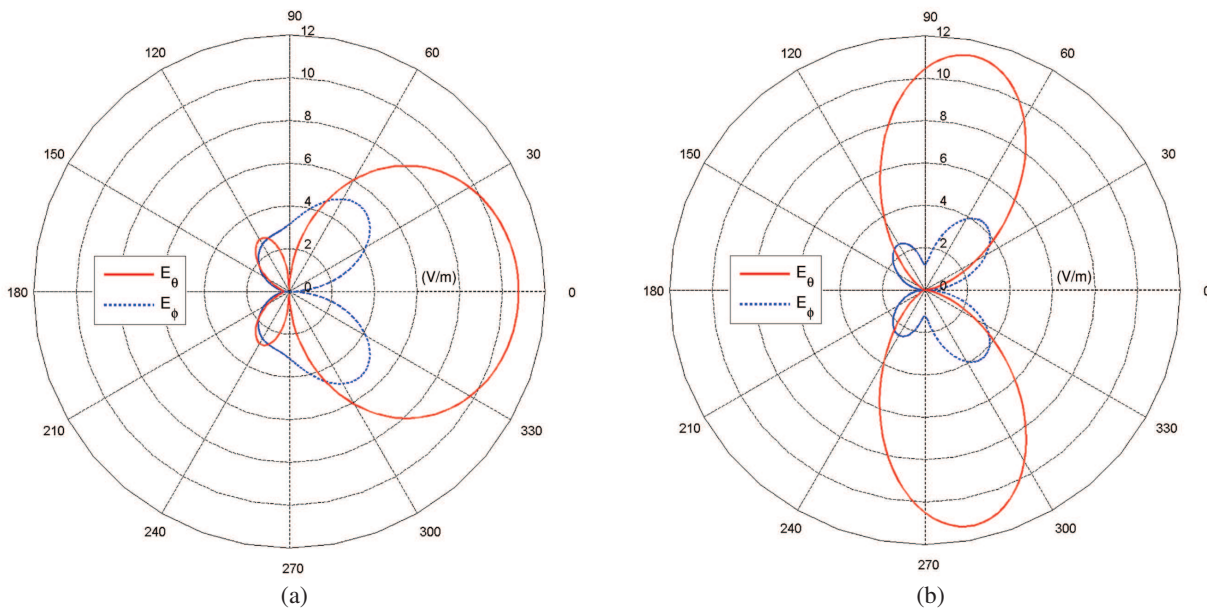


Figure 3: The radiation pattern for four-element monopole array on mobile handset. (a) Scenario #1. (b) Scenario #2.

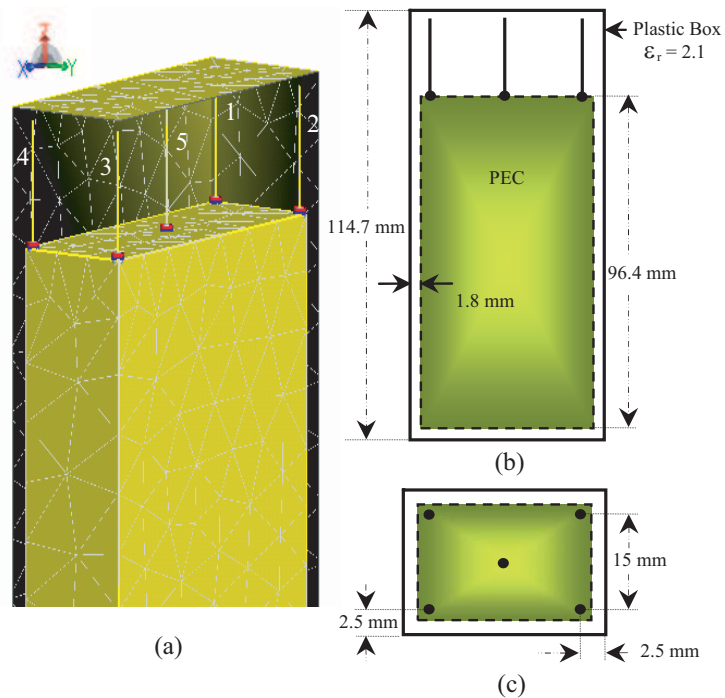


Figure 4: Geometry of five-element monopole array on mobile handset. (a) Numerical model. (b) Elevation view. (c) Top view.

4.2. Five-element Monopole Array on the Handset

The second geometry consists of a 5-element array of $\lambda/4$ monopoles; four elements located at handset corners and the fifth-element located at the center as shown in Figure 4. The same

Table 1: Descriptions of the environmental scenarios.

Scenario #1				Scenario #2			
<i>Desired</i>	<i>Interference</i>			<i>Desired</i>	<i>Interference</i>		
0°	90°	180°	270°	90°	0°	180°	270°

scenarios in Table 1 are considered in this section also.

Figures 5(a) and 5(b) show the capability of the 5-element array geometry to achieve both scenarios 1 and 2. To further illustrate the application of the technique, another case of adaptive beamforming is considered, assuming one desired source and three interferers. The signal of interest SOI impinges from $\varphi_1 = 45^\circ$ while the other three not of interest signals SNOIs are directed from $\varphi_2 = 90^\circ$, $\varphi_3 = 225^\circ$, and $\varphi_4 = 300^\circ$. Figure 5(c) shows the capability of the 5-element array

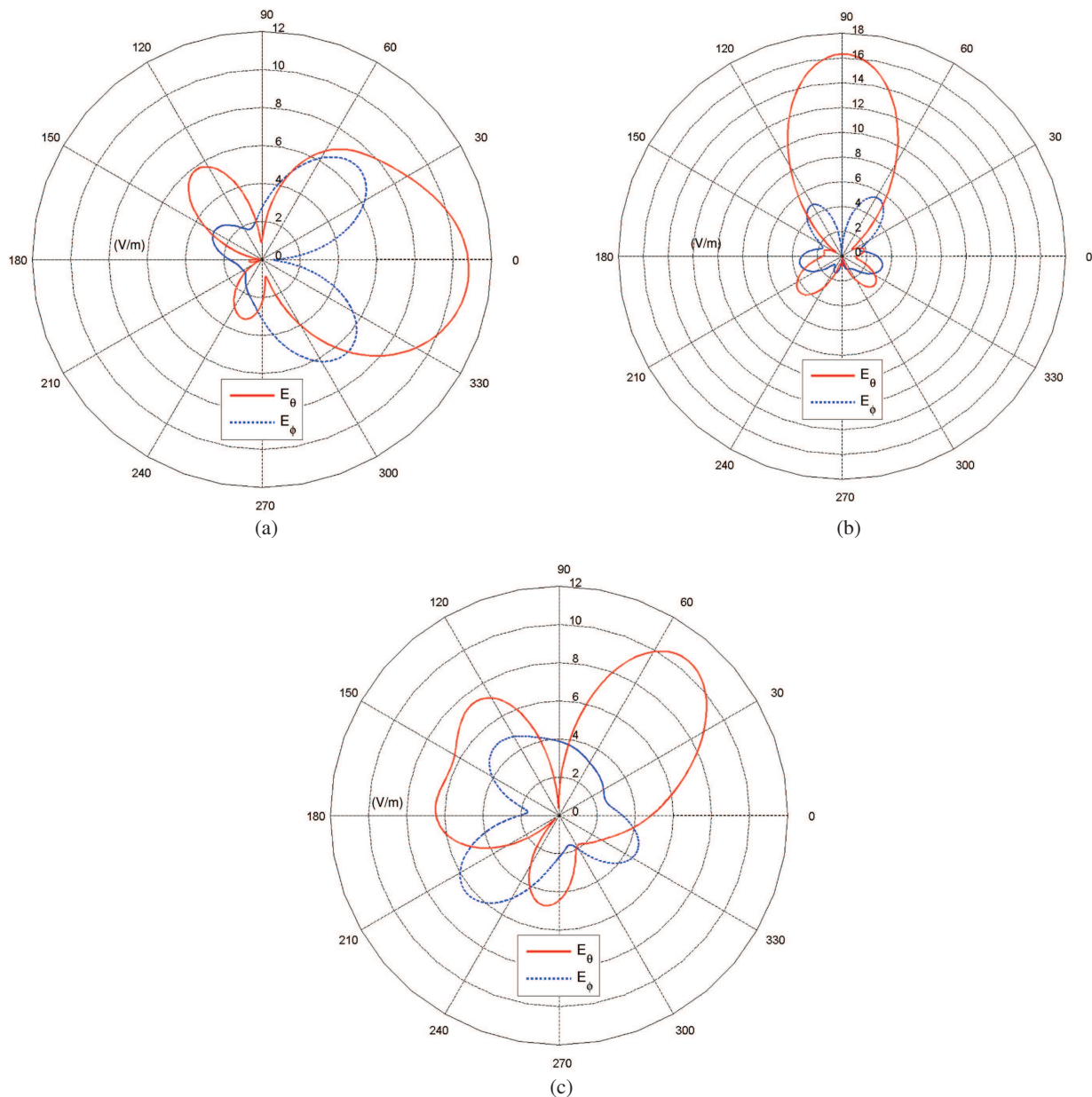


Figure 5: The radiation pattern for five-element monopole array on mobile handset. (a) Scenario #1. (b) Scenario #2. (c) Scenario #3.

Table 2: The required amplitude and phase excitations of each element for 4-element monopole array on handset.

<i>Element No.</i>	Scenario #1		Scenario #2	
	<i>amplitude</i>	<i>phase</i>	<i>amplitude</i>	<i>phase</i>
1	2.11	-139.52°	2.02	-126.28°
2	1.79	155.36°	1.11	162.27°
3	2.56	31.5°	2.31	-131.32°
4	1.50	-46.58°	2.0	147.51°

geometry to give good response in this scenario also. The required amplitude and phase excitations of each element to obtain the beam patterns in Figure 5 are shown in Table 3.

Table 3: The required amplitude and phase excitations of each element for 5-element monopole array on handset.

<i>Element No.</i>	Scenario #1		Scenario #2		Scenario #3	
	<i>amplitude</i>	<i>phase</i>	<i>amplitude</i>	<i>phase</i>	<i>amplitude</i>	<i>phase</i>
1	2.73	19.88°	1.23	22.91°	2.33	25.5°
2	2.69	8.30°	1.95	-119.03°	1.32	-127.94°
3	1.67	121.83°	2.05	-125.33°	1.15	84.1°
4	1.11	-45.55°	1.28	25.61°	2.42	154.41°
5	1.88	-143.53°	2.91	-29.09°	1.57	-146.57°

5. CONCLUSIONS

In this paper we investigated the integration of monopole-antenna arrays into handheld devices for 4G communication systems in the 5.0-GHz band and studied their capability for beamforming synthesis in a mutual coupling environment. The PSO algorithm is used to optimize the complex excitations of the adaptive arrays elements for beamforming. The results indicated that, the 4-element linear array geometry is unable to maximize the electric field in a broadside direction and simultaneously minimize in the opposite direction. Therefore a 5-element array geometry is considered: four elements located at handset corners and the fifth-element located at the center. The numerical simulation results demonstrated the feasibility of handset beamforming to nullify the effects of interfering sources.

REFERENCES

1. Sun, J., J. Sauvola, and D. Howie, "Features in future: 4G visions from a technical perspective," *Global Telecommunications Conference, 2001, GLOBECOM '01, IEEE*, Vol. 6, 3533–3537, San Antonio, TX, USA, 2001.
2. Dietrich, Jr., C. B., W. L. Stutzman, B. Kim, and K. Dietze, "Smart antennas in wireless communications: base-station diversity and handset beamforming," *IEEE Antennas and Propagation Magazine*, Vol. 42, No. 5, 142–151, October 2000.
3. Mahmoud, K. R., M. El-Adawy, R. Bansal, S. H. Zainud-Deen, and S. M. M. Ibrahim, "Analysis of uniform circular arrays for adaptive beamforming applications using particle swarm optimization algorithm," *Int. J. RF Microwave Computed Aided Eng.*, Vol. 18, 42–52, 2008.
4. Mahmoud, K. R., M. El-Adawy, S. M. M. Ibrahim, R. Bansal, and S. H. Zainud-Deen, "A comparison between circular and hexagonal array geometries for smart antenna systems using particle swarm optimization algorithm," *Progress In Electromagnetics Research*, PIER 72, 75–90, 2007.
5. Mahmoud, K. R., M. El-Adawy, R. Bansal, S. H. Zainud-Deen, and S. M. M. Ibrahim, "Performance of circular Yagi-Uda arrays for beamforming applications using particle swarm optimization algorithm," *Journal of Electromagnetic Waves and Applications*, Vol. 22, Nos. 2–3, 353–364, 2008.

6. Hirata, A., S. Mitsuzono, and T. Shiozawa, “Feasibility study of adaptive nulling on handset for 4G mobile communications,” *IEEE Antennas and Wireless Propagation Letters*, Vol. 3, 120–122, 2004.
7. Kennedy, J. and R. Eberhart, “Particle swarm optimization,” *IEEE International Conference on Neural Networks*, Vol. 4, 1942–1948, Perth, Australia, 1995.
8. Jensen, M. A. and Y. Rahmat-Samii, “EM interaction of handset antennas and a human in personal communications,” *Proceedings of the IEEE*, Vol. 83, No. 1, 1106–1113, January 1995.
9. De Salles, A. A., C. R. Ferndadez, and M. Bonadiman, “FDTD simulations and measurements on planar antennas for mobile phones,” *Microwave and Optoelectronics Conference, IMOC 2003, Proceedings of the 2003 SBMO/IEEE MTT-S International*, Vol. 2, 1043–1048, September 2003.

A New Call Handoff Technique for Next Generation Systems

P. P. Bhattacharya and Manidipa Bhattacharya

Department of Electronics and Communication Engineering, Dr. B. C. Roy Engineering College
Jemua Road, Fuljhore, Durgapur-713 206, West Bengal, India

Abstract— Since the number of users in mobile cellular system is increasing day by day, there is scarcity of free channels available for call handoff. Also the handoff process should respond faster and appropriately to maintain satisfactory QoS in microcellular environment. To take care of these problems and constraints, an algorithm is proposed, based on fuzzy logic, which considers signal strengths and availability of free channels in surrounding cells for appropriate handoff decision. The algorithm is studied, tested and found to give satisfactory results.

1. INTRODUCTION

Due to use of microcells and picocells in mobile cellular communication system there are more frequent and large number of call handoff requests which may not be complied with execution at the desired locations due to nonavailability of free channels. Successful execution of call handoff may be possible if the mobile station (MS) takes into consideration all the Base Transceiver Stations (BTS) from where it receives signal. Mobile station can take into account signal strengths from all possible BTS and available channels in each BTS so that it can find an alternative target BTS in case of nonavailability of free channels in the approaching BTS. The mobile station should also take into consideration the direction of its motion and the approaching BTS should be given priority. Considering the above points an efficient algorithm is proposed and explained in the following section.

2. PROPOSED HANDOFF ALGORITHM

Handoff algorithm based on averaging the signal strength [1] needs a suitable balance between probability of handoff and probability of outage. This problem is not there in the algorithms based on least square estimate of path loss parameters [2]. In the paper, signal strengths from two BTSs have been estimated using least square method in a nonuniform environment by changing the number of reflected paths incorporating Rayleigh fading [3]. The results for one set of reflected paths is shown in Fig. 1 and the expanded view of the region near the middle point is shown in Fig. 2 which may be called handoff decision zone. From the graph it is clear that due to random

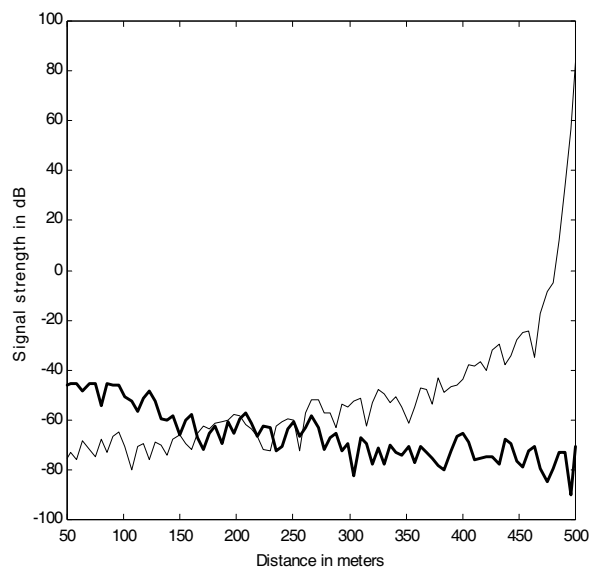


Figure 1: Received signal strength in dBm for strength in 5 and 25 number of reflecting paths. Radius of the cell = 250 meters.

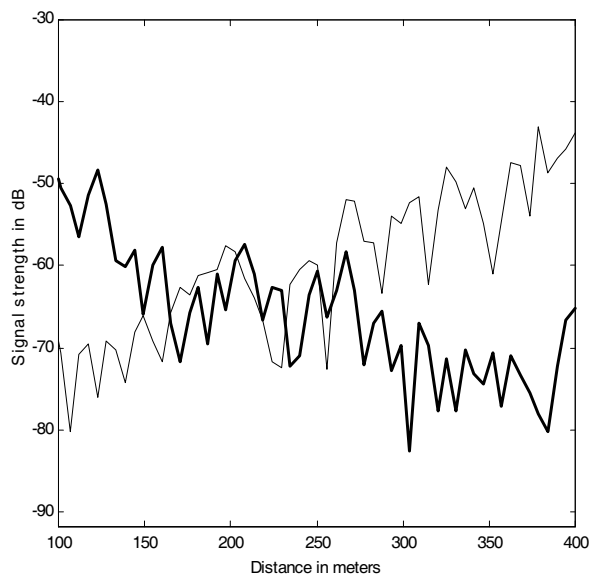


Figure 2: Expanded view of received signal dBm near handoff decision zone.

fluctuations of the signal strengths from two base transceiver stations there is chance of ping pong handoff. So designing an effective handoff algorithm is necessary. A fuzzy logic controlled handoff algorithm is thus proposed which utilizes difference in signal strengths between current BTS with the possible target BTSs, angle between direction of motion of the mobile station with the possible target BTSs and the ratio of the used channels to the total number of channels of the target BTSs as input parameters. The linguistic variables for the differences in signal strengths are assumed to be very low, low, high, very high and the membership function is chosen to be bell shaped rather than triangular or trapezoidal because with bell shaped function fluctuations are minimum and the rise time is also low and shown in Fig. 3.

In a similar way, the fuzzy sets for the angle between direction of motion of the mobile station with the target BTS are very low, low, high, very high and the corresponding bell shaped membership function are also represented in Fig. 3.

The fuzzy sets for the ratio of used channels to the total number of channels are very low, low, high, very high and the corresponding bell shaped membership function is also shown in Fig. 4.

The mobile station estimates the differences in signal strength between the current BTS and all other possible target BTSs from which it receives signal. It also calculates the information regarding the direction of its motion with all possible target BTSs and collects information regarding the used

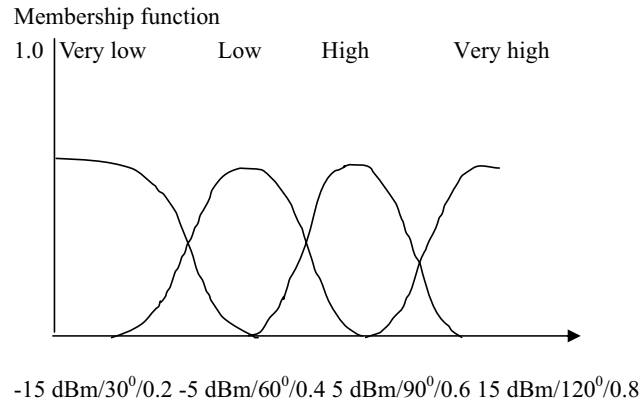


Figure 3: Membership functions for difference in signal strengths/ angle between direction of motion of the mobile station with the target BTS/ratio of used channels to the total number of channels.

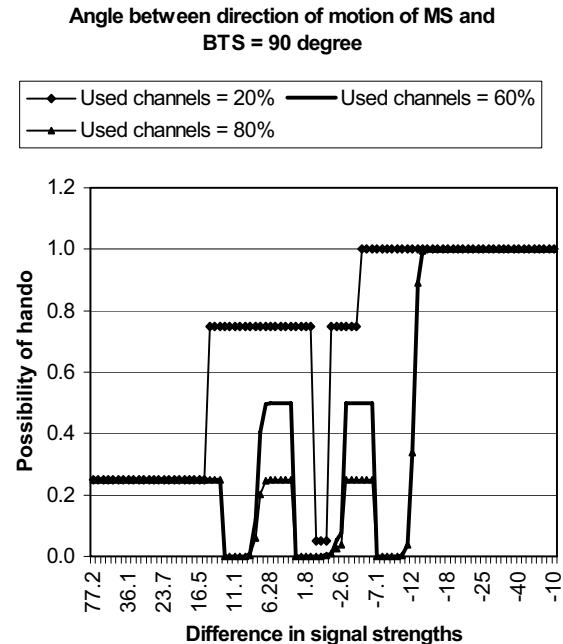
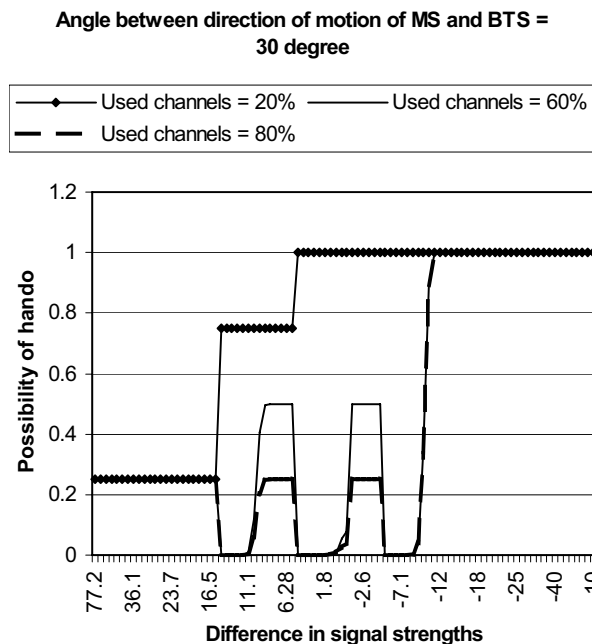


Figure 4: Possibility of handoff for 30 degree angle between motion of MS and target BTS.

Figure 5: Possibility of handoff for 90 degree between motion of MS and target BTS.

channels of the target BTSs. Then it calculates the chance of handoff based on the following fuzzy rules as shown in Table 1. It gives top priority to the BTS which makes minimum angle to its motion and which has got maximum free channels. The call will be handed over to the BTS with maximum value of possibility of handoff.

Handoff state has been defined as NO HANDOFF, WAIT, BE CAREFUL and HANDOFF and the corresponding weights have been taken as 0.25, 0.5, 0.75 and 1 respectively.

Table 1: Fuzzy rules.

Differences in signal strength	Angle between the direction of motion of MS with target BTS	Ratio of used channels to total number of channels	Handoff status		
Very High	Very high	Very high, high, low, very low	NO HANDOFF		
	High	Very high, high, low, very low	NO HANDOFF		
	Low	Very high, high, low, very low	NO HANDOFF		
	Very low	Very high, high, low, very low	NO HANDOFF		
High	Very high	Very high	NO HANDOFF		
		High	WAIT		
		Low, very low	BE CAREFUL		
	High	High	Very high	NO HANDOFF	
			High	WAIT	
			Low, very low	BE CAREFUL	
	Low	Low	Very high	NO HANDOFF	
			High	WAIT	
			Low, very low	BE CAREFUL	
		Very low	Very low	Very high	NO HANDOFF
				High	WAIT
				Low, very low	BE CAREFUL
Low	Very high	Very high	NO HANDOFF		
		High	WAIT		
		Low, very low	BE CAREFUL		
	High	High	Very high	NO HANDOFF	
			High	WAIT	
			Low, very low	BE CAREFUL	
	Low	Low	Very high	NO HANDOFF	
			High	WAIT	
			Low	BE CAREFUL	
		Very low	Very low	Very low	HANDOFF
				Very high	NO HANDOFF
				High	WAIT
	Very low	Very high	Very high, high	WAIT	
			Low, very low	BE CAREFUL	
		High	Very high, high, low	BE CAREFUL	
			Very low	HANDOFF	
Low		Very high, high	BE CAREFUL		
		Low, very low	HANDOFF		
Very low		Very high, high, low, very low	HANDOFF		

3. RESULTS

In the averaging signal strength method handoff takes place much earlier and takes much time to become steady [4]. In this work possibility of handoff requests have been calculated using the fuzzy rules as per Table 1 for different values of angle between MS and target BTS for three sets of values of used number of channels. Possibility of handoff for 30 degree and 90 degree angles between direction of motion of MS and target BTS are shown in Figs. 4 and 5 respectively. Each figure shows three plots for 20%, 60% and 80% values of used channels. The handoff possibility increases for low values of used channels. Since bell shaped membership functions have been chosen the response does not fluctuate much and the rise time is also low. The results are tested with a velocity dependent fuzzy logic based algorithm [5] shown in Fig. 6. The present algorithm performs better because the fluctuations are lower in this case.

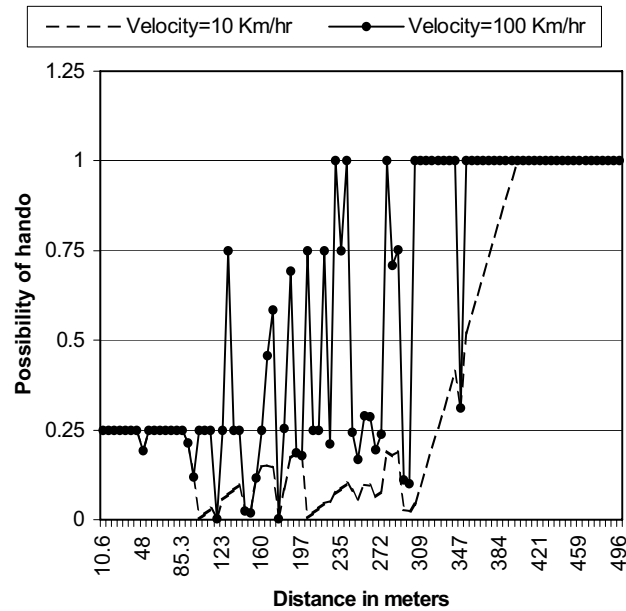


Figure 6: Possibility of handoff for 150 degree angle between motion of MS and target BTS.

4. CONCLUSION

It may be noted from the results that the present algorithm works efficiently and quickly responds to the difference in signal strengths, angle between MS velocity and used soft capacity. The number of fluctuations are also low, so the algorithm can be implemented in a small scale fading environment. Since there is crisis of free channels due to high demand by the users, this algorithm may be an effective solution. The software programs for the proposed algorithm are neither complex nor consumes much time to respond. Hence, it can be easily embedded into application programs and can be implemented in real systems. Since the software has controlled complexity and it is thoroughly tested, the codes can be burned-in at the system ROM.

REFERENCES

1. Vijayan, R., et al., "A model for analyzing handoff algorithms," *IEEE Transaction on Vehicular Technology*, Vol. 42, 351–356, August 1993.
2. Benvenuto, N. and F. Santucci, "A least square path loss estimation approach to handoff algorithms," *IEEE Transaction on Vehicular Technology*, Vol. 48, 437–447, March 1999.
3. Bhattacharya, P. P. and P. K. Banerjee, "A least square path loss estimation for mobile communication under rayleigh fading environment," *Proc. of Computer and Devices for Communication, CODEC 2004*, India.
4. Edwards, G. and R. Sankar, "Microcellular handoff using fuzzy techniques," *Wireless Networks*, Vol. 4, 401–409, 1998.
5. Bhattacharya, P. P. and P. K. Banerjee, "User velocity dependent call handoff management," *International Journal HIT Transaction on ECCN*, Vol. 1, No. 3, 150–155, July 2006.

A GLEMFCFS Coupled Modeling and Inversion for Icing Disaster on High Voltage Lines

Ganquan Xie^{1,2}, Jianhua Li¹, Feng Xie¹, and Tong Kang²

¹GL Geophysical Laboratory, USA

²Communication University of China, China

Abstract— In this paper, we propose a EM-Flow-Cold-Stress (GLEMFCFS) coupled modeling and inversion for icing disaster on high voltage lines, in short, we call it GLEMFCFS ICINGS modeling and inversion. The GLEMFCFS ICINGS modeling imaging can be used to display the EM, flow, temperature, and icing crystal stress field dynamically on the high voltage lines and recover, adjust, monitor, and control the EM, flow, cold temperature, icing stress, distance of iron tower supports, and electric network parameters, such that the icing disaster minim. These simulations show that the GLEMFCFS coupled modeling and inversion can be used to reconstruct high resolution imaging of icing disaster processes on high voltage lines. That is very useful for fabricating no icing materials and icing disaster alert and measurement sensor for protecting high voltage lines network.

1. INTRODUCTION

During Chinese Lunar New year, from January 8 to February 8, 2008, there had been serious icing disaster in South of China and North of Nanling mountain that never been happen in recent 100 years. The icing disasters were extremely serious in Hunan, Guizhou, Jiangxi, Hubei, Anhui, Zhejiang, and Jiangsu etc. provinces. The icing on the high voltage wire lines to form very big and length ice cylinders with diameter 350 mm to 500 mm. The big and length ice cylinders flying on the high voltage wire lines produce big tense forces between the iron and steel towers such that the iron towers collapsed and destroyed power network and caused power down in very large areas of the above provinces. The icing disaster may be repeatedly happen in China or other places in the world. Therefore, in this paper, we propose the GLEMFCFS Icing Coupled modeling and inversion for solving icing disaster on high voltage lines. We have proposed 3D GL and AGILD Electromagnetic (EM)-Flow-Heat-Stress coupled modeling (GLEMFHFS) in PIERS 2007 in Beijing and published the method in PIERS Online [1]. In this paper, we propose a EM-Flow-Cold-Stress (GLEMFCFS) coupled modeling and inversion for icing disaster on high voltage lines. The GLEMFCFS method is necessary and have important and wide applications to investigate and reduce the strange and serious icing, earthquake, and other disaster. On May 11, 2008, Author had wrote alert that after icing disaster, a unknown extremely large disaster will be coming. Next day the Wenchuan Earthquake was happen. The patent of the GLEMFCFS ICINGS modeling and inversion and all rights are reserved by authors in GL Geophysical Laboratory.

The presentation of this paper is as follows. The introduction is described in Section 1. In Section 2, we present the EM, flow, cold and crystal stress coupled model. In Section 3, we propose the Global and Local EM, flow, cold and crystal stress field coupled modeling. The GL magnetic field Modeling in the cylindrical coordinate is proposed in Section 4. In Section 5, we describe the some simulations and conclusions.

2. THE EM, FLOW, COLD, AND STRESS COUPLED MODEL

2.1. The Electromagnetic Model

We consider electromagnetic field in the icing crystal. The Maxwell flow equation governs the EM field and cold flow in around of the high voltage lines. The rotational cold fluid icing and magnetic field generates the induction electric field which couples EM and flow field as follows [3, 4],

$$\begin{aligned}\nabla \times E &= -i\omega\mu H, \\ \nabla \times H &= (\sigma + i\omega\varepsilon)E + (\sigma + i\omega\varepsilon)\mu V \times H + J,\end{aligned}\tag{1}$$

where E is the electric field, H is the magnetic field, V is the cold flow velocity, J is the electric current, σ is the electric conductivity, ε is the dielectric, μ is the magnetic permeability, and ω is the angle frequency.

2.2. The Incompressible Viscous Flow Model

The incompressible viscous steady icing cold flow is governed by the Navier Stocks flow equation [3, 4],

$$-\eta\Delta V + \rho(V \cdot \nabla)V + \nabla p = J \times \mu H - \beta\rho Tg, \quad (2)$$

where V is the flow velocity vector, p the hydrodynamic pressure, H is the magnetic field, T is the cold temperature, ρ is the density which depends on the temperature, η is the viscosity, β is thermal expansion coefficient. g is the gravity acceleration, μ is the magnetic permeability.

2.3. The Thermal Cold Model

In the icing, the magnetic permeability is μ_0 , the conductivity and dielectric are variable. The thermal heat should be coupled into EM field in the icing flow motion as follows [3, 4],

$$\Delta T - q(V \cdot \nabla)T = h(E, H, V) \quad (3)$$

where T is the temperature, $q = \rho/\kappa$, ρ is the density, κ is the thermal conductivity, V is the flow velocity vector, h is the cold source which is nonlinear function of the electric field E , magnetic field H , and flow velocity V .

2.4. The Boundary Condition

The magnetic field H , flow velocity field V , and temperature T are coupled by the Equations (1), (2), and (3) nonlinearly. The magnetic field H and temperature T are of the far field radiation at the infinite. The boundary condition of the velocity is two phase.

2.5. The Displacement and Stress Model in Icing Crystal

The water solidification displacement and stress model in the icing crystal are governed by the following elastic-plastic flow thermal magnetic joint equation [3, 4],

$$\begin{aligned} \frac{\partial \sigma_{s,ij}}{\partial x_j} + \omega_s^2 \rho_s \mu_s &= f_i(B, p, T), \\ \sigma_{s,ij} &= D(\lambda_s, \mu_s) \varepsilon_s(\mu_s), \end{aligned} \quad (4)$$

and the corresponding boundary condition or radiation boundary conditions, where $\sigma_{s,ij}$ is solidification stress tensor which symbol is different from the electric conductivity, μ_s is the displacement which symbol is different from the vortex $\mu = \nabla \times V$, ω_s is displacement frequency which is very low and different from the EM field frequency ω , ρ_s is the density which is different from the resistivity, λ_s, μ_s are the Lamé constants, μ_s is different from the magnetic permeability. ε_s is the strain field which is different from the dielectric parameter, the right hand of the (4), $f_i(B, pT)$, depends on the magnetic flux B , pressure p , and temperature T .

3. GL EMFCS COUPLED MODELING

The novel Global and Local field modeling and inversion is proposed in [3], we propose GL EMFCS COUPLED MODELING in this section [4–6].

3.1. Iteration for Solving the Coupled Nonlinear Equations

We use the following iteration to solve the EM, Navier Stocks flow, heat, and mechanical coupled nonlinear Equations (1)–(4).

$$\nabla \times \frac{1}{(\sigma + i\omega\varepsilon)} \nabla \times H^{(n)} + \left(\nabla \times \mu V^{(n-1)} \times H^{(n)} \right) = Q_M, \quad (5)$$

$$-\eta\Delta V^{(n)} + \rho \left(V^{(n-1)} \cdot \nabla \right) V^{(n)} + \nabla p = J^{(n)} \times \mu H^{(n)} - \beta\rho T^{(n-1)}g, \quad (6)$$

$$\Delta T^{(n)} - q \left(V^{(n)} \cdot \nabla \right) T^{(n)} = h \left(E^{(n)}, H^{(n)}, V^{(n)} \right). \quad (7)$$

We solve the linearization Equations (5), (6), and (7) in order to form the n th circle of the iteration. Then we solve the following elastic-plastic flow thermal magnetic joint Equation (4) to find the icing solidification displacement, strain and stress,

$$\frac{\partial \sigma_{s,ij}^{(n)}}{\partial x_j} + \omega_s^2 \rho_s u_s^{(n)} = f_i \left(B^{(n)}, p^{(n)}, T^{(n)} \right), \quad \sigma_{s,ij}^{(n)} = D(\lambda_s, \mu_s) \varepsilon_s \left(u^{(n)} \right). \quad (8)$$

3.2. Division of the Domain

The inhomogeneous EM, flow, thermal, and mechanical parameter domain Ω is divided into a set of the several sub domains $\{\Omega_k\}$, $k = 1, 2, \dots, N$. such that $\Omega = \bigcup_{k=1}^N \Omega_k$. The division is mesh or meshless.

3.3. GL Modeling for Solving the Magnetic Field Linearization Equation (5)

(3.3.1) In each Ω_k , $k = 1, 2, \dots, N$, we solve the adjoint Green's magnetic field differential integral equation of the Equation (4). By the dual curl procession, the adjoint Green's magnetic field differential integral equations are reduced into 3×3 matrix equations. By solving the 3×3 matrix equations, the 3×3 magnetic Green's function tensor $G_k^{M,(n)}(r', r)$ is calculated.

(3.3.2) The global magnetic field is updated by the following local scattering magnetic field differential integral equation

$$H_k^{(n)}(r) = H_{k-1}^{(n)}(r) + \int_{\Omega_k} \left(\frac{1}{(\sigma + i\omega\varepsilon)_{k-1}} - \frac{1}{(\sigma + i\omega\varepsilon)_k} \right) \nabla \times G_k^{M,(n)}(r', r) \left(\nabla \times H_{k-1}^{(n)}(r') \right) dr' \\ + \int_{\Omega_k} \left(\nabla \times \left(G_k^{M,(n)}(r', r) \right) \times \mu \left(V_{k-1}^{(n)} - V_k^{(n)} \right) \right) H_{k-1}^{(n)}(r') dr'. \quad (9)$$

The $H^{(n)}(r) = H_N^{(n)}(r)$ is the GL magnetic field solution of the Equation (5) [4, 5].

3.4. GL Modeling for Solving the Flow Field Linearization Equation (6)

Let $u = \nabla \times V$, the Navier Stocks flow Equation (6) is reduced to

$$\Delta u^{(n)} - \kappa \left(V^{(n-1)} \cdot \nabla \right) u^{(n)} = M \left(E^{(n)}, H^{(n)}, T^{(n)} \right), \quad (10)$$

where $\kappa = \rho/\eta$,

(3.4.1) In each Ω_k , $k = 1, 2, \dots, N$, we solve the adjoint Green's flow field differential integral equation of the Navier Stocks Equation (10). By the dual gradient procession, the adjoint Green's flow field differential integral equations are reduced into 3×3 matrix equations. By solving the 3×3 matrix equations, the 3×3 magnetic Green's function tensor $G_k^{F,(n)}(r', r)$ is calculated.

(3.4.2) The Global flow field is updated by the following local scattering flow field differential integral equation

$$u_k^{(n)}(r) = u_{k-1}^{(n)}(r) + \int_{\Omega} \nabla \cdot \left(\left(\kappa_k V_k^{(n-1)}(r') - \kappa_{k-1} V_{k-1}^{(n)}(r') \right) G_k^{F,(n)}(r', r) \right) u_{k-1}^{(n)}(r') dr', \quad (11)$$

The $u^{(n)}(r) = u_N^{(n)}(r)$ is the GL flow field solution of the Equation (10). $V^{(n)} = \frac{1}{4\pi} \int_{\Omega} \frac{\nabla \times u^{(n)}(r')}{|r'-r|} dr'$

is the GL Navier Stocks flow velocity solution of the Equation (6), The pressure $p^{(n)} = \frac{1}{4\pi} \int_{\Omega} \frac{\nabla \cdot (\rho(V^{(n)} \cdot \nabla)V^{(n)}) + \nabla \cdot (J^{(n)} \times \mu H^{(n)} - \beta \rho T^{(n-1)} g)}{|r'-r|} dr'$ is obtained [4, 5].

3.5. GL Modeling for Solving the Thermal Temperature Field Linearization Equation (7)

(3.5.1) In each Ω_k , $k = 1, 2, \dots, N$, we solve the adjoint Green's thermal field differential integral equation of the heat Equation (7). By the dual gradient procession, the adjoint Green's temperature field differential integral equations are reduced into 3×3 matrix equations. By solving the 3×3 matrix equations, the 3×3 temperature Green's function tensor $G_k^{H,(n)}(r', r)$ is calculated.

(3.5.2) The Global temperature field is updated by the following local scattering temperature field differential integral equation

$$T_k^{(n)}(r) = T_{k-1}^{(n)}(r) + \int_{\Omega} \nabla \cdot \left(\left(q_k V_k^{(n)}(r') - q_{k-1} V_{k-1}^{(n)}(r') \right) G_k^{H,(n)}(r', r) \right) T_{k-1}^{(n)}(r') dr'. \quad (12)$$

The $T^{(n)}(r) = T_N^{(n)}(r)$ is the GL temperature field solution of the Equation (7) [4, 5].

3.6. GL Modeling for Solving the Elastic-plastic Flow Thermal Magnetic Linearization Equation (8)

(3.6.1) In each Ω_k , $k = 1, 2, \dots, N$, we solve the adjoint Green's flow field differential integral equation of the mechanical elastic Equation (8). By the dual gradient procession, the adjoint Green's displacement field differential integral equations are reduced into 3×3 matrix equations. By solving the 3×3 matrix equations, the 3×3 magnetic Green's function tensor $G_k^{D,(n)}(r', r)$ is calculated.

(3.6.2) The Global displacement field is updated by the following local scattering displacement and strain field differential integral equation

$$\vec{u}_{s,k}^{(n)}(r) = \vec{u}_{s,k-1}^{(n)}(r) - \int_{\Omega_k} \vec{\varepsilon}^T \left(\vec{G}_k^{D,(n)}(r', r) \right) D(\lambda_{s,k} - \lambda_{s,k-1}, \mu_{s,k} - \mu_{s,k-1}) \vec{\varepsilon} \left(\vec{u}_{s,k-1}^{(n)}(r') \right) dr', \quad (13)$$

The $\vec{u}_s^{(n)}(r) = \vec{u}_{s,N}^{(n)}(r)$ is the GL displacement field solution of the Equation (8), $\sigma_{s,ij}^{(n)} = D(\lambda_s, \mu_s)$ $\varepsilon_s(u_{s,N}^{(n)})$ is the solidification stress tensor [4, 5].

4. GL EMFCS COUPLED MODELING IN CYLINDRICAL SYSTEM

We derive the 3D and 2.5D magnetic differential integral equations in the space frequency domain in the cylindrical coordinate system in this section [2, 3]. We call the equations to be the cylindrical magnetic field differential integral equations. Using these cylindrical magnetic flow, cold temperature, crystal stress field differential integral equations, we construct new GLEMFCS coupled modeling in cylindrical system.

4.1. The 3D Cylindrical Magnetic Field Differential Integral Equation

Upon substituting the field and coordinate transformation between the rectangle and cylindrical coordinate system, we derive the 3D magnetic field differential integral equation in the cylindrical coordinate system is as follows

$$\begin{aligned} FH3(H, H_{b\rho}, H_b^{M\rho}, E_b^{M\rho}) &= H_{b\rho} + \int_{\Omega} \frac{((\sigma + i\omega\varepsilon) - (\sigma_b + i\omega\varepsilon_b))}{(\sigma + i\omega\varepsilon)} \left\{ E_{b\rho}^{M\rho} \left(\frac{1}{\rho'} \frac{\partial H_z}{\partial \theta} - \frac{\partial H_\theta}{\partial z} \right) \right. \\ &\quad \left. + E_{b\theta}^{M\rho} \left(\frac{\partial H_\rho}{\partial z} - \frac{\partial H_z}{\partial \rho'} \right) + E_{bz}^{M\rho} \left(\frac{1}{\rho'} \frac{\partial}{\partial \rho'} (\rho' H)_\theta - \frac{1}{\rho'} \frac{\partial H_\rho}{\partial \theta} \right) \right\} \rho' d\rho' d\theta dz, \quad (14) \\ H_\rho(r) &= FH3(H, H_{b\rho}, H_b^{M\rho}, E_b^{M\rho}) \\ H_\theta(r) &= FH3(H, H_{b\theta}, H_b^{M\theta}, E_b^{M\theta}) \\ H_z(r) &= FH3(H, H_{bz}, H_b^{Mz}, E_b^{Mz}) \end{aligned} \quad (15)$$

where E is the electric field, H is the magnetic field, E_b^m and H_b^m is Green function exciting by the magnetic dipole source, $E_b^m(r', r)$ has weak and integrative singular at $r = r'$, the r locates in the outside boundary of strip or in the subsurface with $\rho' = 0$, the r' locates in $\partial\Omega$ -, the internal boundary of the strip, therefore, the 3D strip magnetic field differential integral equation has no coordinate singular at pole $\rho' = 0$. It has integrative weak singular kernel.

4.2. The 2.5D Magnetic Field Differential Integral Equation

Substituting the EM field Fourier series, $H(\rho, \theta, z) = \sum_{m=-\infty}^{\infty} H_m(\rho, z)e^{im\theta}$, into the 3D cylindrical magnetic field differential integral Equation (14), we derive the 2.5D equations in the cylindrical coordinate system.

4.3. GL EMFCS Coupled Modeling in Cylindrical System

Similar with the 3D cylindrical magnetic field differential integral equation in Subsection 4.1 and 2.5 D cylindrical magnetic field differential integral equation in Subsection 4.2, we can derive the 3D and 2.5D EM, Flow, Cold temperature, crystal stress field differential integral equations and corresponding Green's function tensor equations in the cylindrical coordinate system. Using these cylindrical magnetic, flow, cold temperature, crystal stress field differential integral equations, we construct new GLEMFCS coupled modeling in cylindrical system.



Figure 1: A practical icing crystal cylinder with diameter 500 mm.



Figure 2: Simulation of icing crystal deformation on January 13, 2008, the diameter of the icing crystal cylinder is 100 mm.

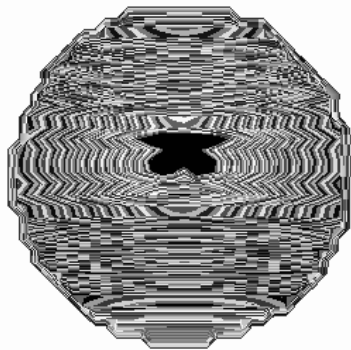


Figure 3: Simulation of icing crystal deformation on January 22, 2008, the diameter of the icing crystal cylinder is 300 mm.

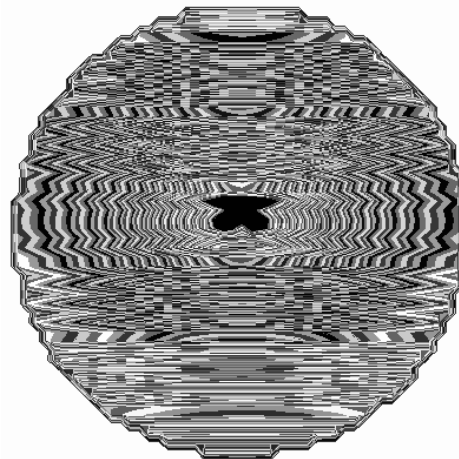


Figure 4: Simulation of icing crystal deformation on February 1, 2008, the diameter of the icing crystal cylinder is 500 mm.

5. SIMULATIONS AND CONCLUSIONS

A practical icing crystal cylinder on high voltage lines is shown in the Figure 1. The several simulations of the GLEMFCs coupled modeling and inversion for icing disaster on high voltage lines are performed. The icing crystal development and its crystal deformation are shown in the Figures 2, 3, and 4. Figure 2 shows the simulation of icing crystal deformation with diameter 100 mm on January 13, 2008. Figure 3 shows the simulation of icing crystal deformation with diameter 300 mm on January 21, 2008. Figure 4 shows the simulation of icing crystal deformation with diameter 500 mm on February 1, 2008. Because gravity and cold temperature are not axis symmetry, the crystal deformation are not axis symmetry. These simulations show that the GLEMFCs coupled modeling and inversion have advantages [5, 6] over FEM and FD method and can be used to reconstruct high resolution imaging of icing disaster processes on high voltage lines. That is very useful for fabricating no icing materials and icing disaster alert and measurement sensor for protecting high voltage lines network. After these simulation, author found that the icing disaster in Southern of China and other phenomenon that the day became dark night in Beijing from 9:30 AM to 10:30 AM on May 3, 2008 are very strange electromagnetic and flow changing around the mainland. These phenomenon is directly relative to Earth temperature and gravity and stress being changed. On May 11, 2008, Author had wrote alert that a unknown extremely large disaster will be coming. Next day the Wenchuan earthquake was happen.

ACKNOWLEDGMENT

The authors are grateful to Professor P. D. Lax Professor and Feng Duan for his attention and encouragement to our research works. Authors are grateful to Professor Yuesheng Li for his discussion. Authors grateful to Professor Lin and Professor Cui in Chinese Academy, Professor Cai in Beijing University, Professor Wang and Professor Huang in Tsinghua University, Professor Tian in Changsha Technology University, Professor Lu in Hunan Road Bridge Company, President Lv and Professor Lu in Chinese Communication University for their discussion and help.

REFERENCES

1. Xie, G., J. Li, L. Xie, F. Xie, and J. Li, "The 3D GL EM-Flow-Heat-Stress coupled modeling," *PIERS Online*, Vol. 3, No. 4, 411–417, 2007.
2. Xie, G., J. H. Li, J. Li, and F. Xie, "3D and 2.5D AGLID EMS stirring modeling in the cylindrical coordinate system," *PIERS Online*, Vol. 2, No. 5, 505–509, 2006.
3. Xie, G., J. Li, and J. H. Li, "New AGILD EMS electromagnetic field modeling," *PIERS Online*, Vol. 1, No. 2, 168–172, 2005.
4. Li, J., L. Xie, G. Xie, and J. Li, "A GLEMFHS EMS imaging using the GL EM-Flow-Heat-Stress coupled modeling," *Progress In Electromagnetics Research Symposium Abstracts*, 178, Hangzhou, 2008.
5. Xie, G., F. Xie, L. Xie, and J. Li, "New GL method and its advantages for resolving historical difficulties," *Progress In Electromagnetics Research*, PIER 63, 141–152, 2006.
6. Xie, G., J. Li, L. Xie, and F. Xie, "GL metro carlo EM inversion," *Journal of Electromagnetic Waves and Applications*, Vol. 20, No. 14, 1991–2000, 2006.

The Computation of Electromagnetic Field on Torus Knots

Jianshu Luo and Xufeng Zhang

College of Science, National University of Defence Technology, Changsha 410073, China

Abstract— In this paper, we study the applications of low-dimensional topology — knot theory in the calculation of electromagnetic fields. The electromagnetic properties of a kind of special form of knot-torus knot are discussed, and the main content and innovative results are as follows:

First, in order to analyse the antenna radiation and scattering properties, the surface current distribution of antenna under the excitation of incident or impressed field is needed, which requires solution of the electric field or magnetic field integral equation (EFIE or MFIE). In this paper, a new EFIE is derived based on another famous Electric Field Integral Equation-Hallen Integral Equation for an arbitrary curved wire.

Second, for the torus knot wire, proved that its self-inductance also can be calculated by the Neumann formula by making use of the concept of knot's Seifert surface, and gives the formula and numerical analysis.

1. INTRODUCTION

Since the period of Gauss and Maxwell, they have realized that topology played a very important part in the computation of electromagnetic field. At present, topology has already had various applications in the computation of electromagnetic field [1], and what's more, it acts a much more important role in a branch of low dimension–knot theory.

In 1980s, the breakthrough of low dimensional topology attracted many a scholars, not only on mathematics, but also a lot on other science subjects and engineering. Besides the applications in the different fields, such as plasma physics, polymer science and molecular biology [2, 3], knot theory even has made significant progress. The knot theory is used to be combined with the Maxwell equation in electromagnetics to study the related electromagnetism characteristics, which is mainly about how the topology of knot and geometric properties affect the electromagnetic field.

O. Manuar and D. L. Jaggard in Pennsylvania University did some research on the electromagnetic scattering of the ideal fine knot conductor. Their original study shows that the chirality and the degree of the kink can be derived by the backscatter of electromagnetic wave [4]. Their research were based on the trefoil knot, because trefoil knot is the most simple non-trivial knot, which can be made by knotting a rope and then combining the two ends. They further compared the different backscatter qualities between trefoil knot and the corresponding trivial knot (trivial trefoil knot) [5, 6]. The different topological characteristics between the two cause the significant differences of their scattering natures. Additionally, they studied the important role symmetrical characteristic played in scattering [7]. Douglas H. Werner in Pennsylvania University did a lot of important work on the radiation and scattering natures of the ideal fine knot conductor. He made use of the parameterization expression of torus knot and deduced the radiation expression and scattering natures of the ideal fine knot conductor. He obtained the special integral equation which was suited for the analysis of torus knot radiation and scatter problems, and he illustrated that the familiar loop antenna could be gained as the special form of torus knot [8, 9]. In addition to that, he extended the above-mentioned achievements to elliptic torus knot and proved that torus knot, loop antenna and electric dipole could also be gained as the special form of elliptic torus knot [10].

On the other hand, a great many of achievements on magnetic field containing torsional field structure has been obtained. Woltjer introduced the concept of helicity to magnetic field, which can be expressed as $\mathcal{H} = \int_V \vec{A} \cdot \vec{B} dV$. The helicity is the constant of lossless magnetohydrodynamics equation of motion and a gauge invariant in simply connected region. Arnold brought in the concept of asymptotic Hopf invariant [11] and showed helicity as an average of a pair of field lines asymptotic linking numbers. There is a strong connection among helicity, knot theory and related linking theory, which can be expressed as the helicity sum of torsion, wringing and linking. Helicity is also closely connected with magnetic energy [12–14], which is showed as

$$E = \frac{1}{2} \int_V \vec{J} \cdot \vec{A} dV = \frac{1}{2\mu_0} \int_V \vec{A} \cdot (\nabla \times \vec{B}) dV = \frac{1}{2\mu_0} \int_V \alpha \vec{A} \cdot \vec{B} dV$$

for forceless field. When α is a constant, it can be moved outside of the integral symbol. The magnetic energy field equals to the product of α and total magnetic helicity. A. Y. K. Chui, H. K. Moffatt and G. E. Marsh studied the computation of magnetic energy in multiply connected domain [15–17]. Additionally, Ranada utilized Hopf invariant to give a definition to electromagnetic knot, which is a vacuum radiation field where $\vec{E} \cdot \vec{B} = 0$. He proved that except for a measure zero, any radiation field equals to the sum of this kind of fields partly.

2. SELF INDUCTANCE AND SELF-INDUCTION COEFFICIENT

When electricity of a coil changes, its magnetic field changes according to its own magnetic flux (or magnetic linkage), which makes the coil itself generate induced electromotive force. This kind of induction phenomena caused by the changes of electricity in coils is called self inductance, and the induced electromotive force it generated is self induction electromotive force. We have already known that magnetic induction generated by the electricity in coils is directly proportional to the electricity; therefore, magnetic linkage is proportional to the electricity, that is,

$$\Psi = LI \quad (1)$$

In this expression, L is proportionality coefficient and has nothing to do with the electricity in coils (this only happens when ferromagnetic substance doesn't exist. If it does, then proportionality coefficient is possibly related to the electricity in coils). It just depends on the size, geometrical shape, number of turns and the surrounding magnetic medium of the coils. When the electricity in coils is changing, Ψ will be changing at the same time. According to faraday's law, the induced electromotive force should be,

$$\varepsilon = -L \frac{dI}{dt} \quad (2)$$

From this expression, we could see, for the same current rate, the bigger the proportionality coefficient L is, the stronger induction electromotive force coils can generate, namely, the stronger the self inductance will be. The proportionality coefficient L is called self-induction coefficient, self-induction for short, and H is its unit.

When coils are connected with current source, because of self-induction, the current $i(t)$ won't turn to stable value I from 0 immediately. Instead, the change has to go through a period of time. In this course, the current will be accumulating. Thus, there will be reverse induction electromotive force. External power ε not only has to supply circuit with energy to generate joule heat, but oppose self induction electromotive force applying work. During the period dt , the work done when the electromotive force of current source opposes self induction electromotive force, the work should be,

$$dW = -\varepsilon_L i dt$$

In this expression, $i = i(t)$ is the instantaneous value, and ε_L is $\varepsilon_L = -L \frac{dI}{dt}$
Thus

$$dW = L i di$$

In the entire course of the building of current, the work made by the opposition of electromotive force of current source to self induction electromotive force is,

$$E = \int dE = \int_0^I L i di = \frac{1}{2} L I^2$$

The work is stored in the coils in the form of energy. When the current is cut, the current will be reduced to 0 from the stable value I , and the coils will generate self induction electromotive force with the same direction as the current. All the original energy stored in coils will be released through self induction electromotive force. The work made by self induction electromotive force in the reduction course of current is

$$E' = \int \varepsilon_L i dt = - \int_I^0 L i di = \frac{1}{2} L I^2$$

This shows that self induction coil is able to store energy. If we set up a current, whose strength is I , in the coil whose self induction coefficient is L , the energy stored in the coils will be,

$$E_L = \frac{1}{2} L I^2 \quad (3)$$

While discharging, this part of energy releases again, which is called self induction magnetic energy. Inductance coefficient is actually the measure of current magnetic field energy, which is the most essential meaning of inductance coefficient.

Self inductance is widely applied in electronics and radio technology. Coils can block the current to change. Taking advantage of this character, we could stabilize the current in the circuit. Radio equipment frequently combines it and capacitor to construct resonance circuit and filter, and the illustration Figure 1 is a kind of LC resonance circuit. To the circuit containing inductor, as the current changes rapidly, it will generate high pressure, and in very narrow space interval, the existence of peak voltage is equal to the existence of large electric field. The energy stored can be released via electric arc after aero ionization, which is used in a lot of actual ignition devices. In microwave engineering, self induction component can be used as power storage equipment. However, under some circumstances, the self inductance is very harmful. For instance, when the circuit with the maximal self induction coil is cut off, since the current changes too quickly in the circuit, there will be a great self induction electromotive force, which may break the coil's insulation protection; or the strong electric arc will probably burned switch. All these problems should be avoided in the practical work.



Figure 1: LC resonance circuit.

Self inductance is classified into two categories: inside self inductance and outside self inductance. The magnetic linkage outside conductor is called outside linkage, which is expressed by Ψ_o , and the self inductance computed by it is called outside self inductance L_o . The magnetic linkage through the conductor is called inside linkage, which is expressed by Ψ_i , and the self inductance computed by it is called inside self inductance L_i . Thus, the self inductance of conductor circuit can be expressed as,

$$L = L_o + L_i \quad (4)$$

Normally, there are two means for the computation of self inductance, one is computing directly according to the definition, i.e.,

$$L = \frac{\Psi}{I} \quad (5)$$

The other is the utilization of the nature that inductance coefficient is the measure of current magnetic field energy. The computation of magnetic energy comes first, then the one of self-induction coefficient.

Namely, first is the computation of magnetic energy:

$$E = \int_V \frac{1}{2} \vec{B} \cdot \vec{H} dV$$

So the self-induction coefficient is:

$$L = \frac{2E}{I^2} \quad (6)$$

The following computation applies the former,

(1) The computation of self-induction coefficient inside the cylinder conductor.

Assume the radius of cylinder conductor is a , as in Figure 2, then the magnetic flux through $\rho < a$ is inside magnetic flux, which is only interlinked with partial current. When axis length l cross at the spot of $\rho < a$, the meta magnetic flux of rectangular surface with width of $d\rho$ is

$$d\phi_i = B_i ds = \frac{\mu_0 I \rho}{2\pi a^2} l d\rho \quad (7)$$

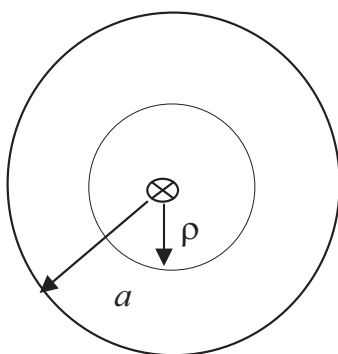


Figure 2: The self-induction coefficient inside the cylinder conductor.

The current interlinked with this magnetic flux is not I , but just a part of it, I' .

$$I' = \frac{I}{\pi a^2} \cdot \pi \rho^2 = \frac{\rho^2}{a^2} I \quad (8)$$

This is to say, the number of turns N interlinked with $d\phi_i$ is less than 1, i.e.,

$$N = \frac{I'}{I} = \frac{\rho^2}{a^2} \quad (9)$$

Thus, infinitesimal magnetic linkage is

$$d\Psi_i = N d\phi_i = \frac{\rho^2}{a^2} \cdot \frac{\mu_0 I \rho}{2\pi a^2} l d\rho$$

inside linkage in the conductor, whose length is l , should be

$$\Psi_i = \frac{\mu_0 I l}{2\pi a^4} \int_0^a \rho^3 d\rho = \frac{\mu_0 I l}{8\pi} \quad (10)$$

So, when the length of a cylinder conductor is l , the self-induction coefficient inside it should be

$$L_i = \frac{\Psi_i}{I} = \frac{\mu_0 l}{8\pi} \quad (11)$$

This expression proves that the inside self inductance of cylinder conductor bears no relationship with the radius of the conductor, but is only related with the length of the conductor.

(2) The computation for outside self inductance in the conductor circuit

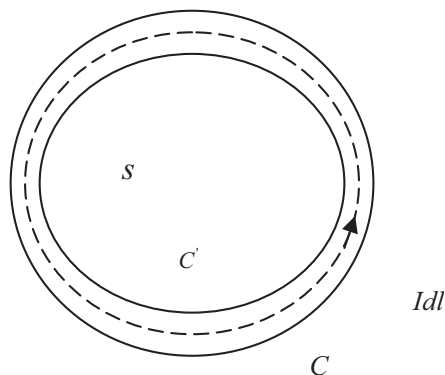


Figure 3: The structure of conductor circuit.

To any conductor circuit, the current can be approximately regarded that it concentrates on the central axis C of the conductor, as illustrated in Figure 3. For single-turn circuit, the magnetic

vector potential generated by circuit C on some point within inner board C' of the conductor should be,

$$\vec{A} = \frac{\mu I}{4\pi} \oint_C \frac{d\vec{l}}{R} \quad (12)$$

By Stokes theorem,

$$\int_S \vec{B} \cdot d\vec{s} = \oint_{C'} \vec{A} \cdot d\vec{l}'$$

In the expression, s is the area surrounded by inner boundary C' of the conductor, then the outside linkage of the conductor circuit interlinkage is

$$\Psi_o = \int_s (\nabla \times \vec{A}) \cdot d\vec{s} = \oint_{C'} \vec{A} \cdot d\vec{l}' = \frac{\mu I}{4\pi} \oint_C \oint_{C'} \frac{d\vec{l} \cdot d\vec{l}'}{R} \quad (13)$$

Then, the outside self inductance of single-turn circuit is,

$$L_o = \frac{\Psi_o}{I} = \frac{\mu}{4\pi} \oint_C \oint_{C'} \frac{d\vec{l} \cdot d\vec{l}'}{R} \quad (14)$$

In this expression C and C' are respectively the axis and inner boundary of the conductor. l and l' are their corresponding arc of length parameter. This expression is called Neumann formula of outside self inductance.

3. THE COMPUTATION OF SELF-INDUCTION COEFFICIENT OF TORUS KNOT CONDUCTOR

since inside self inductance is only related with the length of the conductor, we only discuss the computation of outside self inductance for knots. Assume a cylinder conductor whose radius is r is twisted into a knot, the magnetic conductivity in the entire space is μ_0 , the knots of axis C and inner boundary C' are

$$\begin{cases} x = (a + b \cos(\Psi + qs)) \cos(ps) \\ y = (a + b \cos(\Psi + qs)) \sin(ps) \\ z = b \sin(\Psi + qs) \end{cases} \quad (15)$$

And

$$\begin{cases} x' = (a + b' \cos(\Psi + qs')) \cos(ps') \\ y' = (a + b' \cos(\Psi + qs')) \sin(ps') \\ z' = b' \sin(\Psi + qs') \end{cases} \quad (16)$$

In the expression mentioned above, $0 \leq s' \leq 2\pi$, $b' = b - r$.

The geometric shape of torus knot conductor is complicated, the area surrounded by curve has complex geometrical and topological structure, so whether the self-induction coefficient can be computed based on Neumann Formula depends on if Stokes Formula calls into being for knot curve. It is easily to find that the inner boundary knot C' of the conductor is the boundary of its Seifert surface. Suppose this Seifert surface is Σ , and then Σ is a compact, connected and orientable surface, whose boundary is C' , then the expression

$$\Phi_\Sigma = \int_\Sigma \vec{B} \cdot d\vec{s}$$

Make sense, and Stokes theorem calls into being, that is

$$\int_\Sigma \vec{B} \cdot d\vec{s} = \int_{C'} \vec{A} \cdot d\vec{l}$$

Φ_Σ is the outside magnetic flux of torus knot conductor, then

$$\Phi_\Sigma = \int_\Sigma \vec{B} \cdot d\vec{s} = \int_{C'} \vec{A} \cdot d\vec{l} \quad (17)$$

Thus, it can also be computed by Neumann Formula, i.e.,

$$L_o = \frac{\Phi_\Sigma}{I} = \frac{\mu}{4\pi} \oint_C \oint_{C'} \frac{d\vec{l} \cdot d\vec{l}'}{R} \quad (18)$$

By (18), only the computation of R and $d\vec{l} \cdot d\vec{l}'$ is necessary to get the figure of outside self inductance.

The unit tangent vector of the two knots C and C' can be expressed as

$$\hat{l} = \frac{\vec{V}}{|\vec{V}|}, \quad \hat{l}' = \frac{\vec{V}'}{|\vec{V}'|} \quad (19)$$

Then

$$d\vec{l} = dl\hat{l} = |\vec{V}| \frac{\vec{V}}{|\vec{V}|} ds = \vec{V} ds \quad (20a)$$

$$d\vec{l}' = dl'\hat{l}' = |\vec{V}'| \frac{\vec{V}'}{|\vec{V}'|} ds' = \vec{V}' ds' \quad (20b)$$

Substitute (20) in (18) and then the outside self inductance of torus knot will be

$$L_o = \frac{\mu_0}{4\pi} \int_0^{2\pi} \int_0^{2\pi} \frac{\vec{V} \cdot \vec{V}'}{R} ds ds' \quad (21)$$

When $b = 0$, $p = 1$, the knot will turn into ordinary torus conductor. Then C and C' can be assumed as

$$\begin{cases} x = a \cos s \\ y = a \sin s \end{cases} \quad (22)$$

And

$$\begin{cases} x' = a' \cos s' \\ y' = a' \sin s' \end{cases} \quad (a' = a - r) \quad (23)$$

outside self inductance of torus conductor is

$$L_o = \frac{\mu_0}{4\pi} \int_0^{2\pi} \int_0^{2\pi} \frac{aa' \cos(s - s')}{\sqrt{a^2 + a'^2 - 2aa' \cos(s - s')}} ds ds' \quad (24)$$

4. THE NUMERICAL CALCULATION AND ANALYSIS

Assume that the conductor is ideal, the magnetic conductivity in the entire space is μ_0 , the radius of the conductor is $r = 1.0 \times 10^{-4}$ m, and the length of the conductor is $L = 0.4227$ m. When the conductor is twisted into a ring, by (4), we could get $L_o = 0.4432\mu_0$, which agrees to the computed result of the expression $L_o = \mu_0 a (\ln \frac{8a}{r} - 2)$ [29, 41]. To trefoil knot, namely, $p = 2$, $q = 3$, when b/a

Table 1: The self-induction coefficient of trefoil knot when $\frac{b}{a}$ is substituted different numbers.

b/a	a	$L_i(\mu_0)$	$L_o(\mu_0)$
1/2	2.65×10^{-2}	0.0168	0.3974
1/3	3.00×10^{-2}	0.0168	0.4238
1/4	3.15×10^{-2}	0.0168	0.4443
1/5	3.22×10^{-2}	0.0168	0.4603
1/10	3.33×10^{-2}	0.0168	0.5100
1/50	3.36×10^{-2}	0.0168	0.6232

takes different number, different shapes of trefoil knots will be obtained, and their self-induction coefficients are showed in Table 1. In this table, L_i is the inside self inductance and L_o is the outside self inductance.

From Table 1, when the conductors with the same length are twisted into the same kind of torus knot, we could change their self-induction coefficient by changing their geometrical shape, and the self-induction coefficient is be in inverse proportion to b/a . Therefore, to the torus knot conductor with the same length of the same category, the

self-induction coefficient can be augmented by increasing a and decreasing b . When b/a is about $1/4$, the self-induction coefficient approximated to torus conductor can be gained.

Assume that the conductor is ideal, the magnetic conductivity in the entire space is μ_0 , and the radius of the conductor is $r = 1.0 \times 10^{-4}$ m. Encircle different knots around the one ring with $a = 2.65 \times 10^{-2}$ m, $b = \frac{1}{2}a$, and their self-induction coefficients are showed in the Table 2. L , L_i , L_o are the arc, inside self inductance and outside self inductance of torus knot.

Table 2: The self-induction coefficients of the different knots on the same ring.

p	q	L	$L_i(\mu_0)$	$L_o(\mu_0)$
2	3	0.4227	0.0168	0.3974
2	5	0.5411	0.0242	0.5040
3	4	0.6090	0.0025	0.6294
3	5	0.6605	0.0262	0.6810
2	7	0.6790	0.0270	0.6428
3	7	0.7795	0.0310	0.8091
4	5	0.7962	0.0316	0.9097
4	7	0.8992	0.0357	1.0295
5	7	1.0313	0.0410	1.3013
6	7	1.1716	0.0466	1.6229

From Table 2 we could see, for the different torus knot encircled around the same ring, their self-induction coefficients are in direct proportion to the arc length of the torus knot, and outside self inductance is approximate to the arc length.

Compare Table 1 with Table 2, we could see that for torus knot conductor, the ring it encircles has obvious effect on self-induction coefficient, while for the knots encircled around the same ring, their self-induction coefficients bear crucial relationship with their arc length of the knots.

With the utilization of self inductance it is easily to figure out the stored magnetic energy in torus knot conductor. In this thesis, we discussed that the computation of self inductance when the conductor is twisted into (p, q) -torus knot. Although torus knot has complex geometrical and topological structure, it is also the boundary of its Seifert surface. Thus, by the nature of Seifert surface, we could prove that Neumann Formula is suited for torus knot. In addition to this, we offer computing formula. What is more, we make comparative analysis the torus knots of the same category whose geometrical shapes twisted by the conductors with the same length, and the self-induction coefficients of different torus knots on the same ring. The result shows that, for torus knot conductor, the ring it encircles has great effect on self-induction coefficient. The torus knot conductor with same length of the same category not only can change self-induction coefficient by changing geometrical shape, but also can obtain bigger self-induction coefficient than that of torus conductor with the same length. for the different torus knot encircled around the same ring, their self-induction coefficients are in direct proportion to the arc length of the torus knot, and outside self inductance is approximate to the arc length.

REFERENCES

1. Gross, P. W. and P. R. Kotiuga, *Electromagnetic Theory and Computation: A Topological Approach*, Cambridge University Press, 2004.
2. Waaerman, S., J. Dungan, and N. Cozzarelli, "Discovery of a predicted DNA knot substantiates a model for site-specific recombination," *Science*, Vol. 299, 171–174, July 1985.

3. Schlick, T. and W. K. Olson, “Trefoil knotting revealed by molecular dynamics simulations of supercoiled DNA,” *Science*, Vol. 257, 1110–1115, 1992.
4. Manuar, O. and D. L. Jaggard, “Backscatter signatures of knots,” *Optics Letters*, Vol. 20, No. 2, 115–117, Jan. 1995.
5. Jaggard, D. L. and O. Manuar, “Can One ‘hear’ the handedness or topology of a kno?” *Proceedings of the IEEE Antennas and Propagation Society International Symposium and URSI Radio Science Meeting, Newport Beach, URSI Digest*, 244, Colifornia, June 18–23, 1995.
6. Manuar, O. and D. L. Jaggard, “Wave interaction with trefoils and untrefoils,” *Proceedings of the IEEE Antennas and Propagation Society International Symposium and URSI Radio Science Meeting, URSI Digest*, 279, Baltimore, MD, July 21–26, 1996.
7. Manuar, O. and D. L. Jaggard, “Scattering from knots and unknots: The role of symmetry,” *Elec. Lett.*, Vol. 33, No. 4, 278–280, February 1997.
8. Werner, D. H., “The electrodynamics of torus knot,” *IEEE Antennas and Propagation Society International Symposium Digest*, Vol. 2, 1468–1471, Montreal, Canada, July 1997.
9. Werner, D. H., “Radiation and Scattering from thin toroidally knotted wires,” *IEEE Trans. Antennas Propagat*, Vol. 47, No. 8, August 1999.
10. Werner, D. H., “Radiation and scattering from elliptical torus knots,” *Proceedings of the IEEE Antennas and Propagation Society International Symposium*, Vol. 2, 858–861, Atlanta, GA, June 21–26, 1998.
11. Arnold, V. I., “The asymptotic hopf invariant and its applications,” *Sel. Math. Sov.*, Vol. 5, 327, 1986.
12. Marsh, G. E., “Magnetic energy, multiply connected domains, and force-free fields,” *Phys. Rev. A*, Vol. 46, 2117–2123, 1992.
13. Marsh, G. E., “Force-free magnetic fields: Solutions, topology and applications,” *World Scientific*, Singapore, 1996.
14. Berger, M. A. and G. E. Field, “The topological properties of magnetic helicity,” *J. Fluidmech*, Vol. 147, 133, 1984.
15. Moffatt, H. K., *Magnetic Field Generation in Electrically Conducting Fluids*, Section 2.1, Cambridge Univerity Press, Cambridge, UK, 1978.
16. Moffatt, H. K., “The energy spectrum of knots and links,” *Nature*, Vol. 347, 367, 1990.
17. Chui, A. Y. K. and H. K. Moffatt, “The energy and helicity of knotted magnetic flux tubes,” *Proc. R. Soc. Lond. A*, Vol. 451, 609–629, 1995.

Analysis of a 1:2 Rectangular Waveguide Power Divider for Phased Array Application Using Multiple Cavity Modeling Technique

Debendra Kumar Panda and Ajay Chakraborty

IEEE, India

Abstract— A method of moment based analysis of the feed network of a waveguide fed two dimensional array antennas has been presented using Multi Cavity Modeling Technique (MCMT) in transmitting mode. The proposed power divider is unlikely to the family of Tees. The output ports are in the same planes as the input which is an advantage for phased array applications. The proposed 1:2 power divider has good agreement with the theory, CST microwave studio simulated and measured data over entire X-band frequency range.

1. INTRODUCTION

Low cost, Low Profile two dimensional scanning phased array antennas have wide application in Low Earth Orbit (LEO), Middle Earth Orbit (MEO) and Geostationary Earth Orbit (GEO) satellite communication. Multi-port Power divider has already found wide applications in phased array techniques. Basic requirements for the considered class of beam forming networks are: Low losses in the operational frequency band, the high accuracy of power splitting (With necessary amplitude and phase distribution at the outputs). Today, a large number of configurations and power divider constructions are known [1–6]. However the problems of theoretical analysis of high quality power divider remain unsolved. Effort has been made to miniaturize (dimensionally) a 1:2 power divider with wide band frequency response.

Present work was performed for theoretical analysis of a 1:2 power divider for phased array application using Multi Cavity Modeling Technique (MCMT) [7] and compared with the practical data. The technique involves in replacing all the apertures and discontinuities of the waveguide structures, with equivalent magnetic current densities so that the given structure can be analyzed using only Magnetic Field Integral Equation (MFIE). Since only the magnetic currents present in the apertures are considered the methodology involves only solving simple magnetic integral equation rather than the complex integral equation involving both the electric and magnetic current densities.

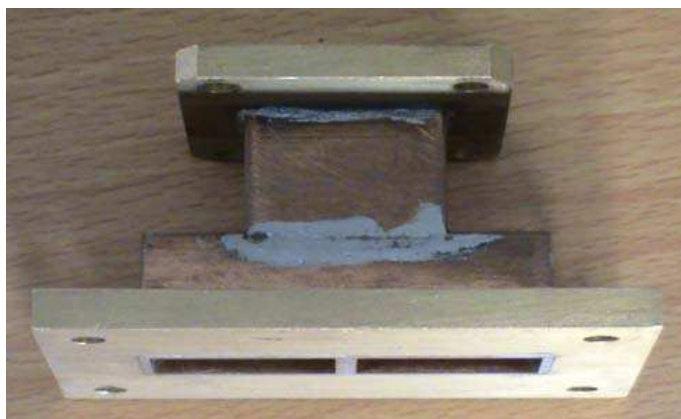


Figure 1: Photograph of a 1:2 power divider.

2. FORMULATION OF THEORY

The photograph of a basic 1:2 power divider is shown in Figure 1 and with its cavity modeling and details of region which shows that the structures have 3 waveguide regions and 1 cavity region shown in Figure 2. The interfacing apertures between different regions are replaced by equivalent magnetic current densities. The electric field at the aperture is assumed to be

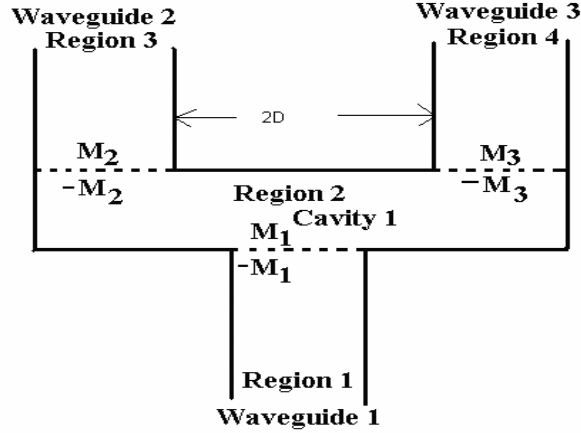


Figure 2: Cavity modeling and details of regions of a basic 1:2 power divider.

$$\vec{E} = \hat{u}_x \sum_{p=1}^M E_{px} e_{px} + \hat{u}_y \sum_{p=1}^M E_{py} e_{py} \quad (1)$$

where the basis function e_p ($p = 1, 2, 3, \dots, M$) are defined by

$$e_p^{i,y} = \begin{cases} \sin \left\{ \frac{p\pi}{2L} (x - x_w + L) \right\} & \text{for } x_w - L \leq x \leq x_w + L \\ 0 & \text{elsewhere} \end{cases} \quad (2a)$$

$$e_p^{i,x} = \begin{cases} \sin \left\{ \frac{p\pi}{2W} (y - y_w + W) \right\} & \text{for } y_w - W \leq y \leq y_w + W \\ 0 & \text{elsewhere} \end{cases} \quad (2b)$$

In the above expressions:

- $L = a$, $W = b$, $x_w = 0$ and $y_w = 0$ for aperture 1, aperture 2 and aperture 3 with respect to waveguide co-ordinate.
- $L = a$, $W = b$, $x_w = 0$ and $y_w = 0$ for aperture 1 with respect to cavity axis.
- $L = a$, $W = b$, $x_w = D + a$ and $y_w = 0$ for aperture 2 with respect to cavity axis.
- $L = a$, $W = b$, $x_w = D - a$ and $y_w = 0$ for aperture 3 with respect to cavity axis.
- where $a = 22.86$ mm, $b = 10.16$ mm, $D = 1.27$ mm.
- where $2D$ is the distance between waveguide-2 and waveguide-3.

The X -component of incident magnetic field at the aperture for the transmitting mode is a dominant TE_{10} mode and is given by

$$H_x^{inc} = -Y_0 \cos \left(\frac{\pi x}{2a} \right) e^{-j\beta z}$$

3. EVALUATION OF THE INTERNALLY SCATTERED FIELD

The internally scattered field is obtained by using the modal expansion approach presented in [8]. The internally scattered electric field is given in [9]. Once the electric field is obtained, the corresponding magnetic fields can be derived.

The modal voltages are given by (considering only $e_{pq}^{i,tn}$ part of the aperture electric field):

$$V_{mn}^e = \sqrt{2ab} [E_{px} - E_{py}] \quad (3)$$

$$V_{mn}^m = 0 \quad (4)$$

The x -component of internally scattered magnetic field can be obtained as,

$$H_x^{wvg} (E_p^i, y) = H_x^{wvg} (M_p^i, x) = \begin{cases} -\sum_{m=1}^{\infty} Y_{m0}^e \sin \left\{ \frac{m\pi}{2a} (x+a) \right\} & \text{for } p=m \text{ and } n=0 \\ 0 & \text{Otherwise} \end{cases} \quad (5)$$

$$H_x^{wvg} (E_p^i, x) = -H_x^{wvg} (M_p^i, y) = 0 \quad (6)$$

$$H_y^{wvg} (E_p^i, y) = H_y^{wvg} (M_p^i, x) = 0 \quad (7)$$

$$H_y^{wvg} (E_p^i, x) = -H_y^{wvg} (M_p^i, y) = \begin{cases} \sum_{n=0}^{\infty} Y_{0n}^e \sin \left\{ \frac{n\pi}{2b} (y+b) \right\} & \text{for } p=n \text{ and } m=0 \\ 0 & \text{Otherwise} \end{cases} \quad (8)$$

4. EVALUATION OF THE CAVITY SCATTERED FIELD

The tangential components of the cavity scattered fields are derived in [5]. The final form of the tangential components of the cavity scattered field will be same as given in [6], where L_c is the length and W_c is the width of the cavity. L_i and W_i are the half length and half width of i th aperture.

$$\begin{aligned} H_x^{cav^j} (M_i^x) &= -\frac{j\omega\varepsilon}{k^2} \sum_{m=1}^{\infty} \sum_{n=0}^{\infty} \frac{\varepsilon_m \varepsilon_n L_i W_i}{2L_c W_c} \left\{ k^2 - \left(\frac{m\pi}{2L_c} \right)^2 \right\} \sin \left\{ \frac{m\pi}{2L_c} (x+L_c) \right\} \\ &\times \cos \left\{ \frac{n\pi}{2W_c} (y+W_c) \right\} \cos \left\{ \frac{n\pi}{2W_c} (y_w+W_c) \right\} \sin c \left\{ \frac{n\pi}{2W_c} W_i \right\} F_x(p) \\ &\times \frac{(-1)}{\Gamma_{mn} \sin \{2\Gamma_{mn} t_c\}} \begin{cases} \cos \{ \Gamma_{mn} (z-t_c) \} \cos \{ \Gamma_{mn} (z_0+t_c) \} & z > z_0 \\ \cos \{ \Gamma_{mn} (z_0-t_c) \} \cos \{ \Gamma_{mn} (z+t_c) \} & z < z_0 \end{cases} \end{aligned} \quad (9)$$

$$\begin{aligned} H_x^{cav^j} (M_i^y) &= \frac{j\omega\varepsilon}{k^2} \sum_{m=1}^{\infty} \sum_{n=0}^{\infty} \frac{\varepsilon_m \varepsilon_n L_i W_i}{2L_c W_c} \frac{m\pi}{2L_c} \frac{n\pi}{2W_c} \sin \left\{ \frac{m\pi}{2L_c} (x+L_c) \right\} \\ &\times \cos \left\{ \frac{n\pi}{2W_c} (y+W_c) \right\} \cos \left\{ \frac{m\pi}{2L_c} (x_w+L_c) \right\} \sin c \left\{ \frac{m\pi}{2L_c} L_i \right\} F_y(p) \\ &\times \frac{(-1)}{\Gamma_{mn} \sin \{2\Gamma_{mn} t_c\}} \begin{cases} \cos \{ \Gamma_{mn} (z-t_c) \} \cos \{ \Gamma_{mn} (z_0+t_c) \} & z > z_0 \\ \cos \{ \Gamma_{mn} (z_0-t_c) \} \cos \{ \Gamma_{mn} (z+t_c) \} & z < z_0 \end{cases} \end{aligned} \quad (10)$$

$$\begin{aligned} H_y^{cav^j} (M_i^x) &= \frac{j\omega\varepsilon}{k^2} \sum_{m=1}^{\infty} \sum_{n=0}^{\infty} \frac{\varepsilon_m \varepsilon_n L_i W_i}{2L_c W_c} \frac{m\pi}{2L_c} \frac{n\pi}{2W_c} \cos \left\{ \frac{m\pi}{2L_c} (x+L_c) \right\} \\ &\times \sin \left\{ \frac{n\pi}{2W_c} (y+W_c) \right\} \cos \left\{ \frac{n\pi}{2W_c} (y_w+W_c) \right\} \sin c \left\{ \frac{n\pi}{2W_c} W_i \right\} F_x(p) \\ &\times \frac{(-1)}{\Gamma_{mn} \sin \{2\Gamma_{mn} t_c\}} \begin{cases} \cos \{ \Gamma_{mn} (z-t_c) \} \cos \{ \Gamma_{mn} (z_0+t_c) \} & z > z_0 \\ \cos \{ \Gamma_{mn} (z_0-t_c) \} \cos \{ \Gamma_{mn} (z+t_c) \} & z < z_0 \end{cases} \end{aligned} \quad (11)$$

$$\begin{aligned} H_y^{cav^j} (M_i^y) &= -\frac{j\omega\varepsilon}{k^2} \sum_{m=1}^{\infty} \sum_{n=0}^{\infty} \frac{\varepsilon_m \varepsilon_n L_i W_i}{2L_c W_c} \left\{ k^2 - \left(\frac{n\pi}{2W_c} \right)^2 \right\} \cos \left\{ \frac{m\pi}{2L_c} (x+L_c) \right\} \\ &\times \sin \left\{ \frac{n\pi}{2W_c} (y+W_c) \right\} \cos \left\{ \frac{m\pi}{2L_c} (x_w+L_c) \right\} \sin c \left\{ \frac{m\pi}{2L_c} L_i \right\} F_y(p) \\ &\times \frac{(-1)}{\Gamma_{mn} \sin \{2\Gamma_{mn} t_c\}} \begin{cases} \cos \{ \Gamma_{mn} (z-t_c) \} \cos \{ \Gamma_{mn} (z_0+t_c) \} & z > z_0 \\ \cos \{ \Gamma_{mn} (z_0-t_c) \} \cos \{ \Gamma_{mn} (z+t_c) \} & z < z_0 \end{cases} \end{aligned} \quad (12)$$

At the region of the window, the tangential component of the magnetic field in the aperture should be identical and applying the proper boundary conditions at the aperture the electric fields can be evaluated [6].

5. IMPOSITION OF THE BOUNDARY CONDITION

At the region of the window, the tangential component of the magnetic field in the aperture should be identical and is given by:

$$H_x^{wvg1}(M_1^x) + H_x^{cav}(M_1^x) + H_x^{wvg1}(M_1^y) + H_x^{cav}(M_1^y) - H_x^{cav}(M_2^x) - H_x^{cav}(M_2^y) - H_x^{cav}(M_3^x) - H_x^{cav}(M_3^y) = 2H_x^{inc} \quad (13)$$

$$H_y^{wvg1}(M_1^x) + H_y^{cav}(M_1^x) + H_y^{wvg1}(M_1^y) + H_y^{cav}(M_1^y) - H_y^{cav}(M_2^x) - H_y^{cav}(M_2^y) - H_y^{cav}(M_3^x) - H_y^{cav}(M_3^y) = 0 \quad (14)$$

$$-H_x^{cty}(M_1^x) - H_x^{cav}(M_1^y) + H_x^{cav}(M_2^x) + H_x^{wvg2}(M_2^x) + H_x^{cav}(M_2^y) + H_x^{wvg2}(M_2^y) + H_x^{cav}(M_3^x) + H_x^{cav}(M_3^y) = 0 \quad (15)$$

$$-H_y^{cav}(M_1^x) - H_y^{cav}(M_1^y) + H_y^{cav}(M_2^x) + H_y^{wvg2}(M_2^x) + H_y^{cav}(M_2^y) + H_x^{wvg2}(M_2^y) + H_y^{cav}(M_3^x) + H_y^{cav}(M_3^y) = 0 \quad (16)$$

$$-H_x^{cav}(M_1^x) - H_x^{cav}(M_1^y) + H_x^{cav}(M_2^x) + H_x^{cav}(M_2^y) + H_x^{cav}(M_3^x) + H_x^{wvg3}(M_2^x) + H_x^{cav}(M_3^y) + H_x^{wvg3}(M_3^y) = 0 \quad (17)$$

$$-H_y^{cav}(M_1^x) - H_y^{cav}(M_1^y) + H_y^{cav}(M_2^x) + H_y^{cav}(M_2^y) + H_y^{cav}(M_3^x) + H_y^{wvg3}(M_2^x) + H_y^{cav}(M_3^y) + H_y^{wvg3}(M_3^y) = 0 \quad (18)$$

6. SOLVING FOR THE ELECTRIC FIELD

To determine the electric field distribution at the window aperture, it is necessary to determine the basis function coefficients $E_p^{i,x/y}$ at both the apertures. Since the each component of the field is described by M basis functions, 6M unknowns are to be determined from the boundary conditions. The Galerkin's specialization of the method of moments is used to obtain 6M-different equations from the boundary condition to enable determination of $E_p^{i,x/y}$ [10]. The weighting function $w_q^{i,x/y}(x, y, z)$ is selected to be of the same form as the basis function $e_p^{i,x/y}$. The weighting function is defined as follows:

$$w_q^{i,y} = \begin{cases} \sin\left\{\frac{q\pi}{2L}(x - x_w + L)\right\} & \text{for } x_w - L \leq x \leq x_w + L \\ 0 & \text{elsewhere} \end{cases} \quad (19a)$$

$$w_q^{i,x} = \begin{cases} \sin\left\{\frac{q\pi}{2W}(y - y_w + W)\right\} & \text{for } y_w - W \leq y \leq y_w + W \\ 0 & \text{elsewhere} \end{cases} \quad (19b)$$

The inner product is defined by

$$\langle H, w_q \rangle = \iint_{\text{Aperture}} H \cdot w_q d\xi d\psi \quad (20)$$

Using the boundary condition given by Equations (13) to (18) and the definition of Equation (20),

$$\langle \{H_x^{wvg1}(M_1^x) + H_x^{cav}(M_1^x)\}, w_q^{1,y} \rangle + \langle \{H_x^{wvg1}(M_1^y) + H_x^{cav}(M_1^y)\}, w_q^{1,y} \rangle - \langle H_x^{cav}(M_2^x), w_q^{1,y} \rangle - \langle H_x^{cav}(M_2^y), w_q^{1,y} \rangle - \langle H_x^{cav}(M_3^x), w_q^{1,y} \rangle - \langle H_x^{cav}(M_3^y), w_q^{1,y} \rangle = 2\langle H_x^{inc}, w_q^{1,x} \rangle \quad (21)$$

$$\langle \{H_y^{wvg1}(M_1^x) + H_y^{cav}(M_1^x)\}, w_q^{1,x} \rangle + \langle \{H_y^{wvg1}(M_1^y) + H_y^{cav}(M_1^y)\}, w_q^{1,x} \rangle - \langle H_y^{cav}(M_2^x), w_q^{1,x} \rangle - \langle H_y^{cav}(M_2^y), w_q^{1,x} \rangle - \langle H_y^{cav}(M_3^x), w_q^{1,x} \rangle - \langle H_y^{cav}(M_3^y), w_q^{1,x} \rangle = 0 \quad (22)$$

$$\begin{aligned}
& -\langle H_x^{cav}(M_1^x), w_q^{2,y} \rangle - \langle H_x^{cav}(M_1^y), w_q^{2,y} \rangle + \langle \{H_x^{cav}(M_2^x) + H_x^{wvg2}(M_2^x)\}, w_q^{2,y} \rangle \\
& + \langle \{H_x^{cav}(M_2^y) + H_x^{wvg2}(M_2^y)\}, w_q^{2,y} \rangle + \langle H_x^{cav}(M_3^x), w_q^{2,y} \rangle + \langle H_x^{cav}(M_3^y), w_q^{2,y} \rangle = 0 \quad (23)
\end{aligned}$$

$$\begin{aligned}
& -\langle H_y^{cav}(M_1^x), w_{qy,2} \rangle - \langle H_y^{cav}(M_1^y), w_q^{2,x} \rangle + \langle \{H_y^{cav}(M_2^x) + H_y^{wvg2}(M_2^x)\}, w_q^{2,x} \rangle \\
& + \langle \{H_y^{cav}(M_2^y) + H_y^{wvg2}(M_2^y)\}, w_q^{2,x} \rangle + \langle H_y^{cav}(M_3^x), w_q^{2,x} \rangle + \langle H_y^{cav}(M_3^y), w_q^{2,x} \rangle = 0 \quad (24)
\end{aligned}$$

$$\begin{aligned}
& -\langle H_x^{cav}(M_1^x), w_q^{3,y} \rangle - \langle H_x^{cav}(M_1^y), w_q^{3,y} \rangle + \langle H_x^{cav}(M_2^x), w_q^{3,y} \rangle + \langle H_x^{cav}(M_2^y), w_q^{3,y} \rangle \\
& + \langle \{H_x^{cav}(M_3^x) + H_x^{wvg3}(M_3^x)\}, w_q^{3,y} \rangle + \langle \{H_x^{cav}(M_3^y) + H_x^{wvg3}(M_3^y)\}, w_q^{3,y} \rangle = 0 \quad (25)
\end{aligned}$$

$$\begin{aligned}
& -\langle H_y^{cav}(M_1^x), w_q^{3,x} \rangle - \langle H_y^{cav}(M_1^y), w_q^{3,x} \rangle + \langle H_y^{cav}(M_2^x), w_q^{3,x} \rangle + \langle H_y^{cav}(M_2^y), w_q^{3,x} \rangle \\
& + \langle \{H_y^{cav}(M_3^x) + H_y^{wvg3}(M_3^x)\}, w_q^{3,x} \rangle + \langle \{H_y^{cav}(M_3^y) + H_y^{wvg3}(M_3^y)\}, w_q^{3,x} \rangle = 0 \quad (26)
\end{aligned}$$

where the elements of the moment matrices are derived as follows:

$$\langle H_x^{inc}, w_q^{1,y} \rangle = \begin{cases} -2abY_0 & \text{for } q = 1 \\ 0 & \text{Otherwise} \end{cases} \quad (27)$$

$$\langle H_x^{wvg}(M_x), w_q^{i,y} \rangle = \begin{cases} -2abY_{m0}^e & \text{for } p = q = m \text{ and } n = 0 \\ 0 & \text{Otherwise} \end{cases} \quad (28)$$

$$\langle H_x^{wvg}(M_y), w_q^{i,y} \rangle = 0 \quad (29)$$

$$\langle H_y^{wvg}(M_x), w_q^{i,x} \rangle = 0 \quad (30)$$

$$\langle H_y^{wvg}(M_y), w_q^{i,x} \rangle = \begin{cases} -2abY_{0n}^e & \text{for } p = q = n \text{ and } m = 0 \\ 0 & \text{Otherwise} \end{cases} \quad (31)$$

$$\begin{aligned}
\langle H_x^{cav}(M_x), w_q^{i,y} \rangle &= -\frac{j\omega\varepsilon L_s W_s L_o W_o}{k^2 2L_c W_c} \sum_{m=1}^{\infty} \sum_{n=0}^{\infty} \varepsilon_m \varepsilon_n \left\{ k^2 - \left(\frac{m\pi}{2L_c} \right)^2 \right\} \\
&\times \cos \left\{ \frac{n\pi}{2W_c} (y_{ws} + W_c) \right\} \sin c \left\{ \frac{n\pi}{2W_c} W_s \right\} \cos \left\{ \frac{n\pi}{2W_c} (y_{wo} + W_c) \right\} \sin c \left\{ \frac{n\pi}{2W_c} W_o \right\} \\
&\times \frac{\{-F_{xs}(p) F_{xo}(q)\}}{\Gamma_{mn} \sin \{2\Gamma_{mn} t_c\}} \begin{cases} \cos \{\Gamma_{mn}(z - t_c)\} \cos \{\Gamma_{mn}(z_0 + t_c)\} & z > z_0 \\ \cos \{\Gamma_{mn}(z_0 - t_c)\} \cos \{\Gamma_{mn}(z + t_c)\} & z < z_0 \end{cases} \quad (32)
\end{aligned}$$

$$\begin{aligned}
\langle H_x^{cav}(M_y), w_q^{i,y} \rangle &= \frac{j\omega\varepsilon L_s W_s L_o W_o}{k^2 2L_c W_c} \sum_{m=0}^{\infty} \sum_{n=1}^{\infty} \varepsilon_m \varepsilon_n \frac{m\pi}{2L_c} \frac{n\pi}{2W_c} \\
&\times \cos \left\{ \frac{m\pi}{2L_c} (x_{ws} + L_c) \right\} \sin c \left\{ \frac{m\pi}{2L_c} L_s \right\} \cos \left\{ \frac{n\pi}{2W_c} (y_{wo} + W_c) \right\} \sin c \left\{ \frac{n\pi}{2W_c} W_o \right\} \\
&\times \frac{\{-F_{ys}(p) F_{yo}(q)\}}{\Gamma_{mn} \sin \{2\Gamma_{mn} t_c\}} \begin{cases} \cos \{\Gamma_{mn}(z - t_c)\} \cos \{\Gamma_{mn}(z_0 + t_c)\} & z > z_0 \\ \cos \{\Gamma_{mn}(z_0 - t_c)\} \cos \{\Gamma_{mn}(z + t_c)\} & z < z_0 \end{cases} \quad (33)
\end{aligned}$$

$$\begin{aligned}
\langle H_y^{cav}(M_x), w_q^{i,x} \rangle &= \frac{j\omega\varepsilon L_s W_s L_o W_o}{k^2 2L_c W_c} \sum_{m=1}^{\infty} \sum_{n=0}^{\infty} \varepsilon_m \varepsilon_n \frac{m\pi}{2L_c} \frac{n\pi}{2W_c} \\
&\times \cos \left\{ \frac{m\pi}{2L_c} (x_{wo} + L_c) \right\} \sin c \left\{ \frac{m\pi}{2L_c} L_o \right\} \cos \left\{ \frac{n\pi}{2W_c} (y_{ws} + W_c) \right\} \sin c \left\{ \frac{n\pi}{2W_c} W_s \right\} \\
&\times \frac{\{-F_{xs}(p) F_{yo}(q)\}}{\Gamma_{mn} \sin \{2\Gamma_{mn} t_c\}} \begin{cases} \cos \{\Gamma_{mn}(z - t_c)\} \cos \{\Gamma_{mn}(z_0 + t_c)\} & z > z_0 \\ \cos \{\Gamma_{mn}(z_0 - t_c)\} \cos \{\Gamma_{mn}(z + t_c)\} & z < z_0 \end{cases} \quad (34)
\end{aligned}$$

$$\begin{aligned}
\langle H_y^{cav}(M_y), w_q^{i,x} \rangle &= -\frac{j\omega\varepsilon L_s W_s L_o W_o}{k^2 2L_c W_c} \sum_{m=0}^{\infty} \sum_{n=1}^{\infty} \varepsilon_m \varepsilon_n \left\{ k^2 - \left(\frac{n\pi}{2W_c} \right)^2 \right\} \\
&\times \cos \left\{ \frac{m\pi}{2L_c} (x_{ws} + L_c) \right\} \sin c \left\{ \frac{m\pi}{2L_c} L_s \right\} \cos \left\{ \frac{m\pi}{2L_c} (x_{wo} + L_c) \right\} \sin c \left\{ \frac{m\pi}{2L_c} L_o \right\} \\
&\times \frac{\{-F_{ys}(p) F_{yo}(q)\}}{\Gamma_{mn} \sin \{2\Gamma_{mn} t_c\}} \begin{cases} \cos \{\Gamma_{mn}(z - t_c)\} \cos \{\Gamma_{mn}(z_0 + t_c)\} & z > z_0 \\ \cos \{\Gamma_{mn}(z_0 - t_c)\} \cos \{\Gamma_{mn}(z + t_c)\} & z < z_0 \end{cases} \quad (35)
\end{aligned}$$

where suffix 's' and 'o' represents the source and observation aperture dimensions respectively.

Rewriting Equations (27) and (35) in the matrix form, for all p and q :

$$\begin{bmatrix}
 [Y_{11}^{xx}] & [Y_{11}^{xy}] & -[Y_{12}^{xx}] & -[Y_{12}^{xy}] & -[Y_{13}^{xx}] & -[Y_{13}^{xy}] \\
 [Y_{11}^{yx}] & [Y_{11}^{yy}] & -[Y_{12}^{yx}] & -[Y_{12}^{yy}] & -[Y_{13}^{yx}] & -[Y_{13}^{yy}] \\
 -[Y_{21}^{xx}] & -[Y_{21}^{xy}] & [Y_{22}^{xx}] & [Y_{22}^{xy}] & [Y_{23}^{xx}] & [Y_{23}^{xy}] \\
 -[Y_{21}^{yx}] & -[Y_{21}^{yy}] & [Y_{22}^{yx}] & [Y_{22}^{yy}] & [Y_{23}^{yx}] & [Y_{23}^{yy}] \\
 -[Y_{31}^{xx}] & -[Y_{31}^{xy}] & [Y_{32}^{xx}] & [Y_{32}^{xy}] & [Y_{33}^{xx}] & [Y_{33}^{xy}] \\
 -[Y_{31}^{yx}] & -[Y_{31}^{yy}] & [Y_{32}^{yx}] & [Y_{32}^{yy}] & [Y_{33}^{yx}] & [Y_{33}^{yy}]
 \end{bmatrix}
 \begin{Bmatrix}
 \{E^{1,y}\} \\
 \{E^{1,x}\} \\
 \{E^{2,y}\} \\
 \{E^{2,x}\} \\
 \{E^{3,y}\} \\
 \{E^{3,x}\}
 \end{Bmatrix}
 =
 \begin{Bmatrix}
 2\{h_x^{inc}\} \\
 \{0\} \\
 \{0\} \\
 \{0\} \\
 \{0\} \\
 \{0\}
 \end{Bmatrix}
 \quad (36)$$



Figure 3: Photograph of arrangements of H -plane bends for measurement purpose.

7. REFLECTION COEFFICIENT AND TRANSMISSION COEFFICIENT

The procedure for derivation of reflection and transmission coefficients is given in [11]. Following the same procedure the expressions for Γ and T is given by:

$$\Gamma = \frac{E_y^1 + E_y^2}{E_y^{inc}} = -1 - E_1^{1,y} \quad (37)$$

$$T_{21/31} = \frac{E_y^{transmitted}}{E_y^{inc}} = -E_1^{2/3,y} \quad (38)$$

8. NUMERICAL RESULTS AND DISCUSSION

Theoretical data for the magnitude of scattering parameters for an H -plane 1:2 WR-90 waveguide power divider at X-band has been compared with CST Microwave Studio simulated data and measured data in Figure 4.

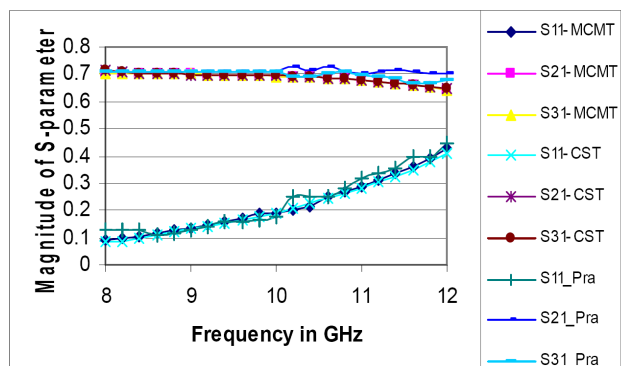


Figure 4: Comparison of theoretical, CST microwave studio simulated and measured data for an H -plane 1:2 WR-90 waveguide power divider for $2t = 12.2$ mm.

MATLAB codes have been written for analyzing the structure and numerical data have been obtained after running the codes. The structure was also simulated using CST microwave studio while measurements were performed using Agilent 8410C Vector Network Analyzer. The theory has been validated by the excellent agreement between the theoretical, CST Microwave Studio simulated data and Measured Data in Figure 4. In Figure 5, S_{11} is presented for various values of the length of cavity ($2t$) and in Figure 6 for S_{21} and S_{31} . The scattering parameters for the circuit, when excited through port -2 and port -3 have not been presented in this section because these are less important in the study of a power divider.

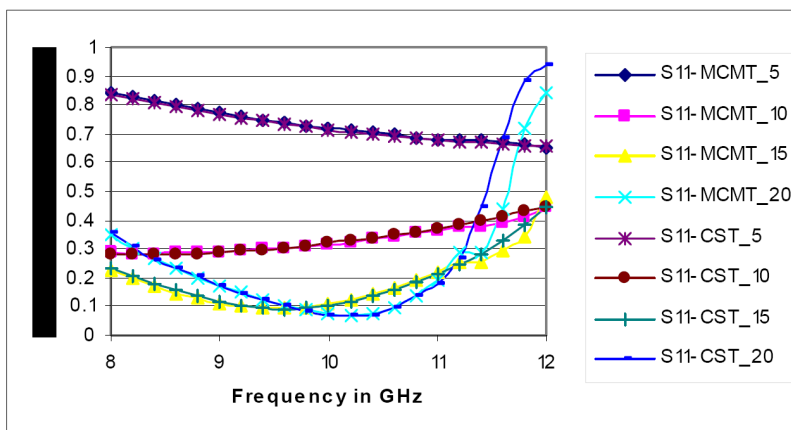


Figure 5: S_{11} of an H -plane 2:1 WR-90 waveguide power divider with $2t = 5$ mm, 10 mm, 15 mm and 20 mm.

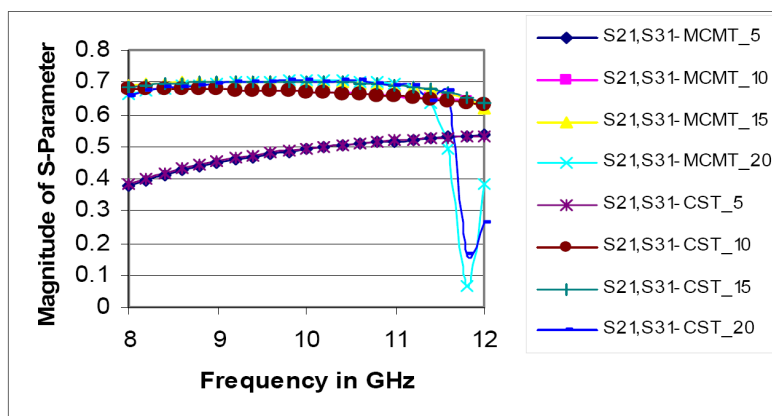


Figure 6: S_{21} and S_{31} of an H -plane 2:1 WR-90 waveguide power divider with $2t = 5$ mm, 10 mm, 15 mm, and 20 mm.

ACKNOWLEDGMENT

The support provided by Kalpana Chawla Space Technology Cell, IIT Kharagpur is gratefully acknowledged.

REFERENCES

1. Takeda, F., O. Ishida, and Y. Isoda, "Waveguide power divider using metallic septum with resistive coupling slot," *Microwave Symposium Digest, MTT-S International*, Vol. 82, No. 1, 527–528, June 1982.
2. Soroka, A. S., A. O. Silin, V. I. Tkachenko, and I. S. Tsakanyan, "Simulation of multichannel waveguide power dividers," *MSMW'98 Symposium Proceedings*, 634–635, Kharkov, Ukraine, September 15–17, 1998.
3. Chen, S., "A radial waveguide power divider for Ka band phase array antenna," *3rd International Conference on Microwave and Millimeter Wave Technology*, 948–951, 2002.

4. Gardner, P. and B. H. Ong, “Mode matching design of three-way waveguide power dividers,” *IEE Colloquium on Advances in Passive Microwave Components*, 5/1–5/4, May 22, 1997.
5. Das, S. and A. Chakrabarty, “Analysis of waveguide based power divider using multiple cavity modeling technique and performance improvement,” *IRSI-2005*, Bangalore, India.
6. Panda, D. K. and A. Chakraborty, “Multiple cavity modeling of a feed network for two dimensional phased array application,” *Progress In Electromagnetics Research Letters*, Vol. 2, 135–140, 2008.
7. Das, S. and A. Chakraborty, “A novel modeling technique to solve a class of rectangular waveguide based circuits and radiators,” *Progress In Electromagnetic Research*, PIER 61, 231–252, MIT, USA, May 2006.
8. Harrington, R. F., *Time-harmonic Electromagnetic Fields*, McGraw-Hill Book Company, New York, 1961.
9. Collins, R. E., *Field Theory of Guided Waves*, IEEE Press, 1991.
10. Harrington, R. F., *Field Computation by Moment Methods*, Roger E. Krieger Publishing Company, USA.
11. Das, S., “Analysis of rectangular waveguide based passive devices and antennas using multiple cavity modeling technique,” PhD Dissertation, Department of E & ECE, I. I. T Kharagpur, India, 2007.

A GL EMFHS Coupled Modeling for Wenchuan Earthquake

Ganquan Xie¹, Jianhua Li¹, Michael Oristaglio², and Xianwei Zhou³

¹GL Geophysical Laboratory, USA

²Schlumberger Doll Research, USA

³University of Science and Technology Beijing, Beijing, China

Abstract— In this paper, we propose a Global and Local Electromagnetic, Mud Stone Flow, Earth Heat, and Earth Mechanical Stress field coupled modeling to simulate the Wenchuan earthquake which just has been happen in the Sichuan Province of China. This coupled model couples 4 field which is massive nonlinear complex computational tasks. The traditional FD and FEM methods have serious difficulties for this simulation. By using GLGEO's GL and AGILD methods and software, we do not need to solve any large matrix and do not need any artificial boundary conditions. We overcome FEM' and FD's difficulty to solve massive matrix equations, and on inaccurate artificial boundary condition. Several results to simulate Wenchuan earthquake have been obtained.

1. INTRODUCTION

In the measurement and simulation of the Wenchuan earthquake which just has been happen in the Sichuan province of China, we fund that it is necessary to measure the Gravity, EM, flow, heat, and seismic data in the period of before earthquake and aftershock. Before Wenchuan earthquake, the electromagnetic measurement is lack in the earthquake measurement. After Wenchuan, Tangshan, and ChiChi earthquakes, we propose Global and Local Electromagnetic, Mud Stone Flow, Earth Heat, and Earth Mechanical Stress field coupled earthquake modeling, in short, GL EMFHS earthquake modeling. We emphasize that the measurements of EM and gravity field are same important as other field. Because one can not predict the earthquake's time and location, it is impossible to measure Gravity, EM, flow, heat, and seismic data in the exact location in before earthquake. Therefore, it is very necessary to measure the Gravity, EM, flow, heat, and seismic field data in the earthquake center and in the period of the aftershock. We propose that the natural earthquake and artificial seismic research should be combination in the earth sciences. We can use controlled artificial seismic to induce and reduce the damage of natural earthquake.

The description plan of the paper is as follows. The introduction is presented in Section 1. In Section 2, we develop the EM, flow, heat, and stress coupled model for the earthquake. In Section 3, we propose GL EMFHS coupled modeling. The advantages of the GL EMFHS coupled modeling are described in Section 4. In Section 5, the conclusion is made.

2. THE GL EM, FLOW, HEAT, AND STRESS COUPLED EARTHQUAKE MODEL

2.1. The Electromagnetic Model

We consider electromagnetic field and mud stone flow in the Earth.

$$\begin{aligned}\nabla \times E &= -i\omega\mu H, \\ \nabla \times H &= (\sigma + i\omega\varepsilon) E + (\sigma + i\omega\varepsilon) \mu V \times H + j,\end{aligned}\tag{1}$$

where E is the electric field, H is the magnetic field, V is the mud stone flow velocity, j is the initial electric current, σ is the electric conductivity, ε is the electric, μ is the magnetic permeability, and ω is the angle frequency, ρ is local density.

2.2. The Incompressible Viscous Flow Model

The incompressible viscous steady flow is governed by the Navier Stocks flow equation

$$-\eta\Delta V + \rho(V \cdot \nabla)V + \nabla p = J \times \mu H - \beta T \rho g,\tag{2}$$

where V is the flow velocity vector, p the hydrodynamic pressure, H is the magnetic field, T is the temperature, ρ is the density which depends on the temperature, η is the viscosity, β is thermal expansion coefficient. μ is the magnetic permeability, g is gravity acceleration. J is total electric current which includes initial and induce currents.

2.3. The Thermal Heat Model

In the Earth, the magnetic permeability is μ_0 . The thermal heat should be coupled into the EM and mud stone flow motion as follows

$$\Delta T - q(V \cdot \nabla)T = h(E, H, V), \quad (3)$$

where T is the temperature, $q = \rho/\kappa$, ρ is the density, κ is the thermal conductivity, V is the flow velocity vector, h is the weight sum of heat sources including dispersive and radiation source which is function [2, 5] of the electric field E , field H , and flow velocity V , which is determined by inversion updating [4] and the empirical formulas in the geology.

2.4. The Boundary Condition

The magnetic field H , flow velocity field V , and temperature T are coupled by the Equations (1), (2), and (3) nonlinearly. The magnetic field H and temperature T are of the far field radiation at the infinite.

2.5. The Displacement and Stress Model

The solidification displacement and stress model is governed by the following elastic-plastic flow thermal magnetic joint equation,

$$\frac{\partial \sigma_{s,ij}}{\partial x_j} + \omega_s^2 \rho_s u_s = f_i(B, p, T), \quad \sigma_{s,ij} = D(\lambda_s, \mu_s) \varepsilon_s(u_s), \quad (4)$$

and the corresponding boundary condition or radiation boundary conditions, where $\sigma_{s,ij}$ is solidification stress tensor which symbol is different from the electric conductivity, u_s is the displacement which symbol is different from the vortex $u = \nabla \times V$, ω_s is displacement field frequency which is very low and different from the EM field frequency ω , ρ_s is the density which is different from the resistivity, λ_s, μ_s are the Lamé constants, μ_s is different from the magnetic permeability. ε_s is the strain field which is different from the dielectric parameter, the right hand of the (4), $f_i(B, p, T)$ is weight sum of the Lorenz force depended on the magnetic flux B and flow velocity, the heat force depended on the grading of temperature, and the pressure p [2].

3. GL EMFHS COUPLED MODELING

The novel Global and Local field modeling and inversion is proposed in [3], we propose GL EMFHS COUPLED MODELING [1–3] in this section.

3.1. Iteration for Solving the Coupled Nonlinear Equations

We use the following iteration to solve the EM, Navier Stocks flow, heat, and mechanical coupled nonlinear Equations (1)–(4).

$$\nabla \times \frac{1}{(\sigma + i\omega\varepsilon)} \nabla \times H^{(n)} + \left(\nabla \times \mu V^{(n-1)} \times H^{(n)} \right) = Q_M, \quad (5)$$

$$-\eta \Delta V^{(n)} + \rho \left(V^{(n-1)} \cdot \nabla \right) V^{(n)} + \nabla p = J^{(n)} \times \mu H^{(n)} - \beta \rho T^{(n-1)} g, \quad (6)$$

$$\Delta T^{(n)} - q \left(V^{(n)} \cdot \nabla \right) T^{(n)} = h \left(E^{(n)}, H^{(n)}, V^{(n)} \right). \quad (7)$$

We solve the linearization equations (5), (6), and (7) in order to form the n th circle of the iteration. Then we solve the following elastic-plastic flow thermal magnetic joint Equation (4) to find the solidification displacement, strain and stress,

$$\frac{\partial \sigma_{s,ij}^{(n)}}{\partial x_j} + \omega_s^2 \rho_s u_s^{(n)} = f_i \left(B^{(n)}, p^{(n)}, T^{(n)} \right), \quad \sigma_{s,ij}^{(n)} = D(\lambda_s, \mu_s) \varepsilon_s \left(u^{(n)} \right). \quad (8)$$

3.2. Division of the Domain

The inhomogeneous EM, flow, thermal, and mechanical parameter domain Ω is divided into a set of the several sub domains $\{\Omega_k\}$, $k = 1, 2, \dots, N$. such that $\Omega = \bigcup_{k=1}^N \Omega_k$. The division is mesh or meshless.

3.3. GL Modeling for Solving the Magnetic Field Linearization Equation (5)

(3.3.1) In each Ω_k , $k = 1, 2, \dots, N$, we solve the adjoint Green's magnetic field differential integral equation of the Equation (4). By the dual curl procession, the adjoint Green's magnetic field differential integral equations are reduced into 3×3 matrix equations. By solving the 3×3 matrix equations, the 3×3 magnetic Green's function tensor $G_k^{M,(n)}(r', r)$.

(3.3.2) The global magnetic field is updated by the following local scattering magnetic field differential integral equation

$$H_k^{(n)}(r) = H_{k-1}^{(n)}(r) + \int_{\Omega_k} \left(\frac{1}{(\sigma + i\omega\varepsilon)_{k-1}} - \frac{1}{(\sigma + i\omega\varepsilon)_k} \right) \nabla \times G_k^{M,(n)}(r', r) \left(\nabla \times H_{k-1}^{(n)}(r') \right) dr' \\ + \int_{\Omega_k} \left(\nabla \times \left(G_k^{M,(n)}(r', r) \right) \times \mu \left(V_{k-1}^{(n)} - V_k^{(n)} \right) \right) H_{k-1}^{(n)}(r') dr'. \quad (9)$$

The $H^{(n)}(r) = H_N^{(n)}(r)$ is the GL magnetic field solution of the Equation (5).

3.4. GL Modeling for Solving the Flow Field Linearization Equation (6)

Let $u = \nabla \times V$, the Navier Stocks flow Equation (6) is reduced to

$$\Delta u^{(n)} - \kappa \left(V^{(n-1)} \cdot \nabla \right) u^{(n)} = M \left(E^{(n)}, H^{(n)}, T^{(n)} \right), \quad (10)$$

where $\kappa = \rho/\eta$,

(3.4.1) In each Ω_k , $k = 1, 2, \dots, N$, we solve the adjoint Green's flow field differential integral equation of the Navier Stocks Equation (10). By the dual gradient procession, the adjoint Green's flow field differential integral equations are reduced into 3×3 matrix equations. By solving the 3×3 matrix equations, the 3×3 magnetic Green's function tensor $G_k^{F,(n)}(r', r)$ is calculated.

(3.4.2) The Global flow field is updated by the following local scattering flow field differential integral equation

$$u_k^{(n)}(r) = u_{k-1}^{(n)}(r) + \int_{\Omega} \nabla \cdot \left(\left(\kappa_k V_k^{(n-1)}(r') - \kappa_{k-1} V_{k-1}^{(n)}(r') \right) G_k^{F,(n)}(r', r) \right) u_{k-1}^{(n)}(r') dr', \quad (11)$$

The $u^{(n)}(r) = u_N^{(n)}(r)$ is the GL flow field solution of the Equation (10). $V^{(n)} = \frac{1}{4\pi} \int_{\Omega} \frac{\nabla \times u^{(n)}(r')}{|r'-r|} dr'$

is the GL Navier Stocks flow velocity solution of the Equation (6), The Earth pressure $p^{(n)} = \frac{1}{4\pi} \int_{\Omega} \frac{\nabla \cdot (\rho(V^{(n)} \cdot \nabla)V^{(n)}) + \nabla \cdot (J^{(n)} \times \mu H^{(n)} - \beta \rho T^{(n-1)} g)}{|r'-r|} dr'$ is obtained.

3.5. GL Modeling for Solving the Thermal Temperature Field Linearization Equation (7)

(3.5.1) In each Ω_k , $k = 1, 2, \dots, N$, we solve the adjoint Green's thermal field differential integral equation of the heat Equation (7). By the dual gradient procession, the adjoint Green's temperature field differential integral equations are reduced into 3×3 matrix equations. By solving the 3×3 matrix equations, the 3×3 temperature Green's function tensor $G_k^{H,(n)}(r', r)$ is calculated.

(3.5.2) The Global temperature field is updated by the following local scattering temperature field differential integral equation

$$T_k^{(n)}(r) = T_{k-1}^{(n)}(r) + \int_{\Omega} \nabla \cdot \left(\left(q_k V_k^{(n)}(r') - q_{k-1} V_{k-1}^{(n)}(r') \right) G_k^{H,(n)}(r', r) \right) T_{k-1}^{(n)}(r') dr'. \quad (12)$$

The $T^{(n)}(r) = T_N^{(n)}(r)$ is the GL temperature field solution of the Equation (7).

3.6. GL Modeling for Solving the Elastic-plastic Flow Thermal Magnetic Linearization Equation (8)

(3.6.1) In each Ω_k , $k = 1, 2, \dots, N$, we solve the adjoint Green's flow field differential integral equation of the mechanical elastic Equation (8). By the dual gradient procession, the adjoint

Green's displacement field differential integral equations are reduced into 3×3 matrix equations. By solving the 3×3 matrix equations, the 3×3 magnetic Green's function tensor $G_k^{D,(n)}(r', r)$ is calculated.

(3.6.2) The Global displacement field is updated by the following local scattering displacement and strain field differential integral equation

$$\vec{u}_{s,k}^{(n)}(r) = \vec{u}_{s,k-1}^{(n)}(r) - \int_{\Omega_k} \vec{\varepsilon}^T \left(\vec{G}_k^{D,(n)}(r', r) \right) D(\lambda_{s,k} - \lambda_{s,k-1}, \mu_{s,k} - \mu_{s,k-1}) \vec{\varepsilon} \left(\vec{u}_{s,k-1}^{(n)}(r') \right) dr', \quad (13)$$

The $\vec{u}_s^{(n)}(r) = \vec{u}_{s,N}^{(n)}(r)$ is the GL displacement field solution of the Equation (8), $\sigma_{s,ij}^{(n)} = D(\lambda_s, \mu_s)$ $\varepsilon_s(u_{s,N}^{(n)})$ is the solidification stress tensor.

4. THE ADVANTAGES OF THE GL EMFHS COUPLED MODELING

The GL and AGILD method and software are GL Geophysical Lab's production. The GL method has advantages for resolving the historical difficulties in FEM and FD and Born methods [3]. We describe the advantages of the GL EMFHS modeling in this section.

4.1. There Is No Matrix Equation in the GL EMFHS Modeling

Our GL EMFHS coupled modeling has advantages to overcome the difficulties of the FEM and FD methods. Because using the FEM and implicit FD method, the EM, flow, thermal heat, and stress modeling are discretized into the big matrix equations. The cost to solve the coupled big matrix equations is very high. In the GL EMFHS coupled modeling, there is only 3×3 matrix equations need to be solved to obtain adjoint Green's function. There is no big matrix equation to be solved in the GL EMFHS coupled modeling that greatly reduces the computational cost.

4.2. There Is No Artificial Boundary and No Absorption Condition in the GL EMFHS Modeling

The absorption condition on the artificial boundary is necessary for FEM or implicit FD modeling. The error reflections from the numerical absorption condition on the artificial boundary degrade the accuracy of the FEM and FD modeling. To avoid of using the complex artificial boundary condition, paper [4] used the electric current instead of the magnetic field that caused very heavier cost to solve big full matrix equation. The temperature boundary condition on the wall is an approximation in [4]. The approximation thermal boundary condition is removed in the GL EMFHS coupled modeling, therefore the GL EMFHS modeling increases the accuracy of coupled EM, flow, temperature, displacement and stress field.

4.3. There Is No Coordinate Singularity in the GL EMFHS Modeling

There are $1/\rho$ and $1/\rho^2$ coordinate singularity at the pole point $\rho = 0$ in the cylindrical coordinate EM, flow, heat, and displacement equations. The coordinate singularity appears in the FEM and FD discretization equations of the EM, flow, heat, and Lamé displacement equations that is a difficulty. Because there is no coordinate singularity in the analytic Green's function, the GL EMFHS overcomes the coordinate singularity difficulty.

4.4. GL EMFHS Parallel Modeling

The big matrix equation, complicated and inaccurate absorption boundary condition, and coordinate singularity discretization are difficulties and obstacles to parallelize FEM and FD modeling. The GL EMFHS has no big matrix equation, no artificial absorption condition, and no coordinate singularity that greatly reduce the computational cost, complexity, and increase the accurate, moreover, GL EMFHS is self parallel algorithm.

5. CONCLUSIONS

The GL EMFHS coupled modeling is proposed and validated in this paper. The simulations show that the GL EMFHS coupled modeling is accurate, stable, and fast. The adjoint differential integral Equations (9), (11), (12), and (13) are new equation. The GL EMFHS coupled modeling has wide application in the Earthquake, EM stirring in the caster, atmosphere, environment, geophysics, earth sciences and space sciences and engineering.

We show that it is necessary to measure the Gravity, EM, flow, heat, and seismic data in the period of before Earthquake and aftershock. Before Wenchuan earthquake, the Electromagnetic

measurement is lack in the Earthquake measurement. After Wenchuan, Tangshan, and ChiChi Earthquakes, we propose Global and Local Electromagnetic, Mud Stone Flow, Earth Heat, and Earth Mechanical Stress field coupled earthquake modeling and emphasize the EM and gravity field measurements are same important as other field. Also, because we can not know the earthquake' time and location, it is impossible to measure Gravity, EM, flow, heat, and seismic data in the exact location in before earthquake, therefore, it is very necessary to measure the Gravity, EM, flow, heat, and seismic field data in the Earthquake center and in the period of the aftershock. We will add gravity field in our coupled Earthquake model in next paper. We propose that the natural Earthquake and artificial seismic should be combination in the Earth sciences. The controlled artificial seismic will be used to induce and reduce natural earthquake.

ACKNOWLEDGMENT

The authors are grateful to Professor P. D. Lax for his permanent attention and encouragement to our research works. Authors are grateful to Professor Yuesheng Li for his discussion. Authors thank Professor Wang and his research and measurements Group in Chengdu Technology University for their great help. Authors thank President Ho, Professor Zhu in Chengdu Technology University for their help.

REFERENCES

1. Xie, G., J. Li, and J. H. Li, "New AGILD EMS electromagnetic field modelingng," *PIERS Online*, Vol. 1, No. 2, 168–172, Hangzhou, China, August 22–26, 2005.
2. Xie, G., J. H. Li, J. Li, and F. Xie, "3D and 2.5D AGILD EMS stirring modeling in the cylindrical coordinate system," *PIERS Online*, Vol. 2, No. 5, 505–509, Cambridge, 2006.
3. Xie, G., F. Xie, L. Xie, and J. Li, "New GL method and its advantages for resolving historical difficulties," *PIERS Online*, Vol. 2, No. 3, 306–311, 2006.
4. Xie, G., J. Li, L. Xie, and F. Xie, "GL metro carlo EM inversion," *Journal of Electromagnetic Waves and Applications*, Vol. 20, No. 14, 1991–2000, 2006.
5. Meir, A. J. and P. G. Schmidt, "Analysis and finite element simulation of MHD flows, with an application to liquid metal processing," *Fluid Flow Phenomena in Metals Processing, Proceedings, 1999 TMS Annual Meeting*, 561–569, Pennsylvania, 1999a.

Retrieval of Higher Order Ocean Wave Spectra from Sunglint

G. P. Cureton¹, S. J. Anderson², M. J. Lynch¹, and B. T. McGann¹

¹Department of Imaging and Applied Physics

Curtin University of Technology, Perth WA, Australia

²Defence Science and Technology Organisation, Salisbury SA, Australia

Abstract— Presented in this paper is a method of retrieving higher order statistical functions of the ocean wave surface from sunglint, or solar optical radiation specularly reflected from the surface. An expression was derived for the modelled slope probability density, which contains as parameters the desired cumulants and cumulant functions which we wish to retrieve. We then modelled the higher order statistical functions of the sunglint by integrating the slope density over a clipped domain representing the finite angular extent the solar disk subtends at the wave surface. This relationship was then inverted in order to retrieve the slope cumulant and cumulant functions from the corresponding functions of simulated sunglint data.

1. INTRODUCTION

A thorough knowledge of the dynamics of the ocean surface, in particular with respect to wind generated waves, is relevant for a range of human activities, including the design and operation of ships, the construction and servicing of marine structures such as offshore oil and gas drilling platforms, the management of coastal environments, and, increasingly, for the design and deployment of wave energy extraction systems. Of particular concern is the effect that higher order dynamical processes, often neglected for the sake of simplicity or computational tractability, have on such things as energy transfer between wave modes, and more importantly, energy transfer to human structures.

One approach to the characterization of the the ocean surface is through illumination by optical radiation, a notable example of which is the work of [1], which obtained wind wave slope distributions from aerial photographs of sunglint. More recently, [2] determined a relationship between statistical functions of the wave slope and glint images, which was inverted to obtain the wave elevation power spectra.

The latter approach is here generalized to enable the retrieval of the higher order statistical functions of the wave slope. Knowledge of these functions is necessary in order to characterize the extent of wave-wave coupling, and the resultant diffusion of wave energy from the initial wind forcing to different parts of the wave spectrum.

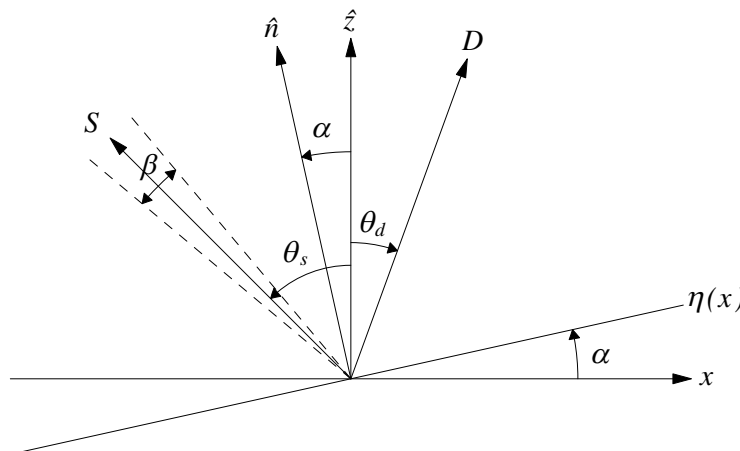


Figure 1: Geometry of the experiment for the case where the specular condition is met.

2. FORWARD MODEL

We have a one dimensional surface elevation $\eta(x)$ with variance $\kappa_\eta^{(2)}$ and zero mean $\kappa_\eta^{(1)}$. The slope of this surface is given by $\xi(x) = \tan \alpha$, with variance $\kappa_\xi^{(2)}$. The surface is illuminated by a source

S with zenith angle θ_s and angular subtense β (Figure 1). The beam is reflected at the specular point and reaches the detector D with zenith angle θ_d .

As we move along the surface we encounter slopes that either do or do not satisfy the specular condition. If we set the slope values that satisfy this condition to unity, and all others to zero, the slopes $\xi(x)$ are mapped to the binary process $L(x)$. For the case where the source S is a point source, $L(x)$ would consist of a series of delta functions, each for a slope ξ_0 which satisfies the specular condition. Since the source of interest, the Sun, subtends a finite solid angle, there are a small range of slopes $\xi_0 \pm \Delta\xi/2$ that satisfy the specular condition. This results in the delta functions becoming peaks of finite extent (Figure 2).

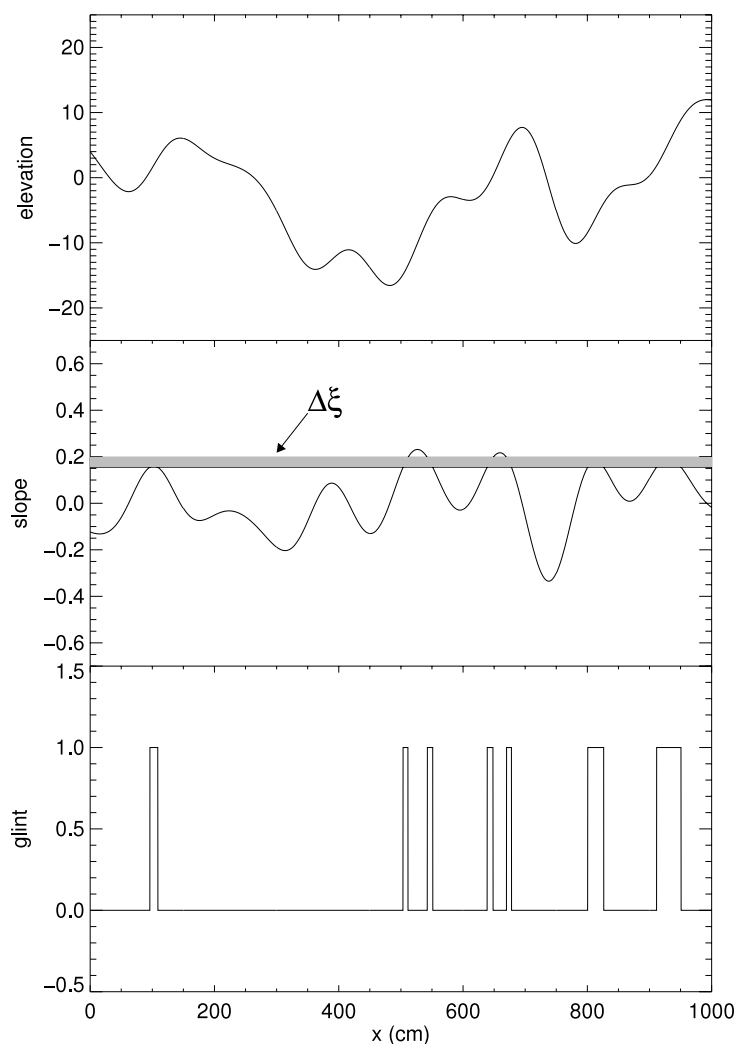


Figure 2: Shown in this figure are the surface elevation $\eta(x)$, the surface slope $\xi(x)$ with the slope range selected by the glitter function $\Delta\xi$, and the glint process $L(x)$.

Using geometric optical considerations, [2] developed the *glitter function* to generate the glint L from the surface slope ξ

$$B(\xi) = \text{rect} \left[\frac{\xi - \xi_0}{(1 + \xi_0^2) (\beta/2)} \right], \quad (1)$$

which is a rectangular function with the range $\xi_- \leq \xi \leq \xi_+$, or

$$\xi_0 - (1 + \xi_0^2) \frac{\beta}{2} \leq \xi \leq \xi_0 + (1 + \xi_0^2) \frac{\beta}{2}. \quad (2)$$

ξ_0 is the specular slope and β is the angle subtended by the source, in our case the Sun. The glint

moments are then calculated using the relationship

$$\mu_L^{(i)} = \int_{-\infty}^{\infty} B(\xi)p(\xi)d\xi, \tag{3}$$

and the glint moment functions from

$$\mu_L^{([n])} M_L^{(\vec{n})}(\tau_1, \dots, \tau_{N-1}) = \int_{\mathbb{R}^N} B^{n_1}(\xi_1)B^{n_2}(\xi_2), \dots, B^{n_N}(\xi_N)p(\vec{\xi})d\xi_1d\xi_2, \dots, d\xi_N, \tag{4}$$

where $\vec{n} = (n_1, n_2, \dots, n_N)$ and $[n] = n_1 + n_2 + \dots + n_N$. The slope density is given by

$$p(\vec{\xi}) = \frac{|\Lambda|^{-\frac{1}{2}}}{(2\pi)^{\frac{N}{2}} \left(\kappa_{\xi}^{(2)}\right)^{\frac{1}{2}1}} \exp\left[-\frac{1}{2}\nu^T \hat{\Lambda} \nu\right] \left[1 + \frac{1}{3!} \sum_{\vec{n}, [n]=3} \binom{3}{\vec{n}} \lambda_{\xi}^{(\vec{n})} He_{\vec{n}}^{\{\hat{\Lambda}\}}(\vec{\nu}) + \dots\right], \tag{5}$$

where ν is the normalised slope, Λ is the slope covariance matrix, $\lambda_{\xi}^{(\vec{n})}$ is the normalised slope cumulant of order $[n]$ and $He_{\vec{n}}^{\{\hat{\Lambda}\}}(\vec{\nu})$ is the Hermite polynomial.

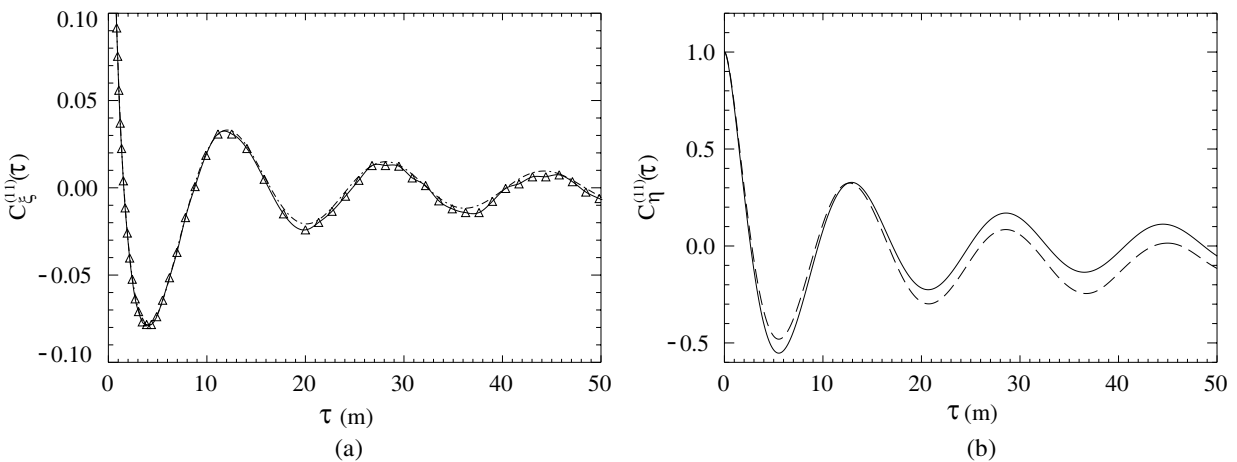


Figure 3: Shown in this figure are the simulated and retrieved slope (a) and elevation autocovariances.

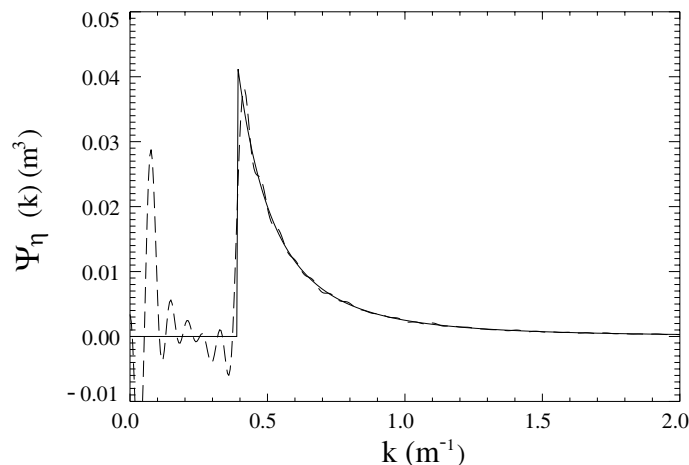


Figure 4: Shown in this figure are the simulated (solid line) and retrieved (dashed line) elevation power spectra.

3. RETRIEVAL OF SYNTHETIC HIGHER ORDER SLOPE CUMULANT FUNCTIONS

Multiple realisations of the glint data were generated for a range of geometries, and the average second and third glint moment functions were computed in each case. Using (3) and (4), this glint data was inverted to retrieve the slope cumulants and cumulant functions. Shown in Figure 3(a) is the simulated and retrieved second slope cumulant function, or autocovariance.

We can see that the retrieval is good for small lag (where the inversion is well posed), and becomes slightly worse at higher lag where the glint-slope autocovariance relationship is less well behaved in the presence of noise. Figure 3(b) shows the simulated and retrieved elevation autocovariances. The retrieved elevation autocovariance is calculated by doubly integrating the slope autocovariance, and hence is particularly sensitive to the retrieved slope cumulants, as these are directly related to the boundary conditions of the integration between each lag step. We can see that the elevation autocovariance retrieval is good for small lag, but becomes progressively worse as the integration wanders from the true solution.

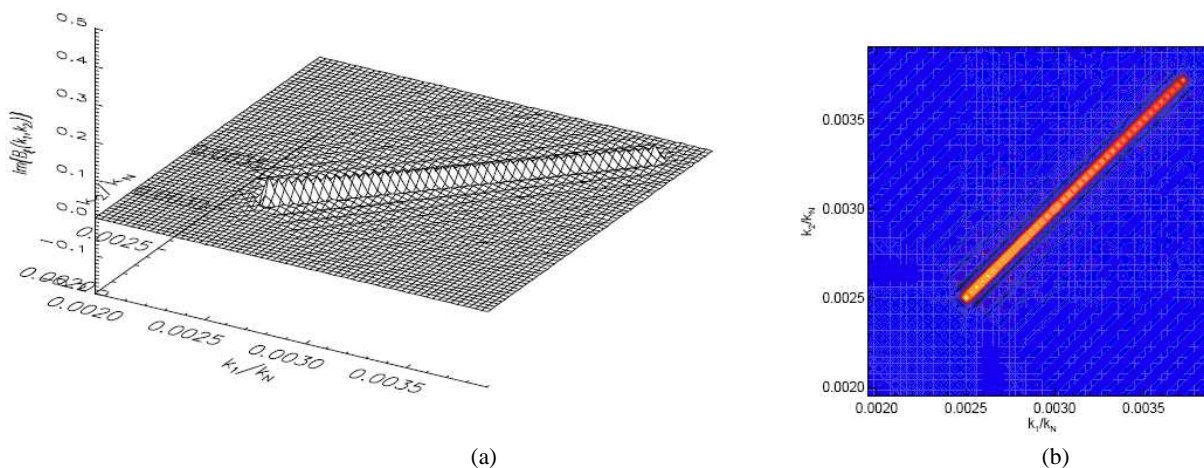


Figure 5: Shown in this figure is the simulated slope bispectrum.

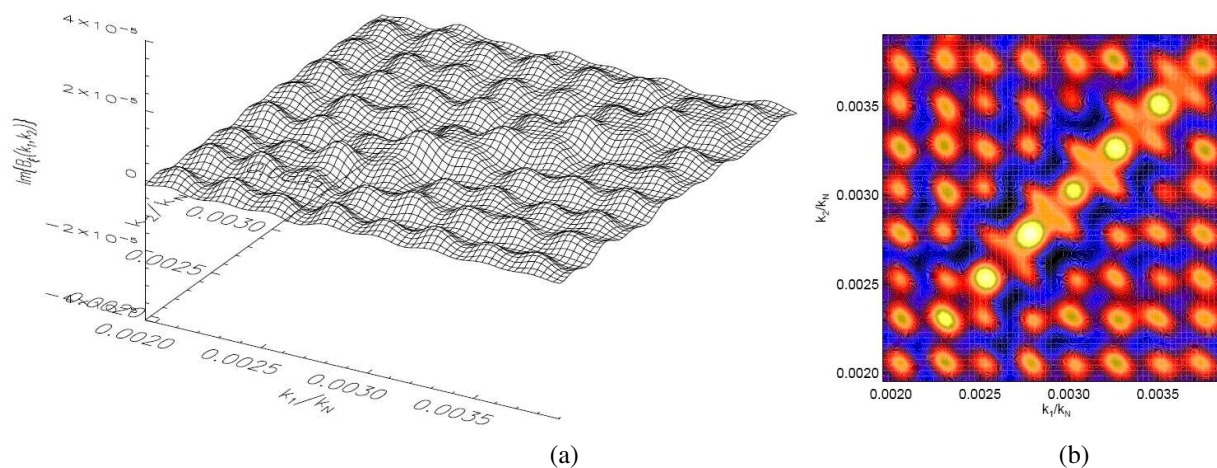


Figure 6: Shown in this figure is the retrieved slope bispectrum.

In Figure 4 are the simulated and retrieved elevation power spectra, calculated by inverse Fourier transforming the corresponding autocovariances. We can see that whilst the gross structure of the power spectrum was retrieved, the sharply varying features at low wavenumber would require an accurate retrieval of the autocovariance at high lag, and errors in this region result in under- and over-shoot of the correct power spectrum values at the low wavenumber cutoff.

Shown in Figures 5 and 6 are the simulated and retrieved slope bispectra, which are the Fourier transforms of the corresponding third slope cumulant functions. If there is any wave coupling between spectral components at wavenumbers k_1 and k_2 in the elevation and slope data (manifested

as phase correlations between those wavenumber components), they arise as non-zero values at (k_1, k_2) in the bispectrum plane.

In Figure 5, we see a series of distinct wave self-interactions (as indicated by the non-zero values along the line $k_1 = k_2$). We can see in Figure 6 that the self-interaction features in the retrieved slope bispectrum along the line $k_1 = k_2$ are only partially resolved. This is somewhat due to the sensitivity of the inversion to the retrieved slope cumulants, themselves dependent on the measured glint moments. Since the glint constitutes such a sparse data set (as shown in Figure 2), stable estimates of the glint moments are difficult to achieve. This situation is even more pronounced for the estimation of the glint bispectrum.

4. CONCLUSION

In this paper we have demonstrated a method of retrieving slope higher order statistical functions from sunglint data. The method works well for the retrieval of second order functions (autocovariance), but is prone to corruption by errors in the estimated glint statistical functions.

REFERENCES

1. Cox, C. and W. Munk, "Measurement of the roughness of the sea surface from photographs of the sun's glitter," *J. Opt. Soc. Am.*, Vol. 44, No. 11, 838–850, 1954.
2. Alvarez-Borrego, J., "Wave height spectrum from sunglint patterns: An inverse problem," *J. Geophys. Res.*, Vol. 98, No. C6, 10245–10258, 1993.

Monitoring of Satellite Thermal Pattern of Ocean Front between Coastal and Ocean Water

S. Nakamura
Kyoto University, Japan

Abstract— A satellite thermal pattern of ocean front facing coastal water is introduced which was obtained by a direct receiving of a satellite signal for sea surface thermal pattern in an infrared band at a station in order to demonstrate the ocean front evolution.

1. INTRODUCTION

The author has introduced several sea surface thermal pattern after directly receiving a satellite signal for the infrared band. This thermal pattern gives us the sea surface temperature distribution in the foot print of the sensor mounted on the satellite. This work is mainly focused for a state of matured eddy formation which can be found as a strongly nonlinear process of a folded ocean front.

2. MONITORING SYSTEM

A simple antenna of cross-bar type and a desk-top personal computer system was used for monitoring the sea surface thermal pattern. The system had worked for a directly receiving of the satellite signal. The pixel size in the pattern was ca 4km square for this case. The obtained sea surface pattern informs the ocean front folding process. In this work, one of the typical cases is introduced. Then, the case make a folding ocean front process.

3. SATELLITE SIGNAL

Satellite signal had been directly received by the system at a station on the coast. The monitoring had been undertaken for a couple of the satellites at passing just above the station. Each of the satellites had a polar orbital motion at about 110 minutes cycle, so that, the station could receive directly the satellite signal of the sea surface infrared signal. The relative shift of the satellite orbits had well arranged to pass at every six hours.

4. MONITORING OF OCEAN FRONT

The satellite signal directly received by the system was analyzed to reduce the pattern of the sea surface in the foot print of the sensor mounted on the satellite.

For the author's convenience, the ocean front is introduced as a result of the pattern of the monitoring in the northwestern Pacific.

After the agreement of the NOAA and the JMA (Japan Meteorological Agency), directly receiving of a couple of the satellites could be possible for the author's research.

It is well understood generally that the ocean front is formed where the coastal water meets the ocean water. The ocean front is approximately taken as a thermal front even though the dynamics of the sea water is controlled by the sea water temperature and the salinity because the densimetric property of the sea water is essential to consider about the sea water motion in the ocean. The ocean front is found on the sea surface though the ocean water motion in the ocean surface layer above about 200m deep is effective to consider the ocean front evolution.

When the sea water has no viscosity and its density is uniform and isotropic, it is easy to have a linear solution of the water motion though it is necessary to consider some factors, for example, viscosity and salinity, temperature and water depth. The motion of the waters in the ocean is controlled finally by the density distribution in the ocean.

The ocean front separates the coastal water and the ocean water, so that it make easy to know what spacial pattern is to find what distribution of the maximum gradient of the sea surface temperature in the ocean. After the planetary effect of the earth, the water motion in the ocean is different from that in the river. However, the ocean front just neighbor the coast, a quite similar pattern found in the case of no earth's motion can be seen around the ocean front. This is the positive point for application of the satellite thermal monitoring of the sea surface.

The ocean front evolution could be seen after reducing the satellite thermal pattern of sea surface when there is an understanding of geophysical hydrodynamics. Nevertheless, the ocean water hydrodynamics has yet many problems even for a linear problem and some nonlinear processes. Then, it is necessary to be aware of the fact that cases in the actual pattern is more complicated rather than a solution of the equation of motion for a simplified model.

5. SEA SURFACE WAVE FACET

The sea surface can be assumed as a part of the planet earth, so that, an assumption of the sea surface can be taken a part of a black body as the earth.

Applying Stefan-Boltzmann Theory for radiation out of a black body, it may be possible to assume a concave part of a wave facet on the sea surface which acts as a radiator of beam with a focus just neighbor of the sensor of the satellite.

An analysis shows that the focusing effect at the sensor is closely related to the radius of the curvature of the wave facet. This focusing is affected by the spacial spectrum of the sea surface waves in the ocean.

6. EXAMPLE OF MONITORED OCEAN FRONT

As is noted above, the ocean front evolution is actually found in a complicated form. Adding to that, several geometrical factors related to the sea surface controls focusing effect.

As for the curvature of the sea surface wave facet, it is useful to refer to the result of hydrodynamics about the sea surface waves.

The altitude of the satellite is also one of the important factors. As far as it concerns of the radiation beam of the infrared band, the solar beam is out of interest in this work. The author knows that the solar beam of the visible band does not affect to the satellite thermal pattern of the sea surface.

With the consideration of the effects in relation to the factors noted above, a thermal pattern obtained after analyzing the directly received satellite signal for the sea surface information about the radiation of the infrared band out of the sea surface.

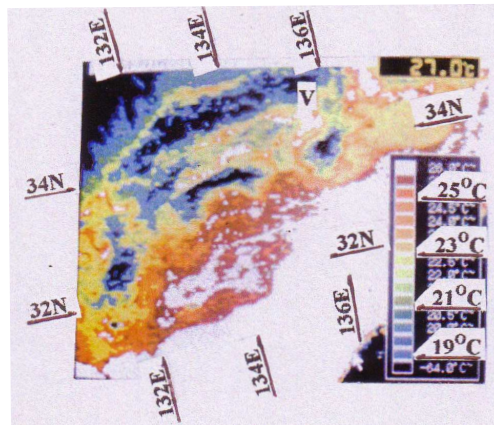


Figure 1: Satellite infrared pattern of ocean front. 1) Directly monitored at 0734-JST on 1994 June 3 [NOAA-12]. 2) Maximum of thermal gradient is formed an ocean front as a line to show coastal water and ocean water contacts. 3) Horizontal shearing effect found. 4) Ocean surface water of a thermal plateau (temperature 26°C <). 5) Coastal surface water (temperature between 23°C and 26°C).

In Fig. 1, a satellite thermal pattern of the ocean front is introduced. In this pattern, the ocean water is in the white area where the sea surface water is higher than 26°C . This white part is almost same temperature so that this area can be called as plateau or thermal plateau. The sea surface temperature of the coastal water is between 23°C and 26°C in this case.

Looking at the thermal pattern of the ocean water, it can be seen that a difference of the sea surface wave spacial spectrum after considering a simple model. By this time, there have been many researches and contributions about timely spectrum of the sea surface waves though the thermal plateau must be understood by the spacial spectrum but timely spectrum.

7. CONCLUSIONS

The author introduced about satellite thermal monitoring of the ocean front evolution. First, an out line of the monitoring system is noted. In this work, a direct receiving of the signal from the satellite is undertaken. Analyzing the signal, a pattern of the sea surface pattern is obtained. With some application of geophysical hydrodynamics, it can be seen about ocean front evolution.

Radar Cross Section of Simple and Complex Targets in the C-band: A Comparison between Anechoic Chamber Measurements and Simulations

M. A. Alves¹, I. M. Martins^{2,3}, M. A. S. Miacci², and M. C. Rezende¹

¹Instituto de Aeronáutica e Espaço, Materials Division, Brazil

²Instituto Tecnológico de Aeronáutica, Brazil

³Universidade de Taubaté, Brazil

Abstract— In order to validate RCS measurements performed in an anechoic chamber, experimental results are compared with simulations made using a commercial electromagnetic software package. The experimental part of this work was performed inside an anechoic chamber, with the radar operating in the C-band (6 GHz). Two metallic targets, a cylindrical body with four square fins and a section of an air-to-air missile, were used for the RCS measurements. In order to improve the accuracy of the experimental data, an active noise suppressing system, based on the principle of phase cancellation, was used. The simulation software FEKO was used to calculate the RCS of models of these two targets. The comparison of simulations and experimental data shows good agreement between them, validating the experimental methods used in the collection of RCS data, as well as the results obtained with the simulation software.

1. INTRODUCTION

Measurement of radar cross section (RCS) of objects is a complex task due to the many factors that may affect these measurements. Instrumental errors, spurious interferences and reflections are some of contributors that degrade the quality of the data. These problems are compounded when one is interested in reducing the RCS of an object, as in this case, the magnitude of these effects can overshadow the true RCS values. Many methods have been proposed and used for the measurement of RCS of several types of targets [1]. Depending on the size of the targets and radar frequencies used, RCS measurements can be performed on outdoor ranges or indoors, inside anechoic chambers [2]. In RCS measurements, it is important that the radar is illuminated by an electromagnetic wave which is uniform in phase and amplitude. For practical purposes, the maximum tolerance for amplitude variation over a target is 0.5 dB, and the phase should not deviate by more than 22.5°. These conditions characterize the far-field condition [3], given by

$$r = \frac{2d^2}{\lambda} \quad (1)$$

where r is the distance between radar and target, d is the largest dimension of the target, and λ is the wavelength of the radar. To ensure good measurements, errors produced by the instrumentation should neither exceed 0.5 dB nor vary in time. Also, the dynamic range of the system should be at least 40 dB when measuring targets with small RCS; dynamic range values in the order of 60 dB or higher are preferable when RCS reduction studies are conducted or when radar absorbent materials are used. In this study, measurements of the RCS of two objects were performed inside an anechoic chamber and a noise suppression circuit [4] was used to improve the accuracy of the data. These results were compared with those obtained from RCS computer simulations performed on the models of these objects using a commercial software.

2. ANECHOIC CHAMBER SET-UP AND METALLIC TARGETS

The experimental part of this work was conducted in the anechoic chamber at the Aeronautics Technology Center (CTA, Brazil) [5]. Figure 1(a) shows the antennas used for the measurements. The distance between target and antennas in the anechoic chamber was about 6 m. The radar operated at 6 GHz (C-band), in horizontal polarization and quasi-monostatic configuration. The high performance corrugated horn antennas, model ANSAT 1.8, are manufactured by Avibras (Brazil). Each antenna has a gain of approximately 17 dBi, symmetric radiation pattern and low level of secondary lobes, which produces a narrower radiation beam and less energy diffusion in regions outside the main beam. Also, these antennas are built so that the coupling between them is minimized.

The source of microwave radiation is a HP8360B synthesized CW generator and the signal receiver is a HP8593E spectrum analyzer. An active noise suppressing system based on the principle of phase cancellation was used to improve the accuracy of the experimental data [4]. This system samples the transmitted signals, discriminates signals from spurious reflections, and translates the phase of the received signals until they are canceled, reducing the noise to a minimum. Undesirable signals are minimized by the application of the canceling principle and by the inversion of phase. RCS measurements of two square flat plates made of aluminum and measuring 0.2×0.2 m and 0.3×0.3 m were used to calibrate the system. Also, an indirect calibration method [6] was used, taking into account some parameters of the system, such as antenna gain, distance between target and antennas, loss in cables, among others. The deviation in the RCS measurements was within 0.7 dB.

Two metallic targets were used for the measurements. The first target, a hypothetical missile, consists of a cylinder made of aluminum, having a length of 0.32 m and a radius of 0.075 m; four square flat aluminum plates measuring 0.15 m on a side are attached to the cylinder (Figure 1(b)). The second target is the front section of a decommissioned air-to-air missile (MAA-1 Piranha, Mectron, Brazil) (Figure 1(c)). Its body and fins are mostly made of aluminum, and its length is 0.72 m. For a frequency of 6.0 GHz, the hypothetical missile and the missile section lengths are 6.4λ and 14.4λ , respectively.

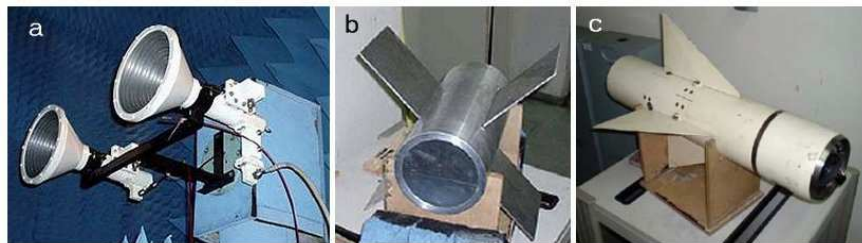


Figure 1: (a) Corrugated horn radar antennas, (b) hypothetical missile and (c) missile section.

3. OVERVIEW OF THE SIMULATION SOFTWARE AND MODELS

In the present study, the Multilevel Fast Multipole Method (MLFMM) [7], as implemented in FEKO software [8], was used for the RCS simulations. MLFMM is an alternative to the more commonly used Method of Moments (MoM). One of MLFMM's main advantages over MoM is that it can be used for large structures. In both MoM and MFLMM, basic functions model the interactions between all triangle elements. MFLMM is different from MoM in that instead of computing the interaction between individual basic functions, MFLMM computes the interaction between groups of basic functions, resulting in significant gains in CPU time. The individual treatment of N basis functions in the MoM results in an N^2 scaling of computer memory requirements to solve the impedance matrix, and N^3 in CPU time to solve the linear set of equations. On the other hand, for the more efficient MFLMM, the scaling of computer memory is $N \cdot \log(N)$, and $N \cdot \log(N) \cdot \log(N)$ in CPU time. Depending on the size of the problem, it can result in the reduction of solution time of orders of magnitude.

Models of the targets used for the RCS measurements were created using Rhinoceros computer-aided design (CAD) software and imported into FEKO, where a Delaunay triangulator was used to generate surface meshes. Figures 2(a) and 2(b) show the models used in the simulations. The meshes are not shown due to the scale of the models. The surfaces of the hypothetical missile and the section of the air-to-air missile were discretized into 22.256 and 47.971 triangular elements, respectively. Note that since the RCS depends on the scattering of the microwave radiation illuminating an object, the external surface of this object is the most important feature to be taken into account in the simulations. Thus, to keep the problem treatable, the internal parts of the targets were not considered in the simulations.

The simulations were carried out using a PC with a 1.8 GHz Pentium processor and 1.7 Gbytes of RAM.

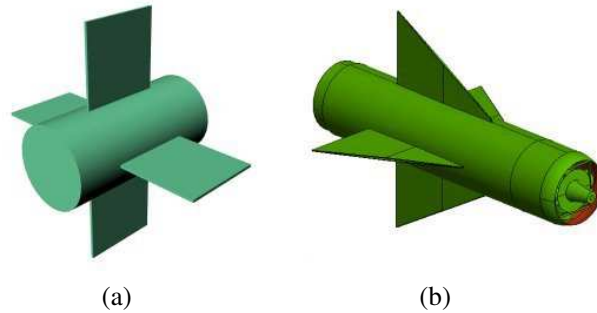


Figure 2: CAD models (not to scale) of the (a) hypothetical missile, and (b) missile section.

4. RESULTS

For both measurements and computer simulation, the targets were rotated about an axis perpendicular to the main axis of their cylindrical bodies. Measurements were taken at 0.5° intervals, the simulated RCS was calculated at 1.0° intervals, and the targets were rotated 360° about the rotation axis. Since the far-field condition (1) is not completely satisfied in the measurements, the simulations were performed taking into account the distance between the target and the radar antenna. In this case, the targets were illuminated by the radiation pattern produced by a point source located at a finite distance, and the scattered near-field was calculated. This procedure is much more computationally intensive than the use of a plane wave to illuminate the targets. The simulation times for the hypothetical missile and the missile section were about 24 h and 90 h, respectively. Figures 3(a) and 3(b) show the comparison of measured and simulated RCS for the hypothetical missile and missile section, respectively.

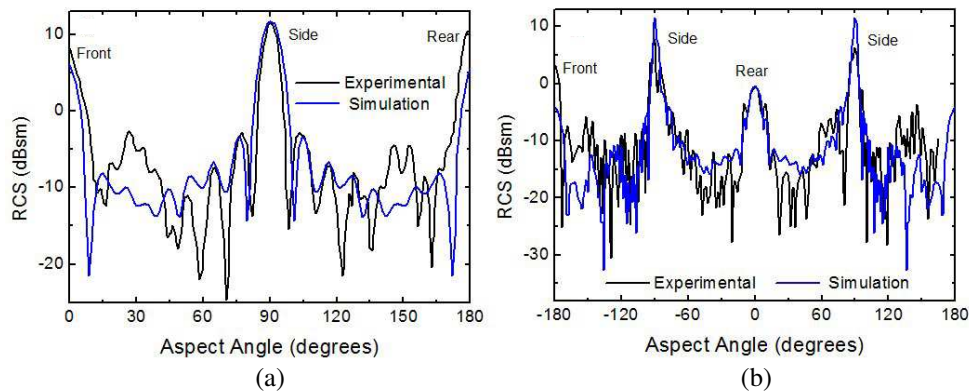


Figure 3: Measured and simulated RCS patterns. (a) Hypothetical missile and (b) missile section.

In both cases, one can observe that there is good agreement with respect to the overall RCS patterns but, upon close inspection, differences between the simulated and the measured RCS can be observed. The measured and simulated RCS patterns for the hypothetical missile show very good agreement for aspect angles between 60° and 120° , RCS lobes produced when the side of the target is illuminated by the radar are very similar in shape and amplitude. For angles between 15° and 60° , and 120° and 165° , the measured RCS pattern is asymmetrical. This asymmetry may be the result of surface irregularities or misalignment of the target with respect to the antennas. Figures 4(a) and 4(b) show the simulated electric currents on the surfaces of the models. This type of information is very important, because it allows the visualization of reflective regions on the surfaces of the models.

In order to compare the RCS patterns produced by the missile section, it is necessary to take into account that this target is a somewhat complex object. Features such as electronic circuitry, cables, rivets, connectors, etc., can alter significantly the symmetry of the RCS pattern produced by the target. On the other hand, the model of the missile section, although well constructed, did not have this level of detail, and therefore its RCS pattern is “simpler” and symmetrical. Still, the

three main RCS peaks produced by the rear and sides of the missile section, -90° , 0° and 90° , show similarities in shape and amplitude.

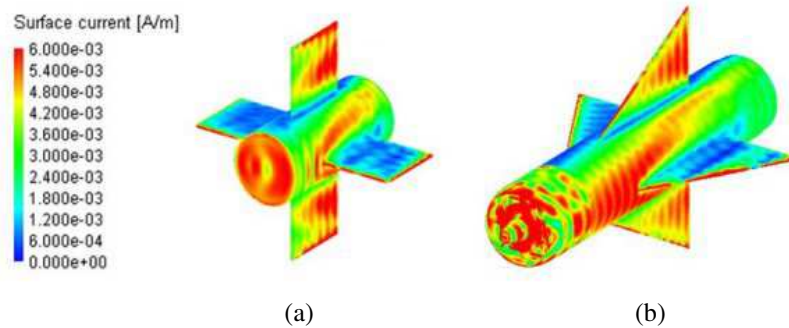


Figure 4: Surface currents on the models: (a) Hypothetical missile and (b) missile section. The radar wave makes an angle of 20° with respect to the direction defined by the main axis of the cylindrical bodies of both models.

5. CONCLUSIONS

The study of electromagnetic scattering is a challenging task due to the complexity of the phenomenon. In this paper, the RCS patterns produced by simple (hypothetical missile) and complex (missile section) targets were measured experimentally in an anechoic chamber and simulated with a simulation software. Despite the great care taken to produce both experimental and simulated results, differences were observed when comparing measurements and simulations. Simulations can be very time consuming, but they allow a better visualization of the phenomena; on the other hand, anechoic chamber measurements can be very precise. These differences serve to point out that measurements and simulations of RCS can, and should, be used simultaneously in order to better characterize a target being studied, as different RCS features can be described and identified using different tools.

ACKNOWLEDGMENT

The authors wish to express their gratitude to the Brazilian funding agencies CNPq (Proj. No. 47193 1/03-9, 301583/06-3, 307455/06-8) and Fapesp (Proj. No. 03/00716-4), for the financial support, and to Instituto Tecnológico de Aeronáutica, Instituto de Aeronáutica e Espaço-Divisão de Materiais, and the Brazilian Air Force, for their collaboration in this project.

REFERENCES

1. Knott, E. F., J. F. Schaeffer, and M. T. Tuley, *Radar Cross Section Measurements*, Artech House Inc., Norwood, 1993.
2. Dybdal, R. B., "Radar cross section measurements," *Proceedings of the IEEE*, 498–516, Los Angeles, April 1987.
3. Solknik, M., *Radar Handbook, 2nd ed.*, McGraw Hill, New York, 1990.
4. Miacci, M. A. S., I. M. Martin, and M. C. Rezende., "Implementation of an active noise suppression system in C-band indoor RCS measurements," *Proceedings of Microwave and Optoelectronics Conference*, 396–400, Salvador, Brazil, November 2007.
5. Miacci, M. A. S., I. M. Martin, and M. C. Rezende., "Radar cross section measurements of complex targets (missile parts) in C-band in anechoic chamber," *Proceedings of Microwave and Optoelectronics Conference*, 401–405, Salvador, Brazil, November 2007.
6. Currie, N. C., *Radar Reflectivity Measurement: Techniques and Applications, 1st ed.*, Artech House Inc., Norwood, 1989.
7. Coifman, R., V. Rokhlin, and V. Wandurza, "The fast multipole method for the wave equation: A pedestrian prescription," *IEE Antennas and Propagation Magazine*, Vol. 35, No. 3, 7–12, 1993.
8. FEKO, EM Software & Systems, Available: <http://www.feko.info>. Accessed February 15, 2008.

Analysis of Two-dimensional Scattering by a Periodic Array of Conducting Cylinders Using the Method of Auxiliary Sources

Naamen Hichem and Taoufik Aguil

Ecole Nationale d'ingénieurs de Tunis

Département Technologie de l'information et de Communications, Tunisia

Abstract— A linear array constituted by a finite number of conducting cylinders is modelled via the conventional method of auxiliary sources (MAS). Initially, the global coupling relating cylinders permits the near and far fields calculation. Finally, taking into account partial coupling describing neighbouring cylinders leads to a partially filled matrix, so therefore the computational cost is significantly reduced. Global and partial coupling reveals the same results for the chosen arrays.

1. INTRODUCTION

The method of auxiliary sources is a numerical technique used extensively to solve boundary problems [1]. According to the MAS, the EM fields within each domain are expressed as a linear combination of analytical solutions of Helmholtz equation. These particular solutions constitute the base of auxiliary sources placed on the auxiliary contour surrounded by the physical one [2].

The MAS is applied to model coupling between different, infinitely, and parallel conducting cylinders, illuminated by a TMz monochromatic plane wave. The global coupling is modelled by the mutual satisfaction of the boundary conditions just on the collocation points of every cylinder.

These boundary conditions lead to a linear system having as solution the amplitude and phase of scattered field [3].

In the general case, every constitutive part of an array interacts with the rest of the array in the purpose to model exact or global coupling between different parts which lead to a completely filled matrix entraining a difficult computation.

In the order to decrease the computational cost, we suppose that every cylinder is coupled with only the adjacent or the two adjacent one. The mathematical calculus show that the global matrix is fully simplified and the implementation code realized with Mathematica justify the low computational cost achieved by this approximation.

Numerical results (RCS, pattern field) reveal good agreement with references [5, 8].

At the end, we have numerical results justifying the technique and the possibility to extend it to macro arrays (or for the other parts of the physical problems involving many mutual interactions...).

An $e^{j\omega t}$ time convention is assumed and suppressed throughout the paper.

2. FORMULATION

A TMz monochromatic plane wave illuminate under the φ_i incidence a linear array of K infinite, PEC, circular cylinders positioned along the x -axis (Fig. 1).

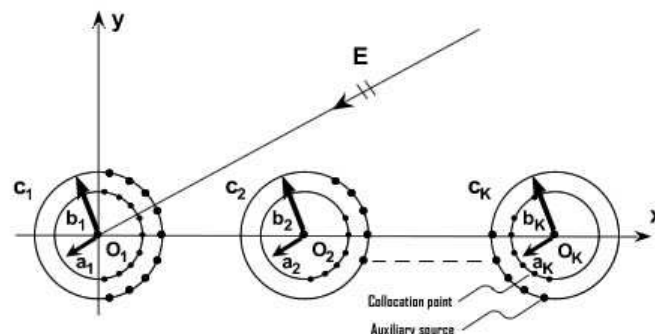


Figure 1: Linear array of K cylinders.

The incident transverse magnetic wave has an electric field:

$$E_i(x, y) = E_{oi} \vec{z} \exp \{jk_0 (x \cos(\varphi_i) + y \sin(\varphi_i))\} \quad (1)$$

Here, \vec{z} denote unit vector in the z direction, since the incident electric field is z directed and independent of z with uniform cylinders along z , then we deduce that the scattered field is z directed too, reducing the scattering problem to a bidirectional one.

For every cylinder, the auxiliary sources are regularly distributed along the auxiliary contour surrounded by the physical one on which are positioned the collocation points.

An auxiliary source (x_n, x_n) produce an electric field expressed as:

$$E_{sn}(x, y) = A_n \vec{z} H_0^{(2)} \left[k_0 \sqrt{(x - x_n)^2 + (y - x_n)^2} \right] \quad (2)$$

Where, $H_0^{(2)}(\cdot)$ is the Hankel function of the second kind of first order and A_n the complex current.

According to the standard impedance boundary condition (SIBC), the tangential component of the total electric field must be continuous on the boundary [4], then for a PEC:

$$n \wedge E_t = 0 \quad (3)$$

Applying this relation on every boundary cylinder, we obtain a linear system composed of K Equations. Where, the unknowns A_n as mentioned before represent the complex currents.

$$\begin{aligned} E_1 + \sum_{j \neq 1} E_{1/j} + E_{i/C_1} &= 0 \\ E_2 + \sum_{j \neq 2} E_{2/j} + E_{i/C_2} &= 0 \\ &\dots\dots\dots \\ &\dots\dots\dots \\ E_K + \sum_{j \neq K} E_{K/j} + E_{i/C_K} &= 0 \end{aligned} \quad (4)$$

E_1 is the scattered field by C_1 .

$E_{1/j}$ is the scattered field by C_j , and calculated on C_1 .

We have N auxiliary sources and $M = N$ collocation points per cylinder, the system (4) have K Equations and $N \cdot K$ unknowns since (3) is verified on just one collocation point per cylinder.

2.1. Global Coupling

The linear system (4) traduce that the electric field on each collocation point take into account the contribution of all the auxiliary sources present in the linear array.

Let us consider a collocation point m_1 on C_1 , then:

$$\begin{aligned} E_{i/m} &= E_{oi} \exp \{jk_0 (x_m \cos(\varphi_i) + y_m \sin(\varphi_i))\} \\ E_{1/m} &= \sum_{n^1=1}^{N^1} A_{n^1} H_0^{(2)} [k_0 R_{m^1 n^1}] \\ E_{1/j} &= \sum_{n^j=1}^{N^j} A_{n^j} H_0^{(2)} [k_0 R_{m^1 n^j}] \end{aligned}$$

n^j Indexes the auxiliary sources and m^j the collocation points on C_j , $E_{i/m}$ is the incident electric field evaluated on the collocation point, $E_{1/m}$ is the auxiliary sources one of C_1 and $E_{1/j}$ the electric field generated by the auxiliary sources of C_j . The first equation of (4) can be written as:

$$\sum_{n^1=1}^{N^1} A_{n^1} H_0^{(2)} [k_0 R_{m^1 n^1}] + \sum_{j=2}^K \sum_{n^j=1}^{N^j} A_{n^j} H_0^{(2)} [k_0 R_{m^1 n^j}] = -E_{i/m} = V_1^m$$

3. NUMERICAL RESULTS

Some examples have been chosen from literature to test the validity of the method. Fig. 2 shows the scattered field magnitude versus φ direction by a linear array of five conducting cylinders ($r = 0.1\lambda$) in near region $\rho = 3\lambda$ and $\rho = 5\lambda$ where λ is the free space wavelength. The distance between the centers of adjacent cylinders is 0.75λ . For the two distances, results obtained from global and partial coupling agree very well with the references one. During the implementation, we took into account the difference between the axes origins used in the reference and MAS model.

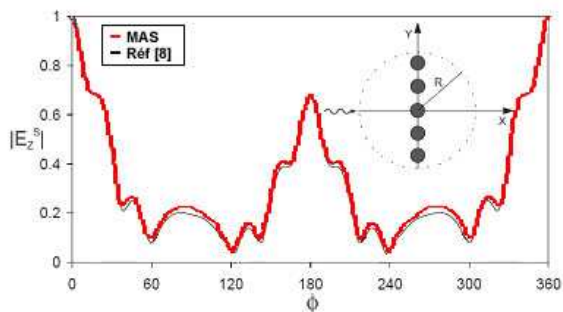


Figure 2: Scattering by five identical conducting cylinders excited in x -direction with $\rho = 3\lambda$.

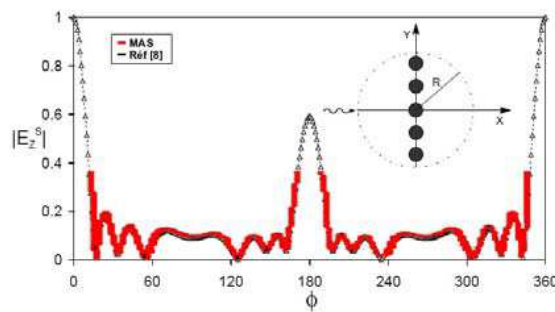


Figure 3: Scattering by five identical conducting cylinders excited in x -direction with $\rho = 5\lambda$.

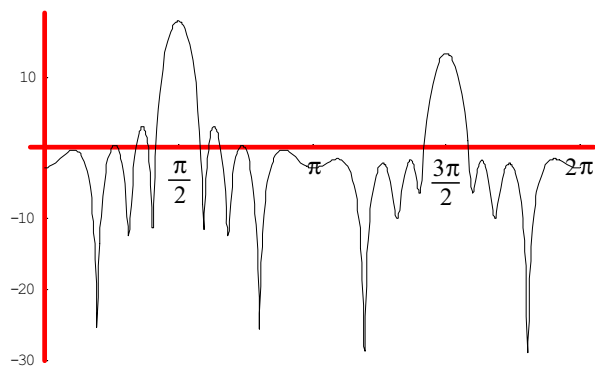


Figure 4: RCS for five cylinders obtained with the global coupling.

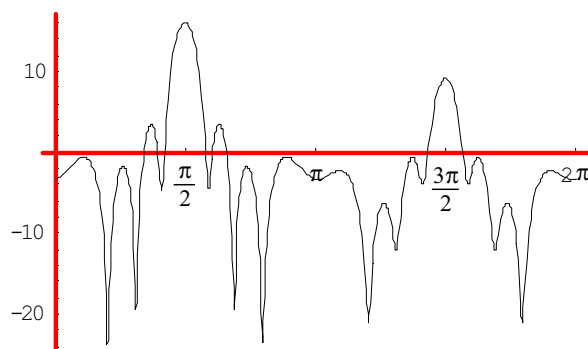


Figure 5: RCS for five cylinders obtained with the partial coupling.

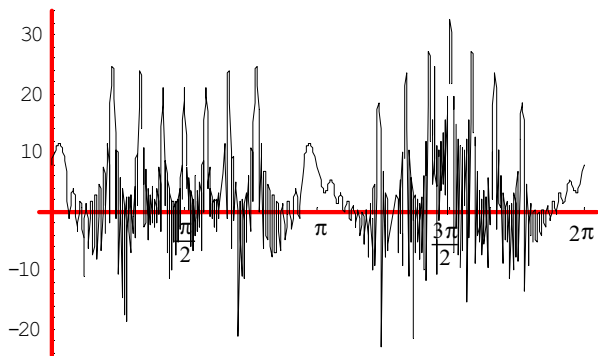


Figure 6: RCS for 10 cylinders according to global coupling.

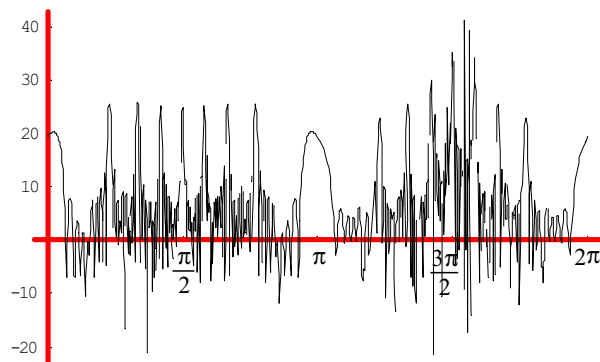


Figure 7: RCS for 10 cylinders according to partial coupling.

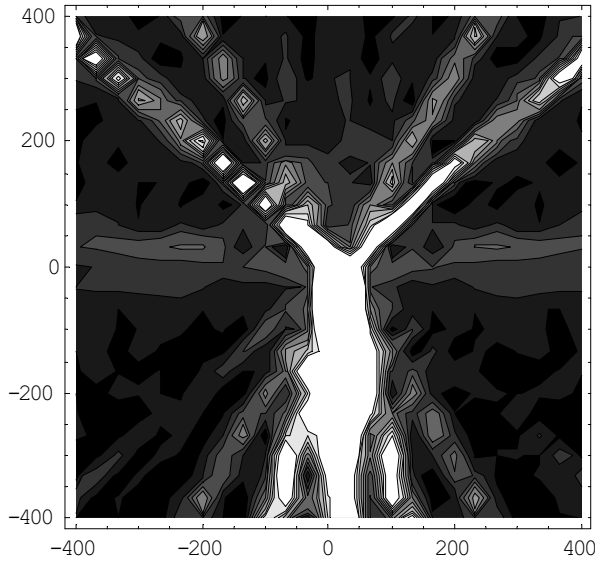


Figure 8: Far scattered field for 10 cylinders according to global coupling.

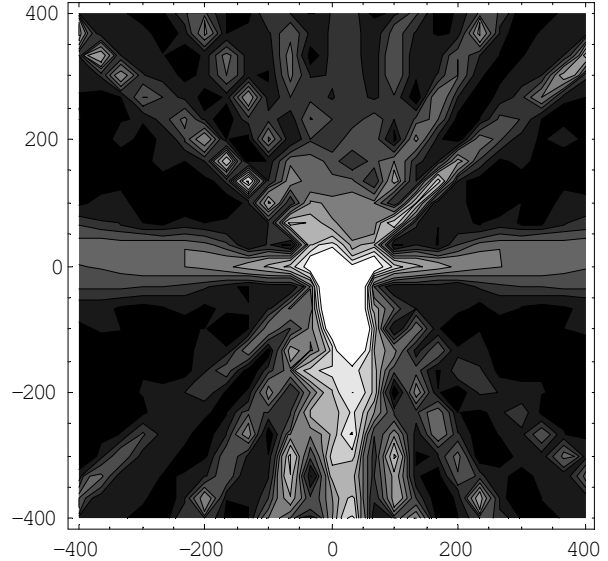


Figure 9: Far scattered field for 10 cylinders according to partial coupling.

4. CONCLUSIONS

The numerical results agree the model of the global and partial coupling for different linear arrays. The MAS is able to model coupling between infinite conducting cylinders and the approximation involved in this paper for the partial coupling agree with the references.

REFERENCES

1. Shubitidze, F., H. T. Anastassiou, and D. I. Kaklamani, "An improved accuracy version of the method of auxiliary sources for computational electromagnetics," *IEEE Transactions on Antennas and Propagation*, Vol. 52, No. 1, January 2004.
2. Anastassiou, H. T., et al., "Electromagnetic scattering analysis of coated conductors with edges using the method of auxiliary sources (MAS) in conjunction with the standard impedance boundary condition (SIBC)," *IEEE Transactions on Antennas and Propagation*, Vol. 50, No. 1, January 2002.
3. Kaklamani, D. I. and H. T. Anastassiou, "Aspects of the method of auxiliary sources (MAS) in computational electromagnetics," *IEEE Transactions on Antennas and Propagation*, Vol. 44, No. 3, June 2002.
4. Harrington, R. F., *Time Harmonic Electromagnetic Fields*, McGraw-Hill, New York, 1961.
5. Henin, B. H., A. Z. Elsherbeni, and M. Al Sharkawy, "Oblique incidence plane wave scattering from an array of dielectric cylinders," *Progress in Electromagnetic Research*, PIER 68, 261–279, 2007.
6. Elsherbeni, A. Z. and M. Hamid, "Scattering by parallel conducting circular cylinders," *IEEE Transactions on Antennas and Propagation*, Vol. AP-35, No. 3, March 1987.
7. Leviatan, Y., A. Boag, and A. Boag, "Analysis of electromagnetic scattering from dielectrically coated conducting cylinders using multifilament current model," *IEEE Transactions on Antennas and Propagation*, Vol. 36, No. 11, November 1988.
8. Polewski, M. and Mazur, "Scattering by an array of conducting, lossy dielectric, ferrite end pseudo-chiral cylinders," *Progress In Electromagnetics Research*, PIER 38, 283–310, 2002.

The Study of Electromagnetic Wave's Absorbing in Micro-periodical Structure

Yan Zhou

Baskin School of Engineering, University of California, Santa Cruz, USA

Abstract— The simulation of the micro-periodical structure's absorbing is present in this paper. Based on the research of structural absorb theory, PBG structure character and HIS controlling patch connection method, multilayer micro-periodical structure unit is set up numerically and connect to each other with the active controlling device-varactor. We establish the effective simulation method with software-HFSS for electromagnetic wave's absorbing in one layer, two layer and multilayer micro-periodical structure. The simulation result prove that multilayer micro-periodical structure could decrease the reflection of vertical incident wave more than 10 dB on same frequency band by the controlling of active device effectively. The relative frequency band will be extended in multilayer micro-periodical structure.

1. INTRODUCTION

Smart skin is one of research hot spots in present high technique field, especially in aircraft shell design, microwave protecting and electromagnetic wave reuse. Active periodical structure is one of methods to release smart skin.

Micro-periodical structure surface or layer could be made of metal-dielectric structure, Polymer Nanocomposites, fiber interweave or other materials. The microstructure of these material are periodical structure mostly. So the analysis of periodical structure is important.

PBG Photonic Band-Gap structures are one type of the typical periodic structures. It could form a type of structures that prevent the propagation of the electromagnetic waves in a specified band of frequency.

HIS (High-impedance surface) consists of an array of metal protrusions on a flat metal sheet. They are arranged in a two-dimensional lattice, and are usually formed as metal plates, connected to the continuous lower conductor by vertical posts. They can be visualized as mushrooms or thumbtacks protruding from the surface.

An example of a top view is shown in Fig. 1. The hexagonal metal patches are raised above the surface, and the dots in the center are vertical connecting posts. The thickness of this medium is $\lambda/4$, so the state of short at the bottom will bring the state of open at the top. The impedance at top of this metal-dielectric will be close to 377Ω .

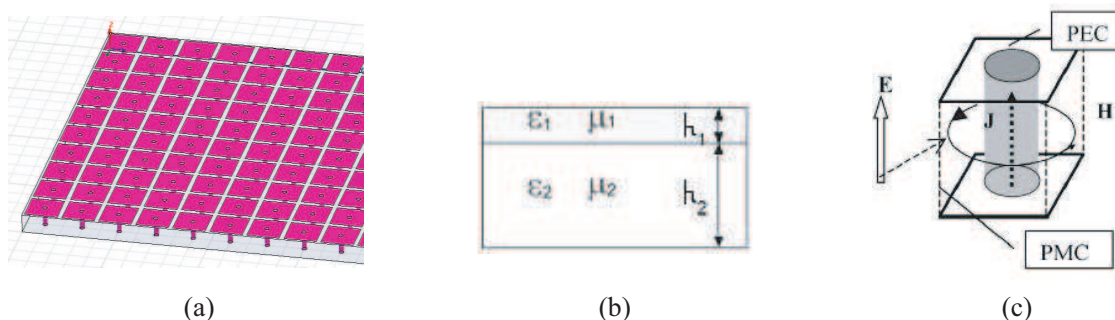


Figure 1: The layered sketch map of single layer periodical structure.

If We want realize the Perfectly Matched Layer Absorbing Boundary physically, We need set up multilayer periodical structure and realize electric parameter's controlling.

To realize the electronic control or to realize active periodical structure, we can Put the varactor diode on the top layer of High Impedance surface. Each metal unit cell in the periodic surface texture is connected to its four neighbors by reverse-biased diodes. By changing the voltage on the diodes, we adjust the capacitance between neighboring cells, and tune the resonance frequency, Such as Fig. 2. Actually, the thickness of dielectric substrate is thinner than $\lambda/4$ for the product

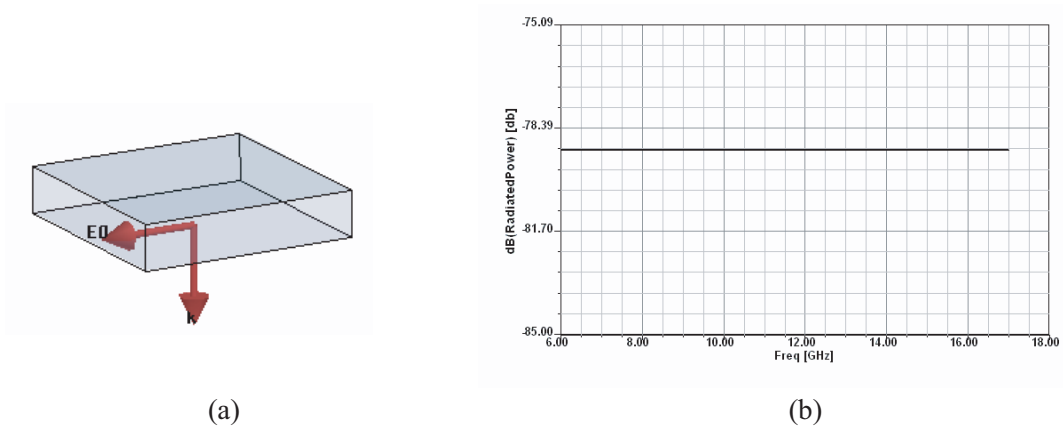


Figure 2: (a) Metal plane with vertical incident wave, (b) Single layer micro-periodical structure unit The radiation power of Metal plane with 5×5 mm (the radiation power is -79.0915 dB ~ -79.103 dB at 6–15 GHz)

condition of circuit process. So we need establish effect simulation model to calculate absorbing ratio for each case.

The Section 2 is discuss the theory of structure absorbing. The Section 3 and 4 is radiation power simulation of each case of periodical structure. And the final is conclusion of simulation and what is looked into the future.

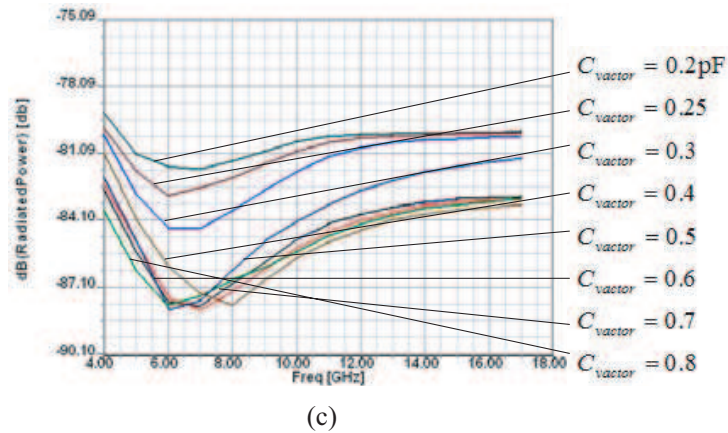
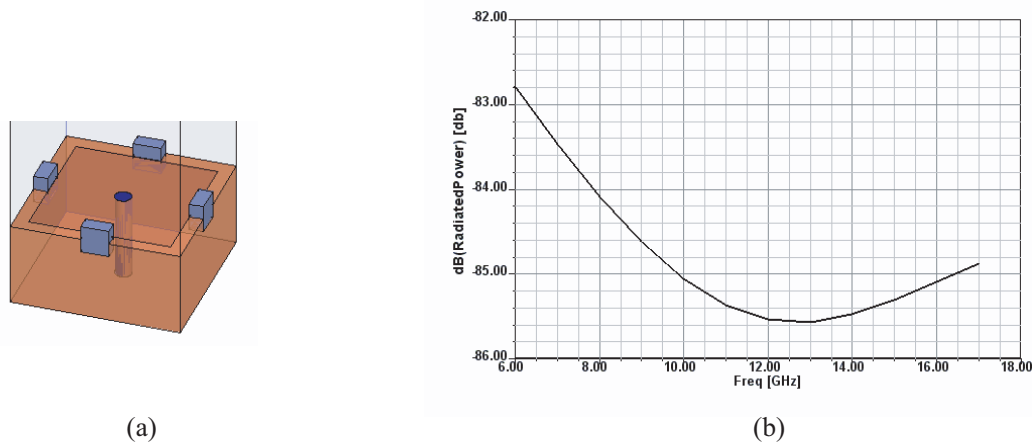


Figure 3: (a) The model founded on HFSS with module simulating the varactor, (b) The radiation power of single layer periodical structure with 5×5 mm periodical boundary condition model ($P_r = -83.5$ dB/7 GHz), (c) With different varactor diode capacitor value, the radiation power display very noticeable variation.

2. THEORY OF STRUCTURE ABSORBING

Periodical structure could be divided into two layers. The top periodical cell layer, or FSS layer, and via layer, yet be called substrate layer as Fig. 1. On the top of substrate layer, the plane could be regarded as perfect electronic condition(PEC), and the sides of substrate layer could be regarded as perfect magnetic condition(PMC).

For top FSS capacitive layer, the relative permeability is:

$$\varepsilon_{y1} = \frac{2a}{\pi h_1} \times \ln \left(\csc \frac{\pi g}{2a} \right) = \frac{1}{\mu_z} \quad (1)$$

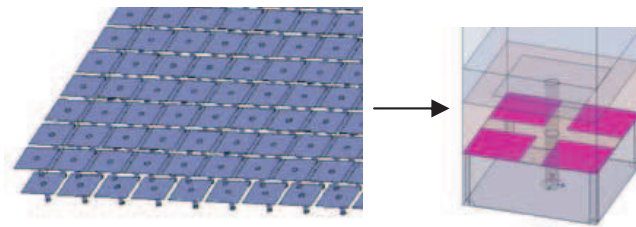
The substrate layer, via-array region, can be regarded as thin rods. To account for the possibility of thicker rods, the effective medium model is derived for the unit cell illustrated. For fields aligned with the vias, the medium can be regarded as highly inductive.

$$L = \frac{1}{2} \int \vec{B} \cdot \vec{H} dv \quad (2)$$

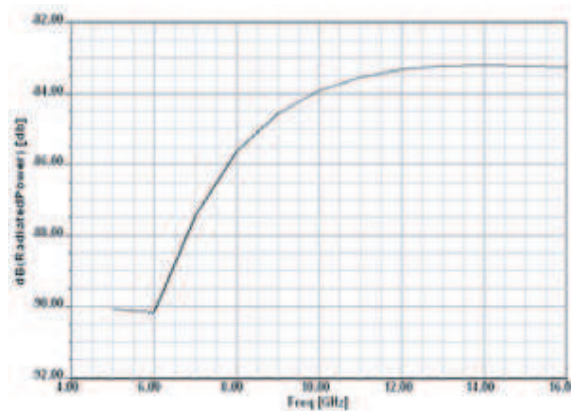
Here, we define the relative permittivity and permeability of the host dielectric that surrounds the vias as ε_D and μ_D . The effective permittivity of the unit cell is:

$$\varepsilon_{z2}(\omega) = \varepsilon_D - \frac{1}{\omega^2 \varepsilon_0 \frac{\mu_D \mu_0 A}{4\pi} \left[\ln \left(\frac{1}{\gamma} \right) + \gamma - 1 \right]} \quad (3)$$

This permittivity is characterized by a negative real part up to a “cutoff” frequency. Above the cutoff frequency it approaches the value of the surrounding medium. With the effective permittivity of layer is controlled artificially in theory, we can set up absorbing model for multi layer periodical structure and simulate its radiation power from its surface.



(a)



(b)

Figure 4: (a) The radiation power of two layer periodical structure with 5×5 mm periodical boundary condition model, (b) The radiation power simulation of two layer periodical structure ($P_r = -87$ dB/7 GHz, $P_r = -90.05$ dB/6 GHz).

3. SIMULATION OF SINGLE LAYER, TWO LAYER AND VARACTOR TUNING

We use Duroid 6010 as the substrate material for each layer, its $\epsilon_r = 10.2$, the cell period is 5 mm, metal patch on top of each layer, the central frequency is designed as 7 GHz. Under this set, we could calculate the radiation power from the surface of the single layer periodical structure, two layer periodical structure with computer, as Fig. 2 and Fig. 4. On the other hand, we could also simulation the variation of one layer periodical structure by tuning the varactor's value, as Fig. 3. All simulation is start with periodical boundary of HFSS and we simulation radiation power of unit cell to demonstrate the capability of absorbing.

4. SIMULATION OF MULTILAYER MICRO-PERIODICAL STRUCTURE'S ABSORBING

Multilayer micro-periodical structure unit has been established. Varactors been put on the 4 layer to connect the each patch of unit. From upper layer to bottom layer, we use rectangular patch, interlace patch, circle patch and interlace circle and square patch. Every layer have special band width and absorbing peak and different response character with varactor's variety.

For the reason of huge time for complex multilayer structure. The tuning of the capacitance's value for 5-layer mirco-periodical structure been replaced by unique varactor value in simulating. We use the varactor value 20 pF.

From the result, it is clear that active periodical structures have absorbed wave markedly. For single layer active periodical structure has reduced radiation power with a largest scope of $83.5 - 79.1 = 4.4$ dB; two layers active periodical structure has reduced radiation power with a largest scope of $87 - 79.1 = 7.9$ dB. With the radiation power reducing, the working frequency band has tuned, such as Fig. 8. This is simulation result with no measure at present environment because of the limit of multi-layers product process.

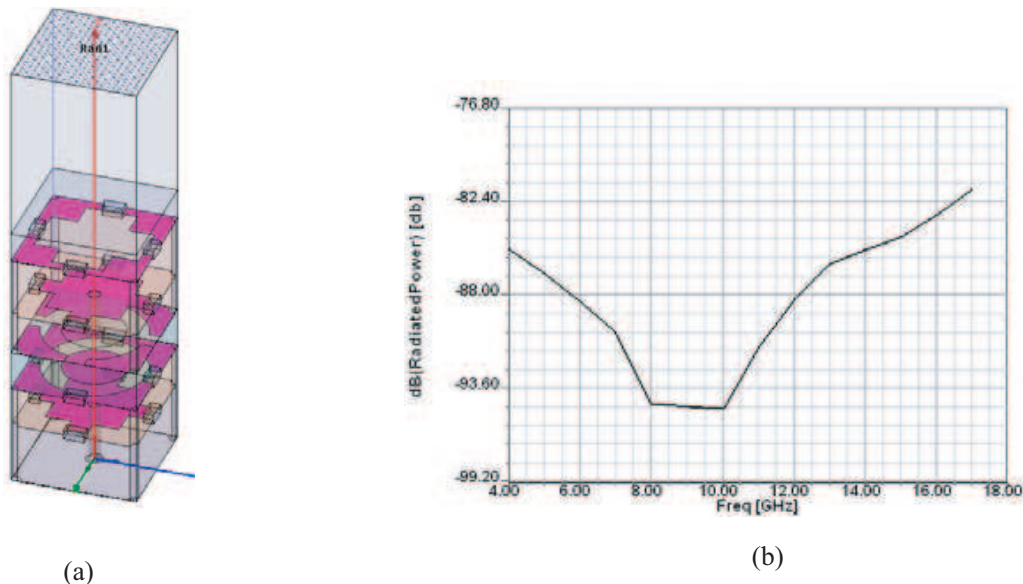


Figure 5: (a) 5 layer micro-periodical structure unit model on HFSS, (b) The radiation power simulation of 5 layer periodical structure with 5×5 mm periodical boundary condition model ($P_r = -94.9 \sim -95.2$ dB/7.9 ~ 10.1 GHz).

5. CONCLUSIONS

Active multilayer micro-periodical structure could be established in many body's surface like air flight vehicle, automobile vehicle or the microwave protective clothing. Diode is active device to control the effective relative permittivity and permeability of micro periodical unit. The simulation test have prove that two layer micro periodical structure could change dielectric layer and whole surface system and reduce disperse incident wave from surface inserting wave about $5 \sim 10$ dB. And the multilayer structure such as 5 layer structure could extend the absorbing frequency band in a relative wide range. If the micro-periodical structure be used in smart skin or human body's

artificial synthesis protective equipment, effective novel electromagnetic wave radiation absorbing, protecting and re-used system could be set up.

REFERENCES

1. Ghodgaonkar, D. K., V. V. Varadan, and V. K. Varadan, "Free-space measurement of complex permittivity and complex permeability of magnetic materials at microwave frequencies," *IEEE Transactions on Instrumentation and Measurement*, Vol. 39, No. 2, 387–394, 1990.
2. Kotsilkova, R., "Design and characterisaion of polymer nanocomposites for microwave absorbing applications," 0-7803-8499-7/04/\$20.00:93~96.
3. Zhang, B., Y. Feng, and J. Xiong, "Microwave-absorbing properties of de-aggregated flake-shaped carbonyl-iron particle composites at 2–18 GHz," *IEEE Transactions on Magnetics*, Vol. 42, No. 7, 1778–1781, July 2006.
4. Su, D. and Y. Zhou, "The study of active periodical structure's absorbing the incident wave," *Journal of Beijing University of Aeronautics and Astronautics*, Vol. 33, No. 2, 164–168, 2007.
5. King, R. J., D. V. Thiel, and K. S. Park, "The synthesis of surface reactances using an artificial dielectric," *IEEE ddf Trans. Antennas Propagat*, Vol. 31, No. 3, 471–476, 1983.
6. Berenger, J.-P., "On the reflection from Cummer's nearly perfectly matched layer," *IEEE Microwave and Wireless Components Letters*, Vol. 14, No. 7, 334–337, 2004.
7. Feng, Y.-B., T. Qiu, and C.-Y. Shen, "Electromagnetic and absorption properties of carbonyl iron/rubber radar absorbing materials," *IEEE Transactions on Magnetics*, Vol. 42, No. 3, 363–368, 2006.
8. Saib, A., L. Bednarz, and R. Daussin, "Carbon nanotube composites for broadband microwave absorbing materials," *IEEE Transactions on Microwave Theory and Techniques*, Vol. 54, No. 6, 1176–1179, 2006.
9. Zhang, B., Y. Feng, and J. Xiong, "Microwave-absorbing properties of de-aggregated flake-shaped carbony-iron particle composites at 2–18 GHz," *IEEE Transactions on Magnetics*, Vol. 42, No. 7, 1778–1781, 2006.
10. Kern, D. J., D. Werner, and A. Monorchio, "The design synthesis of multiband artificial magnetic conductors using high impedance frequency selective surfaces," *IEEE Transactions on Antennas and Propagation*, Vol. 53, No. 1, 8–17, 2005.
11. Clavijo, S., R. E. Diaz, and W. E. McKinzie, "Design methodology for sievenpiper high-impedance surfaces: An artificial magnetic conductor for positive gain electrically small antennas," *IEEE Transactions on Antennas and Propagation*, Vol. 51, No. 10, 2678–2690, 2003.
12. Parchomchuk, P., W. W. Wallender, and R. J. King, "Direct solution for dielectric properties of a lossy two-layered material," *IEEE Transactions on Geoscience and Remote Sensing*, Vol. 27, No. 3, 310–315, 1989.

Scattering by Lossless Double-negative Metamaterial Slabs

G. Gennarelli and G. Riccio

DIIE-University of Salerno

Via Ponte Don Melillo, Fisciano, Salerno 84084, Italy

Abstract— An approach is here proposed for evaluating the scattering by a lossless and isotropic double-negative metamaterial slab illuminated by a plane wave at oblique incidence. The total field at a given point is evaluated by adding the Geometrical Optics contributions and the field diffracted by the edge. This last contribution is determined by using a Uniform Asymptotic Physical Optics solution expressed in terms of the standard transition function of the Uniform Theory of Diffraction. As demonstrated by many numerical simulations, it has resulted to be efficient and simple to implement in a computer code.

1. INTRODUCTION

In the recent years, metamaterial structures have attracted considerable attention because of their interesting properties and potential applications [1].

An approximate method is proposed in this paper for predicting the scattering by a lossless and isotropic double-negative (DNG) metamaterial slab illuminated by a plane wave at skew incidence with respect to the edge (see Figure 1). The derivation of the exact solution for the diffracted field is very difficult for the considered problem and, at best knowledge of the authors, no solutions are available in literature. As a consequence, an approximate “practical” solution, which is efficient, simple to handle and to implement in a computer code becomes very appealing from the engineering point of view.

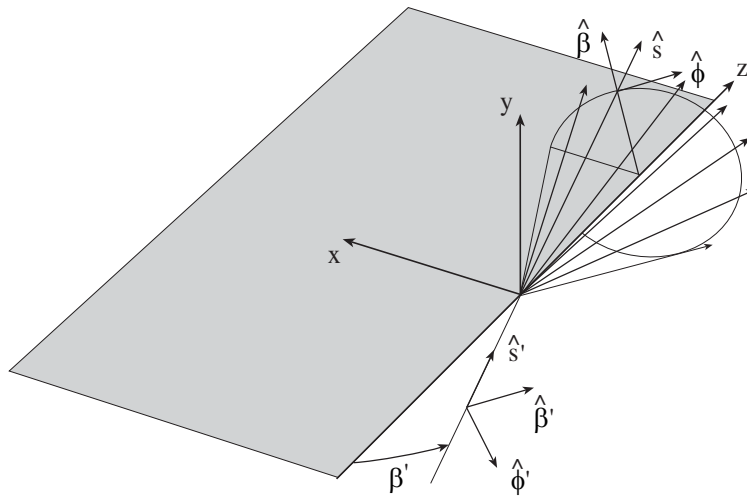


Figure 1: Diffraction from a lossless DNG slab.

The analytical difficulties are attenuated by modelling the structure as an infinitesimally thin sheet, and the effects of geometric, electric and magnetic characteristics are taken into account through proper boundary conditions. In order to evaluate the field diffracted by the edge, electric and magnetic Physical Optics (PO) surface currents are here assumed as equivalent sources originated by the discontinuities of the tangential components of the magnetic and electric fields across the slab, and inserted in the radiation integral. As a result, they can be easily expressed in terms of the Geometrical Optics (GO) response of the structure. The reflection and transmission coefficients of the DNG metamaterial slab are obtained by following an approach similar to that reported in [2]. A useful approximation and a uniform asymptotic evaluation of the resulting radiation integral allow one to obtain the three-dimensional diffraction coefficients, which are expressed in terms of the standard transition function of the Uniform Theory of Diffraction (UTD) [3]. The here proposed solution belongs to the set of the Uniform Asymptotic PO (UAPO) solutions developed in recent years to solve many diffraction problems (see [4] as reference for the approach).

2. GO FIELD PREDICTION MODEL

An arbitrarily polarized plane wave impinging on a lossless DNG metamaterial layer surrounded by free space (see Figure 1) is considered. The layer thickness is d and its electric permittivity and magnetic permeability are $\varepsilon = -|C|\varepsilon_0$ and $\mu = -\mu_0$, respectively.

With reference to the reflection and transmission coefficients, it is convenient to operate in the ordinary plane of incidence, defined as that containing the incident ray and the normal to the surface, and to consider the local ray-fixed reference system shown in Figure 2.

According to [2], the reflection and transmission coefficients of the DNG slab for the parallel and perpendicular polarizations can be expressed as:

$$R_{\parallel, \perp} = \frac{\bar{R}_{12\parallel, \perp} + \bar{R}_{23\parallel, \perp} e^{j2\gamma}}{1 + (\bar{R}_{12\parallel, \perp}) (\bar{R}_{23\parallel, \perp}) e^{j2\gamma}} \quad T_{\parallel, \perp} = \frac{\bar{T}_{12\parallel, \perp} \bar{T}_{23\parallel, \perp} e^{j\gamma}}{1 + (\bar{R}_{12\parallel, \perp}) (\bar{R}_{23\parallel, \perp}) e^{j2\gamma}} \quad (1)$$

wherein $\gamma = k_s d \cos(\vartheta^t)$, being k_s the wave-number in the DNG slab and ϑ^t the negative angle between the refracted ray and the normal direction (see Figure 3). With reference to the parallel polarization it results,

$$\bar{R}_{ij, \parallel} = \frac{k_j \cos(\vartheta^i) - k_i \cos(\vartheta^j)}{k_j \cos(\vartheta^i) + k_i \cos(\vartheta^j)} \quad \bar{T}_{ij, \parallel} = \frac{2k_i \cos(\vartheta^i)}{k_j \cos(\vartheta^i) + k_i \cos(\vartheta^j)} \quad (2)$$

and for what concerns the perpendicular polarization,

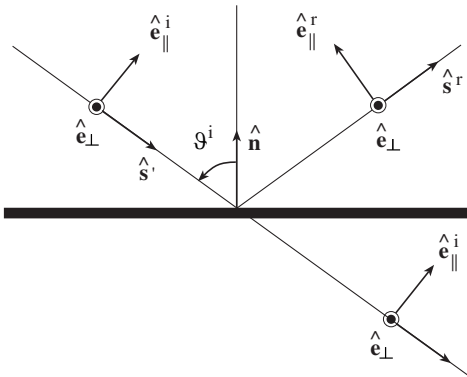


Figure 2: Ray-fixed coordinate system in the incidence plane.

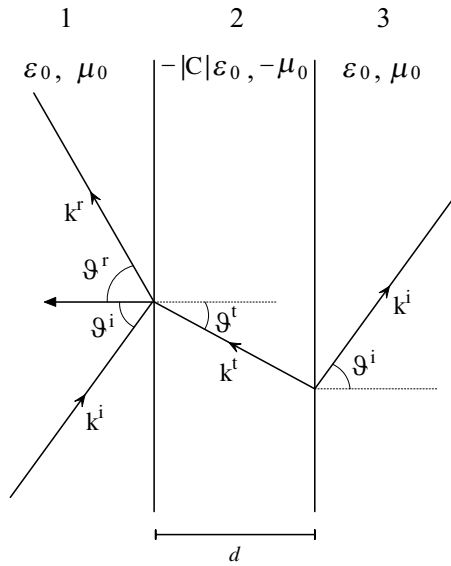


Figure 3: Transmission through the slab.

$$\bar{R}_{ij, \perp} = \frac{k_i \cos(\vartheta^i) - k_j \cos(\vartheta^j)}{k_i \cos(\vartheta^i) + k_j \cos(\vartheta^j)} \quad \bar{T}_{ij, \perp} = \frac{2k_i \cos(\vartheta^i)}{k_i \cos(\vartheta^i) + k_j \cos(\vartheta^j)} \quad (3)$$

being and k_i and k_j the wave numbers of media i and j , respectively, as shown in Figure 3.

3. DIFFRACTED FIELD: UAPO SOLUTION

The incidence direction is fixed by the angles β' , ϕ' . In particular, β' is a measure of the incidence direction skewness with respect to the edge. The observation direction is specified by the angles β , ϕ .

A PO approximation is adopted for the equivalent electric (\mathbf{J}_s^{PO}) and magnetic (\mathbf{J}_{ms}^{PO}) surface currents induced by the incident field. In the far-field approximation, the field generated by these currents can be expressed by means of the well-known radiation integral:

$$\mathbf{E}^s \cong -jk_0 \iint_S \left[(\underline{\underline{\mathbf{I}}} - \hat{\mathbf{R}}\hat{\mathbf{R}}) (\zeta_0 \mathbf{J}_s^{PO}) + \mathbf{J}_{ms}^{PO} \times \hat{\mathbf{R}} \right] G(\mathbf{r}, \mathbf{r}') dS \quad (4)$$

wherein $G(\mathbf{r}, \mathbf{r}') = e^{-jk_0|\mathbf{r}-\mathbf{r}'|}/(4\pi|\mathbf{r}-\mathbf{r}'|)$, k_0 is the free space wave-number, \mathbf{r} and \mathbf{r}' denote the observation and source points, respectively, $\hat{\mathbf{R}}$ is the unit vector from the radiating element at \mathbf{r}' to the observation point, and $\underline{\mathbf{I}}$ is the 3×3 identity matrix. In (4), the equivalent electric and magnetic PO surface currents can be determined by means of the relations:

$$\begin{aligned} \zeta_0 \mathbf{J}_s^{PO} &= \zeta_0 \tilde{\mathbf{J}}_s^{PO} e^{jk_0(\rho' \sin \beta' \cos \phi' - \zeta' \cos \beta')} \\ &= \left\{ [1 - R_\perp - T_\perp] E_\perp^i \cos \vartheta^i \hat{\mathbf{e}}_\perp + [1 + R_\parallel - T_\parallel] E_\parallel^i \hat{\mathbf{t}} \right\} e^{jk_0(\rho' \sin \beta' \cos \phi' - \zeta' \cos \beta')} \end{aligned} \quad (5)$$

$$\begin{aligned} \mathbf{J}_{ms}^{PO} &= \tilde{\mathbf{J}}_{ms}^{PO} e^{jk_0(\rho' \sin \beta' \cos \phi' - \zeta' \cos \beta')} \\ &= \left\{ [1 - R_\parallel - T_\parallel] E_\parallel^i \cos \vartheta^i \hat{\mathbf{e}}_\perp - [1 + R_\perp - T_\perp] E_\perp^i \hat{\mathbf{t}} \right\} e^{jk_0(\rho' \sin \beta' \cos \phi' - \zeta' \cos \beta')} \end{aligned} \quad (6)$$

where (ρ', ζ') are the coordinates of the integration point on the surface and $\hat{\mathbf{t}} = \hat{\mathbf{n}} \times \hat{\mathbf{e}}_\perp$. In the high-frequency approximation, the PO integral can be reduced asymptotically to a sum of ray field contributions from (isolated) interior stationary phase points on S and an edge diffracted field contribution.

Since the diffraction is confined to the Keller's cone for which $\beta = \beta'$, the approximation $\hat{\mathbf{R}} = \hat{\mathbf{s}}$ ($\hat{\mathbf{s}}$ is the unit vector of the diffraction direction) for evaluating the edge diffracted field is permitted [5]. According to [4],

$$\mathbf{E}^s \cong -jk_0 \left[(\underline{\mathbf{I}} - \hat{\mathbf{s}}\hat{\mathbf{s}}) \left(\zeta_0 \tilde{\mathbf{J}}_s^{PO} \right) + \tilde{\mathbf{J}}_{ms}^{PO} \times \hat{\mathbf{s}} \right] I_0 \quad (7)$$

wherein

$$I_0 = \int_0^{+\infty} \int_{-\infty}^{+\infty} e^{jk_0(\rho' \sin \beta' \cos \phi' - \zeta' \cos \beta')} G(\mathbf{r}, \mathbf{r}') d\zeta' d\rho' = \frac{e^{-jk_0 z \cos \beta'}}{2(2\pi j) \sin \beta'} \int_C \frac{e^{-jk_0 \rho \sin \beta' \cos(\alpha \mp \phi)}}{\cos \alpha + \cos \phi'} d\alpha \quad (8)$$

in which C is an appropriate integration path in the complex α -plane and $- (+)$ sign applies if $0 < \phi < \pi$ ($\pi < \phi < 2\pi$).

By applying the Cauchy's theorem, the contribution to the field related to the integration along C (distorted for the presence of singularities in the integrand) is equivalent to the summation of the integral along the Steepest Descent Path (SDP), passing through the pertinent saddle-point, and the residue contributions associated with all those poles that are inside the closed path C +SDP. A uniform asymptotic evaluation of the integral along the SDP provides the edge diffraction contribution in terms of the UTD transition function $F_t(\cdot)$. Accordingly, the UAPO edge diffracted field \mathbf{E}^d can be so expressed in the diffracted ray-fixed coordinate system:

$$\mathbf{E}^d = \begin{bmatrix} E_\beta^d \\ E_\phi^d \end{bmatrix} = \underline{\underline{\mathbf{D}}} \begin{bmatrix} E_{\beta'}^i \\ E_{\phi'}^i \end{bmatrix} \frac{e^{-jk_0 s}}{\sqrt{s}} = \frac{-e^{-j\pi/4}}{2\sqrt{2\pi k_0} \sin^2 \beta'} \frac{F_t(2k_0 s \sin^2 \beta' \cos^2(\phi \pm \phi')/2)}{\cos \phi + \cos \phi'} \underline{\underline{\mathbf{M}}} \begin{bmatrix} E_{\beta'}^i \\ E_{\phi'}^i \end{bmatrix} \frac{e^{-jk_0 s}}{\sqrt{s}} \quad (9)$$

The matrix $\underline{\underline{\mathbf{M}}}$ is given by:

$$\underline{\underline{\mathbf{M}}} = \underline{\underline{\mathbf{M}}}_1 \left[\underline{\underline{\mathbf{M}}}_2 \underline{\underline{\mathbf{M}}}_4 \underline{\underline{\mathbf{M}}}_5 + \underline{\underline{\mathbf{M}}}_3 \underline{\underline{\mathbf{M}}}_4 \underline{\underline{\mathbf{M}}}_6 \right] \underline{\underline{\mathbf{M}}}_7 \quad (10)$$

where $\underline{\underline{\mathbf{M}}}_1$ is the transformation matrix for the edge to ray-fixed coordinate system components, $\underline{\underline{\mathbf{M}}}_4$ is the transformation matrix relating the base $\hat{\mathbf{e}}_\perp$, $\hat{\mathbf{t}}$ to $\hat{\mathbf{x}}$, $\hat{\mathbf{z}}$, and $\underline{\underline{\mathbf{M}}}_7$ relates the base $\hat{\beta}'$, $\hat{\phi}'$ to $\hat{\mathbf{e}}_\parallel^i$, $\hat{\mathbf{e}}_\perp$ in the plane normal to the incidence direction. Moreover,

$$\underline{\underline{\mathbf{M}}}_2 = \begin{bmatrix} 1 - \sin^2 \beta' \cos^2 \phi & -\cos \beta' \sin \beta' \cos \phi \\ -\sin^2 \beta' \sin \phi \cos \phi & -\cos \beta' \sin \beta' \sin \phi \\ -\cos \beta' \sin \beta' \cos \phi & \sin^2 \beta' \end{bmatrix} \quad \underline{\underline{\mathbf{M}}}_3 = \begin{bmatrix} 0 & -\sin \beta' \sin \phi \\ -\cos \beta' & \sin \beta' \cos \phi \\ \sin \beta' \sin \phi & 0 \end{bmatrix} \quad (11)$$

$$\underline{\underline{\mathbf{M}}}_5 = \begin{bmatrix} 0 & [1 - R_\perp - T_\perp] \cos \vartheta^i \\ [1 + R_\parallel - T_\parallel] & 0 \end{bmatrix} \quad \underline{\underline{\mathbf{M}}}_6 = \begin{bmatrix} [1 - R_\parallel - T_\parallel] \cos \vartheta^i & 0 \\ 0 & -[1 + R_\perp - T_\perp] \end{bmatrix} \quad (12)$$

Note that the matrices $\underline{\underline{\mathbf{M}}}_5$ and $\underline{\underline{\mathbf{M}}}_6$ originate from the expressions of the equivalent PO currents.

4. NUMERICAL RESULTS

The effectiveness of the proposed solution has been verified by some numerical tests. A linearly polarized plane wave propagating in the direction $\beta' = 60^\circ$, $\phi' = 45^\circ$ is considered. The incident electric field is assumed to have only the β' — component and unit amplitude ($E_{\beta'}^i = 1$, $E_{\phi'}^i = 0$). The slab is characterized by $\varepsilon = -\varepsilon_0$, $\mu = -\mu_0$ and $d = 0.125\lambda_0$, being λ_0 the free space wavelength. The field is evaluated over a circular path with radius $\rho = 5\lambda_0$. The amplitude of the electric field β , ϕ — components related to the GO response and the UAPO diffracted field contribution are reported in Figures 4 and 5. It can be easily observed that the GO field has two discontinuities in correspondence of the reflection and incident shadow boundaries at $\phi = 135^\circ$ and $\phi = 225^\circ$. On the other hand, the UAPO diffracted field is not negligible in the neighbourhood of such boundaries and this guarantees the continuity of the total field for both polarizations (see Figures 6 and 7).

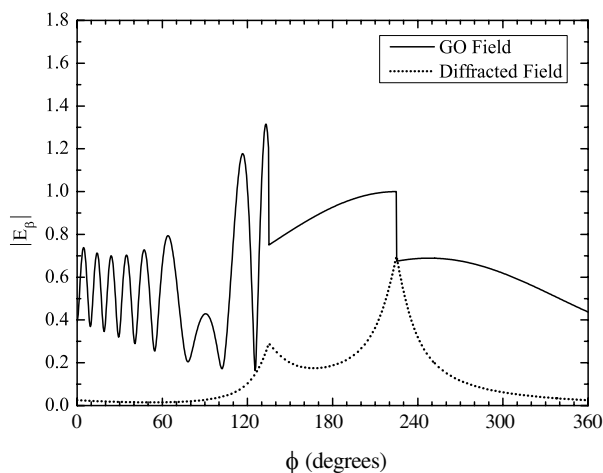


Figure 4: Amplitude of the β — component related to the GO and UAPO diffracted field.

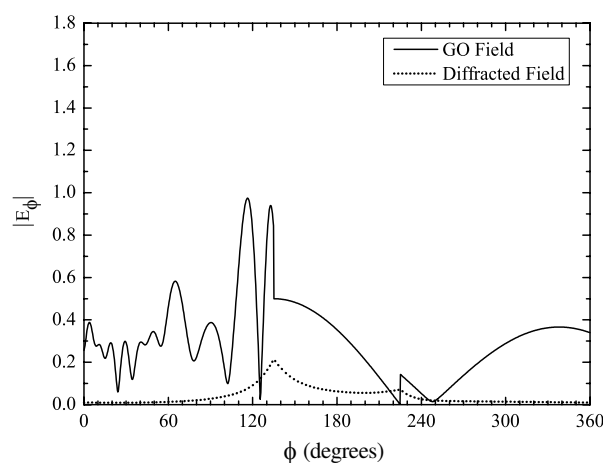


Figure 5: Amplitude of the ϕ — component related to the GO and UAPO diffracted field.

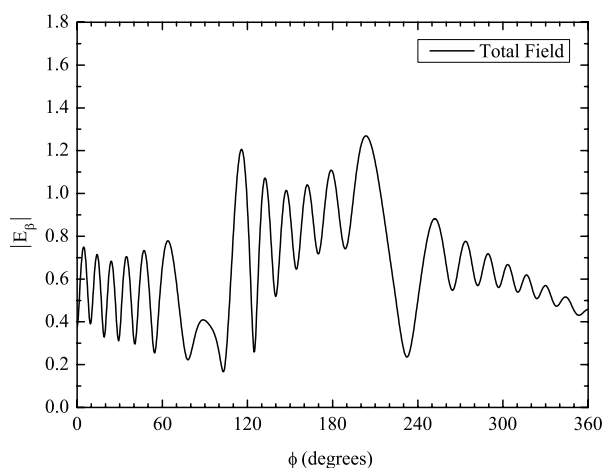


Figure 6: Amplitude of the β — component related to the total field.

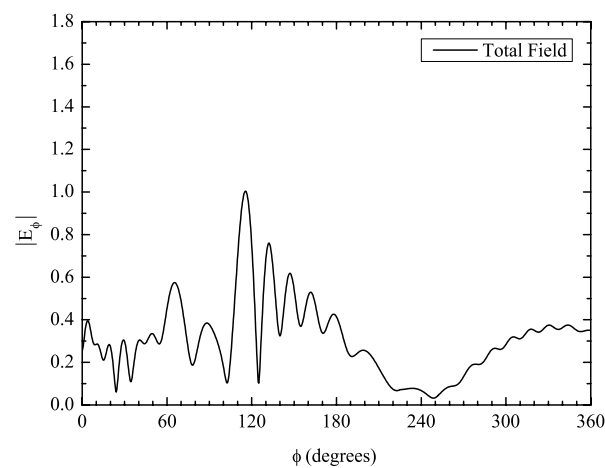


Figure 7: Amplitude of the ϕ — component related to the total field.

5. CONCLUSIONS

A UAPO based solution has been here proposed for evaluating the field scattered by a lossless DNG metamaterial slab illuminated by a plane wave at oblique incidence. As a first step, the GO response of the structure has been obtained. This last has been subsequently used to determine the equivalent electric and magnetic PO currents in the radiation integral. A useful approximation and a uniform asymptotic evaluation of the resulting integral has allowed to obtain the UAPO three-dimensional diffraction coefficients. They are expressed in terms of the standard UTD transition

function. It must be stressed that the here proposed solution perfectly compensates the GO field discontinuities at the reflection and incidence shadow boundaries, it is efficient, easy to handle and simple to implement in a computer code. Moreover, it can be surely useful in all the application wherein the truncation effects in DNG metamaterials cannot be neglected.

REFERENCES

1. Engheta, N. and R. W. Ziolkowski, "A positive future for double-negative metamaterials," *IEEE Trans. Microw. Theory Tech.*, Vol. 53, No. 4, 1535–1556, 2005.
2. Cory, H. and C. Zach, "Wave propagation in metamaterial multi-layered structures," *Microwave Opt. Technol. Lett.*, Vol. 40, No. 6, 460–465, 2004.
3. Kouyoumjian, R. G. and P. H. Pathak, "A uniform geometrical theory of diffraction for an edge in a perfectly conducting surface," *Proc. IEEE*, Vol. 62, No. 11, 1448–1461, 1974.
4. Gennarelli, C., G. Pelosi, C. Pochini, and G. Riccio, "Uniform asymptotic PO diffraction coefficients for an anisotropic impedance half-plane," *Journal of Electromagnetic Waves and Applications*, Vol. 13, No. 7, 963–980, 1999.
5. Senior, T. B. A. and J. L. Volakis, *Approximate Boundary Conditions in Electromagnetic*, IEE *Electromagnetic Waves Series*, London, 1995.

Rectangular Junction Ferrite Component in Millimeter Waves

D. Vincent

Saint-Etienne University, France

Abstract— The design of non reciprocal components still remains an important challenge for integrating new functions in microwave devices. Such passive components usually use magnetic materials like ferrites. For high frequency bands barium ferrite could be used without external magnets when the magnetic moments (a cristal axis) are directed moments. Barium ferrite thin films or composite material should be suitable materials for integrating non reciprocal microwave passive components. In this way a stripline structure as a rectangular ferrite junction is proposed. Two ferrite slabs are located between an inner conductor and two ground plane. Non reciprocal effects are observed and this rectangular junction ferrite component could be used as a circulator. 3D simulations results confirm this first approach.

1. INTRODUCTION

Non reciprocal microwave components in millimeter waves, such as circulators, are based on the gyro-resonance properties of a ferrite material. The integrating of self-biased ferrite devices seems to be possible using thin-film processes [1, 2] or composite materials which can be made from magnetic nano-particles scattered into a host dielectric matrix. To reach upper frequency bands, magnetic materials like barium ferrite, having a high magnetocrystalline anisotropy, can be used for self-biased devices when the magnetic moments (crystal axis) are directed without D.C. field being applied. For lower frequency applications, other ferrites or garnets like YIG, can be used with external magnets which unfortunately does not permit electronic integration.

So, to make high frequency ferrite devices suitable for integration, the use of thin-films with directed magnetic moments seems to be a good approach. The small thickness of these films emphasizes the theoretical approximations made by H. Bosma [3] in order to derive Green's function of a Y-junction circulator.

The circular stripline structure of circulators requires bent access lines for connecting, which could disturb the TEM propagation and cause losses in higher frequency bands. Other circulator shapes and structures have been investigated. Microstrip and coplanar structures with several shapes (triangular, hexagonal.), were proposed [4, 5]. However, for structures different from the stripline structure, Green's function method is not easy to be used. The boundary conditions must be correctly defined to obtain an analytical solution for rapid computing of scattering parameters (S parameters). So, in general, a 3D electromagnetic software is used but the simulation requires more computing time.

In this paper a simple structure, is studied as a “rectangular circulator” made from a stripline structure which allows us to derive Green's function and to use it for the S parameter computing. However, a 3D software (HFSS) is also used because the analytical model still remains too simple to take into account non perfect boundary conditions.

2. THEORETICAL STUDY

The structure of the studied component is shown on Figure 1. The non-reciprocal effect is due to the field displacement when a D.C. magnetic field is applied (which corresponds to an internal field) to the ferrite slabs along the z -axis direction. An analytical model can be developed with the same approximations as the ones used by Bosma [3] for circular Y-junction circulator. Only the z -axis electric field component, the y -axis and x -axis magnetic field components are considered. A magnetic wall is referred to the ferrite edge. Green's function method is used with inhomogeneous boundary conditions (the boundary conditions on E_z and h^* are different on the access lines) to avoid the same location as the source and as the observation points.

The expression that allows to solve our problem and to find the electric field E_z everywhere inside the ferrite thin film is (with τ the ferrite slab volume being bordered by the σ surface) is :

$$E_z(x', y') = \int_{\tau} s(x, y) h^*(x, x', y, y') d\tau + \oint_{\sigma} (h^* \overline{\nabla E_z} - E_z \overline{\nabla h^*}) \cdot \overline{d\sigma} \quad (1)$$

$h^*(x, x', y, y')$ is the adjunct Green's function [6] defined by:

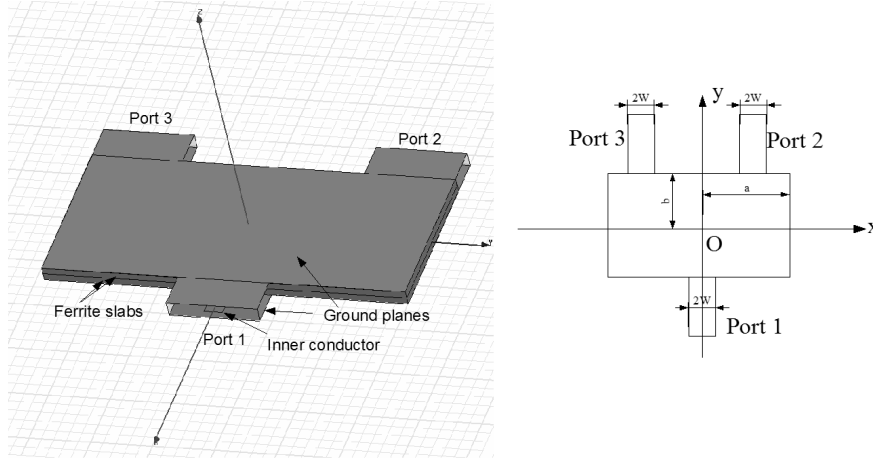


Figure 1: Rectangular structure on study.

$$h^*(x, x', y, y') = g(x', x, y', y) \quad (2)$$

The volume integral (1) is applied to the ferrite slab volume with a possible source $s(x; y)$. However, using inhomogeneous boundary conditions, the final solution of the E_z field is obtained without an internal source and the relation (1) becomes as follows:

$$E_z(x', y') = \oint_{\sigma} (h^* \nabla E_z - E_z \nabla h^*) \cdot d\sigma \quad (3)$$

The initial equation to find Green's function in cartesian coordinates is given by:

$$\left(\frac{\partial^2}{\partial x^2} + \frac{\partial^2}{\partial y^2} + k^2 \right) g = \delta(x - x') \delta(y - y') \quad (4)$$

where $k = \omega \sqrt{\mu_0 \varepsilon_0 \varepsilon_{rf} \mu_{eff}}$ and $\mu_{eff} = \frac{\mu^2 - \kappa^2}{\mu}$ (μ and κ are constitutive parameters of the ferrite permeability tensor).

The derivation of Green's function (when a magnetic wall is fixed as a boundary condition along the ferrite slab) [6] leads to:

$$g(x, y, x', y') = \sum_n \frac{e^{j\alpha_n(x-x')}}{2a} \cdot \begin{cases} \frac{\left(\beta_n \cos(\beta_n(y' - b)) - \alpha_n \frac{\kappa}{\mu} \sin(\beta_n(y' - b)) \right)}{\beta_n \cdot \sin(2\beta_n b)} \\ \frac{\left(\beta_n \cos(\beta_n(y + b)) - \alpha_n \frac{\kappa}{\mu} \sin(\beta_n(y + b)) \right)}{\left(\beta_n^2 + \alpha_n^2 \frac{\kappa^2}{\mu^2} \right)} \Big|_{y < y'} \\ \frac{\left(\beta_n \cos(\beta_n(y' + b)) - \alpha_n \frac{\kappa}{\mu} \sin(\beta_n(y' + b)) \right)}{\beta_n \cdot \sin(2\beta_n b)} \\ \frac{\left(\beta_n \cos(\beta_n(y - b)) - \alpha_n \frac{\kappa}{\mu} \sin(\beta_n(y - b)) \right)}{\left(\beta_n^2 + \alpha_n^2 \frac{\kappa^2}{\mu^2} \right)} \Big|_{y > y'} \end{cases} \quad (5)$$

where $\alpha_n = \frac{n\pi}{a}$ and $\beta_n^2 = k^2 - \alpha_n^2$.

From the integral relation (3) the E_z field can be found on the access lines and the scattering parameters can be determined [7]. Figure 2 shows some results from this analytical model which was slightly modified to take into account non perfect magnetic wall at the ferrite slab edge. Non reciprocal effects are observed since S_{21} and S_{31} are different from 40 to 45 GHz. These results are

in agreement with 3D HFSS simulations which show a large effect in a wide frequency band (see the following paragraph) although some discrepancies are observed. However the model allows us to determine the length of the rectangle giving priority of the first mode:

$$a = \Re \left\{ \frac{\pi}{k} \sqrt{\frac{\mu_{eff}}{\mu}} \right\} \quad (6)$$

Then, the width of the rectangle b is determined by empirical means.

3. 3D SIMULATIONS

Now, the same structure is simulated by the HFSS 3D electromagnetic software. Many simulations were made with several parameters having varied. Figure 3 shows the results (S_{11} , S_{21} and S_{31}) obtained from the same structure as on Figure 2(a). As we have already indicated: similar non reciprocal effects are observed that the ones found by the analytical model, on a wide frequency band around to 40 GHz. However, there are some discrepancies between the results obtained from the HFSS and the analytical model simulations. For example, the bandwidth is larger than the one given by the analytical model. This phenomenon is all greater as the boundary conditions on the ferrite edge depart from a perfect magnetic wall.

The three ports are not located in a symmetrical way. Thus, non reciprocal effects are not similar between two successive ports. For example, Figure 4 shows S_{23} , S_{32} parameters part (a)

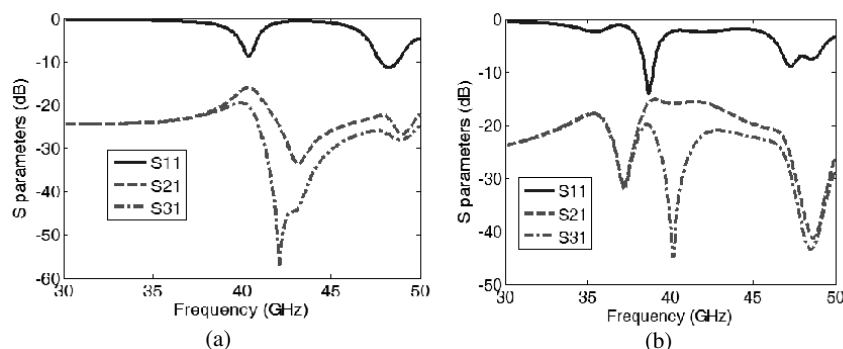


Figure 2: S_{11} , S_{21} and S_{31} of two different rectangular structures obtained from the analytical model with ferrite magnetization $M_s = 382$: kA/m; internal field $H_i = 1400$ kA/m and dimensions: (a) $a = 740 \mu\text{m}$ and $b = 300 \mu\text{m}$; (b) $a = 800 \mu\text{m}$ and $b = 500 \mu\text{m}$.

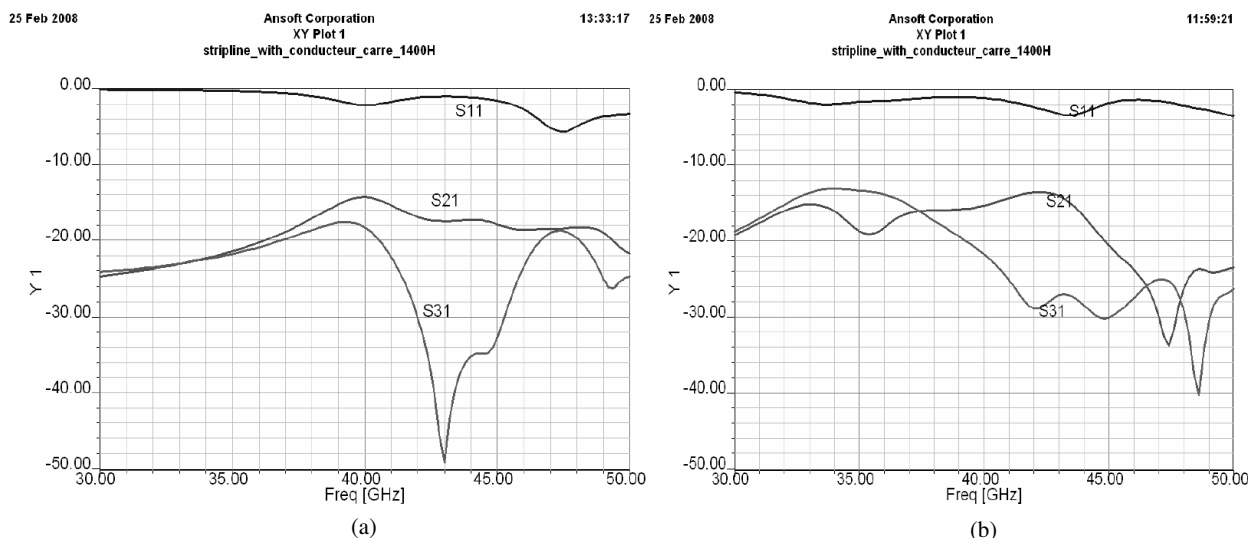


Figure 3: S_{11} , S_{21} and S_{31} of two different rectangular structures obtained from HFSS with ferrite magnetization $M_s = 382$: kA/m; internal field $H_i = 1400$ kA/m and dimensions: (a) $a = 740 \mu\text{m}$ and $b = 300 \mu\text{m}$; (b) $a = 800 \mu\text{m}$ and $b = 500 \mu\text{m}$.

and S_{13} , S_{31} parameters part (b). This drawback could be overcome by a rigorous impedance matching.

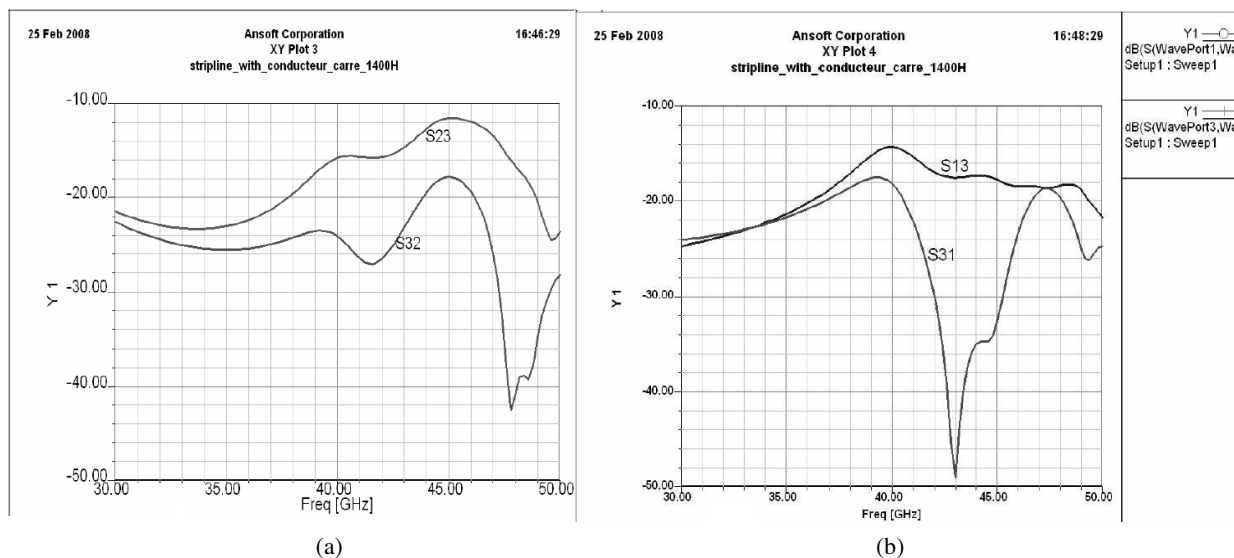


Figure 4: (a) S_{23} , S_{32} parameters, (b) S_{13} , S_{31} parameters for the same structure as on Figure 2 part (a).

The dimensions and the D.C. internal field are determined by using the analytical model, then the optimization is performed in making them vary separately. For example, the results obtained when the internal D.C. field value is 1000 kA/m are shown on Figure 5. Only small effects are observed and this D.C. value is not usable.

The best results are pointed out when the rectangle size is 740 μm by 300 μm and the D.C. field value is 1400 kA/m. The bandwidth value can reach 5 GHz and the relative bandwidth 10.5 per cent. Other parameter influence (access line width...) has been studied but not presented in this paper.

Therefore, important comments could be done: even if the impedance matching is quite wrong (the S_{11} parameter is almost close to 1 everywhere), high non reciprocal effects are shown in a large frequency band. This structure could be used as “rectangular circulator”.

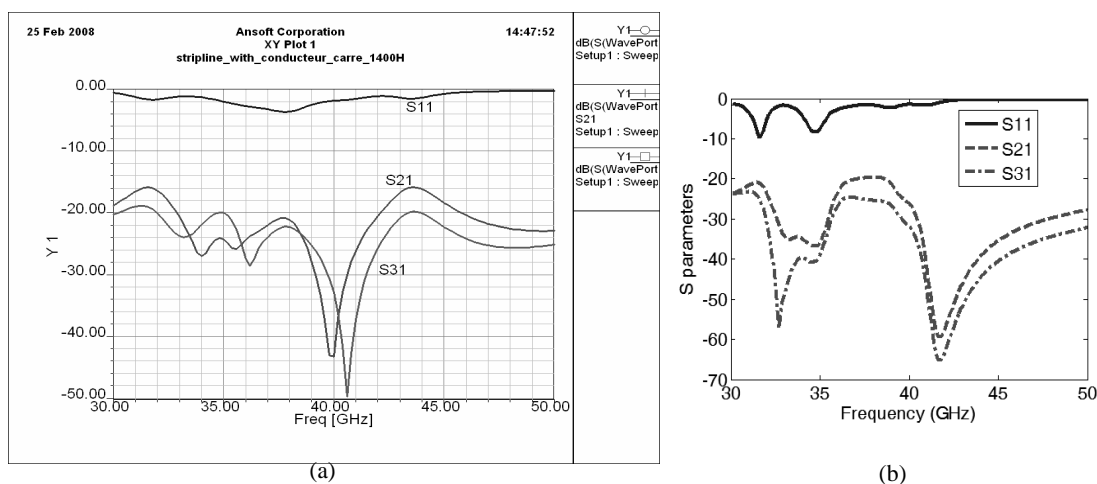


Figure 5: S_{11} , S_{21} and S_{31} obtained for ferrite magnetization $M_s = 382$: kA/m and internal field $H_i = 1000$ kA/m, (a) from HFSS, (b) from the analytical model.

4. CONCLUSION

A rectangular junction ferrite component has been studied. It is made from a stripline structure including two ferrite slabs which are magnetized along the z -axis direction. Using a rectangular

structure avoids the use of bent access lines that could disturb the TEM line propagation. According to the first results, the component must be improved before it is a rectangular circulator. The impedance matching must be performed. The analytical model could be better adjusted if we took into account non perfect boundary conditions used for Green's function derivation.

Barium or strontium ferrites seem to be suitable to operate in millimeter waves. Thin film deposition requires high temperature annealing with a magnetic moment direction. Composite magnetic materials made from directed nano particles scattered into a host dielectric matrix constitute another interesting solution owing to their low temperature processes. This will be true provided that the magnetic moment direction be maintained.

On the same way, other structures as coplanar and microstrip could be investigated.

Research domain of self-biased magnetic material still remains a challenge for integrating non reciprocal components.

REFERENCES

1. Olivier, A., P. Shi, and C. Vittoria, "Integrated self-biased hexaferrite microstrip circulators for millimeter-wavelength applications," *IEEE Trans. Microwave Theory Tech.*, Vol. 49, 385–387, February 2001.
2. Mincho, A. and L. G. M. Tsankov, "Design of self-biased waveguide circulators," *J. Appl. Phys.*, Vol. 73, No. 10, 7018–7020, May 1993.
3. Bosma, H., "On stripline Y-circulation at UHF," *IEEE Trans. Microwave Theory Tech.*, Vol. 12, 61–72, January 1964.
4. Helszajn, J., "Fabrication of very weakly and weakly magnetized microstrip circulators," *IEEE Trans. Microwave Theory Tech.*, Vol. 46, 439–449, May 1998.
5. Ogasawaram, N., "Coplanar-guide and slot-guide junction circulators," *Electronics Letters*, Vol. 7, No. 7, 220–221, May 1998.
6. Dudley, D. G., *Mathematical Foundations for Electromagnetic Theory*, IEEE Press Oxford University Press, 1994.
7. How, H., T. M. Fang, C. Vittoria, and R. Schmidt, "Design of six-port stripline ferrite junction circulators," *IEEE Trans. Microwave Theory Tech.*, Vol. 42, 1272–1275, July 1994.

Modelling SIW Resonators Using Support Vector Regression Machines

G. Angiulli¹, D. de Carlo¹, S. Tringali¹, G. Amendola², and E. Arneri²

¹DIMET, Univ. Mediterranea, 89100 Reggio Calabria, Italy

²DEIS, Univ. Della Calabria, 87036 Rende (Cs), Italy

Abstract— The Substrate Integrated Waveguide (SIW) technology combines the advantages of low cost building processes and the low loss features of waveguide devices. A large number of SIW-based devices have been realized in these last years. Many of them are based on SIW resonators. Very recently, in order to develop fast CAD models of microwave components and devices, Support Vector Regression Machines (SVRMs) have been proposed. In this work we investigate the performances of SVRMs for modeling SIW resonators.

1. INTRODUCTION

Substrate Integrated Waveguide (SIW) circuits [1] are a major subject of interest among engineers because they are an attractive alternative to canonical waveguides since they are cheap and simple to be produced. The building process consists of drilling a board of laminate to create a channel or a cavity for guided propagation. Indeed SIW technology combines waveguide features with the possibility of integration typical of microstrips. In recent times, several types of SIW-based devices have been realized and many of them, like filters, are based on SIW resonators (see [2] and references within). All the way around, a correct design process needs an accurate calculation of the resonant frequencies. For metallic cavities such frequencies can be determined either in a closed form when dealing with canonical geometries or by numerical methods for arbitrary shapes without many efforts, whereas for SIW resonators their accurate calculation is eventually troubling even for standard shaped structures. The basic case of SIW circular resonators is discussed in [3], where the authors consider the mutual scattering by metallic cylinders. Resonant solutions have been computed seeking for frequencies for which the smallest singular value of the moment matrix attains its minimum through the technique presented in [4].

This work exploits the aforementioned method in order to develop both an Artificial Neural Network (ANN) and a Support Vector Machine (SVM) models trying to give accurate characterizations of a circular SIW resonator. Numerical experiments demonstrate the effectiveness of this approach as a well-founded alternative to standard systematic plans. In fact, classical schemes often fail to take advantage from previous simulations of similar cases, e.g., when a geometrical parameter is just slightly changed. To overcome these limitations, models for microwave components and devices based on ANNs have received a lot of attention in the very last years (see [5] and references within). In some detail, ANN models succeed in providing a meaningful reduction of the overall computational burden due to numerical simulation of devices, especially with respect to standard techniques. This not standing, ANNs have some drawbacks, e.g., the lack of effective methods for prearranging the number of hidden layers and hidden nodes. Furthermore, ANNs have difficulties with generalization, hence producing models that can overfit the data. This is a consequence of both the optimization algorithms used for parameter selection and the statistical measures employed to sort the “best model” out. So an alternative approach to microwave modeling based on SVMs, that partially overcomes such problems, has been recently proposed [6]. Firstly introduced by Vapnik and co-workers [7], SVMs are getting more and more popular for overcoming the limitations typical to ANNs. This is because the Structural Risk Minimization principle embodied by SVMs has been proved to be more effective than the traditional Empirical Risk Minimization principle employed by ANNs (see [7] and references within), hence equipping the former with a greater ability to generalize, when compared with the latter. Moreover it is remarkable that, even if SVMs were initially thought for solving uniquely classification problems (see for example [8] and references within), they have been subsequently extended to operate in the survey of regression problems [9], introducing the age of the so-called Support Vector Regression Machines (SVRMs). Here we present some results on the feasibility of the application of the SVRMs to model SIW resonators.

2. LOCALIZATION OF RESONANCES

The analysis of a SIW waveguide through the magnetic dyadic Green's function has been presented in [2]. The application of the boundary conditions involves two systems of algebraic linear equations (one for the TM scattering, the other for the TE case), that can be expressed in a matrix form as

$$[\mathbf{L}]^{\text{TE, TM}}[\mathbf{A}]^{\text{TE, TM}} = [\mathbf{\Gamma}]^{\text{TE, TM}} \quad (1)$$

Theoretically SIW resonances are the frequencies in the complex plane for which

$$\det([\mathbf{L}]^{\text{TE, TM}}(\omega)) = 0 \quad (2)$$

However, from a practical point of view, $[\mathbf{L}]^{\text{TE, TM}}$ can be efficiently tested to be singular only by the Singular Value Decomposition (SVD). In numerical algebra, SVD permits an arbitrarily $n \times n$ complex matrix $[\mathbf{L}]^{\text{TE, TM}}$ to be factorized in the form $\mathbf{U}\mathbf{\Sigma}\mathbf{W}^*$, where \mathbf{U} and \mathbf{W} are n -by- n unitary matrices, $*$ denotes the conjugated transposition and $\mathbf{\Sigma} = \text{diag}(\sigma_1, \sigma_2, \dots, \sigma_n)$ is an n -by- n diagonal matrix, whose entries $\sigma_1, \sigma_2, \dots, \sigma_n$ are non negative real numbers (namely, *singular values*), rearranged in such a way that $\sigma_1 \geq \sigma_2 \geq \dots \geq \sigma_n \geq 0$. Then, in order to prove whether $[\mathbf{L}]^{\text{TE, TM}}$ is singular or not, first of all we recall that the smallest singular value σ_n represents the actual distance between $[\mathbf{L}]^{\text{TE, TM}}$ and the set of all matrices whose rank is $\leq n - 1$. Hence, provided a threshold $\epsilon > 0$, we state $[\mathbf{L}]^{\text{TE, TM}}$ is ϵ -singular, whenever $\sigma_n \leq \epsilon$. Starting from this condition, the set Ω of the complex resonant frequencies $\omega = \omega_{re} + j\omega_{im}$ (for which the matrix $[\mathbf{L}]^{\text{TE, TM}}$ is ϵ -singular) can be determined seeking for the minima of the two variable function $\sigma_n = \sigma_n(\omega_{re}, \omega_{im})$ in a given frequency band $[\omega_{min}, \omega_{max}]$. In [4] an effective search strategy is discussed, basically consisting of an approximate computation of σ_n rather than a direct complete SVD factorization. First σ_n is restricted to a real function for locating its minima on the real axis. Then these are used as starting points of a Müller routine for a spread seeking through the whole complex plane.

3. BASICS ON SVRMS

SVMs are learning machines performing pattern recognition tasks. By means of non linear transformations they map the n -dimensional input space into a higher dimensional space in which the data can actually be linearly separated [7]. SVMs can also be employed to solve regression problems, which is the case when they specialize in Support Vector Regression Machines (SVRMs). As for classification, non linear transformations are adopted to map incoming data into a higher dimensional space, where a linear regression can be carried out. Loosely speaking, like in canonical regression problems, the relationship between dependent and independent variables is supposed to be the sum of an unknown smooth function f plus some additive noise. The main task is to find an analytical closed form for f granting for the possibility to predict the behavior of brand new cases the SVM has never been presented with. This can be achieved by training the SVM by a suitable training set. The overall process involves sequential optimization of an error (or loss) function [7].

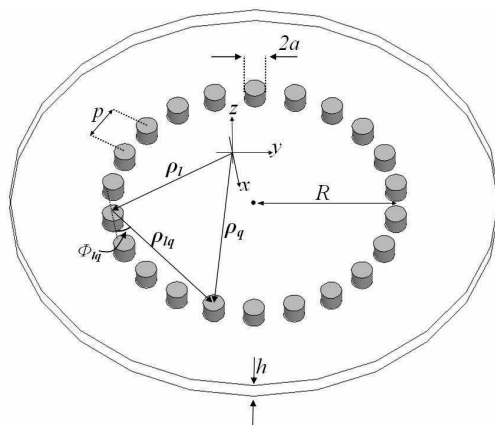


Figure 1: A circular SIW resonator, where in particular the pitch p , the via hole radius a , the SIW radius R and the dielectric substrate height h are shown.

4. TRAINING PROCESS AND NUMERICAL RESULTS

Following [3], we consider the circular SIW model in Fig. 1 for our experiments and introduce a design parameter $\chi = R\sqrt{\epsilon_r} \cdot f_{res}$. Here R indicates the resonator radius, ϵ_r the substrate dielectric permittivity and f_{res} the network resonant frequency. When completely specified over a band, χ permits to evaluate the SIW radius R , once f_{res} is known or viceversa (at least for a fixed ϵ_r). Hence admitting χ is a continuous function of the geometrical design parameters p (the pitch dimension) and a (the metallic via holes radius), we have trained several ANNs and SVRMs in order to obtain suitable neural and regression models for its prediction. Particularly for the ANN, we have employed an optimized neural network consisting of one input, two hidden and one output layers (see Fig. 2).

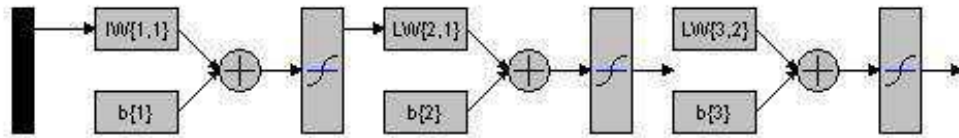


Figure 2: ANN architecture.

A suitable training data set has been carried out by numerical simulations exploiting a MatLab Full Wave code based on the theory described in [2]. For all the considered ANN architectures we have embodied each neuron with the sigmoid function for simulating the relationship between inputs and outputs. Moreover, all the thresholds have been assumed to be zero and all activation gains have been assumed unitary. Finally we have normalized all variables to limit their values in $[-1, 1]$. The back-propagation algorithm has been used to train more than a thousand of architectures. The best of all has turned out to be a network consisting of two neurons in the input layer, a variable numbers of neurons in the first and second hidden layer and one neuron in the output layer (see Fig. 2). After about 168 epochs, the ANN has given a root square mean error less than $1.126053e-005$. Fig. 3 shows the best diffusion diagrams obtained with ANNs. With the same data set has been trained the SVMs. Also in these simulations we have normalized all variables between the values $[-1, 1]$. Figs. 3 and 4 (regression analysis of ANNs and SVRMs respectively) show the linear profiles having 45° slope confirm a good agreement between estimates and computed values of χ in all cases and over the whole range of the geometrical and electrical parameters under analysis (see [3] for details). All the simulations have been carried out for the following dielectric substrates: ROGERS RT/DUROID 5880 ($h = 0.5$ mm, $\epsilon_r = 2.2$) and ROGERS TMM10 ($h = 0.318$ mm, $\epsilon_r = 9.8$).

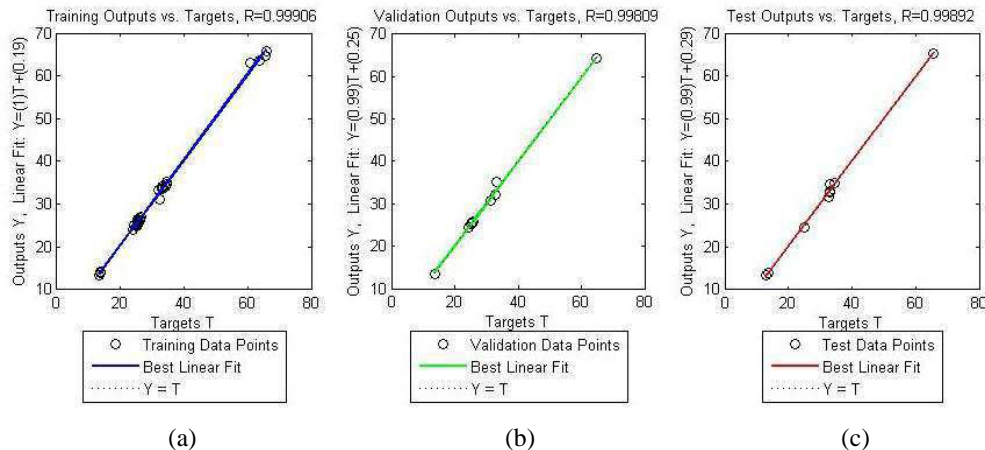


Figure 3: ANN regression analysis: (a) Training outputs vs. targets; (b) Validation outputs vs. targets; (c) Tests outputs vs. targets.

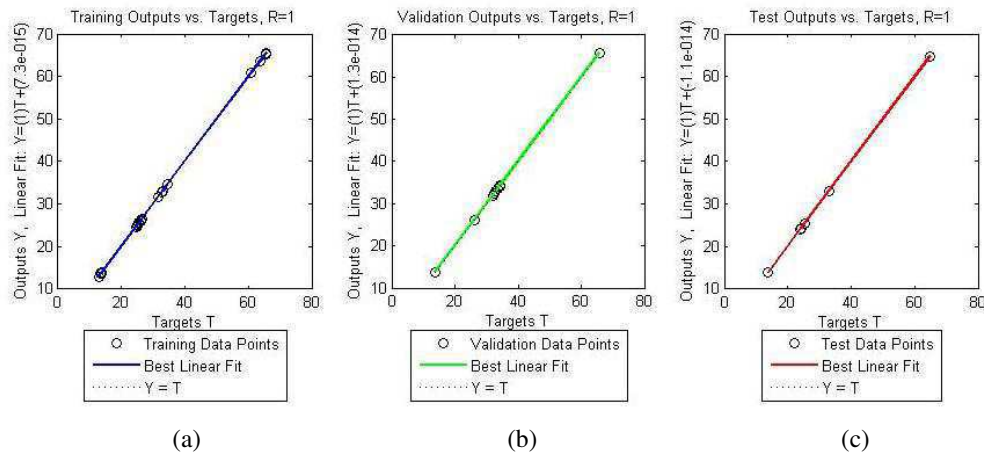


Figure 4: SVRM regression analysis: (a) Training outputs vs. targets; (b) Validation outputs vs. targets; (c) Tests outputs vs. targets.

5. CONCLUSION

In this work an ANN and SVM models of circular SIW resonators has been developed. The obtained numerical results demonstrate their ability to give data as accurate as those obtained from Full Wave simulations. It has underline that, once trained, the computation time and accuracy of numerical results of the SVM respect to ANN model, are clearly better. Nevertheless, both models are suitable to use in microwave CAD tools. I particular, as shown in Fig. 4, experimental results are very promising and suggest that SVRMs can be protably employed for fast microwave CAD applications.

REFERENCES

- Deslandes, D. and K. Wu, "Single substrate integration technique of planar circuits and waveguide filters," *IEEE Trans. Microwave Theory Tech.*, Vol. 51, No. 2, 165–171, 2003.
- Arneri, E. and G. Amendola, "A Green's function approach to the analysis of substrate integrated waveguide circuits," *IEEE Trans. Microw. Theory Tech.*, submitted for publication.
- Amendola, G., G. Angiulli, E. Arneri, and L. Boccia, "Analysis and characterization of circular substrate integrated resonators," *IEEE Microwave and Wireless Components Letters*, Vol. 20, No. 4, 2008.
- Angiulli, G., "On the computation of nonlinear eigenvalues in electromagnetic problems," *Journal of Electromagnetic Waves and Applications*, Vol. 21, No. 4, 527–532, 2007.
- Zhang, Q. J., K. C. Gupta, and V. K. Devabhaktuni, "Artificial neural networks for RF and microwave design-from theory to practice," *IEEE Trans. on Microwave Theory Tech.*, Vol. 51, No. 4, 1339–1350, 2003.
- Angiulli, G., M. Cacciola, and M. Versaci, "Microwave devices and antennas modelling by support vector regression machines," *IEEE Transactions on Magnetics*, Vol. 43, No. 4, 1589–1592, 2007.
- Cortes, C. and V. Vapnik, "Support vector network," *Machine Learning*, Vol. 20, 273–297, 1997.
- Angiulli, G., M. Cacciola, and V. Barrile, "SAR imagery classification using multi class support vector machines," *Journal of Electromagnetic Waves and Applications*, Vol. 19, No. 14, 1865–1872, 2005.
- Gunn, S. R., "Support vector machines for classification and regression," *ISIS Technical Report*, 1998.

Microwave Unpolar Organic Reactions Using Microwave Absorber

Chunyan Huo, Jianhua Chen, Haisheng Xu, and Dong Shen

Laboratory of Chemical Physics, East China University of Science and Technology
Shanghai 200237, China

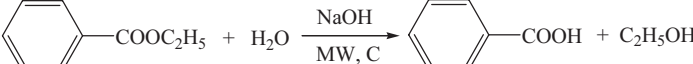
Abstract— Different configurations of carbon were applied as energy transfer medium in the microwave assisted organic reactions, their effect on the reactions was studied, among them active carbon shows the best safety and efficiency.

1. INTRODUCTION

Using microwave as energy resource to induce organic reactions attracts more and more attentions as it has so many advantages compared with convenient oil heating organic reactions, it was predicted that the microwave assisted organic reactions will be performed as a standard technique in research laboratory and chemical industry [1]. However, organic reactions with low polarity are excluded by the microwave-assisted reactions because of the poor microwave absorption of the reaction mixtures. To solve this problem, some methods such as ionic liquid [2], polar solvent [3], or cylinder of sintered silicon carbide were reported to adding to the reactions [4]. Compared with the ionic liquids and polar solvents, cylinder of sintered silicon carbide has the advantages of thermo-stability and chemical inertance. As an inorganic additive, SiC can't be dissolved in the reaction mediums, so the transferring of energy is not the most efficient due to the limited interface; however, using cylinder of sintered silicon carbide can enhance the unpolar microwave reactions significantly.

Another inorganic microwave absorber, C, attracted our attention because of its strong microwave absorption [5], similar to SiC, as an inorganic material to be used in microwave assisted organic reactions, carbon can't be dissolved in organic solvents, so their efficiency of energy transferring depends on their size and configuration, when the material is smaller, the effect should be better. Carbon has some different configurations and their physical properties are different. To find a suitable energy transferor, different configurations of C, active carbon, graphite powder, micrometer and nanometer carbon were applied in the low polar or nonpolar reactions, the results showed that active carbon was the best.

Table 1: The yields of adding different quantities of microwave absorber in different irradiation time.^a



Microwave absorber	Mount (g)	Y ₁ ^b (%) 20 min. ^c	Y ₂ (%) 30 min.
Active Carbon	0.0	30.44	56.64
	0.1	88.93	91.80
	0.3	91.18	92.82
Graphite powder	0.1	92.62	93.03
	0.3	95.49	95.70
Nanometer carbon	0.1	84.26	86.19
	0.2	86.42	88.82
	0.3	87.43	90.26

^a Reaction condition: 3.0 g (20.0 mmol) ethyl benzoate, 30 mL 10% NaOH (aq).

^b Isolated yield, average of two runs.

^c Irradiation time, 700 W, 20% duty, the reactions were performed without stirring.

2. RESULTS AND DISCUSSION

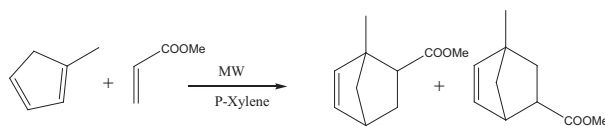
2.1. Hydrolysis of Ethyl Benzoate

The hydrolysis of benzoate is a well known reaction in microwave organic chemistry [6]. The solvent, water, has medium microwave absorption ($\tan \delta$ 0.123) [1]. The reason why this reaction was chosen for investigation was to test the safety and efficiency of carbon, because carbon has strong microwave absorption, under irradiation of microwave it is heated very rapidly, if it can not transfer the absorbed energy to reaction medium, its temperature will be very high and oxidation with Oxygen even ignition could be happened. So the reactions using carbon were firstly performed without stirring for the hydrolysis of ester, as the hydrous reaction medium is much safer than organic solvents for the microwave assisted reactions. The results showed that all of the applied configurations of carbon could enhance the reactions efficiently (Table 1). Among them, graphite powder was the most efficient but had flame, and the yields of the reactions with micrometer carbon were unstable, probably the material was not stable, so they were not further applied for the unpolar reactions. Nanometer carbon had the similar efficiency with active carbon but is much more expensive. When the reactions were performed with stirring, they were enhanced more efficiently and needed only half time to achieve same yields.

2.2. Diels-Alder Reaction of Methyl Acrylate with Methylcyclopentadiene

Active carbon, nanometer carbon were used further for the low polar reactions. As a comparison, the effect of micrometer SiC (14 μm) and nanometer SiC (50 nm) were also studied. The results were shown in Table 2. For this low polar reaction, more irradiation time and power were needed to get desirable conversions, active carbon was still the best one, whereas the reaction with nanometer carbon could not be finished because flame was observed. Nanometer SiC had the similar effect with active carbon in short irradiation time, and the conversions with micrometer SiC were a little lower.

Table 2: The yields of adding different microwave absorber in different irradiation time.^a



Microwave absorber	Y ^b (%)	Y(%)
	30 min. ^c	50 min.
No microwave absorber	58.28	/
Active carbon	77.96	90.78
Nanometer carbon	/	/
Micrometer SiC	71.47	82.16
Nanometer SiC	77.67	82.27

^a Reaction condition: 0.86 g (10.0 mmol) methyl acrylate, 0.88 g (11.0 mmol) methylcyclopentadiene, 30 mL p-xylene, microwave absorber 0.3 g.

^b Conversion, determined by GC, average of two runs.

^c Irradiation time, 700 W, 50% duty. The reactions were performed with stirring.

For unpolar reaction, we have reported that active carbon could enhance the Diels-Alder reaction of anthracene with *trans*-dibutyl fumarate in p-xylene assisted with microwave efficiently [7]. It is surprised that in most cases active carbon is even more efficient than nanometer carbon although it has much more large size, maybe it was because of its strong absorption of reagents.

In conclusion, among the applied microwave absorbers in this paper, active carbon is the best one for application, it is efficient, can help finish the unpolar even middle polar reactions in short time, it is safe for using in microwave assisted reactions, no ignition of active carbon was observed in our experiments whatever the reaction was stirred or not, its application in chemical industry is expected.

3. EXPERIMENTAL

All reactions were performed in a Yamei W700A multimode microwave reactor equipped with condenser and stirrer. Micrometer carbon ($< 100 \mu\text{m}$) and nanometer carbon (96.3 nm) were provided by school of chemical engineering, East China University of Science and Technology. Other reagents and solvents were obtained from commercial sources. GC analysis was performed using GC9790 (Wenling Analytical Instrument, Co., LTD).

General procedure of hydrolysis of ethyl benzoate: A mixture of 3.0 g (20.0 mmol) of ethyl benzoate, 30 mL 10% aqueous NaOH solution and appropriate microwave absorber was irradiated under microwave (700 W, 20% duty) for an appointed time and then was cooled down to room temperature. Microwave absorber was filtered off and washed with 30 mL petroleum ether, 15 mL aqueous Na_2CO_3 solution. The aqueous phase was separated and acidified with concentrated hydrochloride (33%) to $\text{pH} = 1$. Then the solution was extracted with CH_2Cl_2 , dried with anhydrous MgSO_4 , the solvent was removed and the product was obtained in white solid, m.p. 122–125 °C.

General procedure of Diels-Alder reaction of methylcyclopentadiene with methyl acrylate: A mixture of 0.86 g (10.0 mmol) of methyl acrylate, 0.88 g (11.0 mmol) of methylcyclopentadiene, 30 mL p-xylene and appropriate microwave absorber was irradiated under microwave (700 W, 50% duty) for an appointed time, and was then cooled down to room temperature, microwave absorber was then filtered off and washed with p-xylene 2–3 times, the filtrate was weighed, 0.07 g toluene was added to a sample of 2.0 g filtrate, the conversion of methyl acrylate was detected by GC.

ACKNOWLEDGMENT

This work was financially supported by ECUST (Fund of Fundamental Theory).

REFERENCES

1. Kappe, C. O., "Controlled microwave heating in modern organic synthesis," *Angew. Chem., Int. Ed.*, Vol. 43, 6250, 2004.
2. Hoffmann, J., M. Nuechter, B. Ondruschka, and P. Wasserscheid, "Ionic liquids and their heating behaviour during microwave irradiation-A state of the art report and challenge to assessment," *Green Chem.*, Vol. 5, No. 3, 296, 2003.
3. Bose, A. K., M. S. Manhas, M. Ghosh, M. Shah, V. S. Raju, and S. S. Bari, "Microwave induced organic reaction enhancement chemistry. 2. Simplified techniques," *J. Org. Chem.*, Vol. 56, No. 25, 6968, 1991.
4. Kremsner, J. M. and C. O. Kappe, "Silicon carbide passive heating elements in microwave-assisted organic synthesis," *J. Org. Chem.*, Vol. 71, 4651, 2006.
5. Wang, L. and Q. Zhang, "Present research state and perspective of wave-absorbing agents," *Mater. Rev.*, Vol. 19, No. 9, 26, 2005.
6. Jin, Q. H., *Microwave Chem.*, Science Press, Beijing, 1999.
7. Li, Z., J. Chen, H. Xu, S. Hu, and D. Shen, "Enhancement of microwave-assisted organic reactions using active carbon," *PIERS Proceedings*, 544–547, Hangzhou, China, March 24–28, 2008.

A Novel Broadband Compact Circular Disk Microstrip Antenna for Wireless Applications

H. A. Osman¹, E. A. Abdallah², and A. A. Abdel Rhim¹

¹Arab Academy for Science & Technology and Maritime Transport, Egypt

²Electronics Research Institute, Egypt

Abstract— A novel shape of microstrip antenna which is electromagnetically coupled to a conventional circular disk microstrip antenna (CMSA) mounted on a ground plane and spaced by a layer of foam is studied by simulation and experiment to operate at 5.2 GHz for Wireless Local Area Networks (WLANs). The novel shape proposed has a size reduction of 85% as compared to the conventional circular disk patch antenna operating at the same frequency. It is found that the bandwidth of this antenna ranges from 4.8 GHz up to 6.15 GHz considerably when an optimum foam thickness is provided. The suggested design is optimized using the full wave simulation software package Zeland IE3D based on the method of moments (MoM). The experimental results agree well with the simulated one.

1. INTRODUCTION

Microstrip antennas have the attractive features of low profile, light weight, easy fabrication process, and conformability, but these antennas inherently suffer from the narrow bandwidth. Since the world is going wireless, current advancements in communication technology and significant growth in the wireless communication market and consumer demand demonstrate the need for smaller, broadband and reliable antennas. Therefore, bandwidth enhancement and size reduction are becoming the major design considerations for practical applications. Several useful techniques applied to improve the bandwidth and size reduction are presented in [1]. In particular, adding a capacitive component to the input impedance of the radiating patch that compensate for the inductive component of the feeder by embedding a cutting slots in it such as E-shape [2, 3], V-shape [4], and U-shape [5, 6] leads to increasing the percentage bandwidth as long as the resonance frequencies of the patch and the slot are close to each other. Moreover, using more than one layer of resonance patch that is coupled electromagnetically to each other instead of planar structure in order to meet the demand of small size will effectively enable the bandwidth to increase. These parallel layers are incorporated to introduce another resonance. Since the bandwidth is inversely proportional to the dielectric constant ϵ_r of the substrate, a layer of foam is employed to decrease the effective dielectric constant ϵ_{eff} and increasing the total thickness of the antenna at the same time.

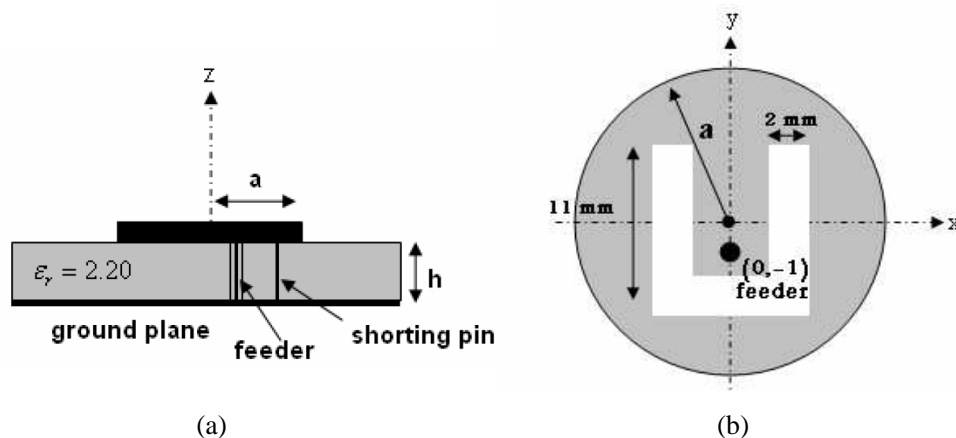


Figure 1: Configuration of CMSA (a) CMSA with shorting pin (b) CMSA with U-slot.

However, the bandwidth of the single layer conventional CMSA at 5.2 GHz is found to be 3.4% of compact size compared to [7], and when applying a shorting pin, size can be decreased but with lower bandwidth that is inconvenient for our applications. On the other hand, the bandwidth of CMSA

with U-slot is found to be increased to 21%. The configurations of these antennas are illustrated in Figure 1, and the return loss is shown in Figure 2. A study of CMSA supported by a layer of foam was done in both the normal and inverted configurations by changing the foam thickness where the optimum percentage bandwidth is found to be 15.5% and 12.36%, respectively. Consequently, more than one of aforementioned technique are combined together to obtain compactness and broadband. In this paper, a novel shape of CMSA is proposed having a reduction of size by 85% compared to the conventional circular disk patch antenna which is electromagnetically coupled to a circular patch spaced by a layer of foam at an optimum thickness is investigated. Alternatively, the feeding patch is simple CMSA and the radiating patch considered is the novel shape. The dimensions of the two patches are optimized to attain over 30% impedance bandwidth for WLANs operating at 5.2 GHz.

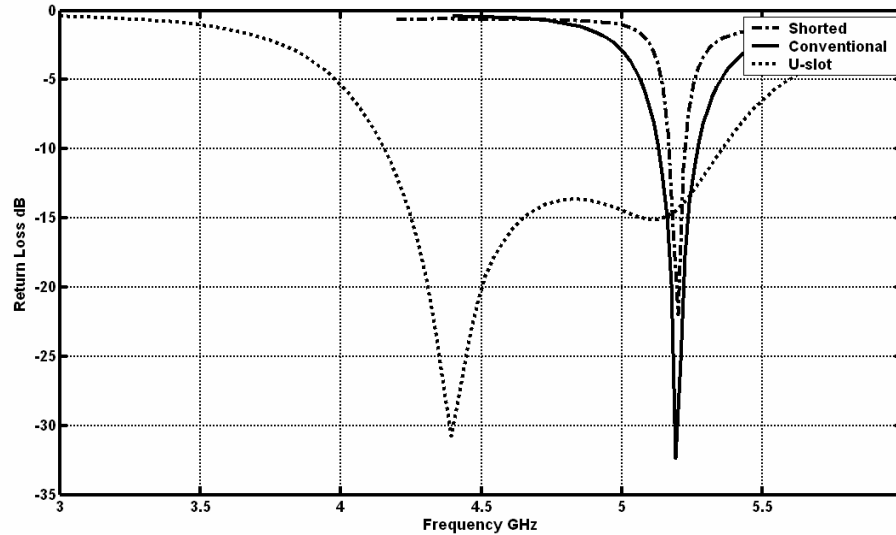


Figure 2: Return loss Vs Frequency of CSMA.

Conventional: $a = 10.65$ mm, $\epsilon_r = 2.20$, $h = 1.575$ mm, $X_f = 3.3$ mm, $r_f = 0.3$ mm, BW = 3.4%.

Shorted: $a = 3.47$ mm, $\epsilon_r = 2.20$, $h = 1.575$ mm, $X_f = 2.585$ mm, $X_p = 3$ mm, $r_f = r_p = 0.4$ mm, BW = 2.7%.

U-slot: $a = 10.65$ mm, $h = 1.575$ mm, $\epsilon_r = 2.20$, $r_f = 0.3$ mm, $(X_f, Y_f) = (0, -1)$, BW = 21%.

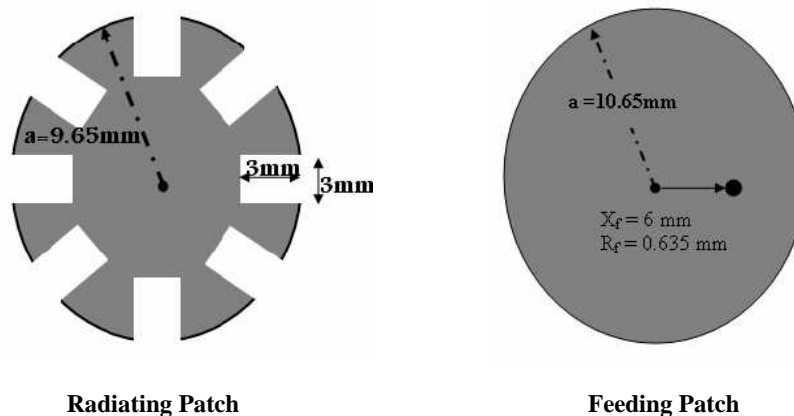


Figure 3: Configuration of the radiating and feeding patches.

2. ANTENNA CONFIGURATION

The feeding layer contains a simple CMSA of radius 10.65 mm which is fed by 50 Ohms-SMA connector of diameter 1.27 mm located at 6 mm from the center of the patch, while the radiating layer contains a novel shaped patch as shown in Figure 3. The proposed shape is based on a square

cut of length 3 mm in the edges of the circular patch of radius 9.65 mm. A finite number of slits (8-slits) is incorporated to obtain a compact size. The structure of this design is illustrated in Figure 4. A layer of foam $\epsilon_r = 1.07$ at an optimum thickness of 3.2 mm is employed between the two layers in order to decrease the effective dielectric constant and increase the total thickness of the antenna.

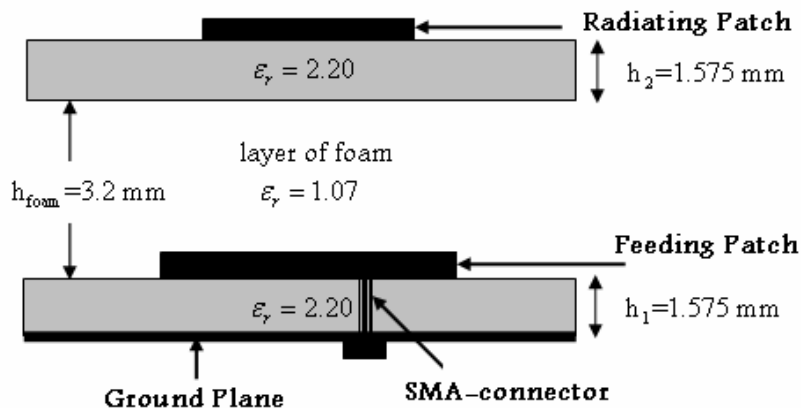


Figure 4: Structure of the antenna for bandwidth enhancement technique.

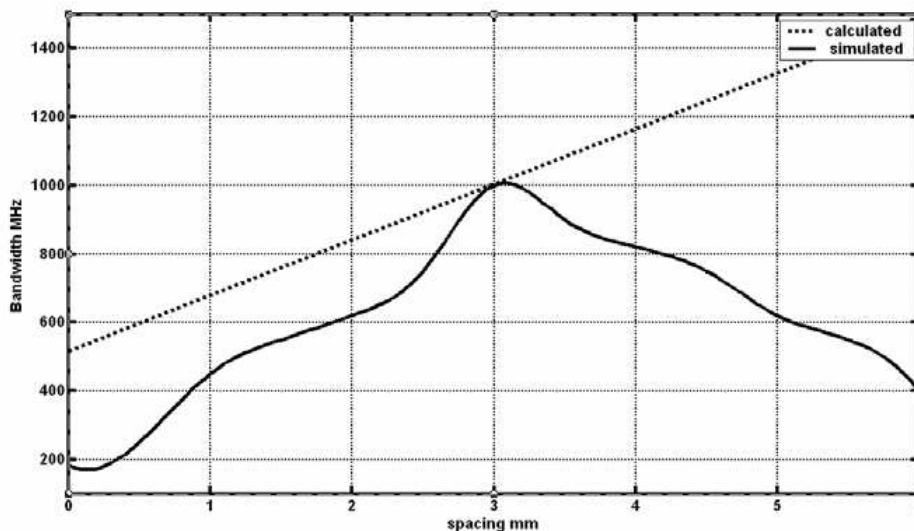


Figure 5: Comparison between the calculated and simulated results for an optimum foam thickness.

The change in the foam thickness is playing a role in change the total thickness of the antenna and its size which influences the bandwidth [8]. Figure 5 shows a comparison between the calculated and simulated results to determine the exact thickness required to obtain a wide bandwidth. The calculated results are obtained according to [9]:

$$BW = \frac{VSWR - 1}{Q_T \sqrt{VSWR}} \tag{1}$$

The bandwidth is taken at $VSWR = 2$, so that

$$BW = \frac{1}{\sqrt{2}Q_T} \tag{2}$$

where

$$Q_T = \left[\tan \delta + \frac{1}{h_T \sqrt{\pi f_0 \mu_0 \sigma}} + \frac{h_T f_0 \mu_0 (k_0 a)^2 I}{30 ((ka)^2 - n^2)} \right]^{-1} \quad (3)$$

$\tan \delta = 0.001$, $f_0 = 5.2$ GHz, $\mu_0 = 4.7 \times 10^{-7}$ H/m, $h_T = h_1 + h_2 + h_{foam}$, $h_1 = h_2 = 1.575$ mm, $k = \sqrt{\epsilon_r} k_0$ and $k_0 = \frac{\omega_0}{\text{speed of light}}$.

For the dominant mode, $n = 1$. By substituting Equation (3) into Equation (2), then

$$BW = \frac{1}{\sqrt{2}} \left[\tan \delta + \frac{1}{h_T \sqrt{\pi f_0 \mu_0 \sigma}} + \frac{h_T f_0 \mu_0 (k_0 a)^2 I}{30 ((ka)^2 - 1)} \right] \quad (4)$$

where

$$I = \int_0^{2\pi} \left[J_1'^2(k_0 a \sin \theta) + \cos^2 \theta \frac{J_1^2(k_0 a \sin \theta)}{(k_0 a \sin \theta)^2} \right] \sin \theta d\theta \quad (5)$$

This integration is evaluated numerically yields to $I = 0.1957$. Obviously, the calculated bandwidth according to Equation (4) is found to be 1 GHz at an optimum thickness of 3 mm which coincided with the maximum bandwidth simulated using IE3D electromagnetic simulator as shown in Figure 5.

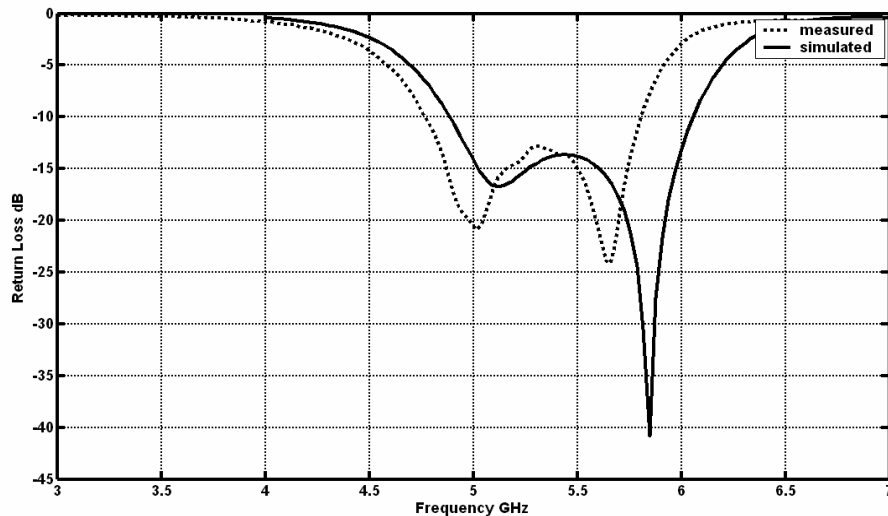


Figure 6: Simulated and measured return loss.

3. RESULTS

The simulated results are optimized based on IE3D software. Numerous iterations were done to obtain the optimum configuration. The optimized configuration is fabricated using photolithographic technique. Figure 6 shows the measured and simulated results of the return loss. Obviously, the general shapes of both results are very close. Furthermore, the simulation clears that a bandwidth ranges from 4.8 GHz up to 6.15 GHz which is quite enough to cover the band of 5 GHz compared to a slight shift in the measured results. It is seen that around the resonant frequency the antenna input impedance is very close to 50Ω as shown in Figure 7. The measured antenna gain and radiation efficiency were 7.47 dB and 90%, respectively. The simulated radiation patterns are illustrated in Figure 8. Through the simulation it has been noticed that the most important parameter that affect the resonance performance is the width of the cutting slits. The fabricated antenna is photographed in Figure 9.

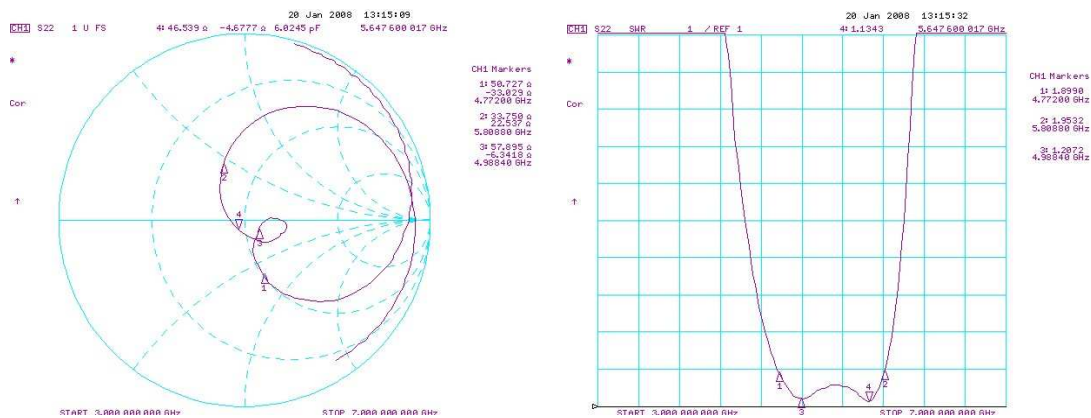


Figure 7: Measured input impedance and VSWR.

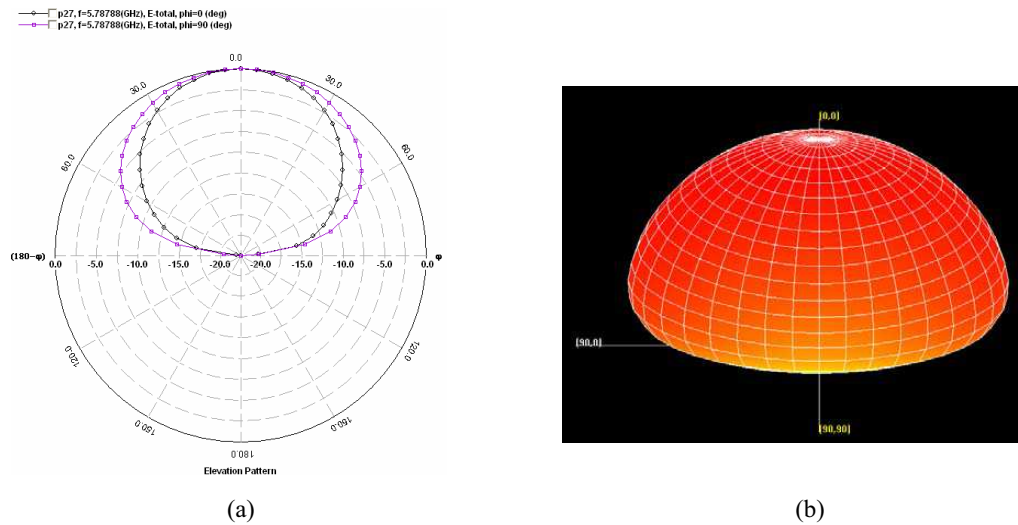


Figure 8: Simulated radiation patterns using Zeland IE3D (a) *E*-plane & *H*-plane (b) 3D view.



Figure 9: Fabricated microstrip antenna.

4. CONCLUSIONS

Two stacked layers of microstrip antennas have been designed and investigated experimentally. The feeding patch is CMSA coupled electromagnetically to a compact novel shaped spaced by a layer of foam. Simulation and experimental studies are performed. When the thickness of the foam layer is changed, variation in the percentage bandwidth could be obtained. The advantage

of simplicity and compactness of this structure make it useful for WLANs applications than other designs. This approach is clearly enhancing the percentage bandwidth of the microstrip antennas used for WLANs. Using combinations of several techniques is promising idea to obtain a broadband microstrip antenna. There will be advantages and disadvantages which means that a trade-off have to be considered in the design.

ACKNOWLEDGMENT

The authors would like to thank the staff of Electronics Research Institute for their outstanding concern and support.

REFERENCES

1. Wong, K. L., *Compact Broadband Microstrip Antenna*, John Wiley & Sons, New York, 2002.
2. Ge, Y., K. P. Esselle, and T. S. Bird, "E-shaped patch antennas for high-speed wireless networks," *IEEE Trans. on Antennas and Propagation*, Vol. 52, No. 12, 3213–3219, 2004.
3. Ang, B. K. and B. K. Chung, "A wideband E-shaped microstrip patch antenna for 5–6 GHz wireless communications," *Progress In Electromagnetics Research*, PIER 75, 397–407, 2007.
4. Rafi, G. and L. Shafai, "Broadband microstrip patch antenna with V-slot," *IEE Proc. Microwave Antenna Propagation*, Vol. 151, No. 5, 435–440, 2004.
5. Luk, K. M., K. F. Lee, and W. L. Tam, "Circular U-slot patch with dielectric superstrate," *Electronics Letters*, Vol. 33, No. 12, 1001–1002, 1997.
6. Bhallah, R. and L. Shafai, "Resonance behaviour of single U-slot microstrip patch antenna," *Microwave and Optical Technology Letters*, Vol. 32, No. 5, 333–335, 2002.
7. Guo, Y. J., A. Paez, R. A. Sadeghzadeh, and S. K. Barton, "A circular patch antenna for radio LANs," *IEEE Trans. on Antenna and Propagation*, Vol. 45, No. 1, 177–178, 1997.
8. Abdullah, R., D. Yoharaaj, and A. Ismail, "Bandwidth enhancement technique in microstrip antenna for wireless application," *PIERS Online*, Vol. 2, No. 6, 633–639, 2006.
9. Ramesh, G., B. Prakash, B. Inder, and I. Apisak, *Microstrip Antenna Design Handbook*, Artech House, USA, 2001.

Experimental Investigation of Transformer Coupled Toroidal Discharges

I. M. Ulanov, M. V. Isupov, and A. Yu. Litvinsev

Kutateladze Institute of Thermophysics SB RAS

Lavrentiev av. 1, Novosibirsk 630090, Russia

Abstract— The transformer coupled toroidal discharge (TCTD) was studied experimentally in the mixture of mercury vapours with argon and in pure neon. New experimental data on electric field strength and emission yield to visible and UV-range were obtained as functions of the discharge parameters. It was proved that the dependencies of electrical and optical characteristics of TCTD on the discharge current, gas pressure and tube diameter are close to those of dc arc discharges in mercury vapour and neon correspondingly. The possible reasons for parameter deviations were considered.

1. INTRODUCTION

As it is known, production of low-temperature plasma by induction (electrodeless) gas discharges is one of the most promising methods to increase the efficiency and service life of the gas-discharge light sources. The urgency of this problem is obvious because of the wide application of gas-discharge lamps in different fields of lighting technology (room and street illumination, biomedical and technical applications, etc).

There are several types of induction gas discharges, differing both by the construction of inductor and gasdischarge chamber and by the frequency of discharge current, among which the transformer coupled toroidal discharges (TCTD's) should be mentioned specially.

While differing in detail such as the position of excitation coils and chamber materials, all TCTD's feature a closed plasma loop in the discharge chamber, which acts as a single-turn secondary winding of excitation transformer. With consideration of electromagnetic induction the criterion of TCTD generation is written as [1]

$$\oint_L E dl = -d\Phi/dt = -2\pi S f B_m \cos(2\pi ft) \quad (1)$$

where E is the strength of electric field in discharge, B_m is amplitude of magnetic induction in the core, S is the core cross-section, f is current frequency; integral is taken by the close circuit of discharge L . Since B_m in ferromagnetic materials can reach high values (~ 1 T), the required strengths of field E can be obtained at relatively low current frequencies of ~ 10 – 100 kHz (typical frequencies of RF induction discharges is about ~ 1 – 10 MHz). Thus, the long lifetime and relatively low frequencies make TCTD promising for creating the new electrodeless discharge devices for the practical application: low temperature plasma generators [2, 3] and light sources [4, 5].

To develop new electrodeless long-life sources of visible and UV radiation, experimental investigations of the TCTD in a mixture of argon and mercury vapour were carried out for a wide range of discharge parameters: mercury vapour pressure (0.1–40 000 Pa), discharge current (1–260 A), diameter of a gas-discharge tube (20–75 mm) and current frequency (10–250 kHz). Also, experimental investigations of the TCTD in pure neon were carried out for neon pressures of 10–600 Pa, discharge currents 1–30 A, tube diameters 20–58 mm and driving frequencies 25–250 kHz.

2. EXPERIMENTAL SETUP

The common scheme of the experimental setup is shown in Fig. 1. The main elements of the setup are as follows: 1-quartz toroidal gas-discharge chamber; 2-system of ferromagnetic cores with primary winding 3; 4-high-frequency power source; 5-accommodation unit between power source and TCTD.

To measure the strength of discharge current I , current transformer 6 was used. To measure the voltage U that drives the TCTD, measurement coil 7, enveloping the gas-discharge chamber over perimeter L was used. At that, the strength of electric field E was determined as a ratio between measured voltage U and the discharge perimeter along the middle line: $E = U/L$. The

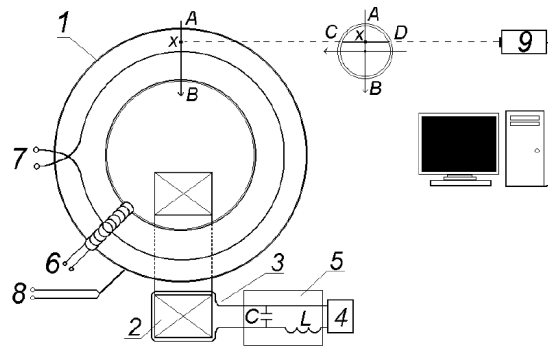


Figure 1: The scheme of experimental setup. 1-quartz gas-discharge chamber; 2-ferromagnetic cores; 3-primary winding; 4-power supply; 5-accommodation unit; 6-current transformer; 7-measuring coil; 8-thermocouples; 9-optic probes.

wall temperature of gas-discharge chamber T was controlled by thermocouples 8, which allowed us to determine the mercury vapour pressures p in the discharge chamber using the known dependence between the pressure of saturated mercury vapour and the temperature. For TCTD in neon the ILMVAC PIZA 111 vacuum meter was used for pressure measurements. To measure the optical and spectral characteristics, the following optic probes 9 were used:

- Luxmeter, UV-radiometer TKA-PKM (model 06), intended for measuring illumination (lx) within a visible range and UV-irradiation (mW/m^2) within the range 280–400 nm (A + B zones).
- UV-radiometer TKA-PKM (model 12), intended for measurements of UV-irradiation within three ranges: UVA (315–400 nm), UV-B (280–315 nm) and UV-C (200–280 nm).
- The hardware-software system of control for spectrometric measurements “SVET” allows registration for spectra of spatially inhomogeneous emitting objects, analysis of energy characteristics of radiation in the spectral range of 360–800 nm (developed in Petrozavodsk State University, Russia).

3. EXPERIMENTAL RESULTS: TCTD IN MERCURY VAPOURS

Dependence E versus p is shown in Fig. 2, for different diameters of the discharge tube (current density $J = 1 \text{ A}/\text{cm}^2$). Dependence $E(p)$ for a dc arc discharge is shown for comparison ($D = 32 \text{ mm}$, $J = 0.35 \text{ A}/\text{cm}^2$, [6]). According to Fig. 2, in the range of mercury vapour pressure of $\sim 3\text{--}30 \text{ Pa}$, the electric field strength of TCTD has a local minimum. With a further increase in pressure, the electric field strength increases as $E \sim p^{1/3}$. For the case of dc arc discharges in mercury vapour, dependence $E(p)$ takes a qualitatively similar form [6].

For the dc arc discharges in the long cylindrical tubes with specific discharge power of 20–50 W/cm and the middle or high pressure of mercury vapour, the interaction between electric field strength, diameter of the gasdischarge tube and specific mass of evaporated mercury m is presented by the known dependence, derived by Elenbaas [7]

$$E \cdot D^{3/2} \approx 370 \cdot m^{7/12} \quad (2)$$

where value E is presented in V/cm, D is in millimetres, and the specific mass of evaporated mercury m is in mg/cm. The dependence of $E \cdot D^{3/2}$ on specific mass of evaporated mercury m (mg/cm) is shown in Fig. 3 for the fixed specific power of TCTD of $P = 40 \text{ W}/\text{cm}$. Data shown in Fig. 3 corresponds to the range of mercury vapour pressures of 10–40 kPa, and the tube diameter of 35–75 mm. A similar dependence, obtained by Elenbaas for the mercury dc arc discharges in the long cylindrical tubes with diameters 12–38 mm are also shown in Fig. 3 [7]. As seen from Fig. 3, the experimental data obtained for the TCTD are laid perfectly on the line, described by expression (2). This proves the fact that, at least, in the range of mercury vapour pressure of 10–40 kPa and diameters of gas discharge tube of 35–75 mm, the electrical characteristics of TCTD are similar to those of the dc arc discharges.

The dependence of TCTD light efficiency on the pressure of mercury vapour is shown in Fig. 4. Dependence of dc arc discharge light efficiency is shown in Fig. 4 for comparison ($D = 27 \text{ mm}$,

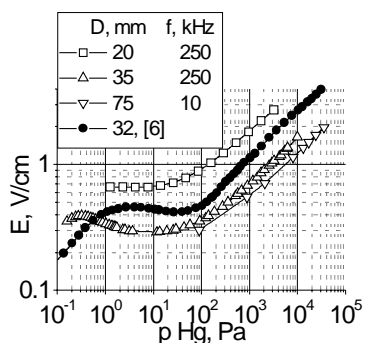


Figure 2: Electric field strength E versus mercury vapour pressure p , for different diameters of chambers. ($J = 1 \text{ A/cm}^2$).

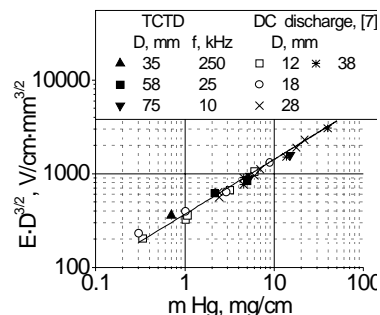


Figure 3: Interaction between electric field strength E , diameter of gas-discharge chamber D and specific amount of evaporated mercury m , for TCTD and dc arc discharges.

$I = 4 \text{ A}$, [7]). According to Fig. 4, the dependence of light efficiency of TCTD and DC arc discharge on mercury vapour pressure are qualitatively similar. It can also be seen from Fig. 4 that with an increase in the diameter of the gas-discharge tube, the light efficiency of TCTD increases; a similar dependence is observed for the dc arc discharges [8].

The dependence of the emission yield (as a percentage of input power) to non-resonance lines of the UV spectrum range (280–400 nm) on the pressure of mercury vapour is shown in Fig. 5 for the fixed discharge current. According to Figs. 4 and 5, the efficiency of non-resonance lines of the UV and visible ranges of the TCTD radiation spectrum similarly depend on the pressure of mercury vapour and the diameter of the gasdischarge tube.

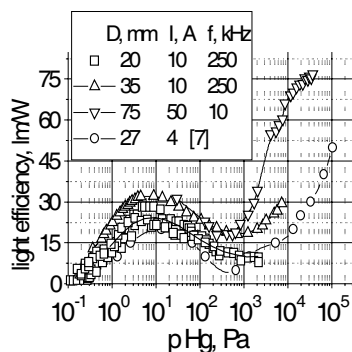


Figure 4: Light efficiency versus mercury vapour pressure for the fixed TCTD current.

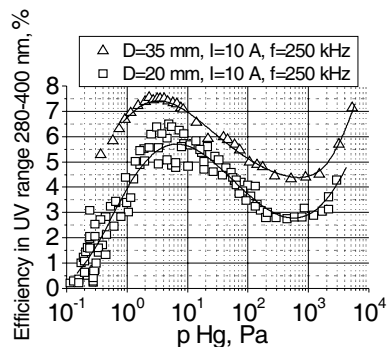


Figure 5: Emission yield to nonresonance lines of the UV-range 280–400 nm versus mercury vapour pressure for the fixed TCTD current.

The dependence of the emission yield to resonance line of 253.7 nm on the tube wall temperature is shown in Fig. 6 ($D = 35 \text{ mm}$). Since the maximal radiation yield to resonance line 253.7 nm can be obtained in a very narrow temperature range (30–50 °C), a series of experiments was carried out using a three-component mercury amalgam of the following composition: 90%In–5%Ag–5%Hg.

As seen from the Fig. 6, using mercury amalgam, the maximum of resonance radiation yield moves to the area of the higher temperatures (>70 °C), and the temperature range corresponding to the maximal efficiency of resonance line 253.7 nm becomes significantly wider (70–120 °C).

On the basis of experimental studies of the TCTD with amalgam filling, the pilot samples of bactericidal induction UV lamps with the power of 50, 100, 200 (Fig. 7), and 500 W and the frequency of current $f = 150 \text{ kHz}$ were constructed; their emission yield to line 253.7 nm is ~30–35% of consumed electric power. Also, the middle pressure induction lamp with a power of 3 kW, light efficiency of 65 lm/W and emission yield in the range 250–400 nm of ~14% of consumed electric power was constructed.

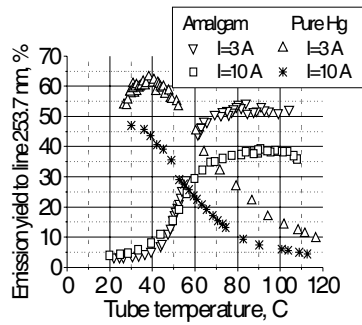


Figure 6: Emission yield to line 253.7 nm versus wall temperature for the fixed current of TCTD (amalgam and pure mercury filling).



Figure 7: Pilot samples of electrodeless amalgam UV lamps with the power of 100, 200 and 50 W (from the left to the right).

4. EXPERIMENTAL RESULTS: TCTD IN NEON

Electro-physical characteristics of TCTD in neon are shown in Fig. 8; dependence of the light efficiency of TCTD (lm/W) on neon pressure is shown in Fig. 9; dependence of the light efficiency on current is shown in Fig. 10. Characteristics of the DC arc discharges [9] and characteristics of TCTD in neon at current frequency of 450 kHz [10] are shown for comparison. According to Figs. 8, 9 and 10, dependencies of electric field strength and light efficiency on discharge parameters (p, D, I), observed for TCTD in neon, qualitatively coincide with similar dependencies, obtained for the positive column of a gas discharge in neon.

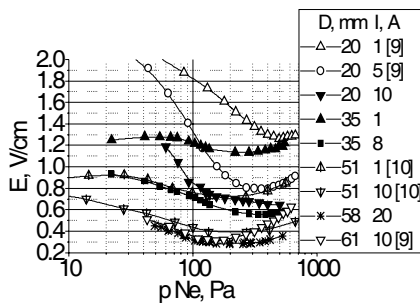


Figure 8: Dependence $E(p)$ at the fixed discharge current.

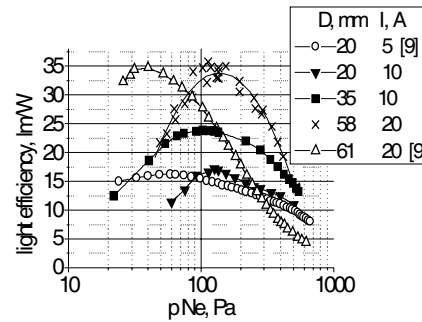


Figure 9: Dependence of TCTD light efficiency on neon pressure.

Radial distributions of brightness $F_{\lambda}(x)$ of different neon lines, measured within bulb cross-section $A - B$ are shown in Fig. 11 in the normalised form (Fig. 1, point $x = 0$ is in the middle line of torus, axis x is directed “inwards” torus, $x = 1$ corresponds to point B , $x = -1$ corresponds to point A). Radial distributions of line brightness $2p^53p - 2p^53s$ and $2p^54d - 2p^53p$ of radiate transitions were studied.

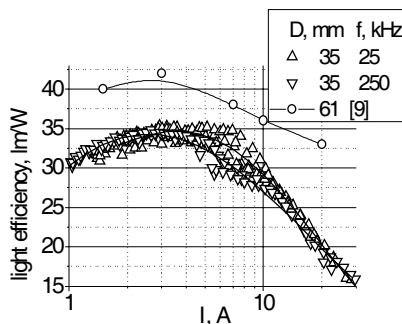


Figure 10: Dependence of TCTD light efficiency on discharge current.

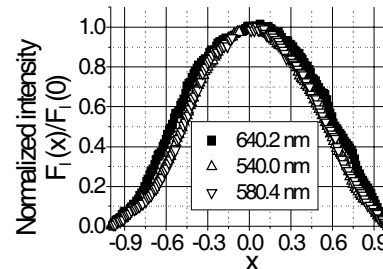


Figure 11: Radial distributions of spectral line brightness for neon. $p = 1$ Torr, $D = 35$ mm, $J = 1$ A/cm², $L/D = 11$.

According to Fig. 11, the studied radial distributions are asymmetric. The main reason, providing an increased energy release in the inner zones of the toroidal gas-discharge bulb, is a change in the value of longitudinal electric field $E(x)$ with a change in coordinate x . Thus, it follows from Equation (1) for the toroidal shape of discharge that $E(x) = E/(1 - \pi xD/L)$, where E is the strength of electric field in the discharge axis.

The absolute intensities of spectral lines were determined under the same conditions of discharge glow in different discharge zones, what allowed us to calculate population of excited levels in plasma of TCTD. Calculation results (normalised on statweights g_k of corresponding excited states k) are shown in Fig. 12. Analysis of data shown in Fig. 12 demonstrates that the filling character of $2p^53p$ and $2p^54d$, $5s$ of excited state at transition from the central to peripheral zones of the induction discharge does not change qualitatively, only quantitative changes are observed. This proves the fact that the electron temperature both in the central and peripheral zones is the same.

As a result of experimental research we have developed and constructed the pilot samples of neon induction lamps with the power of 100–500 W and light efficiency of ~ 30 –35 lm/W (Fig. 13).

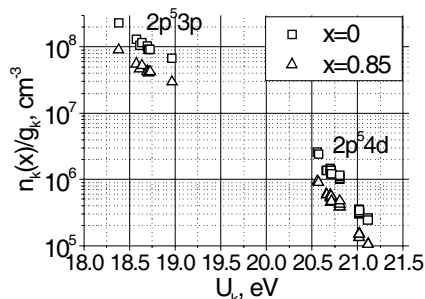


Figure 12: Dependence of normalised concentration of excited atoms of neon $n_k(x)/g_k$ on excitation potential U_k .



Figure 13: Induction neon lamp with the power of 500 W.

5. DISCUSSION

First of all, it is necessary to emphasise the fact that in contrast to RF induction discharges, the TCTD can be considered as the analogue of an arc discharge with electrodes, combined in one plane [11]. Therefore, it is interesting to apply the standard models of arc discharges for the description of the TCTD. However, it should be noted that the most standard models of arc discharges are developed for description of dc discharges in the long cylindrical tubes. Nevertheless, it can be assumed that for some cases, the standard models of axisymmetric DC arc discharges will satisfactorily describe the TCTD characteristics. Let us consider the main conditions, when the TCTD can be described by the standard models:

- A small curvature radius of the toroidal gas-discharge chamber. Apparently, in this case deviations from cylindrical symmetry in a discharge are minimal.
- Fulfilment of condition $f \cdot \tau > 1$, where f is the current frequency and τ is the typical time of plasma ‘damping’. In this case, the parameters of discharge plasma do not change during discharge current passing through zero, and the TCTD can be considered and used as the analogue of a dc discharge.
- An absence of the skin-effect on the electrical characteristics of a discharge.

The authors of the current paper consider the possibility of using the standard ‘channel’ model of axisymmetric dc arc discharges [7, 8], based on an assumption of the LTE presence in discharge plasma, for the calculation of the TCTD parameters in mercury vapour. According to this model, electric field strength E in a mercury discharge is determined by expressions

$$E \approx \frac{C_1 p^{7/12} P^{1/2}}{(P - P_T)^{1/3} D^{1/3}}, \quad \text{or} \quad E \approx \frac{C_2 m^{7/12} P^{1/2}}{(P - P_T)^{1/3} D^{3/2}} \quad (3)$$

where C_1 , C_2 are constants, P_T is the value of specific heat losses of discharge, P is specific discharge power, m is a specific amount of evaporated mercury and D is the tube diameter.

According to formula (3), field strength E for a fixed pressure of mercury vapour depends on the tube diameter as $E \sim D^{-1/3}$. The analysis of data in Fig. 2 demonstrates that an increase in the tube diameter from 35 to 75 mm really provides a reduction of the field strength by a factor of 1.3, whereas for the TCTD with a tube diameter of 20 mm, the experiment gives too high a value of the field strength. However, it should be noted that in this experiment the ratio of perimeter and diameter L/D for the toroidal chamber was ~ 10 , whereas, for the lamps with the tube diameter of 35–75 mm, the parameter L/D varied from 15 to 25. It can be assumed that for $L/D \sim 10$, the condition of axial symmetry is disturbed considerably, thereof and the standard models of axisymmetric gas discharges cannot be applied for this situation. Indirectly, this assumption is proved by “distortion” of radial distributions of spectral line brightness, observed for TCTD in neon at $L/D = 11$ (Fig. 11).

As seen from Fig. 3, for the TCTD with chamber diameter of 35–75 mm and fixed discharge power $P \approx 40$ W/cm, product $E \cdot D^{3/2}$ can be perfectly described by formula (3) with constants, obtained by Elenbaas by the analysis of characteristics of the arc axisymmetric mercury discharges. Therefore, for the pressures of mercury vapour above 10 kPa and ratio $L/D > 15$, the TCTD in mercury vapour can be approximately considered as the axisymmetric, and the ‘channel’ model of axisymmetric discharges can be used for calculation and analysis of discharge parameters.

6. CONCLUSIONS

1. The processes in a TCTD with mercury vapour, and in a TCTD with neon were studied in a wide range of plasma conditions. It was found out that electric and emissive functions of pressure and current are qualitatively similar to the functions of DC arc discharge.
2. It is shown that for the pressure of mercury vapour above 10 kPa and ratio $L/D > 15$, the electrical characteristics of TCTD can be approximately calculated by the standard “channel” model of the DC arc discharges.
3. Basing on the obtained experimental results, we have developed and created the pilot samples of electrodeless lamps: mercury induction middle-pressure lamp with the emission yield of 65 lm/W, and power of 3 kW; germicide UV induction lamps of a low pressure with power of 50, 100, 200 and 500 W, and emission yield to the resonant line 253.7 nm at the level of ~ 30 –35% of consumed power; neon induction lamps with the power of 100–500 W and light efficiency ~ 30 –35 Lm/W.

REFERENCES

1. Eckert, H. U., “Induction plasmas at low frequencies,” *AIAA J.*, Vol. 9, 1452–1456, 1971.
2. Kogan, V. A. and I. M. Ulanov, “Investigation of the prospect for the design of transformer-type plasmotrons,” *High Temperature*, Vol. 31, No. 1, 129–135, 1993.
3. Shabalin, A., “High-pressure operation of a toroidal, inductively coupled discharge,” *Plasma Sources Sci. Technol.*, Vol. 13, No. 4, 588–593, 2004.
4. Anderson, J. M., “Electrodeless fluorescent lamps excited by solenoidal electric fields,” *Illuminating Engineering*, Vol. 64, No. 4, 236, 1969.
5. Curry, J. J., G. G. Lister, and J. E. Lawler, “Experimental and numerical study of a low-pressure Hg-Ar discharge at high current densities,” *J. Phys. D: Appl. Phys.*, Vol. 35, 2945–2953, 2002.
6. Klarfeld, B. N., “Measurements of power, consumed on the walls of the positive column,” *Zhurnal Tekhnicheskoy Fiziki*, Vol. 7, No. 10, 1017–1038, 1937 (in Russian).
7. Elenbaas, W., *The High Pressure Mercury Vapour Discharge*, North-Holland Publ. Comp., Amsterdam, 1951.
8. Rokhlin, G. N., *Discharge Light Sources*, Energoatomizdat, Moscow, 1991 (in Russian).
9. Klarfeld, B. N. and I. M. Taraskov, “Economy of glowing and gradient of potential in the positive column of discharge in neon,” *Technical Physics*, Vol. 4, No. 3, 504, 1934 (in Russian).
10. Piejak, R., V. Godyak, and B. Alexandrovich, “Electric field in inductively coupled gas discharges,” *J. Appl. Phys.*, Vol. 89, No. 7, 3590–3593, 2001.
11. Kulumbaev, E. B. and V. M. Lelevkin, “Calculation of the characteristics of an induction toroidal discharge of transformer type,” *High Temperature*, Vol. 37, No. 2, 187–193, 1999.

Particle-in-cell Simulation of a Novel High Power Terahertz Vacuum Electron Device

Hai Zhang¹, Jianguo Wang^{1,2}, and Changjiang Tong²

¹School of Electronics and Information Engineering, Xi'an Jiaotong University, Xi'an 710049, China

²Northwest Institute of Nuclear Technology, Xi'an 710024, China

Abstract— New micromachining techniques now provide the technology to fabricate the vacuum electron devices with dimensions suitable for operation in the terahertz region of the electromagnetic spectrum. In this paper, results of theoretical and numerical simulation studies of a MW-class, large diameter terahertz backward wave oscillator are presented. The device consists of a large cross-section (overmoded), slow wave structure with a unique profile of wall radius specifically designed to support surface wave and to provide a strong beam-wave coupling at moderate voltage. A novel full electromagnetic Particle-in-cell simulation tool UNIPIC is also developed. With this method, we investigated the characteristics of the device at the frequency of 0.14 THz. It is found that the steady-state, single-frequency operation in this overmoded situation could be realized by the property of surface wave at “ π ” point. And the comparison of computational results between UNIPIC and KARAT demonstrates that UNIPIC is a reliable and promising software for the design of high power terahertz vacuum electron devices.

1. INTRODUCTION

“Terahertz (THz) fields” is a generic term for the electromagnetic waves within frequencies between 0.1 and 10 THz [1]. A wide variety of scientific and commercial applications, such as imaging of biological tissue, spectroscopic identification of complex molecules, broad-band communications, which rely on the physical properties of terahertz waves are currently under investigation [2]. These systems all require THz frequency power sources which, ideally, are compact and inexpensive. Recent advances in micromachining technologies suggested that it was a “natural” route to fabricate small structures, such as cavities, waveguides, and slow wave structures (SWS) that might be used in a scaled-down vacuum electron tube operating at THz frequencies.

In order to achieve and optimize the performance of these THz vacuum electron devices (VEDs), apart from a detailed understanding of its operating principle, it is also necessary to develop accurate simulation tools where the main peculiarities derived from operating conditions and the device dimensions are taken into account. Although there are many available codes devoted to the simulation of VEDs, they are limited in their application to terahertz frequency devices. Therefore, we have recently developed a Particle-in-Cell (PIC) simulation software UNIPIC, which is based on the Monte-Carlo algorithm and is specifically designed for the analysis and optimization of micromachined VEDs. In this paper, a 140 GHz MW-Class backward wave oscillator (BWO, one of the most important and promising devices of THz VEDs) was designed and investigated using this software, and the simulation results were compared with that of KARAT (a traditional, famous PIC code in HPM field) under the same operating conditions.

2. PHYSICAL CONSIDERATIONS

2.1. Operation Principle of THz BWO

The BWO consists essentially of an electron beam confined radially by a strong longitudinal magnetic field and propagating axially through a cylindrical resonant cavity containing SWS, which provides a set of electromagnetic wave modes with phase velocities parallel to the beam less than the speed of light. These slow waves interact resonantly with the slower space-charge wave supported by the beam, which leads to an instability that transfers energy from the beam to the electromagnetic field. It is characterized by the fact that the SWS mode involved in the resonance has a negative group velocity; accordingly, the wave energy transfer is backward along the beam, with a Poynting vector antiparallel to the beam velocity. The structural configuration of BWO system is shown in Fig. 1, and a spatially periodic structure with the rectangular profile was employed as the SWS in BWO, because it can supply both slow waves and strong coupling, and even can provide the fabrication convenience in the millimeter range.

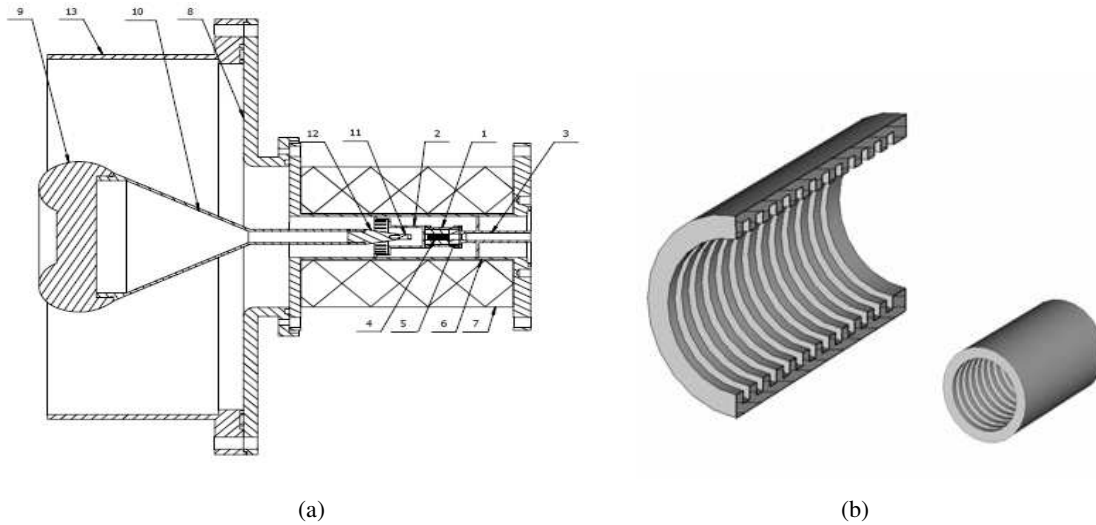


Figure 1: (a) Physical configuration of BWO, where parts 1 to 3 represent the outer-shell related components; part 4 is the kernel of BWO, rectangular SWS; parts 5 is the drift tube; parts 6 and 7 denote the focusing magnetic system; parts 8 to 12 constitute the foilless diode system of electron source; and part 13 is connected to the S-5N electron accelerator. (b) Model of SWS with rectangular rippled wall.

2.2. Characteristics of the SWS

For a TM_{01} mode propagating in the SWS, an approximate relation [3] between the maximum power P_{\max} and the maximum strength of electric field allowable at the wall, E_{\max} , can be given by

$$P_{\max} = 8.707 \left(\frac{E_{\max} \cdot \lambda}{511} \right)^2 \frac{\pi^2}{2} \sigma'^4 \sqrt{1 - \left(\frac{v_{0,1}}{2\pi D'} \right)^2} \frac{1}{v_{0,1}^2} \quad (1)$$

where, $D' = \pi D/\lambda$, D is the transverse diameter, λ is the free-space wavelength, and $v_{0,1}$ is the first root of the zero-order Bessel function. From Eq. (1), we can find that the output power P_{\max} is dramatically increased with the enlargement of D . If $D/\lambda \geq 1.76$, the SWS is referred to as an overmoded SWS.

In this paper, the transverse diameter of SWS is designed to be several times of the free-space wavelength λ ($D/\lambda \cong 3$) thereby reducing the internal field stress for the same power flow, and in other words, it can efficiently increase the power-handling capacities of the high power THz devices. However, in this overmoded device there might simultaneously exist multiple eigenmodes for the same operating frequency, which could lead to the modes competition and the resulting power decay.

One useful approach to solve this problem is to shift the operating point close to the upper edge of pass band (π point) because of the following two reasons. First, in this region, the Q factor is relatively large due to both large reflection and small group velocity, which can efficiently decrease the starting current for oscillation. Secondly, operating in the near π mode, the device could behave as a pure surface wave generator, where only the lowest mode (TM_{01}) is excited on benefit of the relatively large coupling impedance (or high efficient beam-wave interaction) compared with that of other volumetric wave modes. Fig. 2 shows the dispersion curves of three main competitive modes as well as the electron Doppler line corresponding to 550 keV beam energy near the π point. The values of structural parameters of SWS in the calculation were set as follows. Inner radius of cylindrical waveguide equals 3.0 mm; depth of each slot is equal to 0.2 mm; length of each spatial period equals 0.9 mm. It can be seen that the operating frequency (point of intersection) approximately equals 0.145 THz under this condition, and according to the further calculation from the diagram, we found that the voltage range from 450 kV to 610 kV was necessary to excite the oscillations with frequencies above 0.14 THz.

3. SIMULATION TOOL

3.1. General Characteristics of UNIPIC

UNIPIC is a novel simulation programme that can be configured at run time by selecting appropriate geometry, material properties, boundary conditions, field algorithms, particle algorithms, and output specifications. Default configurations provide good accuracy in reasonable time for the novice who does not wish to or may not know how to specify some aspects of an electromagnetic PIC simulation. The basic electromagnetic computational processing cycle is shown in Fig. 3.

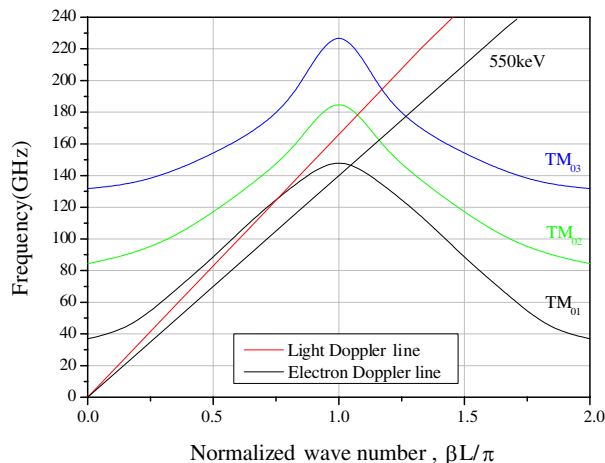


Figure 2: Dispersion diagrams of three competitive modes.

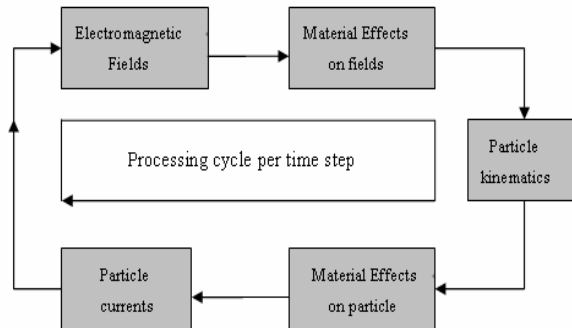


Figure 3: Computational flow chart of UNIPIC.

The fields in Maxwell's equations are represented on a finite-difference grid. From an alternative, engineering viewpoint, the grid creates a circuit element at each location in space, which is coupled to elements at neighboring locations. UNIPIC can use a variety of field algorithms with a range of speed, stability, and numerical smoothness; when advantageous, it employs the engineering viewpoint to provide special models that treat material properties and complex, fine-structure geometric details.

Particles are represented using the PIC approach, in which a computational particle (referred to as a macro particle) represents a large number of physical particles of the same species (e.g., electrons). A variety of algorithms for emission processes, particle kinematics, and current density allocation are available, all based upon the same mathematical foundation, but each individually optimized for different density, velocity, and field strength regimes.

Material models provide accurate treatment of the complexities of real systems and can include both field and particle effects. Some quantum effects are modeled using phenomenological models. Material models are designed to be compatible with all field and particle algorithm combinations.

3.2. Volume-weighting Cloud-in-cell Technique of UNIPIC

Early PIC methods along with a zero-order weighting model usually produced high noises, when a particle was passing through a cell boundary. Birdsall introduced an area-weighting cloud-in-cell (AW-CIC) model, which gives a first order accuracy in a Cartesian coordinate system to reduce the noise to an acceptable range. In 2.5D simulations of Cartesian coordinate system, the AW-CIC model works very well. However, since most of the vacuum electron tubes are in axially symmetric shapes, like the BWO we discussed in this paper, 2.5D simulations of these devices have to be done in the z - r axially symmetric plane of cylindrical system, where the accuracy of AW-CIC decreases, especially on the points near the axis.

Therefore, a volume-weighting cloud-in-cell (VW-CIC) model was developed to implement particle simulation in a cylindrical system. The main highlight of this algorithm is that both the charge assignment on the four adjacent points and the current determination along cell edges can be calculated by the volume-weighting method, which can give a second order accuracy superior to that of area-weighting algorithm. The VW-CIC model is incorporated in the UNIPIC code and the more details were discussed in another contribution [4].

4. PARTICLE-IN-CELL SIMULATION AND RESULT ANALYSIS

The simulation is performed by using the full electromagnetic PIC software UNIPIC. The simulation model is shown in Fig. 4, where proper boundary conditions were set as follows. The rectangular rippled-wall waveguide is perfect conductor, and the z axis performs as the azimuthally symmetric axis. The electromagnetic wave at the right end of the structure was truncated by using the convolutional perfectly matched layer [5]. As the initial condition for the simulation, there were no electromagnetic fields in the BWO, and the electron beam was just incident at the left-end side of the structure. The values of the structural parameters were set as mentioned above, and 20 periods were used in the simulation.

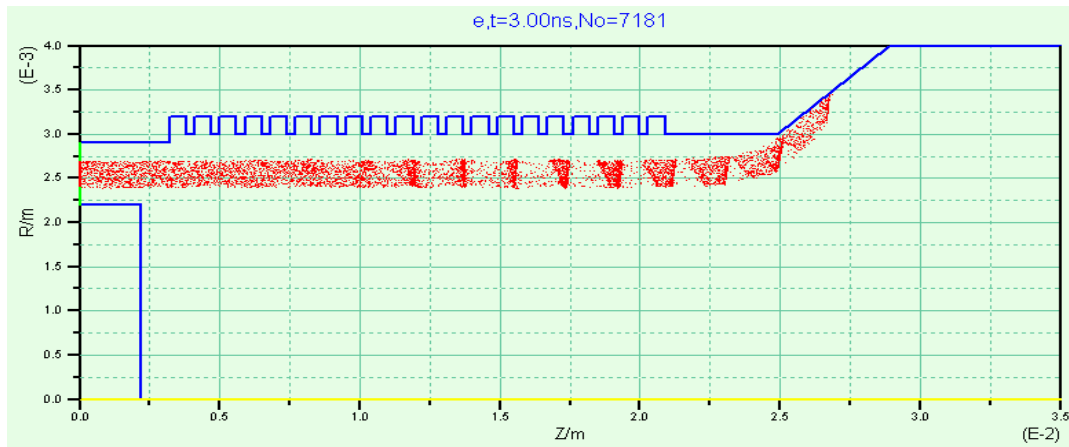


Figure 4: Simulation model of BWO.

Under the condition of 500 kV beam voltage, 1 kA beam current and 4 T axial guiding magnetic field, the oscillator began to work. The behavior of electron bunching in the device can also be observed in Fig. 4. This phenomenon can be understood as follows. As the uniform electron beam propagates through the tube, it reacts with the electromagnetic wave sequentially. Due to the different phase effect, some of the electrons are accelerated by the field while other electrons are decelerated till the bunching is formed. However, the average effect of this motion is that the beam is totally decelerated and gives out its kinetic energy to the field. This is because the center of each bunching is appropriately kept in the negative phase of wave all long time during the operation although it slowly moves toward the positive phase. Therefore, the electromagnetic wave is excited and the useful output power is generated.

Figure 5 shows the temporal behavior of the magnetic field component at a certain point in the BWO as well as the corresponding Fourier transform of this signal. We can find that the signal began to grow up at about 0.7 ns, and became saturated at 1.5 ns. After this time, the device operated in a steady state at the frequency of about 0.143 THz.

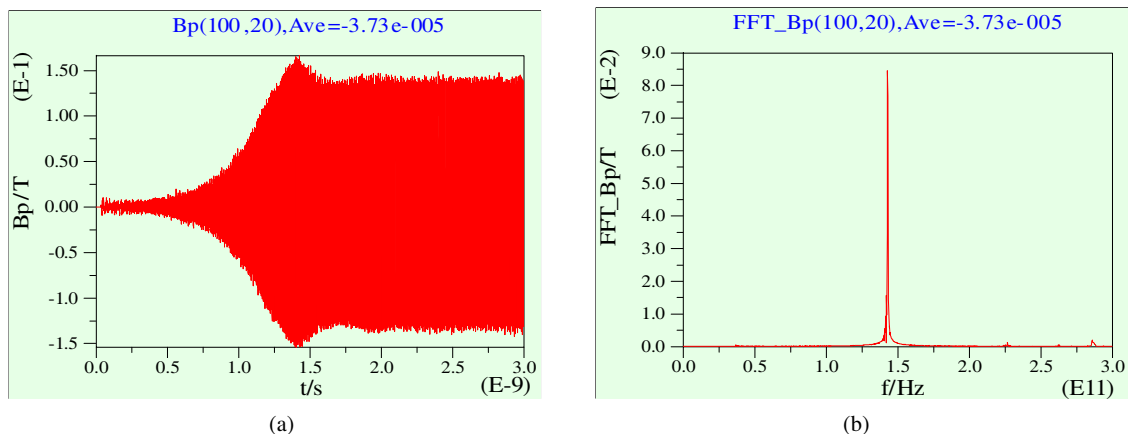


Figure 5: (a) Time plot of the generated THz signal, (b) spectrum of the generated signal.

The 3D distribution pattern of the electric field as well as the magnetic field in the device at 3.0 ns are demonstrated in Fig. 6. It can be seen that both fields have its maximal value on the surface of SWS ($R = 3.0$ mm), and gradually declines along the radial direction. This characteristic proves that the device well operated in the TM_{01} mode and possessed the special property of surface wave.

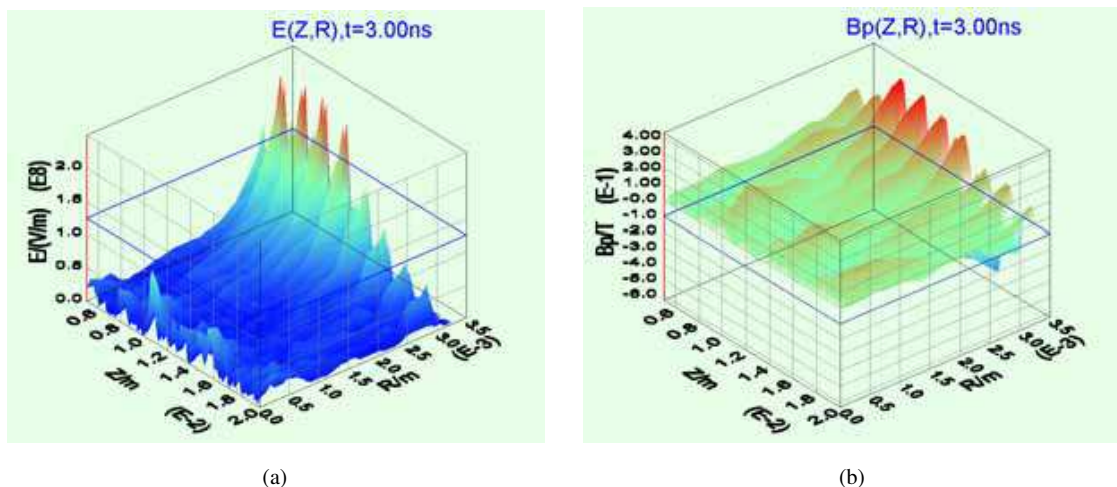


Figure 6: (a) Electrical field distribution in the device, (b) Magnetic field distribution in the device.

The influence of period number (corresponding to the total length of SWS) on output power, for two different voltages, 500 kV and 600 kV, is shown in Fig. 7. For each voltage, simulations were respectively performed using two different programs, UNIPIC and KARAT, in order to compare the computational results from each program. With the same method, the effect of external applied magnetic field on the device behavior is illustrated in Fig. 8. It can be seen that the simulation results of UNIPIC agreed very well with that of KARAT, which is a famous, reliable PIC simulation software. Thus, we can conclude that the UNIPIC has the same computation precision as KARAT, and it can be helpful and reliable in the design of high power terahertz electron devices.

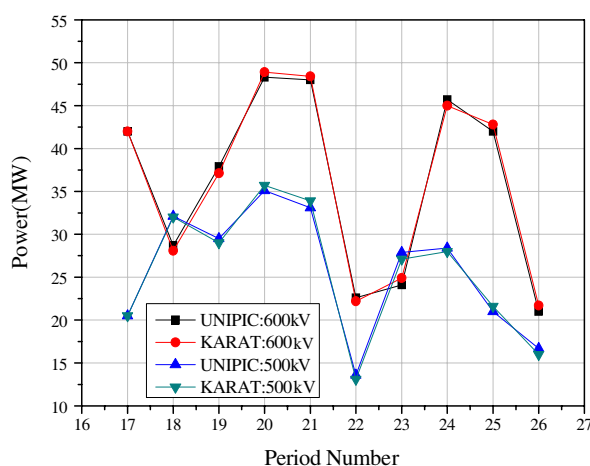


Figure 7: Dependence of output power on number of periods.

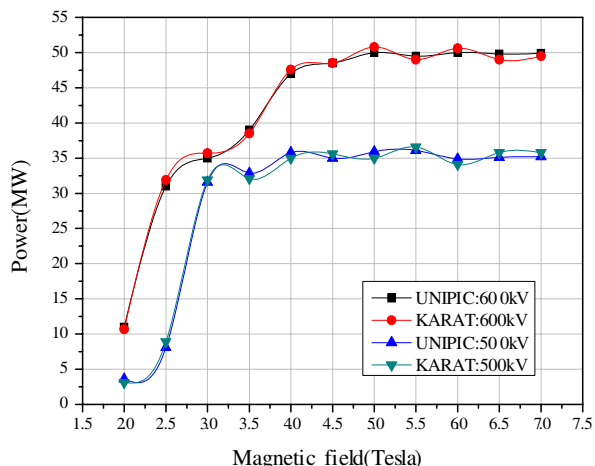


Figure 8: Dependence of output power on guiding magnetic field.

5. CONCLUSION

In this paper, we presented the theoretical analysis and numerical simulation results of an overmoded, MW-class terahertz backward wave oscillator. It was found that an overmoded interaction BWO must support surface waves that are synchronous with the electron beam, and simultaneously exhibit large values of the coupling impedance. The characteristics of surface wave and “ π ” point operation are crucial to avoid mode competition. Furthermore, a novel full electromagnetic

PIC software UNIPIC is developed, and the comparison of simulation results between UNIPIC and KARAT proves that UNIPIC is a reliable, practical and promising software which must ease the complicated design process of high power terahertz electron devices in future.

REFERENCES

1. Dragoman, D. and M. Dragoman, “Terahertz fields and applications,” *Progress in Quantum Electronics*, Vol. 28, No. 1, 1–66, 2004.
2. *IEEE Trans. Microwave Theory Tech.*, (Special Issue), Vol. 48, Apr. 2000.
3. Vlasov, A. N., A. G. Shkvaruntes, J. C. Rodgers, et al., “Overmoded GW-class surface-wave microwave oscillator,” *IEEE Trans. on Plasma. Sci.*, Vol. 28, No. 3, 550–560, 2000.
4. Li, Y. D., F. He, and C. L. Liu, “A volume-weighting cloud-in-cell model for particle simulation of axial symmetric plasma,” *Plasma Science & Technology*, Vol. 7, No. 1, 2653–2655, 2005.
5. Wang, J. G., Y. Wang, and D. H. Zhang, “Truncation of open boundaries of cylindrical waveguides in 2.5-Dimensional problems by using the convolutional perfectly matched layer,” *IEEE Trans. on Plasma. Sci.*, Vol. 34, No. 3, 681–690, 2006.

Bow-tie Wideband Antenna Design for CW THz Photonic Transmitters

J. Zbitou¹, C. Minot^{1,2}, X. Begaud¹, and B. Huyart¹

¹Institut TELECOM, TELECOM ParisTech, LTCI CNRS, 46 rue Barrault, Paris 75013, France

²CNRS-LPN, Route de Nozay, Marcoussis 91460, France

Abstract— The paper presents the design of bow-tie wideband antennas for Continuous Wave terahertz photonic transmitters and their applications. We have optimized two different structures based on the bow-tie antenna concept in coplanar waveguide configuration, suitable for easy integration into a monolithic THz photonic transmitter on GaAs substrate. We have taken into account the impedance characteristics of the photodetector, inserted in series with the antenna as an optically controlled THz generator, as well as strong constraints on isolation from the photodetector DC bias circuit.

1. INTRODUCTION

The terahertz technology attracts more scientists due to the fast growing interest in this spectral region. Thanks to their unique properties, THz waves can penetrate a large number of nonconducting objects and materials. That is why they are attractive for biomedical imaging, packaged goods inspection or security applications, and also because of their remote sensing and spectroscopic capabilities [1,2]. In the recent years, we can find in the literature some new techniques which are being developed and used to generate both Continuous Wave (CW) and pulsed emissions of radiation at THz frequencies [3–5]. In order to generate an extremely high-frequency signal from a photodetector (PD), monolithic integration of the PD with a miniaturized antenna is a promising approach but requires careful and adequate design of the device. In particular, the losses and reflections at electrical transmission line discontinuities must be eliminated or at least strongly minimized [6]. The key point is to achieve good impedance matching between the PD and the antenna. In addition, as the PD must be DC biased, it is essential that the THz circuit be highly isolated from the DC circuit so that the THz power is fully supplied to the antenna. In our study we have used a bow-tie wideband antenna as presented in Fig. 1, and matching and isolation goals must be met over a wide frequency range.

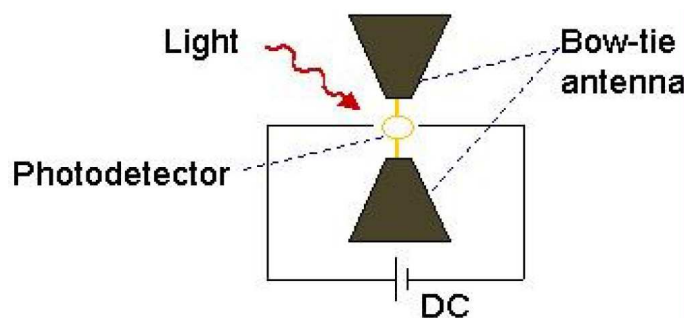


Figure 1: Schematic drawing of the THz photonic transmitter source.

By improving the design of the antenna and the coupling circuit between antenna and photodetector, we demonstrate here two novel coplanar waveguide (CPW) bow-tie antenna structures, suitable for integration into a terahertz photonic transmitter in the range 0.4–2 THz that is composed of an edge-coupled metal-semiconductor-metal traveling-wave photodetector (MSM TPD) and a CPW line in addition to the antenna.

2. BOW-TIE WIDEBAND ANTENNA DESIGN

The MSM-TPD can be an ultrafast photodetector and its wide bandwidth can be fully exploited using the beating frequency between two monochromatic lasers as a light source, provided at least one source is tunable. As a result it is interesting to consider use of wideband antennas as couplers

of THz waves to free space. Fig. 2 shows the layer stack of the MSM-TPD [7]. Thanks to the optical index profile, the impinging light is guided just below the central metallic strip of a narrow low impedance CPW line, and the THz current is generated between the central strip and the ground plane lateral metallic areas. Use of a CPW line as a feed line to the antenna (see top view in Fig. 3) then results into a quite simple geometry in which the narrow CPW line of the MSM-TPD is progressively tapered into a wider line of identical impedance, more adequate for dimension and loss control over large line lengths.

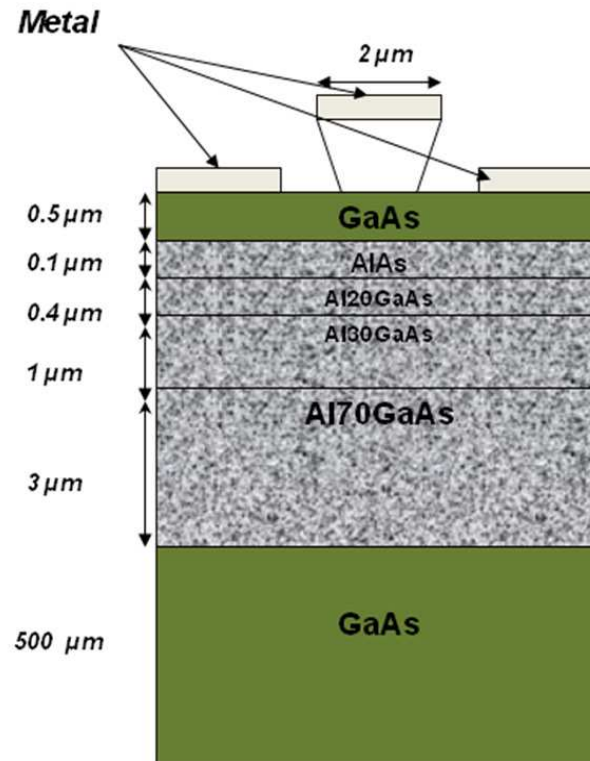


Figure 2: Structure of the photodetector on a 500 μm GaAs substrate.

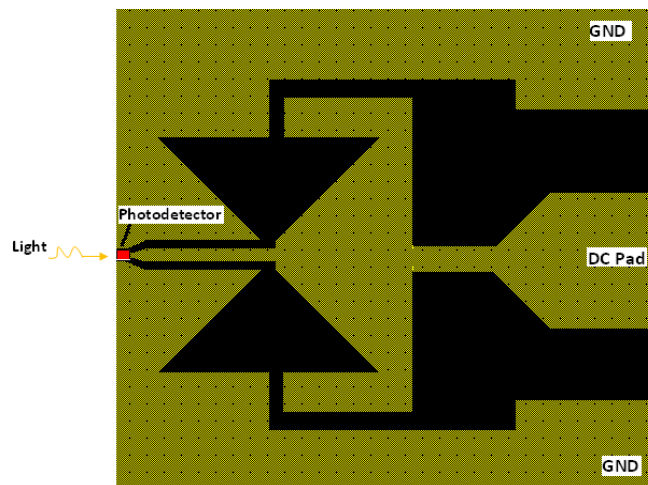


Figure 3: Bow-tie wideband antenna structure with lateral slots.

Another issue carefully taken into account in the design is good isolation between the RF signal generated by the PD and the DC bias used to polarize the PD. This is achieved by two 10 μm wide slots in the metallic plane which delimitates the antenna contour. One side of the antenna is thus connected to the ground plane while the other side is connected to the DC terminal. This bow-tie

slot antenna is a planar version of the well known biconical antenna [8]. Optimization of the whole circuit is done using the electromagnetic ADS/Momentum simulator [9], so as to minimize reflection loss at CPW port 1 ($50\ \Omega$ impedance), i.e., the antenna input port or the output port of the MSM-TPD. Finally, matching of the antenna dimensions and the DC probe pad dimensions raises no difficulty when impedance matching of the bow-tie to the CPW line is good. For operation in a frequency band from 0.4 THz up to 2 THz, the overall surface of the device is then $370 \times 383\ \mu\text{m}^2$.

As a result of optimization the return loss is smaller than $-10\ \text{dB}$ except in a small portion of the considered range where it is only smaller than $-8\ \text{dB}$ (Fig. 4). At the same time good isolation between the DC and RF signals is achieved (see S_{21} in Fig. 5, port 2 is a CPW port at the DC pad), better than $-23\ \text{dB}$.

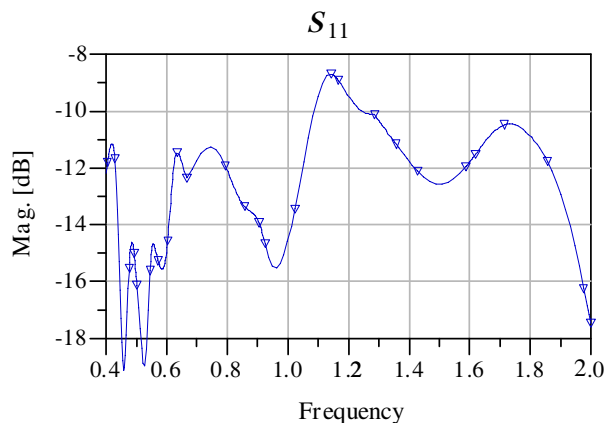


Figure 4: Return losses versus frequency.

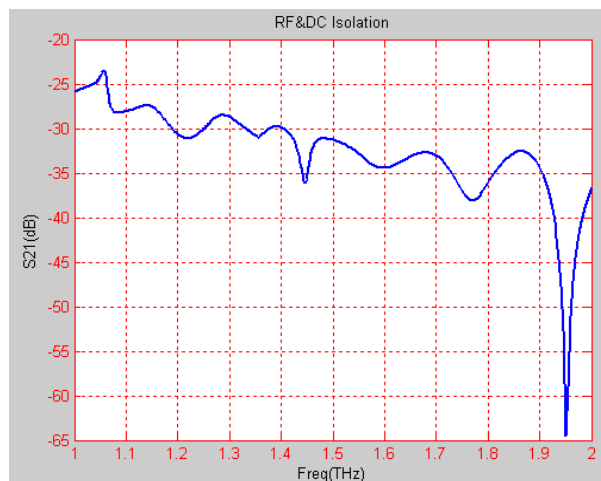


Figure 5: Isolation of THz port from DC port.

3. BOW-TIE ANTENNA INTEGRATED WITH A LOW-PASS PERIODIC FILTER

As the slots on either side of the antenna may add spurious radiation lobes in the above design, we have designed a second structure for a bow-tie antenna achieving good RF-DC isolation through a more conventional filtering approach. It is based on use of a low pass filter which blocks the RF signal and prevents it from reaching the DC line. Also, the filter is made of periodic filtering sub-structures [10], inserted along the CPW line (see repetition unit in Fig. 6). Actually periodic structures exhibit distinctive bandstop characteristics when patterned on the ground plane. They are employed to realize miniature low-pass filters one-tenth the size of conventional filters, with spurious-free response, low insertion loss in the passband and deep attenuation levels using only three cells.

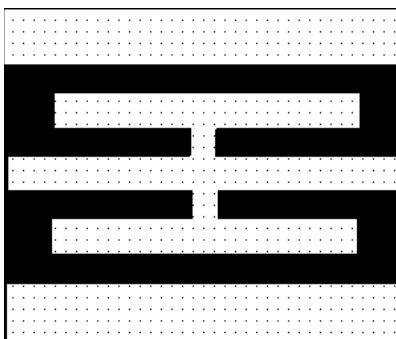


Figure 6: Unit cell of periodic structure CPW low-pass filter.

To design the monolithic THz photonic transmitter, the bow-tie antenna is associated to three cells which we have optimized and simulated using ADS/Momentum software. As shown in Fig. 7, the low pass filter presents a cutoff frequency of 0.45 THz. Deep attenuation levels ($-20\ \text{dB}$) can be observed in the stopband until 1.4 THz.

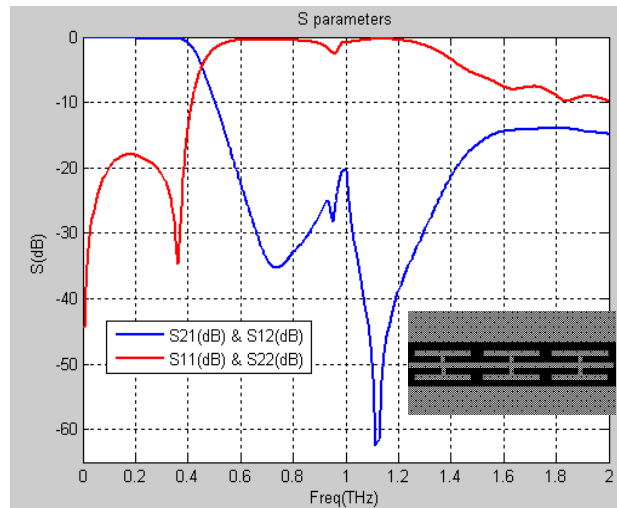


Figure 7: S parameters of periodic structure CPW low-pass filter.

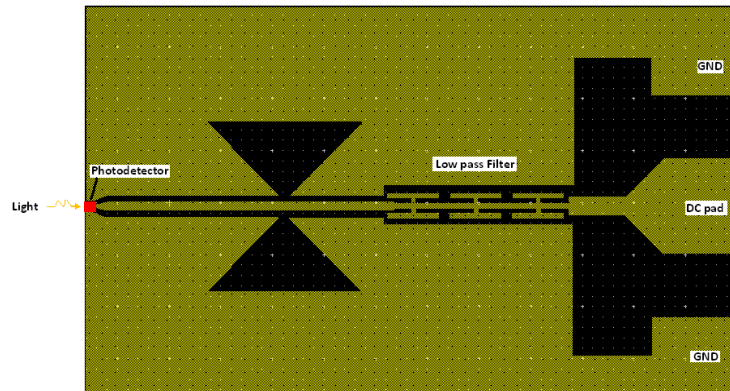


Figure 8: Bow-tie wideband antenna structure with filter.

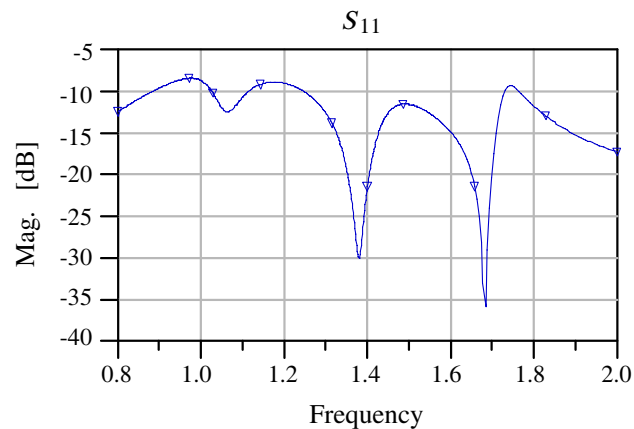


Figure 9: Return losses versus frequency.

Insertion of the low-pass periodic filter behind the bow-tie antenna as presented in Fig. 8 results into overall dimensions of $(635 \times 383) \mu\text{m}^2$. Fig. 9 shows the return loss, smaller than -8 dB and even -10 dB along most of the frequency range up to 2 THz. Good isolation between RF and DC signals, better than -25 dB, prevails over the whole range, slightly better than in the former case.

4. CONCLUSIONS

Compared with other methods to generate THz radiation such as quantum cascade lasers or microwave multipliers, photonic transmitters have the advantages of room temperature operation, broadly tunable THz frequency, and integrability with other optoelectronic devices to become convenient and compact THz sources. In this study, we have designed two CPW wideband bow-tie antenna structures making it possible to realize THz photonic transmitter sources by using one of the two approaches, which are demonstrated owing to the ADS software. These antennas can be integrated into an edge-coupled terahertz photonic transmitter with a metal-semiconductor-metal traveling-wave photodetector (MSM TPD) as the active element, and exhibit ultra-wide frequency tuning range under optical excitation. Processing of such devices has been carried out on low temperature grown GaAs layers (details will be given elsewhere) and characterization in the THz range using two monochromatic lasers is in progress.

REFERENCES

1. Wang, Z., "Generation of terahertz radiation via nonlinear optical methods," *IEEE Transactions on Geoscience and Remote Sensing*, Vol. 1, No. 1, 1–5, Nov. 2001.
2. Gregory, I. S. and C. Baker, "Optimization of photomixers and antennas for continuous-wave terahertz emission," *IEEE Journal of Quantum Electronics*, Vol. 41, No. 5, 717–728, May 2005.
3. Li, Y.-T., J.-W. Shi, and C.-L. Pan, "Sub-THz photonic-transmitters based on separated-transport-recombination photodiodes and a micromachined slot antenna," *IEEE Photonics Technology Letters*, Vol. 19, No. 11, 840–842, Jun. 1, 2007.
4. Malcoci, A. and A. Stohr, "Optical submillimeter-wave generation employing antenna integrated ultra-fast travelling-wave 1.55 μm photodetectors," *IEEE MTT-S*, 143–146, 2003.
5. Ito, H. and T. Furuta, "Photonic generation of continuous THz wave using uni-traveling-carrier photodiode," *Journal of Lightwave Technology*, Vol. 23, No. 12, 4016–4020, Dec. 2005.
6. Duffy, S. M., S. Verghese, K. A. McIntosh, A. Jackson, A. C. Gossard, and S. Matsuura, "Accurate modeling of dual dipole and slot elements used with photomixers for coherent terahertz output power," *IEEE Transactions on Microwave Theory and Techniques*, Vol. 49, No. 6, 1032–1038, Jun. 2001.
7. Shi, J.-W., K.-G. Gan, Y.-J. Chiu, Y.-H. Chen, C.-K. Sun, Y.-J. Yang, and J. E. Bowers, "Metal-semiconductor-metal traveling-wave photodetectors," *IEEE Photonics Technology Letters*, Vol. 13, No. 6, 623–625, Jun. 2001.
8. Stutzman, W. L. and G. A. Thiele, *Antenna Theory and Design*, 2nd edition, 240, Wiley, 1998.
9. Advanced Design System 2006B, Agilent Technologies.
10. Sor, J. and Y. Qian, "Miniature low-loss CPW periodic structures for filter applications," *IEEE Transactions on Microwave Theory and Techniques*, Vol. 49, No. 12, 2336–2341, Dec. 2001.

Accurate Field Distribution Models for RFID Applications Using Hybrid Computational Electromagnetics Techniques

R. A. Abd-Alhameed¹, P. S. Excell¹, C. H. See¹, D. Zhou¹, and K. N. Ramli^{1,2}

¹Mobile and Satellite Communications Research Centre
Bradford University, Bradford, BD7 1DP, UK

²Electrical and Electronic Engineering Faculty
University of Tun Hussein Onn Malaysia (UTHM)
Parit Raja 86400, Batu Pahat Johor, Malaysia

Abstract— An approach to hybridization, linking the Method of Moments, the Finite Difference Time Domain method and sub-gridded FDTD regions is presented. This hybrid method is capable of analysing a system of multiple discrete regions by employing the Principle of Equivalent Sources to excite the coupling surfaces and then using a linear field-interpolation method. The method is developed to suit RFID model analysis for both near- and far-field applications. To develop the approach and test its validity, some examples are given in which the results are shown to compare well with other available data.

1. BACKGROUND AND MOTIVATION

The demand for efficient and accurate field modelling tools for electromagnetic (EM) problems is constantly growing. The various numerical methods can be divided into several categories. One possible division can be made, based on the domain in which the procedure is applied: time domain methods and frequency domain methods.

The applications of these two classes of methods mainly depend on the type of problems to be solved and on the form of the required solution, e.g., impulse response or harmonic solution. It is clear that results can be moved from one domain approach to the other by applying a direct or inverse Fourier transform, applying the proper care to avoid aliasing and to ensure causality. However, there are deeper issues of stability which may also influence the decision on which method to use. A second possible classification for numerical methods is based on the type of formulation used: differential formulation and integral formulation.

Differential formulations are local in nature so that the initial and boundary conditions must be imposed as the algorithm proceeds. They tend to require negligible analytical pre-processing. Integral formulations are global in nature so that initial and boundary conditions are included directly in the algorithm that follows. They often require extensive analytical pre-processing.

At the final stage these two approaches typically lead to systems of equations representing a discretised form of the original problem. Differential formulations lead to large, but sparse, matrices as compared to the very dense but small matrices obtained with integral formulations. Each of the methods in these classes can be said to be specific to certain geometries. In this respect, differential formulations are becoming increasingly popular because of the generality of geometries that can be solved. Generality is intrinsic in the procedure as initial and boundary conditions, geometry and media properties, all enter the method after the basic algorithm has been developed.

This paper focuses on one differential method and one integral method, as shown in Figure 1. The former is the Finite Difference Time Domain (FDTD) method which is a discrete time-domain differential formulation of Maxwell's equations that includes another embedded sub-gridding FDTD method (SGFDTD) to model small complex structures inside a normal FDTD method. The integral method is the 'Method of Moments' (MoM), most widely used in the frequency domain. The objective of this work is to explore subgridding inside the hybrid combinations between these two methods and apply the combined method to different EM scattering applications such as those found in RFID communication systems.

1.1. Hybrid Methods in Computational Electromagnetics

A hybrid approach takes advantage of features offered by several methodologies to increase the efficiency of the problem solving procedure. Hybrid methods are based on a subdivision of the problem into sub-problems to be solved individually. The solution of the sub-problem can then be accomplished with the most suitable method. The sub-solutions interact with each other at their boundaries and thus iterate to a stable solution. Both MoM and FDTD have been hybridised with

but the time-domain MoM is not at the state of maturity and flexibility of the frequency-domain version. Also, there have been some frequency domain MoM and FDTD combination attempts but they employed a unidirectional or explicit coupling [16, 17]. A hybrid time-domain technique that combines the finite element, finite difference and method of moment techniques to solve complex electromagnetic problems was discussed in [18], using the time-domain version of the solution to couple the methods.

A hybrid computational electromagnetics formulation for simulation of antennas coupled to lossy and dielectric volumes was investigated by the present authors [18, 19] in which the coupling of multiple regions was investigated and applied to complex antenna structures: the work was then extended to include a broadband analysis of this hybrid method [20] in which several applications were tackled.

2. STATE OF THE ART AND ORIGINAL CONTRIBUTIONS

The main problem addressed in the present work is the electromagnetic modelling problem involving the coupling of the reader antenna to RFID tag sensor that might be placed on an object having very different electrical properties. It is expected that a hybrid method using frequency domain MoM for modelling the antenna and FDTD for modelling the tag and the objects could have great advantages.

The incident field from the source to the closed surface containing the scattering object is modelled by using a Huygens surface. This excludes the source, i.e., the reader in this case, by replicating the fields incident on the surface (the incident fields on the Huygens surface are represented by the equivalent surface magnetic and electric currents). For each time step, the scatterer fields are obtained and the equivalent surface currents on the Huygens surface are again obtained. An interpolation algorithm is required if the cell mesh size for the source and the object are different. The equivalent surface currents are also used to work back to the source to obtain the induced currents on it. The algorithms are repeated for each time step until a few cycles have passed and the steady state solution is obtained.

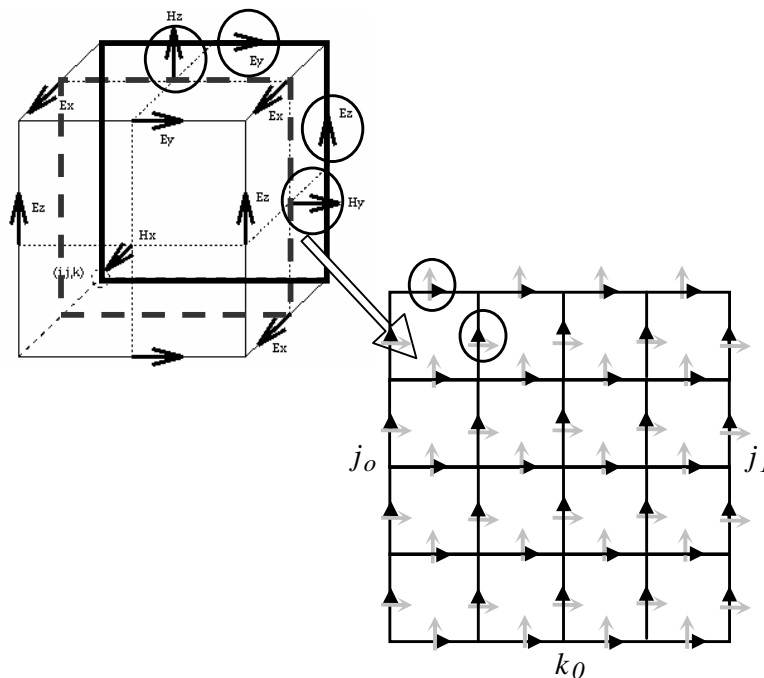


Figure 2: Location of $E_y(\rightarrow)$ and $E_z(\uparrow)$ components in planes $i = i_o$ and $i = i_1$; Location of $H_z(\uparrow)$ and $H_y(\rightarrow)$ components in planes $i = i_o - 1/2$ and $i = i_1 + 1/2$.

The Equivalence Principle surface implementation in FDTD is implemented by the fact that H and E nodes are at different points, a half-cell apart from each other. It follows that this surface can be visualised as two rectangular boxes, the inner box defined by locations where the Huygens electric current sources (tangential magnetic field) are specified, and the magnetic current sources (tangential electric field) on the outer box are to be computed with a special format and applied

to the FDTD updating equations, as follows.

To simplify the large number of equations required, the abbreviated notation used by Taflove in [21] will be adopted. The basic updating equations are here used in the form $\{A\}_{(FDTD)}$ and modified forms for the field component A are then given below by adding appropriate additional terms. Referring to Figure 2, as example, the E_y components at cells referenced ($i = i_o, j = j_o + 1/2, \dots, j_1 - 1/2; k = k_o, \dots, k_1$) are given by:

$$E_{y_{i_o, j, k}}^{n+1} = \left\{ E_{y_{i_o, j, k}}^{n+1} \right\}_{(FDTD)} + C_{b, E_y} \Big|_{i_o, j, k} \cdot H_{z, inc_{i_o-1/2, j, k}}^{n+1/2} \quad (1)$$

E_z components at cells referenced ($i = i_o; j = j_o, \dots, j_1; k = k_o + 1/2, \dots, k_1 - 1/2$):

$$E_{z_{i_o, j, k}}^{n+1} = \left\{ E_{z_{i_o, j, k}}^{n+1} \right\}_{(FDTD)} - C_{b, E_z} \Big|_{i_o, j, k} H_{y, inc_{i_o-1/2, j, k}}^{n+1/2} \quad (2)$$

H_y components at cells referenced ($i = i_o - 1/2; j = j_o, \dots, j_1; k = k_o + 1/2, \dots, k_1 - 1/2$):

$$H_{y_{i_o-1/2, j, k}}^{n+1/2} = \left\{ H_{y_{i_o-1/2, j, k}}^{n+1/2} \right\}_{(FDTD)} - D_{b, H_y} \Big|_{i_o-1/2, j, k} E_{z, inc_{i_o, j, k}}^n \quad (3)$$

H_z components at cells referenced ($i = i_o - 1/2; j = j_o - 1/2, \dots, j_1 + 1/2; k = k_o, \dots, k_1$):

$$H_{z_{i_o-1/2, j, k}}^{n+1/2} = \left\{ H_{z_{i_o-1/2, j, k}}^{n+1/2} \right\}_{(FDTD)} + D_{b, H_z} \Big|_{i_o-1/2, j, k} E_{y, inc_{i_o, j, k}}^n \quad (4)$$

where H_{inc} or E_{inc} are the field points generated from the source at the points that define the Huygens surface. C_b and D_b are constants that define the electrical properties for each cell in the FDTD space given in [20].

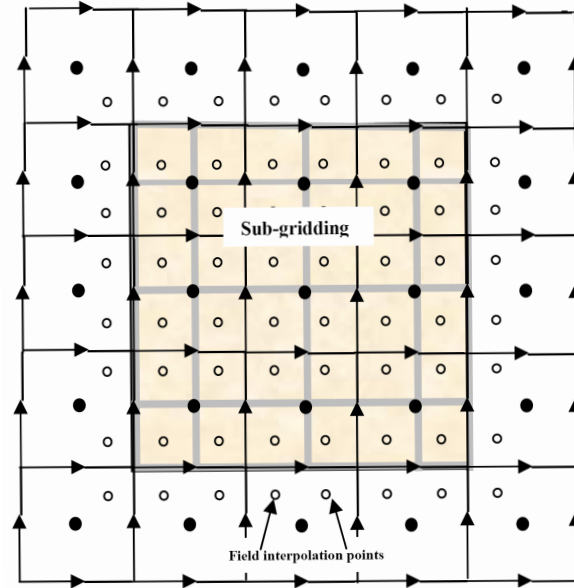


Figure 3: FDTD/SGFDTD configuration that relates the fields points of the FDTD to the SGFDTD grid point.

The above will be done for all other surfaces that describe the Huygens surface. On the other hand the subgridding inside the FDTD will be carried out inside a small volume of the actual FDTD grid as shown in Figure 3. This is of course will contain the tag sensor geometry in which more details can be added, including the loads or a more detailed RF circuit. It should be noted that Figure 3 represents the subgridding scheme used on one of the surfaces that defines the volume under consideration. The excitation fields are derived from normal grid field points using linear interpolation techniques [21]. Each excitation field point was computed from eight field points of the normal FDTD grid that surrounds the excitation point.

3. SIMULATION AND RESULTS

A computer program was written to implement the analysis method given in previous section. The new code was a modified version of the authors' work presented in [20], in which the subgridding technique is included [21]. The following example was chosen to validate the method accuracy.

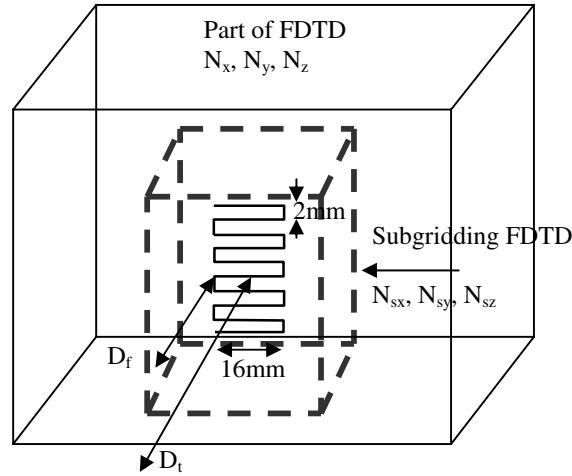


Figure 4: FDTD/SGFDTD basic geometry.

A 900 MHz centre-fed half-wavelength dipole was considered as a transmitter source that represents as example the RFID reader, whereas the RFID tag was considered as a small half-wavelength meander antenna, as shown in Figure 4. Two different distances between the source and the tag were studied and discussed. Two separate simulations were undertaken for each case, one with the far field application and other with near field application as shown in Figure 1. The parameters used are summarized in Table 1. It should be noted that the centres of the source and the sensor (scatterer) were placed on the y axis and they are separated by the distance D_t shown in Figure 4. For both simulations, a thin wire subroutine code inside the subgridded FDTD was used to include the effects of the wire radius of the meander antenna inside the new FDTD subgrid. In this example, for simplicity, the medium surrounding the source and the scatterer was considered as free space; however, the scatterer can be placed on dielectric objects in which part of its volume can be subgridded. A sinusoidal excitation voltage was applied at the centre of the antenna source. The antenna wires were assumed to be perfectly conducting.

Table 1: Input parameters to the hybrid method.

Formulation	Far fields	Near fields
FDTD Problem space	$20 \times 20 \times 30$	$20 \times 40 \times 30$
Hygenc surface	$16 \times 16 \times 26$	$4 \times 4 \times 30$
FDTD volume	$24 \times 24 \times 36$ cm	$24 \times 48 \times 36$ cm
FDTD cell size and time step	12 mm, 16.8 ps	12 mm, 16.8 ps
No, of the FDTD PML cells	8	8
Subgridding cells	$5 \times 5 \times 15$	$5 \times 5 \times 15$
Subgridding FDTD cell size and time step	2 mm, 2.8 ps	2 mm, 2.8 ps
The operating frequency	900 MHz	900 MHz
D_t : distance between the centres of transmitter and the sensor	33 cm	6 cm
D_f : distance between the centre of the sensor to the subgridding FDTD boundary	8 mm	8 mm
The transmitter is a dipole of half wavelength and radius 0.0025 wavelength		

The field distribution over an xz plane 2 cm distant from the sensor (scatterer) for near field and far field techniques is shown in Figures 5 and 6 respectively. The plane size considered here was $20\text{ cm} \times 16\text{ cm}$ for x and z axes respectively. The far field and near field techniques were checked for comparisons of one antenna geometry i.e., D_t was fixed to 6 cm for both techniques, the fields were found identical to the one shown in Figure 5. It should be noted that the resulted field distribution shown in Figure 6 performed by the far field method, uses different distance D_t that was set to 33 cm as shown in Table 1. Both methods show a good stability and the results were convergent within four iterations. However, the total field components was found $\pm 2\%$ when compared to results computed using NEC2 software.

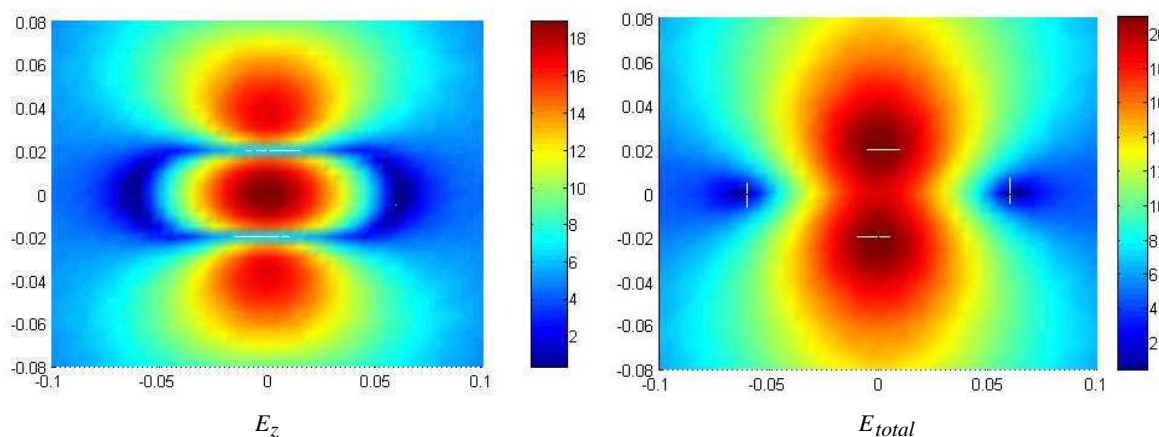


Figure 5: The distribution of the E_z and E_{total} field components in dB at 2 cm away from the sensor, using near field technique.

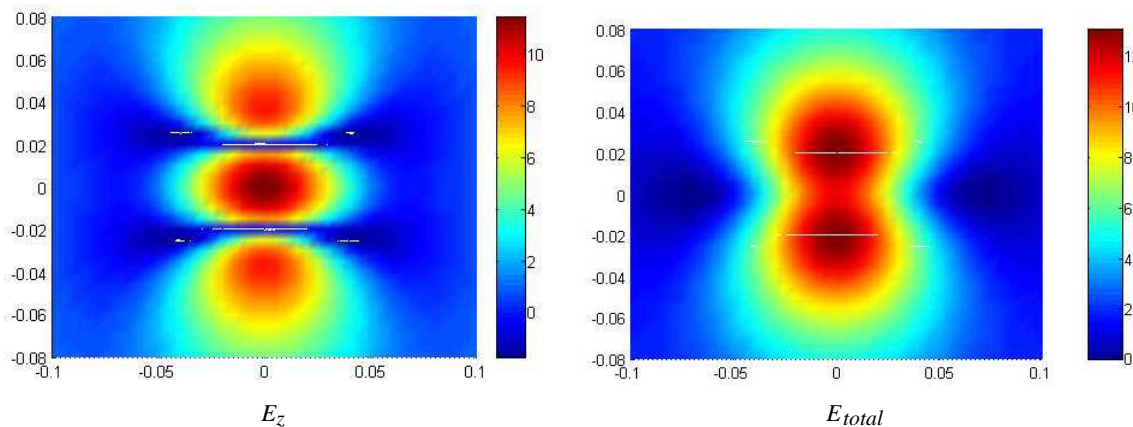


Figure 6: The distribution of the E_z and E_{total} field components in dB at 2 cm away from the sensor using far field technique.

4. CONCLUSIONS

Multiple-region hybrid techniques with frequency-domain Method of Moments, Finite-Difference Time Domain and subgridding were proposed and investigated. The method was validated for far field and near field applications. The present computational electromagnetics technique gave stable and accurate results which are a step towards validation of complex hybrid theory problems such as are found in RFID applications in which the tag sensors are placed or mounted on dielectric or conducting materials.

REFERENCES

1. Kim, J. P., C. W. Lee, and H. Son, "Analysis of corrugated surface wave antenna using hybrid MOM/UTD technique," *Electron. Lett.*, Vol. 35, No. 5, 353–354, 1999.

2. Silvestro, J., “Scattering from slot near conducting wedge using hybrid method of moments/geometrical theory of diffraction: TE case,” *Electron. Lett.*, Vol. 28, No. 11, 1055–1057, 1992.
3. Coffey, E. L. and D. L. Kadlec, “General electromagnetic model for the analysis of complex systems (GEMACS) version 5.0,” Advanced Electromagnetic Corporation for USAF Rome Air Development Center (USA), Report No. RADC-TR-90-360, Volumes I-III, 1990.
4. Jakobus, U. and F. M. Landstorfer, “Improvement of the PO-MoM hybrid method by accounting for effects of perfectly conducting wedges,” *IEEE Trans. Antennas Propagat.*, Vol. 43, No. 10, 1123–1129, 1995.
5. Ali, M. W., T. H. Hubing, and J. L. Drewniak, “A hybrid FEM/MOM technique for electromagnetic scattering and radiation from dielectric objects with attached wires,” *IEEE Trans. Electromag. Compat.*, Vol. 39, No. 4, 304–314, 1997.
6. Reddy, C. J., M. D. Deshpande, C. R. Cockrell, and F. B. Beck, “Radiation characteristics of cavity backed aperture antennas in finite ground plane using the hybrid FEM/MoM technique and geometrical theory of diffraction,” *IEEE Trans. Antennas Propagat.*, Vol. 44, No. 10, 1327–1333, 1996.
7. Kuster, N., Q. Balzano, and J. C. Lin, *Mobile Communication Safety*, first edition, Chapman and Hall, 1997.
8. Coffey, E. L., “Recent enhancements to GEMACS 5.2,” *Ninth Annual Review of Progress in Applied Computational Electromagnetics*, 894–900, Monterey, 1993.
9. Aoyagi, P. H., J.-F. Lee, and R. Mittra, “A hybrid Yee algorithm/scalar-wave equation approach,” *IEEE Trans. Microwave Theory Tech.*, Vol. 41, No. 9, 1593–1600, 1993.
10. Cangellaris, A. C., M. Gribbons, and G. Sohos, “A hybrid spectral/FDTD method for the electromagnetic analysis of guided waves in periodic structures,” *IEEE Microwave Guided Wave Lett.*, Vol. 3, No. 10, 375–377, 1993.
11. Lee, R. and T. T. Chia, “Analysis of electromagnetic scattering from a cavity with a complex termination by means of a hybrid-ray FDTD method,” *IEEE Trans. Antennas Propagat.*, Vol. 41, No. 11, 1560–1569, 1993.
12. Mrozowski, M., “A hybrid PEE-FDTD algorithm for accelerated time domain analysis of electromagnetic waves in shielded structures,” *IEEE Microwave Guided Wave Lett.*, Vol. 4, No. 10, 323–325, 1994.
13. Yang, M., Y. Chen, and R. Mittra, “Hybrid finite-difference/finite-volume time-domain analysis for microwave integrated circuits with curved PEC surfaces using a nonuniform rectangular grid,” *IEEE Trans. Microwave Theory Tech.*, Vol. 48, No. 6, 969–975, 2000.
14. Monorchio, A. and R. Mittra, “Time-domain (FE/FDTD) technique for solving complex electromagnetic problems,” *IEEE Microwave Guided Wave Lett.*, Vol. 8, No. 2, 93–95, 1998.
15. Cerri, G., P. Russo, A. Schiavoni, G. Tribellini, and P. Bielli, “MoM-FDTD hybrid technique for analysing scattering problems,” *Electron. Lett.*, Vol. 34, No. 5, 433–440, 1998.
16. Chen, J., Z. Feng, and J. Jin, “Numerical simulation of SAR and B1-field inhomogeneity of shielded RF coils loaded with human head,” *IEEE Trans. Bio. Eng.*, Vol. 45, No. 5, 650–659, 1998.
17. Forgy, E. A., W. C. Chew, and J. M. Jin, “A hybrid MoM/FDTD technique for studying human head/antenna interactions,” *IEEE Antenna and Propagation Conference*, 81–84, Boston, 1998.
18. Monorchio, A., A. R. Bretones, R. Mittra, G. Manara, and R. G. Martin, “A hybrid time-domain technique that combines the finite element, finite difference and method of moment techniques to solve complex electromagnetic problems,” *IEEE Trans. Antennas and Propagat.*, Vol. 52, No. 10, 2666–2674, Oct. 2004.
19. Abd-Alhameed, R. A., M. A. Mangoud, and P. S. Excell, “A hybrid computational electromagnetic formulation for simulation of antennas coupled to lossy and dielectric volumes,” *IEEE Trans. on Broadcasting*, Vol. 50, No. 3, 253–259, Sept. 2004.
20. Abd-Alhameed, R. A., P. S. Excell, and M. A. Mangoud, “Broadband antenna response using hybrid technique of frequency domain of MoM and FDTD,” *ACES Journal on Computational of Electromagnetics*, Vol. 20, No. 1, 70–77, Mar. 2005.
21. See, C. H., R. A. Abd-Alhameed, R. S. Zadeh, and P. S. Excell, “FDTD subgridding scheme for bioelectromagnetics application,” Commission B, *URSI Symposium*, 11, University of Portsmouth, UK, July 2–3, 2007.

Variational Integrators for Maxwell's Equations with Sources

A. Stern¹, Y. Tong^{1,2}, M. Desbrun¹, and J. E. Marsden¹

¹California Institute of Technology, USA

²Michigan State University, USA

Abstract— In recent years, two important techniques for geometric numerical discretization have been developed. In computational electromagnetics, spatial discretization has been improved by the use of mixed finite elements and discrete differential forms. Simultaneously, the dynamical systems and mechanics communities have developed structure-preserving time integrators, notably variational integrators that are constructed from a Lagrangian action principle. Here, we discuss how to combine these two frameworks to develop *variational spacetime integrators* for Maxwell's equations. Extending our previous work, which first introduced this variational perspective for Maxwell's equations without sources, we also show here how to incorporate free sources of charge and current.

1. INTRODUCTION

In computational electromagnetics, as in an increasing number of other fields in applied science and engineering, there is both practical and theoretical interest in developing *geometric numerical integrators*. These numerical methods preserve, by construction, various geometric properties and invariants of the continuous physical systems that they approximate. This is particularly important for applications where even high-order methods may fail to capture important features of the underlying dynamics. In this short paper, we show that the traditional Yee scheme and extensions can be derived from the Euler-Lagrange equations of a discrete action, i.e., by designing an electromagnetic *variational integrator*, including free sources of charge and current in non-dissipative media. Furthermore, we present how to use this discrete geometric framework to allow for asynchronous time stepping on unstructured grids, as recently introduced in Stern et al. [10].

Variational integrators (not to be confused with variational methods such as finite element schemes) were originally developed for geometric time integration, particularly to simulate dynamical systems in Lagrangian mechanics. The key idea is the following: rather than approximating the equations of motion directly, one discretizes the Lagrangian and its associated action integral (e.g., using a numerical quadrature rule), and then *derives* a structure-preserving approximation to the equations of motion by applying Hamilton's principle of stationary action. Since the numerical method is derived from a Lagrangian variational principle, some important results from Lagrangian dynamics carry over to the discretized system, including Noether's theorem relating symmetries to conserved momentum maps, as well as the fact that the Euler-Lagrange flow is a symplectic mapping. (See Marsden and West [8], Lew et al. [7].)

Overview. To develop a variational integrator for Maxwell's equations, the discrete Hamilton's principle needs to incorporate more than just the time discretization, as in mechanics; spatial discretization also needs to be handled carefully. Building upon mixed finite elements in space [2, 5, 9], we treat the electromagnetic *Lagrangian density* as a discrete differential 4-form in spacetime. Extremizing the integral of this Lagrangian density with fixed boundary conditions directly leads to discrete update rules for the electromagnetic fields, with either uniform or asynchronous time steps across the various spatial elements.

2. REVIEW OF MAXWELL'S EQUATIONS IN SPACETIME

Electromagnetic Forms. Let A be a 1-form on spacetime, called the *electromagnetic potential*, and then define the *Faraday 2-form* to be its exterior derivative $F = dA$. Given a time coordinate t , this splits into the components

$$F = E \wedge dt + B,$$

where E is the electric displacement 1-form and B is the magnetic flux 2-form, both defined on the spacelike Cauchy surfaces Σ with constant t . If $*$ is the Hodge star associated to the spacetime metric, then we can also split the dual 2-form

$$*F = (*_{\mu}B) \wedge dt - *_e E = H \wedge dt - D,$$

where (again, restricted to Cauchy surfaces) H is the magnetic displacement 1-form, D is the electric flux 2-form, and $*_\mu$ and $*_\epsilon$ are respectively the magnetic permeability and electric permittivity. Finally, for systems with free sources, there is a *source 3-form* \mathcal{J} , satisfying the continuity of charge condition $d\mathcal{J} = 0$. In terms of coordinates, this can be split into

$$\mathcal{J} = J \wedge dt - \rho,$$

where J is the current density 2-form and ρ is the charge density 3-form on Cauchy surfaces.

Maxwell's Equations. With the spacetime forms and operators defined above, Maxwell's equations become

$$dF = 0, \quad d*F = \mathcal{J}.$$

Note that the first equation follows automatically from $F = dA$, since taking the exterior derivative of both sides yields $dF = ddA = 0$. The second equation is consistent with the continuity of charge condition, since $d\mathcal{J} = dd*F = 0$.

Lagrangian Formulation. Given the electromagnetic potential 1-form A and source 3-form \mathcal{J} , we can define the Lagrangian density to be the 4-form

$$\mathcal{L} = -\frac{1}{2}dA \wedge *dA + A \wedge \mathcal{J},$$

with the associated action functional $S[A] = \int_X \mathcal{L}$ taken over the spacetime domain X . Suppose that α is a variation of A , vanishing on the boundary ∂X . Varying the action along α yields

$$\mathbf{d}S[A] \cdot \alpha = \int_X (-d\alpha \wedge *dA + \alpha \wedge \mathcal{J}) = \int_X \alpha \wedge (-d*dA + \mathcal{J}).$$

Hamilton's principle of stationary action states that this variation must equal zero for any such α , implying the Euler-Lagrange equations $d*dA = \mathcal{J}$. Finally, substituting $F = dA$ and recalling that $dF = ddA = 0$, we see that this is equivalent to Maxwell's equations.

3. GEOMETRIC PROPERTIES OF MAXWELL'S EQUATIONS

As written in terms of F above, Maxwell's equations have 8 components: 6 dynamical equations, which describe how the fields change in time, and 2 "divergence constraints" containing only spatial derivatives. The fact that these constraints are automatically preserved by the dynamical equations (and can therefore effectively be ignored except at the initial time) comes directly from the differential gauge symmetry and Lagrangian variational structure. We discuss these geometric properties here, with a view towards developing numerical methods that preserve them.

Reduction by Gauge Fixing. Maxwell's equations are invariant under gauge transformations $A \mapsto A + df$ for any scalar function f , since taking the exterior derivative maps $F \mapsto F +ddf = F$. Therefore, given a time coordinate t , we can fix the gauge so that $A \cdot \frac{\partial}{\partial t} = 0$, i.e., A has only spacelike components. This partial gauge fixing is known as the *Weyl gauge*. Restricted to this subspace of potentials, the Lagrangian then becomes

$$\begin{aligned} \mathcal{L} &= -\frac{1}{2}(d_t A + d_\Sigma A) \wedge *(d_t A + d_\Sigma A) + A \wedge \mathcal{J} \\ &= -\frac{1}{2}(d_t A \wedge *d_t A + d_\Sigma A \wedge *d_\Sigma A) + A \wedge J \wedge dt \end{aligned}$$

Here, we have adopted the notation d_t and d_Σ for the exterior derivative taken only in time and in space, respectively; in particular, we then have $d_t A = E \wedge dt$ and $d_\Sigma A = B$.

Next, varying the action along a restricted variation α that vanishes on ∂X ,

$$\begin{aligned} \mathbf{d}S[A] \cdot \alpha &= \int_X (d_t \alpha \wedge D - d_\Sigma \alpha \wedge H \wedge dt + \alpha \wedge J \wedge dt) \\ &= \int_X \alpha \wedge (d_t D - d_\Sigma H \wedge dt + J \wedge dt). \end{aligned} \quad (\star)$$

Setting this equal to zero by Hamilton's principle, one immediately gets Ampère's law as the sole Euler-Lagrange equation. The divergence constraint $d_\Sigma D = \rho$, corresponding to Gauss' law, has been eliminated via the restriction to the Weyl gauge.

Noether’s Theorem Implies Automatic Preservation of Gauss’ Law. There are two ways that one can see why Gauss’ law is automatically preserved, even though it has been eliminated from the Euler-Lagrange equations. The first is to take the “divergence” d_Σ of Ampère’s law, obtaining

$$0 = d_\Sigma d_t D - d_\Sigma d_\Sigma H \wedge dt + d_\Sigma J \wedge dt = d_t (d_\Sigma D - \rho).$$

Therefore, if this condition holds at the initial time, then it holds for all time.

A more “geometric” way to obtain this result is to use Noether’s theorem, with respect to the remaining gauge symmetry $A \mapsto A + d_\Sigma f$ for scalar functions f on Σ . To derive this, let us restrict A to be an Euler-Lagrange solution in the Weyl gauge, but remove the previous requirement that variations α be fixed at the initial time t_0 and final time t_f . Then, varying the action along this new α , the Euler-Lagrange term disappears, but we now pick up an additional boundary term due to integration by parts

$$\mathbf{dS}[A] \cdot \alpha = \int_\Sigma \alpha \wedge D \Big|_{t_0}^{t_f}.$$

If we vary along a gauge transformation $\alpha = d_\Sigma f$, then this becomes

$$\mathbf{dS}[A] \cdot d_\Sigma f = \int_\Sigma d_\Sigma f \wedge D \Big|_{t_0}^{t_f} = - \int_\Sigma f \wedge d_\Sigma D \Big|_{t_0}^{t_f}$$

Alternatively, plugging $\alpha = d_\Sigma f$ into (★), we get

$$\mathbf{dS}[A] \cdot d_\Sigma f = \int_X d_\Sigma f \wedge J \wedge dt = - \int_X f \wedge d_\Sigma J \wedge dt = - \int_X f \wedge d_t \rho = - \int_\Sigma f \wedge \rho \Big|_{t_0}^{t_f}.$$

Since these two expressions are equal, and f is an arbitrary function, it follows that

$$(d_\Sigma D - \rho) \Big|_{t_0}^{t_f} = 0.$$

This indicates that $d_\Sigma D - \rho$ is a conserved quantity, a momentum map, so if Gauss’ law holds at the initial time, then it holds for all subsequent times as well.

4. GEOMETRIC DISCRETIZATION OF MAXWELL’S EQUATIONS

Discretizing Maxwell’s equations, while preserving the geometric properties mentioned above, can be achieved using *cochains* as discrete substitutes for differential forms, as previously done in, e.g., Bossavit [2]. Therefore, to compute Maxwell’s equations, we begin by discretizing the 2-form F on a spacetime mesh K : F assigns a real value to each oriented 2-face of the mesh. The exterior derivative d is discretized by the coboundary operator, so the equation $dF = 0$ states that $\langle dF, \sigma^3 \rangle = \langle F, \partial\sigma^3 \rangle = 0$, where σ^3 is any oriented 3-cell in K and $\partial\sigma^3$ is its 2-chain boundary.

Next, given a discrete Hodge star operator [1, 3, 6, 11], $*F$ is a 2-form on the dual mesh $*K$, while \mathcal{J} is defined as a discrete dual 3-form. Then, for every dual 3-cochain $*\sigma^1$ (where σ^1 is the corresponding primal edge), the equation $d*F = \mathcal{J}$ becomes $\langle d*F, *\sigma^1 \rangle = \langle *F, \partial*\sigma^1 \rangle = \langle \mathcal{J}, *\sigma^1 \rangle$.

When the cells σ^3 and $*\sigma^1$ are spacetime-like, then these correspond to the dynamical components of Maxwell’s equations, and can be used to compute subsequent values of F . When the cells are purely spacelike, they correspond to the divergence constraint equations. The exact expression and update of these fields in time now depends on which type of mesh and time stepping method is desired, as described next.

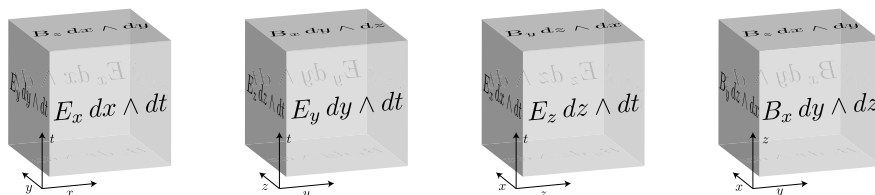


Figure 1: The 2-form $F = E \wedge dt + B$ can be discretized, on a rectangular spacetime mesh, by storing the components of E and B on 2D faces. The resulting numerical method is Yee’s FDTD scheme.

Uniform Time Stepping. For uniform rectangular meshes aligned with the (x, y, z, t) axes, we can emulate the smooth coordinate expression of F as

$$F = E_x dx \wedge dt + E_y dy \wedge dt + E_z dz \wedge dt \\ + B_x dy \wedge dz + B_y dz \wedge dx + B_z dx \wedge dy.$$

This suggests the following discretization of F , shown in Figure 1: store $E_x \Delta x \Delta t$ on the xt -faces, $E_y \Delta y \Delta t$ on the yt -faces, and $E_z \Delta z \Delta t$ on the zt -faces; likewise for B . To discretize \mathcal{J} , we can similarly store $J_x \Delta y \Delta z \Delta t$, $J_y \Delta z \Delta x \Delta t$, $J_z \Delta x \Delta y \Delta t$, and $\rho \Delta x \Delta y \Delta z$ on the corresponding dual 3-cells. If we then enforce the equations $dF = 0$ and $d * F = \mathcal{J}$ in the discrete sense, the result is precisely the finite-difference time-domain (FDTD) integration scheme of Yee [12]. A similar procedure can be applied on unstructured (e.g., simplicial) spatial grids, on which we take uniform time steps Δt (creating prism-shaped spacetime primal elements); in this case, solving the discrete Maxwell’s equations recovers the more recent “Yee-like” method of Bossavit and Kettunen [4].

Asynchronous Time Stepping. As initially mentioned in Stern et al. [10], a more flexible integration scheme can be designed by assigning a different time step per element, in order to focus computational power where needed. A visualization of how to store F on such a mesh structure is shown in Figure 2. This defines an *asynchronous variational integrator* that preserves the numerical properties of the uniform-stepping methods outlined above. The procedure to repeatedly update E and B asynchronously in time is as follows:

1. Select the face for which B needs to be updated next.
2. E advances B , using $dF = 0$.
3. B advances E on neighboring edges, using $d * F = \mathcal{J}$.

Details of this algorithm, along with initial numerical results, can be found in Stern et al. [10], where only the case $\mathcal{J} = 0$ was described.

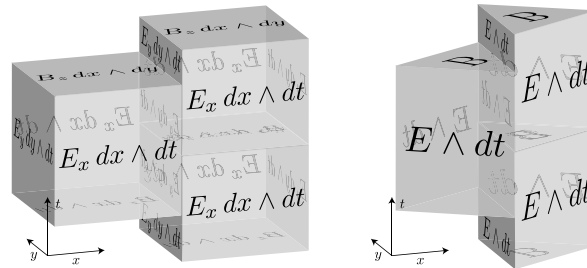


Figure 2: Here, F is discretized on an asynchronous time-stepping grid, where each spatial element takes a different-sized time step from its neighbors. This can be done for either a rectangular spatial grid (left) or an unstructured/simplicial spatial mesh (right).

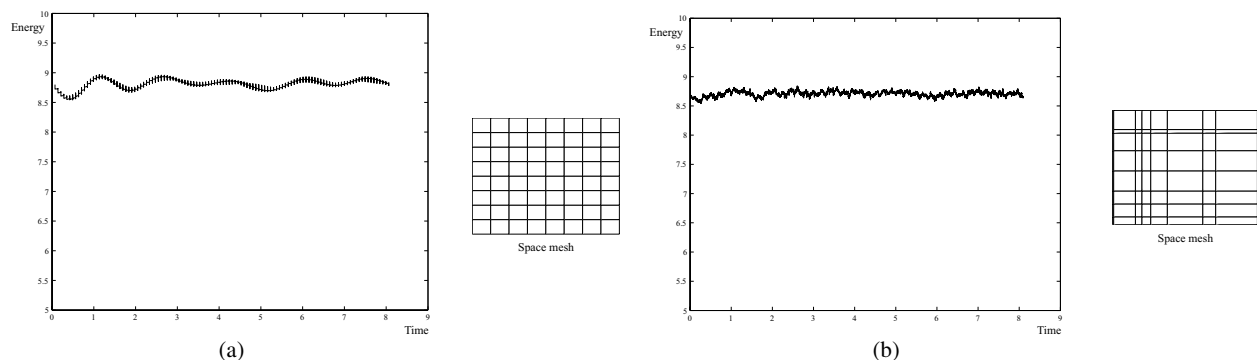


Figure 3: Our geometric integrator robustly maintains near-conservation of energy, even for asynchronous time stepping on a random spatial grid. (a) Regular grid, uniform time steps, (b) random grid, asynchronous time steps.

One promising result from the initial numerical experiments, shown in Figure 3, is that this asynchronous integrator matches the FDTD scheme's excellent energy conservation behavior, even on a highly irregular grid, without exhibiting artificial damping or forcing. Future work is expected to include formal accuracy and stability analysis of this asynchronous integrator, focusing both on the choice of Hodge star and on resonance stability criteria for selecting the individual time steps.

ACKNOWLEDGMENT

Our research was partially supported by a Betty and Gordon Moore fellowship at Caltech, NSF grants CCR-0133983 and DMS-0453145 and DOE contract DE-FG02-04ER25657, and by NSF grant CCF-0528101. We gratefully acknowledge these sponsors for their support of this work.

REFERENCES

1. Auchmann, B. and S. Kurz, "A geometrically defined discrete Hodge operator on simplicial cells," *IEEE Trans. Magn.*, Vol. 42, No. 4, 643–646, 2006.
2. Bossavit, A., Computational electromagnetism, Electromagnetism, Academic Press Inc., Variational formulations, complementarity, edge elements, San Diego, CA, 1998.
3. Bossavit, A. and L. Kettunen, "Yee-like schemes on a tetrahedral mesh, with diagonal lumping," *Int. J. Numer. Modell.*, Vol. 12, Nos. 1–2, 129–142, 1999.
4. Bossavit, A. and L. Kettunen, "Yee-like schemes on staggered cellular grids: A synthesis between FIT and FEM approaches," *IEEE Trans. Magn.*, Vol. 36, No. 4, 861–867, 2000.
5. Gross, P. W. and P. R. Kotiuga, "Electromagnetic theory and computation: A topological approach," *Mathematical Sciences Research Institute Publications*, Vol. 48, Cambridge University Press, Cambridge, 2004.
6. Hiptmair, R., "Discrete Hodge operators," *Numer. Math.*, Vol. 90, No. 2, 265–289, 2001.
7. Lew, A., J. E. Marsden, M. Ortiz, and M. West, "Variational time integrators," *Internat. J. Numer. Methods Engrg.*, Vol. 60, No. 1, 153–212, 2004.
8. Marsden, J. E. and M. West, "Discrete mechanics and variational integrators," *Acta Numer.*, Vol. 10, 357–514, 2001.
9. Nédélec, J. C., "Mixed finite elements in R^3 ," *Numer. Math.*, Vol. 35, No. 3, 315–341, 1980.
10. Stern, A., Y. Tong, M. Desbrun, and J. E. Marsden, "Computational electromagnetism with variational integrators and discrete differential forms," preprint at arXiv: 0707.4470 [math.NA], 2007.
11. Tarhasaari, T., L. Kettunen, and A. Bossavit, "Some realizations of a discrete Hodge operator: A reinterpretation of finite element techniques," *IEEE Trans. Magn.*, Vol. 35, No. 3, 1494–1497, 1999.
12. Yee, K. S., "Numerical solution of initial boundary value problems involving Maxwell's equations in isotropic media," *IEEE Trans. Ant. Prop.*, Vol. 14, No. 3, 302–307, 1966.

Formulation of the MoM in Space Domain with Two Sets of Basis Functions to Analyze a Microstrip Transmission Lines

M. Bassem Ben Salah, Chaker Essid, and Abdelaziz Samet

URCSE, École Polytechnique de Tunisie, Tunisia

Abstract— The Mixed Potential Integral Equation (MPIE) formulation is combined with discrete complex image technique (DCIT) and solved by the method of moments (MoM) to analyze a printed transmission lines. The 2-D space domain Green's functions are analytically obtained from the approximation of its spectral domain. These functions have been efficiency obtained and validated, but the accuracy of this technique is strongly dependent on the choice of basis functions used in the approximation of the unknown current components. In this paper, two formulations are presented with different sets of frequently used basis functions for the canonical case of the microstrip transmission line. The emphasis in this paper is on the relative accuracy, the convergence and the computational efficiency of both sets of basis functions.

1. INTRODUCTION

Several numerical techniques have been applied to solve the propagation characteristics of planar transmission-line structures such as shown in Fig. 1. The full-wave approach is the most suited of this kind of problem, but its computation time requirement is higher. Consequently, the numerical efficiency of the formulation is the key word of the full-wave approach. A sample of this type of work can be found in [1–3]. These works have focused their efforts on the computation of the two-dimensional (2-D) space-domain representation of the potential Green's functions suitable to this kind of problem. But the choice of basis functions also affects on the accuracy and efficiency of this technique. There are different types of functions, the choice depends on the geometry of the structure and affects on the techniques used to compute the MoM matrix entries. In this paper, we present two formulations of the MoM in space domain to analyze the microstrip transmission lines with different sets of frequently used basis functions, the entire and sub-sectional domain basis functions. The first set is presented by first- and second-kind Chebyshev polynomials [1] and the second set is presented by the pulse and triangle functions [3], usually used for non-planar transmission lines [4].

This paper is organized as follows; Section 2 will briefly presents the integral-equation formulation of the problem. In Section 3, it was introduced a few details needed to evaluate MoM matrix entries in both cases formulation. It has shown some techniques used to circumvent the problems of integration and the important analytical expressions to be used. Finally, the two sets of basis functions are applied on microstrip line; the propagation constant and CPU time are compared.

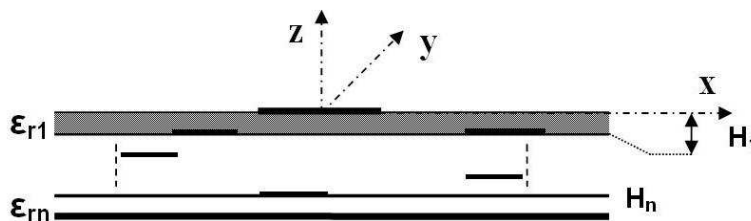


Figure 1: Cross section of the multiconductor transmission line under investigation.

2. FORMULATION

The details of the Mixed Potential Integral Equation (MPIE) formulation can be found in [1–3] (only the most important equations will be stated here for the sake of brevity). Fig. 1 shows the general geometry of the transmission line under investigation. All layers are assumed to be infinite, the metal is assumed to be perfect and of zero thickness. The time dependence is assumed to be

$e^{j\omega t}$ and suppressed throughout. The propagation factor along the longitudinal y -axis is assumed $e^{-j\beta y}$, where β is the unknown propagation constant.

The longitudinal and the transversal current are expanded into basis functions. Substituting these functions into the MPIE and applying Galerkin testing yields the following MoM matrix equation:

$$\begin{pmatrix} M_{xx}^{mn} & M_{xy}^{mn} \\ M_{yx}^{mn} & M_{yy}^{mn} \end{pmatrix} \begin{pmatrix} A_n \\ B_n \end{pmatrix} = 0 \quad (1)$$

where A_n, B_n are the unknown amplitudes of the current expansion functions, and the elements of the MoM matrix can be written as follows:

$$M_{xx}^{mn} = \langle J_x^m | G_{xx}^A(x-x') * J_x^n \rangle - \frac{1}{\omega^2} \left\langle \frac{d}{dx} [J_x^m] \middle| G^\Phi(x-x') * \frac{d}{dx'} [J_x^n] \right\rangle \quad (2)$$

$$M_{xy}^{mn} = j \frac{\beta}{\omega^2} \left\langle \frac{d}{dx} [J_x^m] \middle| G^\Phi(x-x') * J_y^n \right\rangle \quad (3)$$

$$M_{yx}^{mn} = -j \frac{\beta}{\omega^2} \left\langle J_y^m \middle| G^\Phi(x-x') * \frac{d}{dx'} [J_x^n] \right\rangle \quad (4)$$

$$M_{yy}^{mn} = \langle J_y^m | G_{yy}^A(x-x') * J_y^n \rangle - \left(\frac{\beta}{\omega} \right)^2 \langle J_y^m | G^\Phi(x-x') * J_y^n \rangle \quad (5)$$

where $\langle \rangle$ signifies the inner product, and where $*$ signifies convolution. We can write the following expression for the whole 2-D space domain Green's function [2]:

$$G(|x-x'|, \beta) = \frac{C}{\pi} K_0(\alpha|x-x'|) + \sum_{i=1}^{N_{GPOF}} a_i K_0\left(\alpha\sqrt{(x-x')^2 + \gamma_i^2}\right) + \sum_{p=1}^{N_p} \frac{R_p k_{pp}}{\delta_p} e^{-\delta_p|x-x'|} \quad (6)$$

The zeroth order modified Bessel function of the second kind ch. 9, p. 375 from [4], in the 2-D space domain Green's functions, presents a logarithmic singularity that might causes problems in the convolution integral. Once the space-domain kernel of the integral equation has been efficiently obtained, we can apply the Galerkin's method. We should choose a well set of basis functions for planar-type structures. The next step is to calculate the convolution and inner product integrals by using the basis functions and the Green functions in (6). The required propagation constants β force the determinant of the MoM matrix in (1) to vanish. These roots can be obtained using Miller's method.

3. EVALUATION OF THE ENTRIES OF MOM MATRIX

3.1. Integrals Relating to Chebyshev Polynomials Basis Functions

For the first set, we chose the first- and second-kind Chebyshev polynomials. This basis functions weighed by the proper strip edge condition are very suitable for the current expansion [2]. These functions mimic the real behavior of the currents near the edge of the conducting strips and are quasi-orthogonal for the space kernel we are using. This allows us to attain accurate results while using very few basis functions. Thanks to the relationship between first- and second-kind Chebyshev polynomials ch. 22, p. 778 from [4], we only need to compute integrals involving first-kind polynomials. The reaction integrals involving these functions and the closed-form expression of the Green's functions obtained with the complex image method are quasi-analytically computed. This reaction has the following form:

$$I = \int_{-1}^1 \frac{T_i(x)}{\sqrt{1-x^2}} dx \int_{-1}^1 \frac{T_j(x')}{\sqrt{1-x'^2}} dx' \times G(x, x') \quad (7)$$

The function K_0 presents a logarithmic singularity that might cause problems in the convolution integral. Fortunately, the contribution to the convolution integrals of this singularity can be handled in closed form, such as explained in [5]. We can employ this identity to evaluate the integral [3]:

$$\int_{-1}^1 \frac{T_p(x)}{\sqrt{1-x^2}} dx \int_{-1}^1 \frac{T_q(x')}{\sqrt{1-x'^2}} dx' \cdot \log(|x-x'|) = \begin{cases} -1/2 \cdot p & \text{if } p = q \neq 0 \\ 0 & \text{if } p \neq q \\ \log(w/4) & \text{if } p = q = 0 \end{cases} \quad (8)$$

The rest of the kernel (approximation part and SWP of the Green's functions) is regular and does not generate integration problems. Due to the type of singularity present in the basis functions, low-order Chebyshev quadratures are suitable to accurately carry out the integrations involving the regular part of the kernel. In this way, the elements of Galerkin's matrix are generated both very accurately and efficiently.

3.2. Integrals Relating to Pulse and Triangle Basis Functions

The second set of basis functions is represented by the pulse and triangle functions [1, 3], which are defined in sub-intervals. Pulse functions have been used to approximate the axial component of the surface current density (y -component) and triangle functions for the transverse components (x -component). It is worth mentioning that we have used a non-uniform distribution of the basis functions. The basis functions have been concentrated near the edges in order to reproduce in a better way the fast variations of the current density in those regions. The application of the method of moments implies the integration of the kernel of the integral equation over straight segments on the cross section of the conductors (reaction integrals). This integration is fourth order and depends on the distance between two basis functions. The first idea is to move the product of convolution between the Green's functions and basis functions as an inter-correlation function of basis and test functions. The advantage of these functions is that their product Convolution is calculated analytically and leads to polynomials, which facilitates the integration and reduces the order of integrals. The integrals have to be calculated as follows:

$$I = \int G(x) \int J_{xm}(x') J_{xn}(x' - x) dx' dx = \int G(u + u_0) u^k du; \quad 0 \leq k \leq 3 \quad (9)$$

with u_0 is the distance between two basis functions. To improve the efficiency and accuracy of the method, the logarithmic singularity of the kernel has been separately treated and its contribution analytically obtained. This contribution has these integrals form:

$$I_{QST}(u_0) = \int_{D(B,T)} u^k K_0(\alpha|u + u_0|) du \quad (10)$$

For $k = 0$ and 1, we can respectively use Equations 11.1.9 to 11.3.27 from reference [4]. For $k > 1$ we can refer to example 7 p.490 from the same reference, and use the following equation:

$$f_m(x) = x^{-m} \int_0^x t^m \cdot K_0(t) dt = \frac{1}{x^2} [(m-1)^2 f_{m-2}(x) - x^2 \cdot K_1(x) - x(m-1) \cdot K_0(x)] \quad (11)$$

For the contribution of the approximated part of Green's functions, the calculation of this integral is therefore to compute this type of integrals:

$$\int_a^b y^k K_0(a \cdot \sqrt{y^2 - b^2}) dy; \quad 0 \leq k \leq 3 \quad (12)$$

These integrals have been evaluated with very low computational effort: no more than two or three Gauss-Legendre quadrature points have been found to be necessary for every integral. For $k = 1$, we can use this identity:

$$\int_a^b y K_0(a \cdot \sqrt{y^2 - b^2}) dy = -\frac{1}{a} \sqrt{y^2 - b^2} K_1(a \cdot \sqrt{y^2 - b^2}) \quad (13)$$

The contribution of SWP [2] doesn't cause an integration problem and analytically obtained.

4. NUMERICAL RESULTS

We have evaluated the global performance of both formulations. First, we have checked the accuracy and convergence properties of the reaction integrals defining the entries of MoM matrix. We have confirmed that these entries are computed with extreme accuracy using very low-order quadratures and closed-form evaluation of the logarithmic singularity contribution. On the other hand, we have carried out exhaustive comparisons with propagation constants computed using the two sets of basis functions.

As an example, some numerical results for the fundamental and first two higher order modes of a simple microstrip line are included in Table 1. In the case of Chebyshev polynomials, we have used four basis functions for the longitudinal current, three functions for the transverse one and four Chebyshev quadrature points in the evaluation of the reaction integrals. For the pulse and triangle functions, we have used eight basis functions for the longitudinal current, seven functions for the transverse one and three Gauss-Legendre quadrature points in the evaluation of the reaction integrals. The agreement between the various results is total; although the first formulation is more precise but the computational effort (CPU time) is comparable between the two formulations.

Table 1: β/k_0 for the fundamental and two first higher modes of the microstrip in the top figure. $w = 3.0$ mm, $h = 0.635$ mm, and $\epsilon_r = 9.8$. Left-hand-side column: Chebyshev polynomials BF. Right-hand-side column: Pulse and triangle BF.

Frequency (GHz)	EH0		EH1		EH2	
5	2.835	2.841	-	-	-	-
10	2.895	2.887	-	-	-	-
15	2.942	2.942	1.29	1.226	-	-
20	2.977	2.979	2.063	2.052	-	-
25	3.006	3.011	2.395	2.393	-	-
30	3.031	3.028	2.58	2.584	1.334	1.432
35	3.039	3.044	2.696	2.700	1.818	1.901
40	3.058	3.051	2.778	2.781	2.110	2.184
45	3.064	3.067	2.836	2.840	2.306	2.284

5. CONCLUSION

The problem of the microstrip transmission line is formulated in the spatial domain using an MPIE and solved using the MoM. Two different sets of suitable basis functions are used to model current distribution. The evaluation of MoM matrix entries are explained for the two cases. Numerical results for the dispersion characteristics are presented and compared. Based on these results it is concluded that the Chebyshev polynomials basis functions provide high accuracy and efficiency more than pulse and triangle functions to the analysis.

REFERENCES

1. Soliman, E. A., P. Pieters, E. Beyne, and G. A. E. Vandenbosh, "Numerically efficient method for multislotted transmission lines in layered media-Application to multislotted lines in MCM-D technology," *IEEE Trans. Microwave Theory Tech.*, Vol. 47, 1782–1787, Sept. 1999.
2. Bernal, J., F. Medina, R. R. Boix, and M. Horno, "Fast full-wave analysis of multistrip transmission lines based on MPIE and complex image theory," *IEEE Trans. Microwave Theory Tech.*, Vol. 48, 445–452, Mar. 2000.
3. Bernal, J., F. Medina, and R. R. Boix, "Full-wave analysis of nonplanar transmission lines on layered medium by means of MPIE and complex image theory," *IEEE Trans. Microwave Theory Tech.*, Vol. 49, 177–185, Jan. 2001.
4. Abramowitz, M. and I. A. Stegun, *Handbook of Mathematical Functions*, Dover, New York, 1972.
5. Drake, E., F. Mesa, and M. Horno, "Improved quasi-TEM spectral domain analysis of boxed coplanar multiconductor microstrip lines," *IEEE Trans. Microwave Theory Tech.*, Vol. 41, 260–267, Feb. 1993.

Development, Characterization and Simulation of Flexible Single-Layer X-Band Microwave Absorbers Based on Conducting Polyaniline

L. C. Folgueras^{1,2}, M. A. Alves^{1,3}, M. B. Perotoni³, and M. C. Rezende¹

¹Materials Division, Instituto de Aeronáutica e Espaço, Brazil

²Universidade de Taubaté, Brazil

³CST, GmbH, Dramstadt, Germany

Abstract— Two absorbing materials containing conducting polymer polyaniline (PAni) were produced in the form of single-layer flexible sheets. One of the materials consisted of PAni dispersed in a polymer matrix composed of a mixture of polyurethane and polyacrylonitrile. The other material was made of compacted PAni. The electromagnetic properties of these materials were analyzed using the waveguide technique in the frequency range 8–12 GHz (X-Band). To better understand the absorbing properties of these materials, the electromagnetic software package CST Microwave StudioTM was used to simulate the attenuation of an electromagnetic wave incident on the absorbing materials. The results show that these materials have the potential to be used as microwave absorbers, and the simulations performed with CST agreed well with the experimental data.

1. INTRODUCTION

The absorption of electromagnetic energy by a microwave-absorbing material (MAM) depends on many factors. The radiation incident on the material interacts differently if the MAM is composed of dielectric or magnetic materials, or a mixture of these, but regardless of the characteristics of the material, the energy of the incident wave is transformed into heat. The most important properties of a MAM are related to its dielectric and magnetic characteristics, i.e., the electric permittivity (ϵ) and magnetic permeability (μ) [1, 2]. A medium is a perfect dielectric when there are no losses in the material and the density current is null as a consequence of ϵ and μ being real quantities. In contrast, in a lossy material ϵ and μ are complex. The penetration depth of the radiation into the material and the attenuation of the electric field at the surface are also important parameters in the determination of the characteristics of the MAM [3, 4]. Materials having high conductivity and limited ability to store energy have high dielectric losses, the penetration depth approaches zero, and the material behaves as a reflector. On the other hand, in materials with low dielectric losses, the penetration depth is larger, and little energy is absorbed, rendering the material transparent to electromagnetic radiation. In MAMs, most of the electromagnetic energy is attenuated as a result of the interaction of factors, such as dielectric losses, penetration depth, and electric conductivity [5–7].

Organic conducting polymers, also known as “synthetic metals”, belong to a class of materials that combine the chemical and mechanical properties of polymers with the electrical properties of metals and semiconductors [8, 9]. These properties make these materials candidates for applications as MAMs. Polyaniline (PAni) is an example of a conducting polymer that has some of the properties of semiconductors. PAni can be produced with relative ease and at a low cost. Compared to metals, PAni has low specific mass, and its absorptive (or reflective) properties can be modulated during its processing [10]. In this study, two MAMs based on PAni were produced and their electromagnetic characteristics were determined. Also, simulations of the attenuation of electromagnetic radiation by these materials were performed to predict their behavior.

2. SYNTHESIS OF PANI

PAni was produced in laboratory scale using the method described by MacDiarmid [11]. The conductive form of PAni (green color, emeraldine salt) was obtained by the action of the oxidizing agent ammonium peroxydisulfate on aniline in an acidic reaction medium (dodecylbenzenesulfonic acid — DBSA). PAni was obtained in powder form and ready to be used. In the present study PAni was processed in two ways [12]. First, PAni, as obtained from the synthesis, was compacted into a solid sample (material S1). In the second material (S2), PAni was dispersed in a polyurethane (PU) polymeric matrix and processed with the addition of polyacrylonitrile powder (PAN), which

is a polymer transparent to microwave radiation. The formulation of S2 was in the ratio 3:1:0.3 for PANi:PU: PAN, respectively. The material S2 was obtained as a flexible sheet.

3. ELECTROMAGNETIC CHARACTERIZATION

The electromagnetic properties of materials S1 and S2 were analyzed in the frequency range 8–12 GHz using the waveguide technique [13]. Measurements of reflected and absorbed electromagnetic energy, and of the S -parameters were performed. A Hewlett-Packard X 752C waveguide with rectangular cross section was coupled to a system consisting of a frequency generator Hewlett-Packard 8340B, a vector network analyzer Agilent 8510C and an automatic network analyzer (S -parameter test) Hewlett-Packard 8510A. The reflectivity of the processed materials was evaluated after the system was calibrated by measuring the reflectivity of an aluminum plate (100% reflective material). From the values of the S -parameters, the software Agilent 85071E calculated both real and complex values of ϵ and μ for the material. The sample materials were placed in contact with a flat metallic surface at the end of the waveguide during the measurements.

4. OVERVIEW OF THE SIMULATION TOOL

The reflectivity of materials S1 and S2 to microwaves was simulated with the general-purpose electromagnetic software CST Microwave Studio [14] which is based on the Finite Integration Technique (FIT) [15]. FIT is a generalization of the finite difference time domain method and has proved to be a robust numerical tool that can treat several types of electromagnetic problems, from static field calculations to high frequency applications in frequency and time domain. Briefly, FIT can be described as a method where Maxwell's equations, in their integral form, are discretized and transformed into algebraic matrix equations. The computational area of the problem is divided into grids, which in their turn are subdivided into cells, and the electric and magnetic fields are allocated on the edges and areas of the cells, respectively. With this procedure, the analytical properties are conserved in the grid space. Fig. 1 shows schematically the set up of the problem simulated with CST. A linearly polarized plane wave is incident normally on the MAM, which rests on a metallic plate. The simulations were carried out in the frequency range 8–12 GHz. The MAM was assumed to be homogeneous and to have constant thickness.

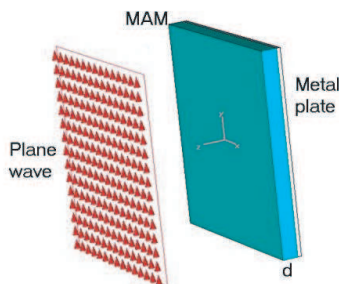


Figure 1: A linearly polarized plane wave is incident normally on the MAM, which rests on a metallic plate. The MAM is characterized by its permittivity (ϵ) and thickness (d).

5. RESULTS

The absorbing properties of the MAM are highly dependent on its thickness. Therefore, great care was taken to assure that the material had a uniform thickness. The measured thickness of materials S1 and S2 was 2.15 mm and 6.10 mm, respectively. The electric permittivity of both materials as a function of frequency is shown in Figs. 2(a) and 2(b). It was observed that the material S1 (Fig. 2(a)) has high dielectric loss, which is characteristic of reflecting materials, even though this material is a polymer with characteristics of a dielectric material. The electric conductivity was measured using the 4-point probe method, and it was found that the electric conductivity of S1 was higher than that of S2. The higher conductivity indicates that S1 has a behavior similar to metals, with low absorption of the incident electromagnetic radiation [6]. The permittivity of S2 (Fig. 2(b)) shows that this material has lower dielectric loss than S1, which is characteristic of dielectric materials having low electric conductivity. Also, the observed decrease in permittivity with increasing frequency is typical of dielectric materials, and may be related to the presence

of high-conductivity polymer particles dispersed in the matrix. These particles can produce local accumulations of charges (formation of conducting islands) as a result of the influence of the incident wave [7].

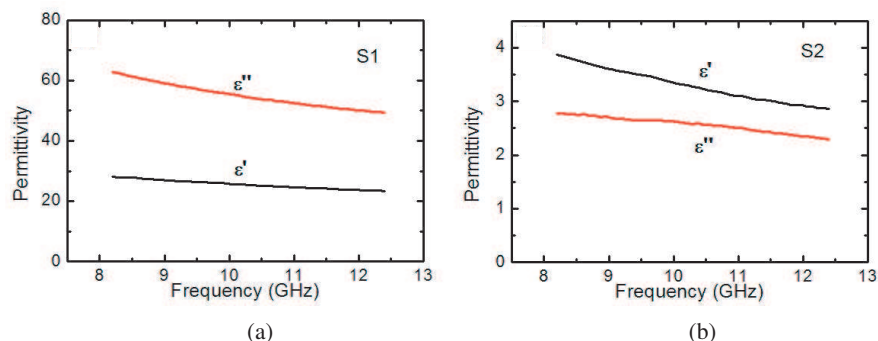


Figure 2: Real and imaginary permittivities, ϵ' and ϵ'' , of the materials (a) S1, and (b) S2 versus frequency.

Figure 3 shows the experimental measurements and results of simulations of electromagnetic absorption by materials S1 and S2 as a function of frequency. The simulations of the absorption characteristics of these materials were performed using the results shown in Fig. 2. It is observed in Fig. 3(a) that the material S1 showed low attenuation values, ranging from 1 dB to 1.7 dB. From the data on Figs. 2(a) and 3(a), it is possible to verify that material S1 has relatively high conductivity and is behaving as a metal. The simulated attenuation, obtained for the same thickness of the sample material ($d = 2.15$ mm), shows good agreement with the experimental measurements, with differences within 0.7 dB. The metallic behavior of S1 was also demonstrated by the simulations; there was little change in attenuation as the thickness of the material was varied.

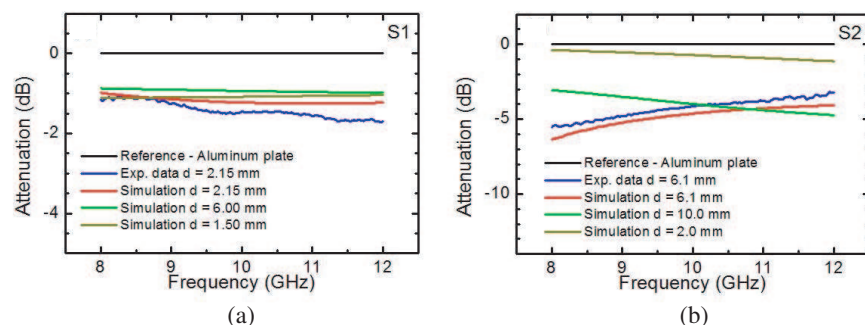


Figure 3: Measured and simulated curves of absorption for the materials (a) S1, and (b) S2 versus frequency.

The measured absorption of material S2 ranged from 3.2 to 5.5 dB. There was a good agreement between the experimental and simulated results when the thickness of the sample was used ($d = 6.10$ mm). Note that in this case, the simulations show that the thickness influences the absorption characteristics of material S2. According to the simulated results, the material may behave as a reflector for small thicknesses ($d = 2.00$ mm); as the thickness increases, the material behaves as a dielectric.

6. CONCLUSIONS

The results obtained in this study suggest that PANi and the dielectric materials developed have the potential to be used as absorbing materials. The results obtained for the compacted PANi material S1, were expected due to the relatively high conductivity of the synthesized PANi. Material S2, consisted of PANi dispersed in a polymer matrix, has properties that may be useful for producing MAMs, due to the attenuation values (3–5 dB) that were attained.

A comparison of the data also shows that simulation may be an important tool in the development of MAMs when permittivity values are known, as they can help determine the thickness that maximizes the absorption of the incident electromagnetic radiation. The materials developed in

this study had low specific mass, less than 1 kg/m^2 , which is smaller than MAMs based on, for example, ferrite materials which have specific masses of $4\text{--}5 \text{ k/gm}^2$. The lower density of PANi-based MAMs increases the number of potential uses for this material.

ACKNOWLEDGMENT

The authors wish to express their gratitude to the Brazilian funding agencies CNPq (Proj. No. 3015-83/06-3 and 151929/2005-0) and FINEP for the financial support, and to Instituto Tecnológico de Aeronáutica, Instituto de Aeronáutica e Espaço — Materials Division and the Brazilian Air Force, for their collaboration in this project.

REFERENCES

1. Balanis, C. A., *Advanced Engineering Electromagnetics*, John Wiley and Sons, New York, 1989.
2. Hippel, A., *Dielectric Materials and Applications*, Artech House, London, 1954.
3. Chung, D. D. L., “Electromagnetic interference shielding effectiveness of carbon materials,” *Carbon*, Vol. 39, No. 2, 279–285, 2001.
4. Balageas, D. and P. Levesque, “EMIR: A photothermal tool for electromagnetic phenomena characterization,” *Revue Generale de Thermique*, Vol. 37, No. 9, 725–739, 1998.
5. Thostenson, E. T. and T. W. Chou, “Microwave processing: fundamentals and applications,” *Composites: Part A: Applied Science and Manufacturing*, Vol. 30, No. 9, 1055–1071, 1999.
6. Oh, J. H., K. S. Oh, C. G. Kim, and C.-S. Hong, “Design of radar absorbing structures using glass/epoxy composite containing carbon black in X-band frequency ranges,” *Composites Part B: Engineering*, Vol. 35, No. 1, 49–56, 2004.
7. Rannou, P., M. Nechtschein, J. P. Travers, D. Berner, A. Wolter, and D. Djurado, “Ageing of PANi: Chemical, structural and transport consequences,” *Synthetic Metals*, Vol. 101, 734–737, 1999.
8. Anand, J., S. Palaniappan, and D. N. Sathyanarayana, “Conducting polyaniline blends and composites,” *Progresses in Polymer Science*, Vol. 23, No. 6, 993–1018, 1998.
9. Falcou, A., A. Duchêne, P. Hourquebie, D. Marsacq, and A. Balland-Longeau, “A new chemical polymerization process for substituted anilines: Application to the synthesis of poly (nalkylanilines) and poly (o-alkylanilines) and comparison of their respective properties,” *Synthetic Metals*, Vol. 149, No. 2–3, 115–122, 2005.
10. Satheesh Kumar, K. K., S. Geetha, and D. C. Trivedi, “Freestanding conducting polyaniline film for the control of electromagnetic radiations,” *Current Applied Physics*, Vol. 5, No. 6, 603–608, 2005.
11. MacDiarmid, A. G., et al., *Conducting Polymers: Special Applications*, L. Alcacer, Ed., Dordrecht, Reidel, 1987.
12. Folgueras, L. C., M. A. Alves, and M. C. Rezende, “Development, characterization and optimization of dielectric radar absorbent materials as flexible sheets for use at X-band,” *Proceedings of Microwave and Optoelectronics Conference*, 488–491, Salvador, Brazil, November 2007.
13. Laverghetta, T. S., *Microwave Measurements and Techniques*, Artech House, Dedham, 1976.
14. CST Microwave Studio, Available: <http://www.cst.com>. Accessed 15 February 2008.
15. Weiland, T., “Time domain electromagnetic field computation with finite difference methods,” *International Journal of Numerical Modelling*, Vol. 9, 295–319, 1996.

Numerical Reconstruction of Permeability Material Using 3-D T - Ω Formulation of Finite Element Method

F. Yassine¹, E. Chaker¹, K. Ahmed², K. B. Ammar³, and S. Abdelaziz¹

¹URCSE, École Polytechnique de Tunisie(EPT), Tunisia

²Electromagneticworks, Canada

³LACIME, École de Technologie Supérieure (ETS), Montréal, Canada

Abstract— Three-Dimensional electromagnetic numerical modelling is used in inversion problems, commonly for determining the distribution of electrical parameters such as conductivity or permeability. This type of problems is a non-linear and ill-conditioned problem needs two phase resolutions: the forward and the inverse phase. In this paper we describe a numerical approach to image the electrical permeability distribution within a given object from a non-destructive evaluation signal. We have solved the forward solution using a three-Dimensional T - Ω formulation of Finite Element Method in order to determine the magnetic field and a classical Gauss-Newton algorithm with regularization to solve and stabilize the solution of the optimisation problem. The permeability of the object is assumed to be linear and isotropic. Results for the permeability imaging have been reconstructed using synthetically generated data.

1. INTRODUCTION

The reconstruction of the electric properties (permittivity, permeability or conductivity) of unknown objects, with three-Dimensional electromagnetic numerical modelling regarded as inverse problem [1–3], became target of much research in the last decade. This topic is up-to-date and it requires a great deal of intention to be paid both at the basic research level and at the level of techniques to be applied as well as results to be achieved. Many non-destructive techniques are used in medical, industrial and geophysical imaging [1–3]. Consider the example of Magnetic Induction Tomography (MIT) or Electrical Induction Tomography (EIT). This type of problems is a non-linear and ill-conditioned problem needs two phase resolutions: the forward and the inverse phase. Finite Difference, Finite element and integral equation approaches are the most applied techniques in forward resolution [4–7].

This paper describes a numerical approach to image the electrical permeability distribution within a given object from a non-destructive evaluation signal. Based on the techniques of induced currents (Eddy-Current Techniques), this technique falls within the framework of tomography based on Magnetic Induction Tomography (MIT) and consists in determining the electric parameter of the object of interest, the distribution of permeability is a case in point. Here we shall follow the measures of impedances within a pair of coils (between an emitter and one for detection). Starting from the measurement of tension in the reception coil, we can determine the electromagnetic field which had already scanned the object of interest. By using a method of an electromagnetic analysis, we can determine the magnetic field that contains information about the distribution of the parameter previously aimed at. We have solved the forward solution using a three-dimensional T - Ω formulation of Finite Element Method [8, 9] in order to determine the magnetic field and a classical Gauss-Newton algorithm with Tikhonov regularization to solve and stabilize the solution of inverse solve.

2. FORWARD FORMULATION

One variation of Finite Element Method in 3-D (FEM-3D) is the T - Ω formulation [8, 9] which consists in expressing the magnetic field H according to the potential current vectors and the potential magnetic scalar Ω . Accordingly, we model the potential current vector T by Edge Basis Functions, the potential magnetic scalar Ω . The use of two types of basic functions (Edge and Nodal), simultaneously, in only one hybrid formulation makes it possible the efficient determination of the magnetic field and consequently the induction voltage of the detection coil. The T - Ω method for 3-D eddy current analysis arises as follows: The analysed region R can be divided into the current free region R_0 and the current carrying region R_c . The quantities of the fields derive from

potentials are expressed by:

$$\vec{H} = \vec{T}_0 + \vec{T} - \overrightarrow{\text{grad}}\Omega \quad (1)$$

$$\vec{J} = \overrightarrow{\text{rot}}\vec{T}_0 + \overrightarrow{\text{rot}}\vec{T} \quad (2)$$

The $\overrightarrow{\text{rot}}\vec{T}_0$ is a current density yielding the prescribed total current in R_0 , and The curl of $\overrightarrow{\text{rot}}\vec{T}$ is a current density yielding current carrying region R_c . Using the Maxwell's equations and the complementary's equations to express each element in Equations (1) and (2), we find the following equation:

$$j\omega \text{div} \left(\mu \vec{T} - \overrightarrow{\text{grad}}\Omega \right) = -j\omega \text{div} \left(\mu \vec{T}_0 \right) \quad (3)$$

Then, we apply the boundary conditions of Dirichlets or Newmann to the vector potentials and scalar potentials, and we approximate the potential vector by Edge Basis Functions and the scalar magnetic potential Ω by Nodal Basis Functions (Equations (5) and (6)).

$$\vec{T} \approx \vec{T}^{(n)} = \sum_{k=1}^{n_e} t_k N_k \quad (4)$$

$$\Omega \approx \Omega^{(n)} = \sum_{k=1}^{n_n} \Omega_k N_k \quad (5)$$

where t_k are the line integrals of T along the edges and Ω_k the nodal values of $\Omega^{(n)}$.

Setting (4) and (5) into (3), apply Dirichlet and Newmann boundary conditions on the vector and scalar potentials and using the basis functions N_i as weighting functions, the Galerkin function to resolve is:

$$- \int_{R_c} j\omega \mu \cdot \text{grad} N_i \cdot \vec{T}^{(n)} dR + \int_{R_c} j\omega \mu N_i \cdot \text{grad} \Omega^{(n)} dR = \int_{R_c} j\omega \mu \text{grad} N_i \cdot \vec{T}_0 dR, \quad i = 1, 2, \dots, n_n \quad (6)$$

After the computing of the magnetic field by the T - Ω formulation, we start the calculation of the tension induced in the receiving coil.

3. INVERSE SOLVER

3.1. Algorithm

We denote by V_m the vector of measured voltages, and $F(\mu)$ the vector of calculated voltages with forward process. The inverse problem corresponds to an algorithm of optimization which makes it possible to calculate μ with an acceptable error. The regularization is the fact of introducing information as a preliminary to this algorithm and that amounts minimizing the following quadratic error function:

$$f(\mu) = \|V_m - F(\mu)\|^2 + \alpha^2 \|L(\mu)\|^2 \quad (7)$$

where $\alpha^2 L(u)$ is a term of penalty. For a judicious choice of $L(u)$, we will have a critical point which will be a minimum corresponding to $\nabla f(\mu) = 0$. We solve this minimization problem by regularized Gauss-Newton method. This minimization leads to linear steps, each of which is the Tikhonov regularized solution to the linearized problem. The equation to solve in each step is:

$$\delta\mu_{n+1} = [J_n^T J_n + \alpha^2 L^T L]^{-1} (J_n^T (V_m - F(\mu)) - \alpha^2 L^T L \mu) \quad (8)$$

where: J_n is the jacobian calculated with permeability μ_n the regularized matrix L is a difference between neighboring pixels. We take L [2, 5, 11] as a first order Laplacian operator in discrete form approximated by finite difference. $L(i, j) = -1$ for $i \neq j$ when two elements sharing one node and $L(i, j) = -\sum_{i \neq j} L(i, j)$.

The algorithm starts with an initial permeability distribution. We compute the calculated voltages with forward solution and we compared with predicted voltages. The permeability is then updated using the jacobian matrix. The process is repeated until the measurement data agree with the calculated voltages.

3.2. Computing Jacobian Matrix

The jacobian matrix (J_n) is the matrix of discretization of f in the step n . Each column of the jacobian matrix is the calculated sensitivity term for an element for all measurements. The general form of the sensitivity formula [2, 5, 10] when coil “ i ” is an excited and coil “ j ” is a sensing coil, by ignoring second order terms is:

$$\int_{\Gamma} \delta E_1 \times H_2 n dS = \int_R (-j\omega \delta \mu H_1 \times H_2 + (\delta \sigma + j\omega \delta \varepsilon) E_1 \times E_2) dV \quad (9)$$

where the left-hand side is representing sensing and excitation by surface integral on surface Γ and the right hand-side is the volume integral over the perturbed region R . H_i and E_i are the magnetic and electrical fields when coil i is excited, $i = 1, 2$. the formula relating to sensitivity of permeability is:

$$\frac{\partial V_{ij}}{\partial \mu} = -\frac{j\omega}{I_i I_j} \int_R H_1 \times H_2 dV \quad (10)$$

Then the sensitivity term for each element is:

$$\frac{\partial V_{ij}}{\partial \mu} = -\frac{j\omega}{I_i I_j} \int_{R_{ek}} t_k^i N_e \cdot t_k^j N_e dV \quad (11)$$

Equation (11) gives the sensitivity of the induced voltages pairs V_{ij} of coil i, j with respect to an element and R_{ek} is the volume of element number k . I_i and I_j are the excitation currents for the coils.

4. RESULTS

The model of simulation we chose was constituted of a cylinder A with permeability $\mu_1 = 3 \text{ Sm}^{-1}$ in which we put another cylinder B with permeability $\mu_2 = 4 \text{ Sm}^{-1}$. the two cylinders to be explored, A and B, have a length of 100 mm. The diameter of A is of 100 mm and that of B is of 50 mm. The set is surrounded with 8 induction coils of cylindrical form as indicated in Figure 1. Each one has a length of 10 mm and a diameter of 50 mm and formed of 20 copper wire turns. The T - Ω forward solver is carried out with COSMOSDesignSTAR, and the image reconstruction software is written in C++. The overall number of tetrahedral elements in forward model was 59386 with 10200 nodes, 70242 edges and 119439 faces. The region of interest (Cylinders A and B) which was used in inverse solution included 3888 tetrahedral elements. The simulation frequency is 5 kHz and the measured tensions are replaced by the tensions calculated by the forward solution for the true permeability of the cylinders which we add 2% of their values as noise and error of measurement.

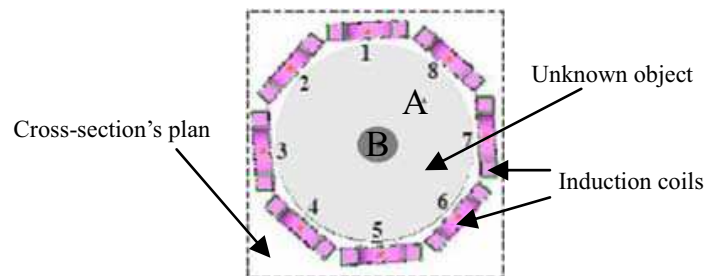


Figure 1: Cross-section of the simulation's model.

After 6 iterations, there is a convergence between the measured voltages and the computed voltages, the average quadratic error is under 8.02×10^{-5} (Figure 2). Figure 3 shows the reconstruction image of the device. At the sixth iteration we have a good result and the image is reconstructed but not yet at first or third iteration.

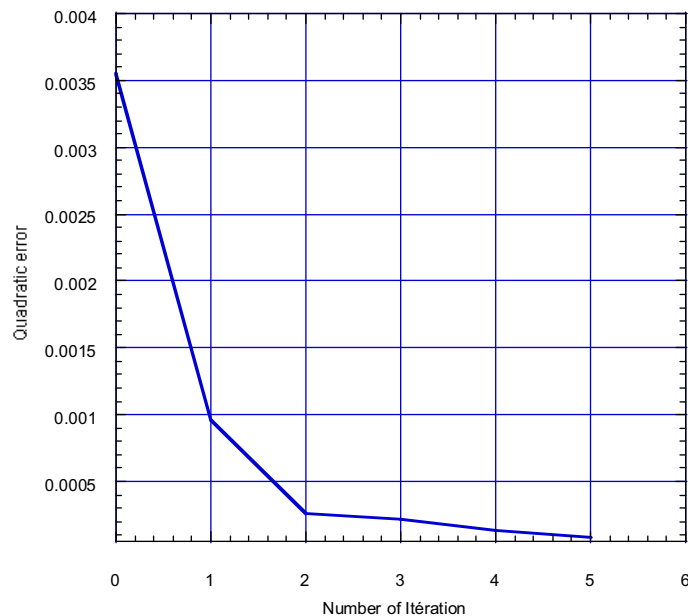


Figure 2: Average quadratic error according to the number of iteration.

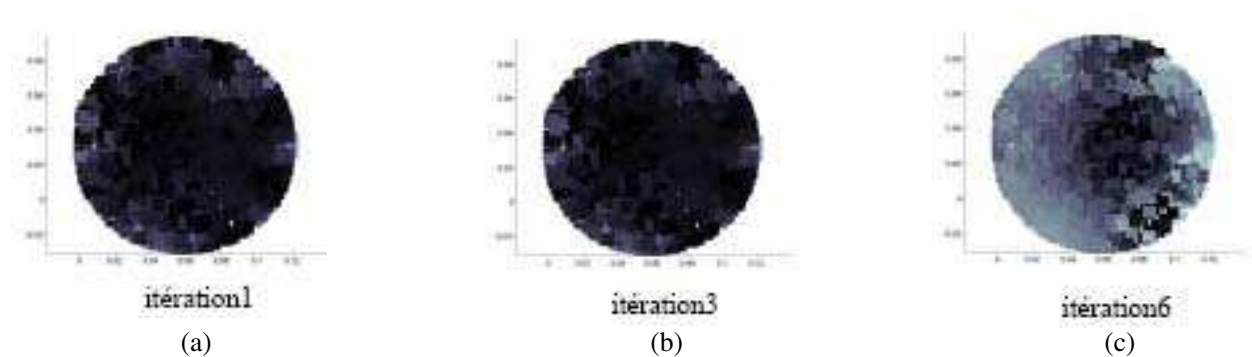


Figure 3: Reconstruction of image: (a) After 1 iteration, (b) After 2 iterations, (b) After 6 iterations.

5. CONCLUSIONS

In this article, we presented a numerical approach to determine the electric distribution of the permeability of a given object starting from measurement of a nondestructive signal. 3-D T - Ω Formulation of Finite Element Method was used to solve efficiently the forward solver and classical Gauss-Newton algorithm with regularization to solve and stabilize the solution of the optimisation problem. In next work, we will study the influence of the presence of several objects having different permeabilities on the performance from this approach, also we will try to improve quality of the image of the explored body.

REFERENCES

1. Norton, S. J. and J. R. Bowler, "Theory of eddy current inversion," *J. Appl. Phys.*, Vol. 73, No. 2, January 1993.
2. Soleimani, M., W. R. B. Lionheart, A. J. Peyton, X. Ma, and S. R. Hignson, "A Three-dimensional inverse finite-element method applied to experimental eddy-current imaging data," *IEEE Transactions on Magnetics*, Vol. 42, No. 5, May 2006.
3. Hollaus, K., C. Gerstenberger, C. Magele, and H. Hutten, "Accurate reconstruction algorithm of the complex conductivity distribution in three dimensions," *IEEE Transactions on Magnetics*, Vol. 40, No. 2, March 2004.
4. Avdeev, D. B., "Three-dimensional electromagnetic modeling and inversion from theory to application," *Surveys in Geophysics*, Vol. 26, 767–799, 2005.

5. Soleimani, M. and K. Jersy-Willuhn, “Image reconstruction for magnetic induction tomography,” *Proceedings of the 26th Annual International Conference of the IEEE EMBS*, San Francisco, CA, USA, September 1–5, 2004.
6. İder, Y. Z. and O. Birgul, “Use of the magnetic field generated by the internal distribution of injected currents for electrical impedance tomography (MR-EIT),” *ELECTRİK*, Vol. 6, No. 3, ©TÜBİTAK, 1998.
7. Babaeizadeh, S., D. H. Brooks, and D. Isaacson, “3-D electrical impedance tomography for piecewise constant domains with known internal boundaries,” *IEEE Transactions on Biomedical Engineering*, Vol. 54, No. 1, January 2007.
8. Babaeizadeh, S., D. H. Brooks, and D. Isaacson, “Improvements of the T - Ω method for 3-D eddy current analysis,” *IEEE Transactions on Magnetism*, Vol. 24, No. 1, January 1988.
9. Bíró, O., “Edge element formulations of eddy current problems,” *Comput. Methods Appl. Mech. Engrg.*, Vol. 169, 391–4057, 1999.
10. Dyck, D. N. and D. A. Lowther, “A method of computing the sensitivity of electromagnetic quantities to changes in materials and sources,” *IEEE Transactions on Magnetism*, Vol. 30, No. 5, September 1994.
11. Borsic, A., W. R. B. Lionheart, and C. N. McLeod “Generation of anisotropic-smoothness regularization filters for EIT,” *IEEE Transactions on Medical Imaging*, Vol. 21, No. 6, June 2002.